FKFS
RESEARCH IN MOTION.

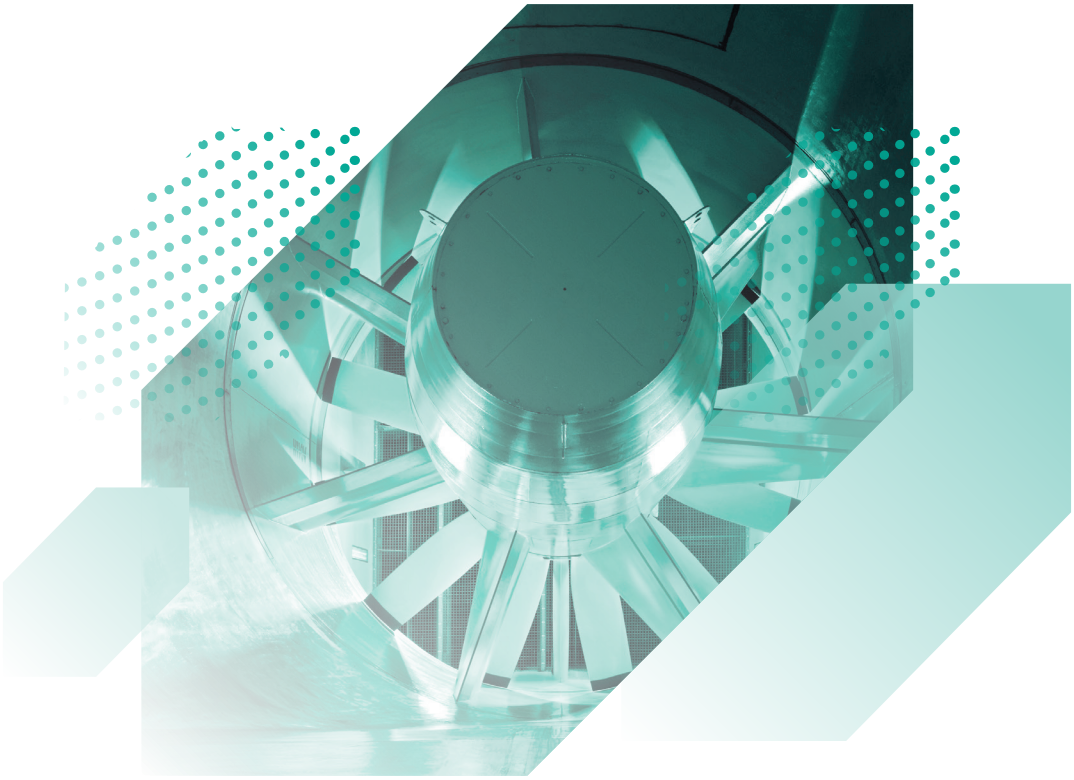

Contributions of:

# 13th FKFS-Conference Vehicle Aerodynamics and Thermal Management

11 – 12 October 2023

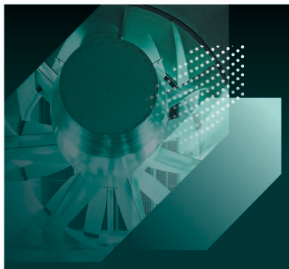

# 13th FKFS-Conference
## Vehicle Aerodynamics and Thermal Management
11 – 12 October 2023

FKFS
RESEARCH IN MOTION.

### Aero Acoustics

**The Identification of Roof Bar Noise Sources using Acoustic Beamforming in a Full-scale Automotive Wind Tunnel**
Oliver Smith, Jaguar Land Rover

**The Effects of LiDAR Sensors on Wind Noise**
Cristiano Pimenta, Volvo Cars

**Towards High Fidelity Aeroacoustics Interior Noise Prediction**
Mauricio Massarotti, Bentley Motors; Simon Martin, ESI Group

### Battery

**Physical & Virtual Assessment Methods for Simulating Thermal Propagation at Cell and Battery Pack level**
Charalampos Tsimis, IDIADA Automotive Technology

**External Thermal Management Concept for BEV Fast Charging**
Marcus Auch, IFS, University of Stuttgart

### Flow Physics

**Stochastic Noise Sources for Broadband CAA at geometrical Variations of a Vehicle**
Philipp Uhl, Mercedes Benz AG

**Low Frequency Aerodynamic and Aeroacoustics Phenomena of Vehicles with Flat Underbody**
Laura Breitenbücher, Dr.-Ing. h.c. F. Porsche AG

**Automotive on-road Flow Quantification with a large scale Stereo-PIV Set-up**
Steffen Hüttig, Volkswagen AG

### Cabin Comfort I

**A Hybrid Approach to the Evaluation of Thermal Comfort in Passenger Vehicles**
Daniel Gehringer, IFS, University of Stuttgart

**A 1D Model for Zonal Comfort Estimation and Control in a Passenger Car Cabin**
Anandh Ramesh Babu, Chalmers University

### Wheels & Tyres

**Generating Tyre Geometries Incorporating Real Tyre Deformation for Aerodynamic CFD Analysis**
Johannes Burgbacher, IFS, University of Stuttgart

### Components

**Transient Thermal Simulations of Cabin-Electronic Components**
Gabor Matulik, DS Simulia

**Empowering Engineering Organizations with Deep Learning: Inverter Cold Plate Optimization for an Automotive Supplier**
Kosmas Kritikos, Neural Concept

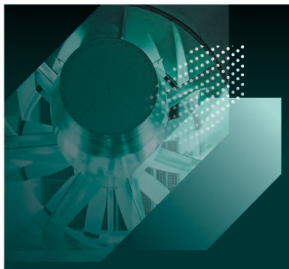

# 13th FKFS-Conference
## Vehicle Aerodynamics and Thermal Management
11 – 12 October 2023

FKFS
RESEARCH IN MOTION.

**Wind Tunnels**

**Upgrade on CAERI Automotive Full-Scale Aero-acoustic Wind Tunnel Introduction**
Qingyang Wang, CAERI

**Reduction of Flow Fluctuation with Vortex Generating System**
Ju Yeol You, Hyundai Motors

**The new DNW-LLF Automotive Test Section**
Henri Vos, DNW

**Vehicle Level Simulation**

**Thermo-Engineering - Simulation-based Modular Development Process for Thermal Management of Electric Vehicles**
Fabian Armbruster, Peter Ambros, TheSys GmbH

**Holistic System Simulation to Address Thermal Management Challenges in Fuel Cell based Mobility Platforms**
Christoph Böttcher, Gamma Technologies

**Aerodynamics I**

**Shape Optimization Investigation of Next Generation Truck Design for Aerodynamic Efficiency**
Brian McAuliffe, NRC Canada

**Aerodynamics II**

**Upgrade of the Ontario Tech ACE Climatic Wind Tunnel to a Climatic and Aerodynamic Wind Tunnel**
John Komar and Patrick Smith, Ontario Tech University

**Thermal Modelling**

**Advanced CHT Simulations for Brake Disc Cooling Applications Using iconCFD**
Christian Taucher, ICON TCP

**Sustainable Thermal Management using multi-fidelity AI-models**
Patrick Vaudrevange, TWT GmbH Science & Innovation

# The Identification of Roof Bar Noise Sources using Acoustic Beamforming in a Full-scale Automotive Wind Tunnel

Oliver Smith, Nicholas Oettle

Aeroacoustics - Vehicle Efficiency
Jaguar Land Rover Ltd.
Gaydon
Warwickshire
CV35 0RR
United Kingdom

osmith@jaguarlandrover.com
noettle@jaguarlandrover.com

**Abstract:** Increasingly, across global markets, external accessories such as roof cross bars are being fitted by vehicle owners not only for temporary functional use but also semi-permanently for their aesthetics. The aerodynamic interaction of the flow around accessories, such as roof bars, and their parent vehicle can generate significant aeroacoustic noise sources. These may be aeolian or highly tonal in nature and of particular annoyance to the occupants. This, in combination with the industry trends of increased refinement, means the aeroacoustic performance of accessories is becoming more important to vehicle designers as the end user expectation and usage case changes.

This paper presents the capture and visualisation of typical aeroacoustics phenomena and acoustic error states that can present around roof bars fitted to a production vehicle. These are namely tonal sources due to vortex shedding and Helmholtz resonance, as well as the broadband sources from the interaction of the roof bars, their mounting system, and the parent vehicle.

The visualisation is conducted by applying both acoustic beamforming in a full-scale aeroacoustic wind tunnel and additionally the use of a validated Lattice Boltzmann Method CFD code. This enables key phenomena to be identified thus demonstrating that the toolsets can be used to design-out or optimise the form to minimise dissatisfactory performance.

# 1 Introduction

As passenger vehicles become more refined, occupants are becoming more sensitive to any increase in cabin noise above that experienced in their standard vehicle. This applies to both broadband and discrete tonal sounds and is exacerbated by the transition to electrified powertrains [1].

One potential source of additional noise is the fitment of roof bars to a vehicle. Traditionally, accessories such as roof bars have been fitted by the user temporarily and for functional purposes such as transportation of large items or leisure activities. This voluntary fitment has typically come with some acceptance of a temporary increase in wind noise. Additionally, in some global markets, users are now fitting accessories semi-permanently for aesthetic appeal and vehicle personalisation. In these latter cases, tolerance to accessory noise may be lower and may lead to customer dissatisfaction and complaint if it is not considered and minimised during the engineering of the vehicle and accessory designs.

A common approach to designing roof bars is to utilise an existing bar profile from a catalogue of extrusions. Much of the established literature highlights that, whilst these profiles may have been empirically developed to mitigate the risk of certain aeroacoustic phenomena [2][3][4][5], they are typically not optimised for refinement explicitly, either in isolation or in context of the airflow around the parent vehicle. This is also true of the mounting system. As a result, roof bars can deliver sub-optimal aeroacoustic performance, delivering elevated broadband noise or excessive aeolian tonal sounds and may be objectionable to the user.

The aim of this paper is to demonstrate the use of large microphone array beamforming to identify, localise and visualise some typical aeroacoustic phenomena that may occur over a roof bar system mounted to the parent vehicle. These include a combination of the broadband noise sources and deliberately induced tonal error states, in order to demonstrate breadth of the toolsets' capabilities. The described methods can allow engineers to identify and mitigate or minimise the noise-generating features during the design process.

# 2 Methodology

## 2.1 Acoustic Beamforming using the FKFS beamforming array

Acoustic beamforming is a visualisation and measurement technique used to extract and identify noise sources within a broadband far-field soundscape, in both frequency and space.

The signal-processing method implemented in this investigation is *delay and sum* beamforming, working with target locations on an investigation area in this case nodes on a planar mesh at a constant distance from the array [6] [7]. There are two stages to the process: time shifting the noise signals from each microphone, based on the knowledge of the speed of sound and the microphone position relative to the target location; followed by the summation of the total number of microphone signals. For a target location when a noise source is present, the sum of the signals will combine constructively, resulting in a high total signal. For target locations where a noise source is not present, the combination of signals will be at a low level.

The acoustic beamforming system of the FKFS wind tunnel comprises two arrays: a 168 microphone array positioned directly above the vehicle, and a 144 microphone side array, which can be positioned on either side of the vehicle [8] [9] [10]. Both arrays are outside of the jet of the wind tunnel to avoid wind interference and consequently a correction is applied to take into account the refraction effects of the shear layer at a given wind speed. A general image of the arrays within the wind tunnel is shown in Figure 2.

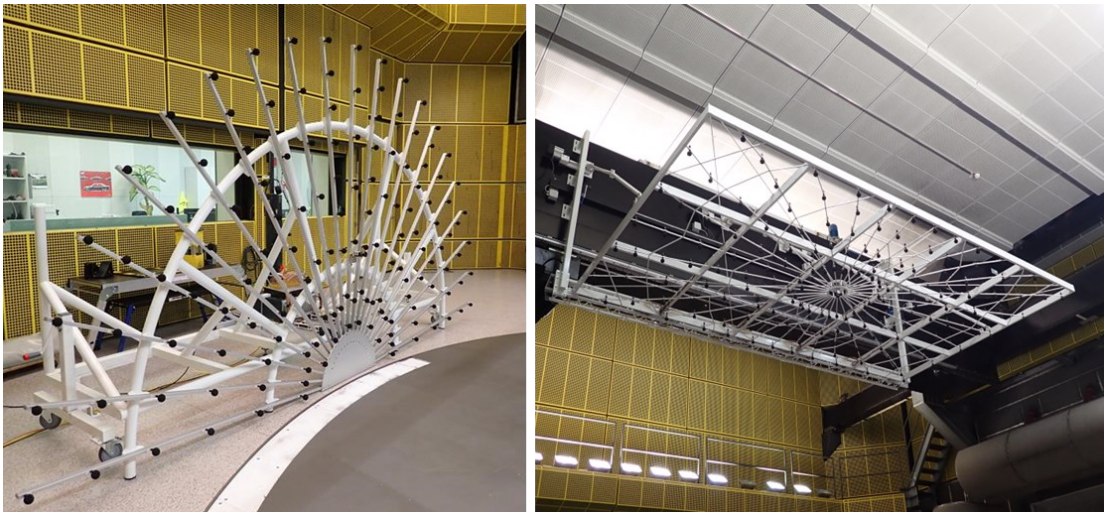

Figure 2: The top and side acoustic arrays of the FKFS wind tunnel

The microphones of each array were connected to separate, time-synchronised, Siemens SCADAS front ends. In addition, a further synchronised front end was positioned in the vehicle, connected to two half-inch microphones positioned between the front and rear seat positions. These were used as reference signals for coherence-based signal processing, allowing exterior noise data to be presented that more coherent to the noise heard inside the cabin and hence identifying exterior sources more relevant to the vehicle occupant. [9] [10]. Acoustic data were recorded for 60 seconds and processed using Siemens Simcenter Test.Lab software.

In addition to the two correlation microphones to support the array measurements, interior cabin noise data were also recorded using HEAD Acoustics HMS IV binaural heads, in each of the four seat positions.

## 2.2 CFD Simulations

To support the engineering of vehicle accessories prior to physical models or parts being available, the phenomena described in this paper can also be captured virtually, using the commercially available CFD code PowerFLOW.

For all simulation examples, the methodology broadly follows the toolset's best practice for capturing and assessing vehicle greenhouse wind noise with some modifications to resolution and measurement for the specific application [11].

## 2.3 Vehicle and Test Conditions

The vehicle was tested experimentally using the FKFS full-scale aeroacoustic wind tunnel of the University of Stuttgart in Germany [12][13]. The comparable virtual vehicle model was externally complete, suitably detailed and meshed to the tool's best practice for aeroacoustic simulation. An image of the physical and virtual vehicle are shown in Figure 3.

Figure 3: The vehicle under test in the wind tunnel and virtual representation

The virtual and physical tests were conducted at a variety of onset flow speeds between 80 and 160 kph, covering a range of typical driving conditions.

The content of this paper focusses the roof bar system in three configurations: the series production installation in order to characterise and visualise roof bar noise with the tools demonstrated; with the rubber T-track cover removed and replaced with a smooth surface, in order to induce von Kármán vortex street in the wake and mid-frequency howling; and with the rubber cover removed to expose the T-track cavity to the airflow, in order to induce Helmholtz resonance and whistling.

# 3 Results

## 3.1 Baseline Roof Bars

As a baseline, the production roof bars were first evaluated. Whilst they are audible in the cabin, they are viewed to perform acceptably and without error state, so this first use case demonstrates how the toolsets can be used to identify specific noise sources within the broadband – potentially providing scope for further optimisation. Figure 4 shows a rendering of the installed bars. Note the castellated rubber 't-track' cover strip along the top surface.

Figure 4: A rendering of the baseline roof bars

Figure 5 shows the resulting interior noise spectra measured at the front microphone position versus wind speed in the wind tunnel. The wind speed in the wind tunnel was progressively increased at a rate of 1 kph/s, during which the interior acoustic data was continuously recorded.

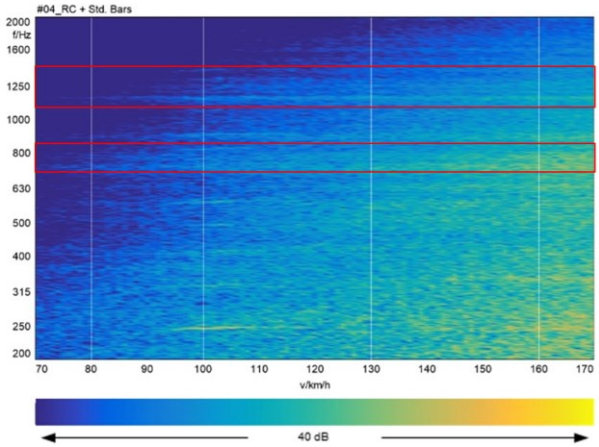


Figure 5: 3D noise map of interior noise spectra versus wind speed for baseline roof bars. 800Hz and 1.25 kHz one third octave bands bound by red boxes.

The figure shows an overall progressive increase in SPL with flow speed, as shown by the colours of the map becoming progressively lighter as the wind speed increases. As these roof bars are considered to perform acceptably for this vehicle, the features and acoustics sources of note are subtle but are highlighted by the horizontal striping patterns on the graph. The frequency of these generally do not change with flow speed, indicating that the sources increase in a broadband manner.

The examples that follow investigate the subtle stripes within both the 800 Hz and 1.25 kHz one-third-octave bands (as highlighted in Figure 5) in order to demonstrating the toolsets' abilities to identify specific noise sources within the broadband soundscape.

Considering the contribution beamforming contours, presenting data coherent to the interior reference microphone in the front of the cabin, for the 800 Hz one-third-octave at 160 kph (Figure 6), it is clearly highlighted that the cross bars as the dominant acoustic source of the striping seen in Figure 5. It is also notable that the rear bar presents a stronger source than the front one. This is due to the wake of the front bar interacting with the rear.

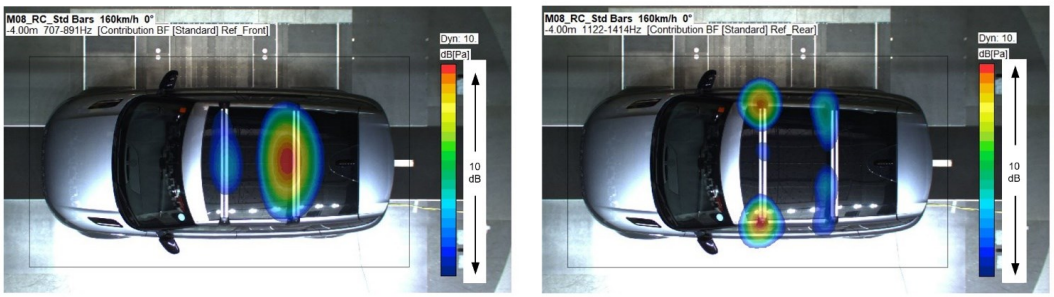


Figure 6: Contribution beamforming of baseline roof bars (800 Hz third-octave left, 1.25 kHz right)

If the performance at 800Hz were deemed to be unacceptable, this result would direct the engineers to consider either the bar profile or relative position of the rear bar to the front in order to reduce the noise generated. When the same correlated beamforming contour results are considered for the 1.25 kHz one-third-octave band, it is instead apparent that the mounting feet are the dominant noise source. This result would guide engineers to further optimise the fairings of the mountings if there was a desire to reduce the noise in these frequencies.

Comparable results are also obtainable from the CFD method, highlighting the dominant noise sources at both frequency bands in Figure 7.

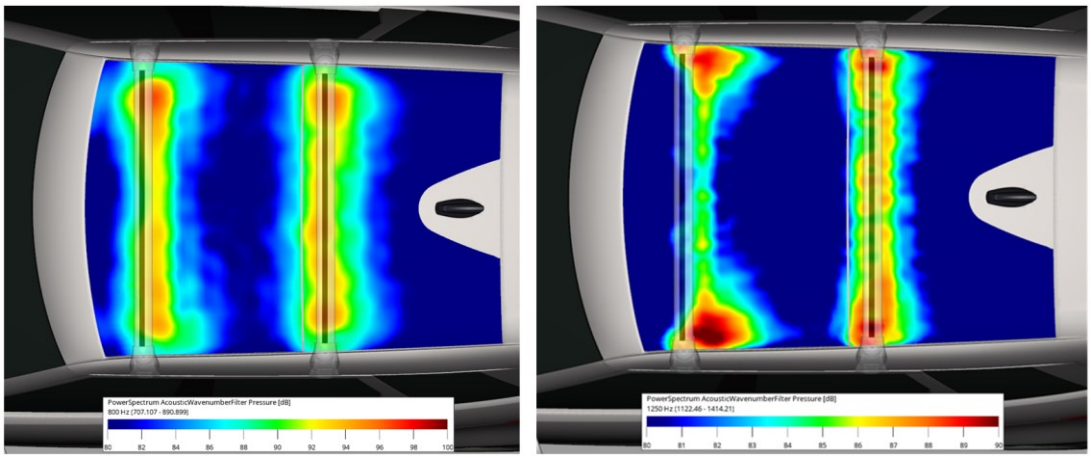

Figure 7: One-third octave band filtered acoustic dB maps of the production roof bars (800 Hz left, 1.25 kHz right)

The use of these techniques demonstrates that even with the cross bars performing in an acceptable manner, the most significant audible noise sources can be identified and could allow further optimisation of bar shape and position, and perhaps more significantly optimisation of the fairing around the mounting feet.

## 3.2 Smooth Roof Bars

On an aerofoil, at higher Reynolds' numbers (greater than $10^5$ based on chord length) or where the boundary layer on an aerofoil is tripped, the boundary layer becomes turbulent. For an aerofoil with a finite thickness where the base pressure is low, the boundary layers from the upper and lower surfaces can interact, forming the well-known von Kármán vortex street behind the aerofoil. The fluctuating unsteady pressures in the wake generate a noise source consistent with that of a dipole [14].

In the case of roof bar profiles that are designed primarily for load carrying, the profile is often rather blunt. This can lead to the aforementioned vortex shedding, unless alleviated through approaches such as the addition of a castellated strip on the baseline bars.

To investigate how the acoustic sources may be visualised in the case of a bar that presents the blunt trailing edge tonal noise, the castellated strip of the baseline bars was removed with the open T-track covered forming a continuous aerofoil profile. This was achieved using thin aluminium tape in the wind tunnel, whereas in the simulation this was achieved though modification to the geometry, as shown in Figure 10.

Figure 10: A rendering of the roof bars with the T-track cover removed and the cavity tangentially covered

Figure 11 shows the interior noise map during a speed sweep in the wind tunnel. A clear tonal feature is visible on the noise map, increasing monotonically with speed, with the peak level remaining relatively constant.

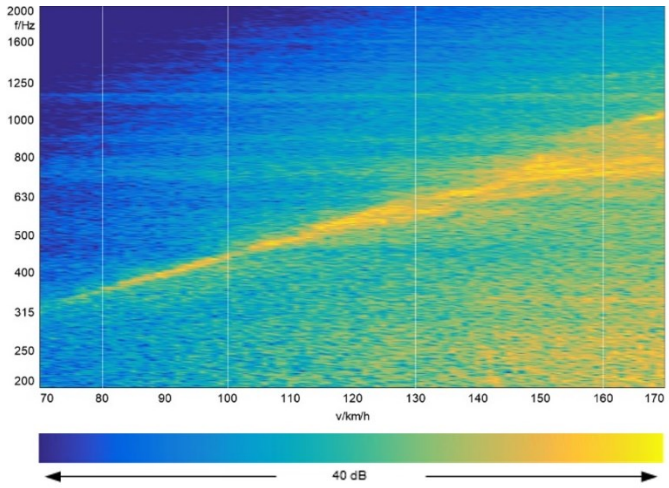


Figure 11: 3D noise map of interior noise spectra versus wind speed for roof bars with T-track cover removed and smoothed over.

Von Kármán vortex shedding can be characterised using non-dimensionalised frequency as the Strouhal number, St, defined by Equation 1, where $f$ is frequency, $U$ is oncoming flow speed and $h$ is a characteristic dimension of the profile.

$$\mathrm{St} = \frac{fU}{h}$$

Equation 1: Strouhal number definition

By non-dimensionalising frequency in terms of Strouhal number, at four sampled velocities, the peak tonal shedding frequency at each flow speed collapse onto a single Strouhal number (Figure 12). This indicates the tone is due to periodic coherent vortex shedding and scales with vehicle velocity. Given the order of magnitude assumptions in terms of characteristic oncoming flow speed and dimension of the bars, the resulting Strouhal number between 0.1 and 1 is consistent with the literature [15] [16].

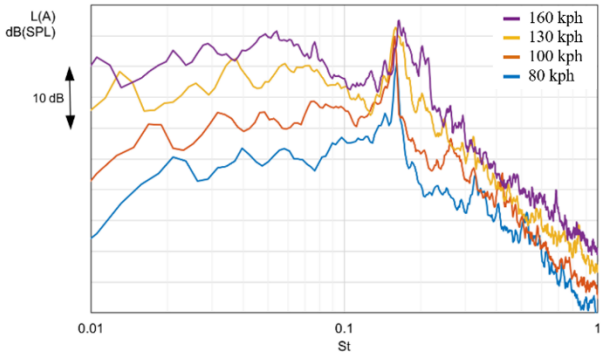


Figure 12: Interior noise spectra at discrete wind speeds of the roof bars with T-track cover removed and smoothed over, based on Strouhal number

Figure 13 shows contribution beamforming contours of the smooth roof bars at 160 kph, presenting data from the 800 Hz third-octave band, which captures the main shedding peak frequency at this speed. capturing shedding peak at 160 kph.

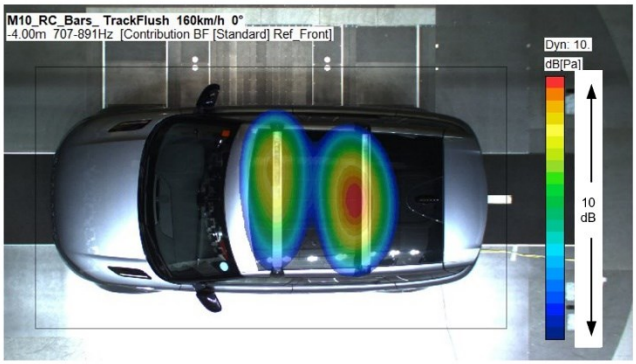


Figure 13: Contribution beamforming of roof bars with T-track cover removed and smoothed over (800 Hz third-octave)

The noise sources from the bars display significantly increased noise generation when compared to Figure 6, particularly from the front bar. This clearly identifies the noise issue, directing development to changing the bar profile (by adding castellated strips or otherwise) in order to reduce this noise.

The regular vortex shedding, characteristic of the von Kármán vortex street, is shown in the velocity magnitude slice from the CFD simulation at 160 kph of Figure 14.

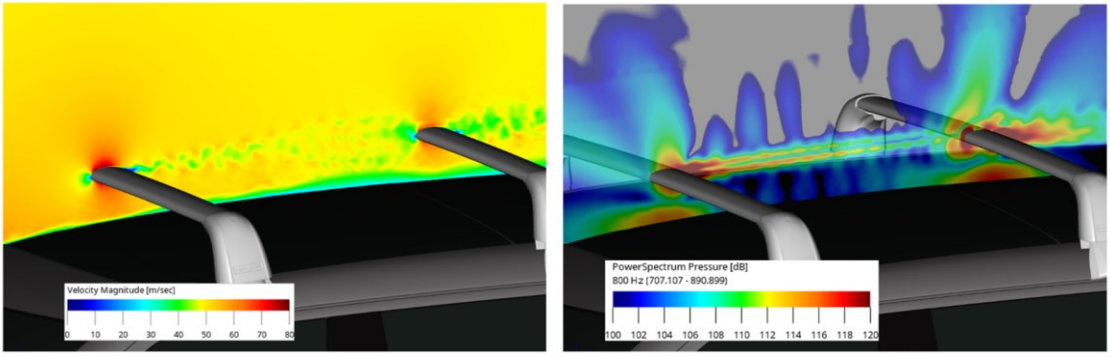


Figure 14: y=0 slice at velocity magnitude (left) and 800 Hz third-octave pressure fluctuations (right) at 160 kph of smooth roof bars

The level of shedding is greater from the rear bar, likely due to a degree of constructive interference with the shedding from the front bar, since the bars are of the same profile and consequently shed at the same Strouhal number. The increased noise generation from the rear bar is identified in the 800 Hz third-octave pressure fluctuation slice, showing good agreement with the equivalent beamforming image of Figure 13, with virtual and physical methods able capture the key aeroacoustic phenomena to guide engineers in performance enhancement.

### 3.3 Open Channel Roof Bars

Another common issue that can occur in roof bar design are high-frequency tonal whistles due to open slots and cavities. Roof bars commonly have such slots to position mounting hardware for load carrying, and manufacturers often provide strips to cover these to prevent acoustic issues. To investigate how these may be visualised, the castellated strip of the baseline bars was removed exposing the open T-track as presented in Figure 16.

Figure 16: A rendering of the roof bars with the T-track open

As before, the bars were added to the vehicle in the wind tunnel and continuous interior noise measurements were made as the wind speed was progressively increased. The resulting noise map, comparable to those measure for the previous two roof bar configuration is shown in Figure 17.

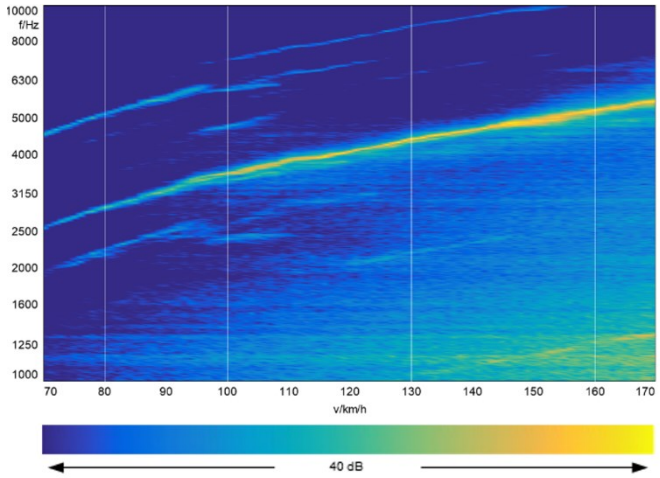


Figure 17: 3D noise map of interior noise spectra versus wind speed for roof bars with T-track open. Strong tonal features are visible and scale with vehicle velocity.

A number of tonal features and harmonics are visible, scaling with wind speed. Cavity noise is produced from a coupling of aerodynamic excitement with an acoustic response. In this case, the mechanism is similar to that of sunroof boom [17]. Here, the transient characteristics of a shear layer instability over a cavity excite an acoustic mode of the open roof bar cavity [18]. Multiple tonal peaks can be generated, due to higher order Rossiter modes coupling with the Helmholtz modes at different speeds. In addition, the roof bars themselves being of finite length have multiple acoustic modes which may also be excited.

Figure 19 shows contribution beamforming contours of the roof bars with the T-track opened at 100 kph, presenting data from the 4 kHz third-octave band, capturing the main shedding peak frequency at this speed.

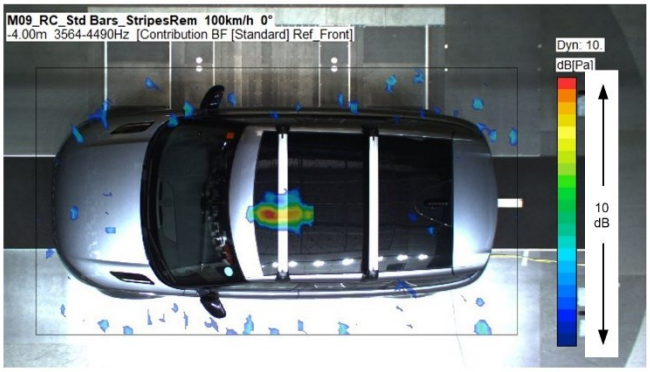


Figure 19: Contribution beamforming of roof bars with T-track open (4 kHz third-octave).

The wind tunnel beamforming contours shows a high-level noise source from front bar, near the centreline of the car. The nature of this is possibly due to the tonal nature of the source coupling with a longitudinal mode of the open roofbar section, with the antinode present at this point.

Visualising the Helmholtz resonance whistling virtually is also possible though the use of slices though the fluid domain. Figure 21 depicts a single frame in the transient simulation shaded by the local time derivative of pressure. The strong acoustic pressure fluctuations from the whistle monopole are clearly visible radiating from the front bar, matching the spatial location observed through acoustic beamforming in the wind tunnel.

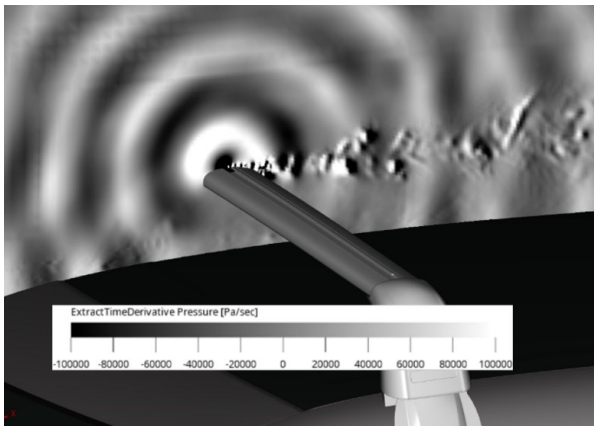


Figure 21: Snapshot of y=0 slice with the time derivative of pressure shown.

## 4 Conclusions

The aim of this paper was to demonstrate the application of large microphone array beam forming to visualise the aeroacoustic performance of roof bars when fitted to a parent vehicle. This includes the identification of deliberately induced aeroacoustic error states that may occur on such systems during development and that would be objectionable to the consumer.

Taking the measured data from inside a vehicle cabin, a number of acoustic features were identified in the acoustic spectra. Through the use of the acoustic array, the source of these features were clearly identified, providing direction to the development process, focussing development to maximise customer benefit. In addition, acoustic beamforming was demonstrated to identify two common roof bar aeroacoustic error states that may occur in development or when exploring a new concept.

Through the use of a prototype parts and an aerodynamic buck or virtually in CFD simulations, these methods therefore may allow for earlier assessment of new cross bar profiles, novel design concepts or vehicle pairings, ultimately reducing the risk of late change and costly empirical fixes being developed.

## 5 Reference list


1. Oettle, Nicholas, and David Sims-Williams. "Automotive aeroacoustics: An overview." Proceedings of the Institution of Mechanical Engineers, Part D: Journal of Automobile Engineering 231, no. 9 (2017): 1177-1189.
2. Karbon, Kenneth J., and Urs D. Dietschi. "Computational analysis and design to minimize vehicle roof rack wind noise." SAE transactions (2005): 649-656.
3. Lee, Myunghan, Jeonghan Lee, and Daehoon Kim. Reduction of Aeolian Noise from Roof Rack Crossbars Using Asymmetric Cross-Section Geometry. No. 2002-01-1275. SAE Technical Paper, 2002.
4. Massarotti, Mauricio R., and William R. Wolf. Understanding the aeroacoustic noise mechanisms and noise control techniques of roof rack systems. No. 2018-36-0025. SAE Technical Paper, 2018.
5. Senthooran, Sivapalan, Bradley D. Duncan, David Freed, Dena Hendriana, Robert E. Powell, and John Nalevanko. "Design of roof-rack crossbars for production automobiles to reduce howl noise using a lattice Boltzmann scheme." SAE Transactions (2007): 1974-1982.
6. J. Christensen and J. Hald, “Technical review: Beamforming,” Brüel Kjær, Tech. Rep., 2004.
7. H. Vickers, “The enhancement of beamforming analysis on road vehicles by the introduction of cross-correlation functionality,” Master’s thesis, Durham University, 2017.
8. Blumrich, R, M. Riegel, N. Oettle, H. Vickers, B. Verrecas, A. Finez, O. Minck, “A Comparison of Wind Tunnel Array-Based Aeroacoustic Measurement Techniques”. International conference on vehicle aerodynamics 2018, Birmingham, 16 – 17 October, 2018.
9. Riegel, M., Reinhard Blumrich, Olivier Minck, Bart Verrecas, Nicholas Oettle, Harriet Vickers. “New Large Microphone Array at the FKFS Wind Tunnel”. 12th FKFS conference, Stuttgart, 1 – 2 October, 2019.
10. Siemens Digital Industries Software, Press release: FKFS achieves a winning difference for its aeroacoustic wind tunnel from Siemens Simcenter. (2019)
11. Smith, O. and Oettle, N., “Visualisation of Roof Bar Noise Sources through the Use of Acoustic Beamforming and Computational Aeroacoustics,” SAE Technical Paper 2023-01-0840, 2023, doi:10.4271/2023-01-0840
12. Blumrich, Reinhard, Nils Widdecke, Jochen Wiedemann, Armin Michelbach, Felix Wittmeier, and Oliver Beland. "New FKFS technology at the full-scale aeroacoustic wind tunnel of University of Stuttgart." SAE International Journal of Passenger Cars-Mechanical Systems 8, no. 2015-01-1557 (2015): 294-305
13. Künstner, Rudi, Jürgen Potthoff, and Ulf Essers. "The aero-acoustic wind tunnel of Stuttgart University." SAE transactions (1995): 1119-1135.
14. Hansen, Colin H., Con J. Doolan, and Kristy L. Hansen. Wind farm noise: measurement, assessment, and control. John Wiley & Sons, 2017.
15. Blake, William K. Mechanics of flow-induced sound and vibration, Volume 2: Complex flow-structure interactions. Academic press, 2017.

16. Brooks, Thomas F., and T. H. Hodgson. "Trailing edge noise prediction from measured surface pressures." Journal of sound and vibration 78, no. 1 (1981): 69-117
17. Oettle, Nicholas, Mohammed Meskine, Sivapalan Senthooran, Andrew Bissell, Gana Balasubramanian, and Robert Powell. "A computational approach to assess buffeting and broadband noise generated by a vehicle sunroof." SAE International Journal of Passenger Cars-Mechanical Systems 8, no. 2015-01-1532 (2015): 196-204
18. Rossiter, J.E., 1964, Wind-tunnel experiments on the flow over rectangular cavities at subsonic and transonic speeds, Aeronautical Research Council Reports and Memoranda, Technical Report 3438, (1964)

# The Effects of LiDAR Sensor shape on Wind Noise

Cristiano Pimenta[1], Danilo Agurto[1], Athanasia Nianioura-Karamousalidou[2]

Volvo Cars

Dassault Systèmes

## Abstract

To enhance driver assistance systems and enable automated driving capabilities for the next generation of vehicle lines, a cutting-edge new technology, LiDAR (light detection and ranging) sensors, has been integrated into vehicles to increase safety and save lives. The implementation of such systems has brought new challenges for the Wind Noise attribute since the LiDAR positioning on the roof is optimal for scanning the surrounding environment. Despite of the technical challenges to integrate LiDAR system, the exterior surface design is very sensitive to Wind Noise, where local flow can reach extremely high velocities.

More often, vehicle designs trend towards full roof glazing, and the addition of a blunt body due to a LiDAR sensor on the roof generates a new source of noise, combined with an easy transfer path for the sound. To validate the current simulation setup, a correlation between high-fidelity aeroacoustics simulations and measurements in a wind tunnel is performed. Wall pressure time history is recorded for positioned microphones and glazing panels. The results are analyzed in the spectral domain, where test and numerical data are compared. Additionally, the transmission of sound through the glass panels is analyzed using Statistical Energy Analysis (SEA) methodology.

[1] Volvo Cars
[2] Dassault Systèmes

## 1 Introduction

In the pursuit of safer and more advanced automated driver-assistance systems (ADAS), LiDAR sensors have gained prominence for their pivotal role in advancing driver assistance systems towards fully autonomous vehicles. LiDAR sensors perform scans of the surrounding environment, translating the physical world into real-time 3D digital images with a high level of accuracy [1]. This technology is based on a laser sensor that is composed of two main components, a transmitter which emits light in a range of wavelengths and a receiver which captures the reflected signal from the environment [1]. To ensure precision, accuracy, and resolution, LiDAR placement on the vehicle's roof is essential for capturing vital environmental and pedestrian information. However, this technology introduces new challenges, particularly concerning to LiDAR cover shape, which intersects with the exterior surface design. Wind noise levels may be affected by the LiDAR installation, as the front area of roof commonly exhibits the highest kinetic energy in the flow field, making it a sensitive area susceptible to flow separation, impacting in noise generation and sound propagation. Moreover, the trend towards extensive roof glazing in contemporary vehicle design exacerbates wind noise issues. This could generate an imbalance feeling for the customer due to the perception of sound emanating from a specific location, in this case the roof [2].

The wind noise team collaborates closely with the design department, directly influencing the exterior styling by providing guidelines and recommendations to enhance the overall driving experience for customers. In the early stages, high-fidelity CFD simulations can be applied to predict wind noise levels and support the design process, identifying and improving specific features that mitigate sources of noise induced by unsteady flow. An assessment of numerical results is required to ensure that the simulation setup can accurately capture the important features in the turbulent flow related to noise generation. Previous validations of high-fidelity CFD simulations for exterior wall pressure fluctuations, specifically focusing on side glass can be found in the literature [3, 4]. Hartmannn et al. [5] conducted an extensive validation of various CFD solvers used to simulate transient pressure loads on side glass, comparing them with experimental data. The integration of the SEA approach to predict vehicle interior noise is well-established, and a detailed correlation of interior noise measurements with numerical results is presented by Moron et al [6].

This paper investigates the impact of LiDAR integration to exterior design and its effect on sound generation. A validation of numerical simulation setup is performed by correlating exterior wall pressure fluctuation with measurements conducted in wind tunnel. The strategic placement of probes was carefully selected to validate the flow field downstream of the LiDAR's exterior shape.

## 2 Methodology

The primary objective of this study is to validate numerical simulations of exterior airflow by establishing correlations between turbulent pressure fluctuations at different positions and corresponding measurements. To achieve this goal, we utilized a high-fidelity CFD solver, SIMULIA PowerFLOW 6-2021.R7, which is based on the Lattice-Boltzmann/Very-Large-Edge-Simulation method [7], to obtain numerical data for the airflow field. Physical measurements were conducted in the state-of-the-art facilities at FKFS (Forschungsinstitut für Kraftfahrwesen und Fahrzeugmotoren Stuttgart), where surface-mounted microphones were strategically positioned on predefined regions of the vehicle's roof. Microphones used here were GRAS 48LX-1 UTP (Ultra-Thin Precision) units with fairings. Figure 1 shows both numerical model (a) used for the simulation and physical object (b) tested in the wind tunnel.


(a) (b)

Figure 1: Figure (a) illustrates the numerical model, while Figure (b) depicts the prototype used for conducting measurements.

The vehicle was assessed in a fully taped condition as shown Figure 1b, where all the split lines and sealing system has been covered with tape. Both experimental and numerical condition were set to 130 km/h and a steady upstream airflow with zero yaw angle. The measurement time in the wind tunnel was set to 30 seconds after the flow field had stabilized.

The numerical methodology aims to replicate the same wind tunnel characteristics to represent a similar flow around the car. The simulation model is presented in Figure 1a, where a complete vehicle is used, and a digital tape is carried out for the same regions as with the test object. The boundary conditions include a velocity field at the inlet as the wind tunnel, frictionless condition at the side walls and the floor, and a ambient static pressure at the outlet. A friction section with the same length as the wind tunnel is employed to develop the turbulent boundary layer upstream. The fluid discretization is defined by regions where the smallest voxel size is 0.5 mm to capture the flow characteristics accurately in regions of interest, and a high sampling rate is employed to save pressure time history for all probes and glazing panels to ensure accurate results up to 6000 Hz. The initial flow condition is defined by a coarse case, which contains less levels of voxels refinement, focus to stabilize the fluid flow. These results are utilized to initialize the initial conditions for the fine simulation, resulting in a fast convergence of the initial transient. The total CFD simulation time corresponds to one second of real-time. The wall pressure time history for all probes is recorded during the last 0.9 seconds, while the wall surface pressure data is saved for the final 0.5 seconds.

For the exterior setup, the selection of microphone positions was guided by prior CFD data as illustrated by Figure 2, with a specific focus on capturing the highest energy content of flow characteristics due to the presence of a LiDAR device installed on the roof. The LiDAR's positioning in the front roof area exhibits the highest kinetic energy within the fluid domain, and the external configuration of the LiDAR cover proves to be particularly susceptible to flow separation. Sound generation resulting from flow separation in this region could be of utmost importance, especially when considering the concept of a glazed roof. To comprehensively evaluate the flow characteristics influenced by the presence of LiDAR, we concentrated on installing microphones in the Y0 section (centre line) behind the LiDAR exterior shape, ensuring accurate representation of the energy content.

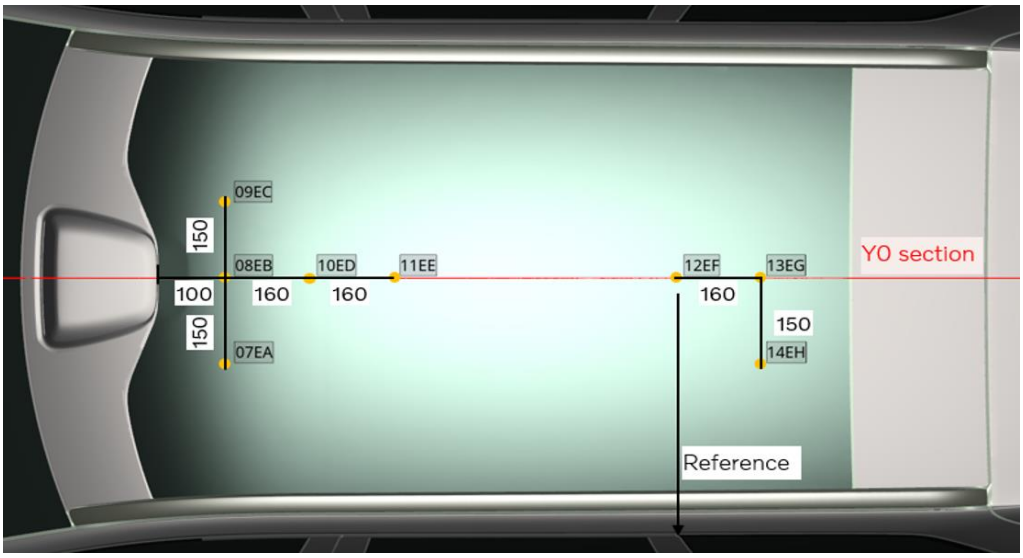


Figure 2: Definition of probe placement on the vehicle roof with LiDAR for numerical simulation and flush-mounted microphone installation.

While the primary objective of this study was to validate numerical simulations of exterior airflow, we also assessed vehicle interior noise. For interior analysis, Statistical Energy Analysis (SEA) methodology is employed [8], offering insights into sound pressure levels and noise distribution within the cabin. The specific SEA model used was from the SUV 4 cabin type of SIMULIA PowerACOUSTICS 6-2021-R4. . For this investigation, only the sound transmitted through the greenhouse was considered with default materials and damping values for the glazing panels.

## 3 Results and Discussion

An assessment of the high-fidelity CFD simulation setup is conducted by correlating wall pressure fluctuations at specific positions from numerical data with measurement data. The objective of this validation is to ensure that CFD simulations can accurately capture all turbulent features responsible for sound generation. LiDAR can be regarded as a blunt body sticking out into the flow field, situated in a region with the highest kinetic energy, making it highly susceptible to inducing flow separation. Ensuring spatial and temporal refinement in the CFD methodology is crucial for achieving accurate results for wind noise. Figure 3 presents the correlation between numerical and experimental data of exterior wall pressure fluctuations for three microphones and a power average of all tested microphones. Our focus is to highlight the results that exhibit the highest energy contribution. Microphone 8EB is the closest one to the trailing edge of the LiDAR exterior shape and is expected to face more challenges in capturing the fluid dynamics in this region. Figure 3a demonstrates that CFD results have estimated higher levels of wall pressure. Nevertheless, the results are well correlated and contain the highest energy among all microphones in both numerical simulation and measurement. This can be explained by the proximity of the LiDAR trailing edge and the flow transition region. Following the center line, microphone 10ED as shown in Figure 3b, exhibits the best correlated results. This indicates that the flow field in this region is more stable. Microphone 11EE is positioned further downstream, allowing us to verify how the turbulent energy generated by LiDAR is advected with the airflow. The results are well correlated as presented in Figure 3c, though some discrepancies are noticeable for high frequency content. This could indicate that some of smaller turbulent edges were dissipated faster in the CFD models compared to the experimental data. Furthermore, the power average of all microphones is shown in Figure 3d, and the results from numerical simulation are representative of the total acoustic energy of the glass roof.

The surface wall pressure time history for roof panel is analyzed using the powerspectrum calculation from PowerACOUSTICS, with 16 Hz frequency resolution. Initially, a Fourier transform is employed to obtain the autospectra (dB maps) in a broad range of frequency, as illustrated in Figure 4a. These dB maps are used as power inputs for acoustic filtering. These results can be interpreted as comprising convective and acoustics pressure waves on the surface, where the convective component is associated to the turbulent load on the panel, and the acoustics component represents sound propagation within the domain. To focus on the acoustics portion of the data, a wavenumber filter is applied to the power spectrum of wall pressure data. This filter isolates the wavelengths associated with acoustic propagation, effectively separating them from the convective waves (also well known as hydrodynamic component) that travel at the speed of turbulent flow, as shown in Figure 4b. Filtering out the acoustic loads is an interesting technique that enables a more comprehensive analysis of the results since the acoustic waves can be directly transmitted into the interior of the cabin.

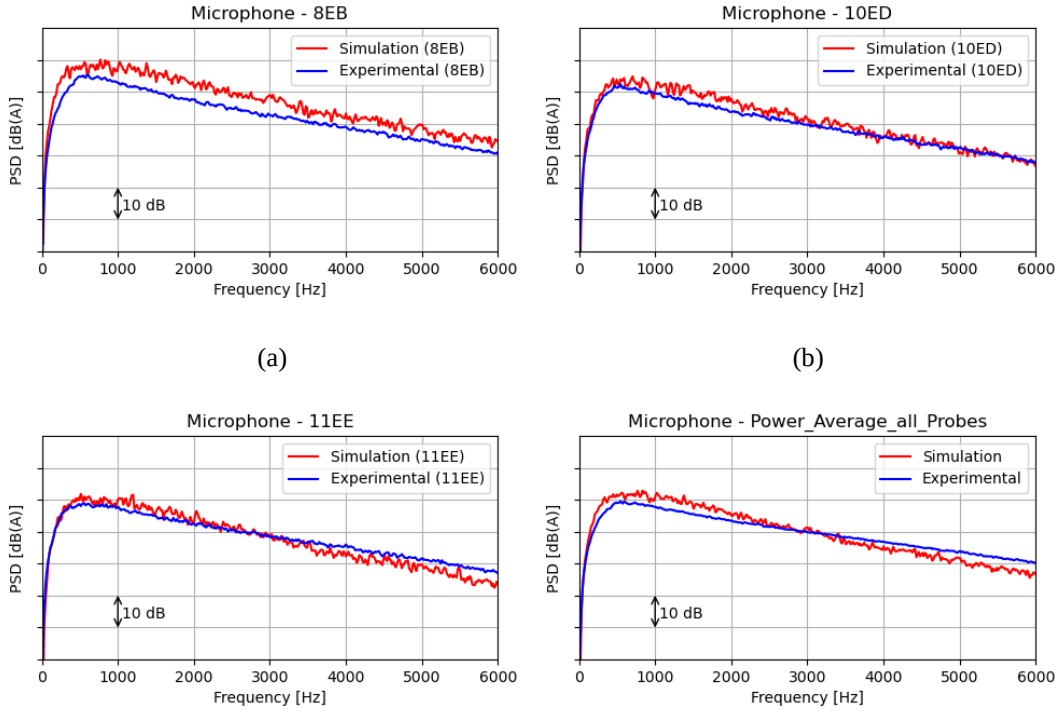


Figure 3: Comparison between experimental and numerical power spectral density for microphone (a) position 8EB, (b) position 10ED, (c) position 11EE and (d) the power average of all probes.

Initially, Figure 4 was used to identify potential positions for installing all the microphones for the current correlation. It's crucial to emphasize that the acoustic load on the roof panel is concentrated closer to the LiDAR device, where we anticipate the dominant noise source associated with the LiDAR's shape. By validating the current simulation setup, both sets of results become valuable tools in the early phases for guiding changes to all features on the LiDAR's surface, with the goal of minimizing noise generation in this specific area.

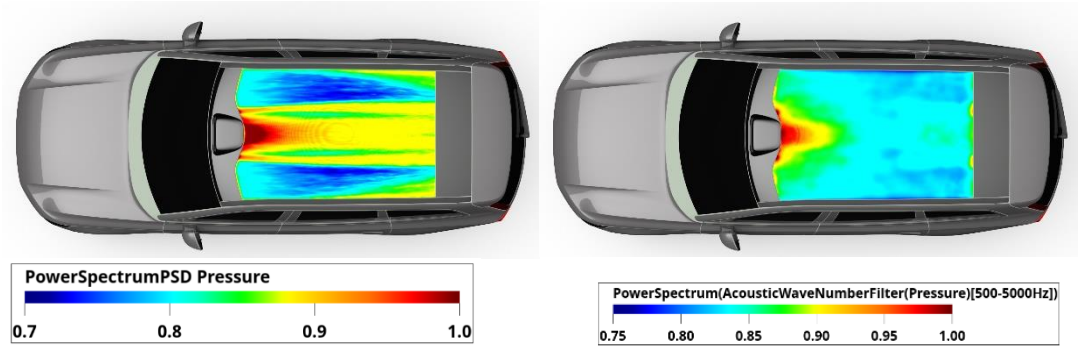


(a) (b)

Figure 4: Wall pressure fluctuation dB map, (a) total pressure load and (b) filtered acoustic load distribution (scales normalized to show maximum value of 1).

The vehicle interior noise estimated by the SEA model is compared with experimental data, as shown in Figure 5. As previously mentioned, the simulation only accounts for the greenhouse contribution, without considering other paths such as the underbody contribution. Despite of the experimental test not being originally intended or prepared for interior noise correlation, the results show a very close match. The predictions capture well the levels and the overall trend quite effectively.

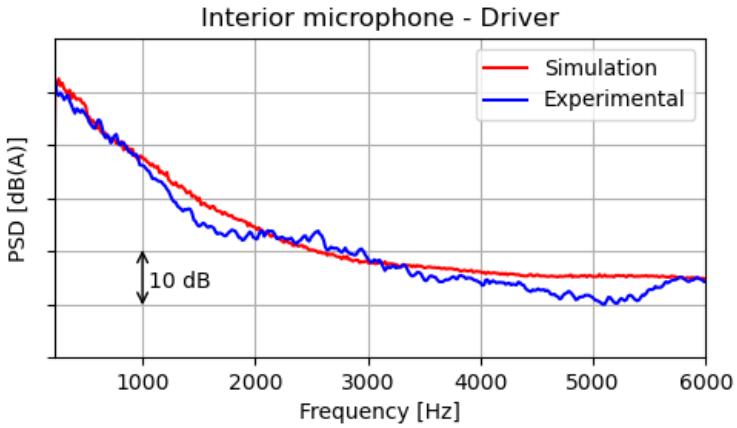


Figure 5: Vehicle interior wind noise at driver position.

## 4 Conclusions

Validation of a high-fidelity aeroacoustics simulation using the SEA model for interior noise prediction is achieved through the correlation of results with measurements conducted in a wind tunnel. With LiDAR device installed on the roof, the comparison between numerical and measurement data reveals a strong correlation for all microphones. However, some discrepancies are observed concerning the measurement positions, where the numerical results from probes closer to the LiDAR exhibit a higher energy content compared to those further downstream. Nevertheless, the power average of all microphone results effectively captures the energy content responsible for the major noise source over the roof area when compared with the measurement data.

The interior noise results were surprisingly good, considering that the primary objective was to validate exterior CFD results. For future advancements, a more comprehensive SEA model validation could be prepared, involving a more detailed numerical model and test object to accurately represent all the physics involved in the transmission of sound to the interior of the cabin. The CFD computations provide accurate results within the frequency range of interest, considering the challenges of representing all aspects of hydrodynamics and propagation in a highly sensitive area. The results presented here demonstrate that the current simulation setup is a useful and reliable tool for predicting wind noise, thereby supporting the implementation of cutting-edge solutions such as the LiDAR system.

## 5 Acknowledgments

We acknowledge Wilhelm Sjödin and Pär Harling for their contribution during the testing phase in FKFS and for their insights into the correlation between simulation and measurement data. We also acknowledge the support provided by Dassault Systèmes with the simulation methodology, and fruitful discussions we had on this topic.

## 6 Bibliography

[1] R. Roriz, J. Cabral und T. Gomes, „Automotive LiDAR technology: A survey,“ *IEEE Transactions on Intelligent Transportation Systems,* Bd. 23, Nr. 7, pp. 6282-6297, 2021.

[2] H. Hoshino und H. Kato, „A New Objective Evaluation Method of Wind Noise In a Car Based on Human Hearing Properties,“ *Acoustical Science and Technology,* Bd. 23, Nr. 1, pp. 17-24, 202.

[3] S. Senthooran, B. Crouse, S. Noelting, D. Freed, B. Duncan, G. Balasubramanian und R. Powell, „Prediction of Wall Pressure Fluctuations on an Automobile Side-Glass Using a Lattice-Boltzmann Method," in *12th AIAA/CEAS Aeroacoustics Conference*, AIAA 2006-2559.

[4] S. Senthooran, B. Crouse, G. Balasubramanian, D. Freed und D. Caridi, „Numerical simulation of wind noise on the sideglass of a production automobile," in *FISITA Paper*, 2006.

[5] M. Hartmann, J. Ocker, T. Lemke, A. Mutzke, V. Schwarz, H. Tokumo, R. Toppinga, P. Unterlechner und G. Wickem, „Wind Noise caused by the A-pillar and the Side Mirror flow of a Generic Vehicle Model," in *18th AIAA/CEAS Aeroacoustics Conference*, Colorado Springs, CO, 2012.

[6] P. Moron, R. Powell, D. Freed, F. Perot, B. Crouse, B. Neuhierl, F. Ullrich, M. Höll, A. Waibl und C. Fertl, „A CFD/SEA Approach for Prediction of Vehicle Interior Noise due to Wind Noise," *SAE Technical Paper*, Nr. 2009-01-2203, 2009.

[7] R. Kotapati, A. Keating, S. Kandasamy, B. Duncan, R. Shock und H. Chen, „The Lattice-Boltzmann-VLES Method for Automotive Fluid, a Review," *SAE Technical Paper*, Nr. 2009-26-057, 2009.

[8] R. H. Lyon, Theory and Application of Statistical Energy Analysis, 1994.

# Towards High Fidelity Aeroacoustics Interior Noise Prediction

Mauricio Massarotti[1], Simon Martin[2], Joseph Venor[2]

[1]Whole-Vehicle Acoustics, Bentley Motors
Crewe, England, United Kingdom
mauricio.ramacciato.massarotti@bentley.co.uk

[2]Vibro-Acoustic Technical Consultancy, ESI Group
Birmingham, England, United Kingdom
simon.martin@esi-group.com, joseph.venor@esi-group.com

**Abstract:** Acoustic refinement is of paramount importance in luxury vehicles, and so therefore is the search for state-of-the-art engineering methods to aid development. This work concerns the application of unsteady compressible CFD and whole-vehicle Aero-Vibroacoustic models to predict interior Aeroacoustic noise from 250 to 5kHz at high cruising speeds. The primary objective of this project is to improve the correlation between fast Greenhouse interior noise predictions to actual measurements made in an Aeroacoustic Wind Tunnel by using the CFD outputs as inputs to whole-vehicle Vibroacoustic SEA models. More accurate base Aeroacoustic predictions lead to more accurate early Project status, a more realistic experience in the NVH Simulator and ultimately robust decisions taken on the overall attribute balancing. Previous studies have demonstrated an interior noise correlation offset of 2 dB across the entire frequency range of interest at an overshot computational cost. Improvements made in fluid discretization, transient time scales, SEA model content and linear panel characterization enabled equally or more accurate results at significantly lower footprint.

## 1 Introduction

Aeroacoustics is one of the primary attributes in luxury vehicles. Within a rapidly developing technology landscape and evolving marketplace, engineers need reliable tools to predict the whole-vehicle Aeroacoustic performance of new products early in the development process. Total Aeroacoustic performance comprises of multiple components such as residual aspiration, discrete phenomena (e.g. aeolian tones, cavity resonance and acoustic feedback), open aperture buffeting and exterior airflow-induced broadband noise, typically known as "Greenhouse Wind Noise". The latter is complex in itself as it encompasses sources of different nature distributed on the Upper Body and Underbody panels, which are transmitted through multiple paths including glazing panels, sealing systems and acoustic lining. In steady-state, the characteristic frequency band is extremely large, audible in the cabin from 250 to 5kHz and above at high cruising speeds. As a rough estimate, sound at frequencies lower than 500-600Hz are typically dominated by sources on the Underbody, and at higher frequency from sources on the Upper Body, as well as their transmission paths. A ride in the Wind Tunnel makes it very clear.

Typically, the first opportunity the Aeroacoustics engineers have to validate the performance of such is by measuring the first off-tooling prototype builds in a Full-Scale Aeroacoustic Wind Tunnel. Common to many OEMs, the vehicles are measured in "masked" condition enabling the separation (root causing analysis) of discrete phenomena, localized aspiration and general source ranking. During Concept phases, Full-Size Clay models built with an acoustic cavity are limited in that purpose as transfer paths are not representative. Numerically, the fast approach, computationally less expensive, is to compute the total pressure field impinging on the glazing panels, either via Hybrid- or Direct Noise Computation, transmit and propagate the noise to the Passenger compartment via multiple Aero-Vibroacoustic formulations based on SEA, FEM and BEM, each with its advantages and limitations [1]. Such approach suffice should one be interested in statusing the Aeroacoustic performance of the vehicle's exterior surface alone, in regards of dipole and quadrupole sound generation mechanisms, as well as assessing the specification of the glazing panels in itself, as unquestionably, some of the glazing panels are the primary transfer path of high frequency broadband Aeroacoustic noise in masked condition.

In luxury vehicles, however, glazing specifications are typically of high specification acoustic attributes, causing other transmission paths to contribute significantly to the whole-vehicle experience. In that sense, it is extremely valid to status (as a key Concept gateway) the predicted whole-vehicle Aeroacoustic performance including Upper Body, Underbody and all the relevant insulation and damping aspects of the Project in scope. To that extent, the reuse of whole-vehicle Vibro-Acoustic SEA models applied to other NVH attributes such as Airborne Road Noise becomes cost attractive.

The method was initially validated on Bentley's third generation luxury sports coupé Continental GT [2]. The final interior 1/3 Octave noise spectra offset between model and test is in the order of 1 to 3 dB across the entire frequency span, proving excellent value. The whole-vehicle SEA model also enables a more complete source ranking including Upper Body and Underbody transfer paths not modelled in typical Greenhouse models. Previous work demonstrated that the transmission of high frequency noise through the A-Pillar body panels and trim is significant in amplitude thus relevant to the front occupants. Those findings are based on a single stationary flow condition at null incidence angle. Once the pressure gradients are higher in non-zero yaw and unsteady flows, the importance of evaluating the A-Pillar transfer path is of critical importance. The CFD computational effort required by the proven method, however, is knowingly excessive as a means of guaranteeing all vorticity scales and target frequencies are captured. As suggested, the present work intends to re-validate the model in a SUV Bodystyle adopting less aggressive grid and time transient scales, whilst maintaining the output quality.

## 2 Fluid Solution

The numerical fluid solution is divided in two different domains: the Upper Body and the Underbody. Each domain is resolved separately at specific grid and time transient scales determined by the target frequencies. Although possible, the solution of the entire domain in a single submission would result in significantly higher computational effort. It is possible to run the simulations separately since the pressure loads are exported independently and coupled to a second Aero-Vibroacoustic solver.

The Upper Body solution requires finer fluid cells iterated at faster pace to account for the smallest vortices and highest frequencies, whilst the Underbody runs on a coarser grid and larger timestep for a longer interval. Figure 1 shows the finest and second finest Volumetric elements (Voxels) in both domains. The total pressure field (hydrodynamic plus acoustic) of both cases is resolved using Lattice-Boltzmann lagrangian formulation (LBM), Very Large Eddy Simulation (VLES) approach and re-normalized (RNG) k-ε Turbulence Model. The Boundary Layer flow over the vehicle surfaces is modelled rather than resolved by an extension of the standard law-of-the-wall formulation, which is acceptable in low Mach applications once source terms within the Turbulent Boundary Layer (TBL) can be neglected. The flow solution is inherently unsteady and compressible, and the near-field sound pressure is computed directly due to low numerical dissipation and dispersion properties. SIMULIA PowerFLOW® is the solver of choice for the fluid computation [3,4]. Characteristic flow properties are described in Table A. Surface and fluid discretization, time transient settings and computational efforts are summarized in Table B. Compared to previous work [2], significant computational savings achieved in both Upper Body and Underbody solutions are attributed to the reduction of the finest Voxel count and number of timesteps run for a shorter physical time.

VR = 1mm VR = 0.5mm

VR = 2mm VR = 1mm

Figure 1: Finest and second finest Voxel resolution on the Upper Body and Underbody fluid domains (VR = Variable Resolution)

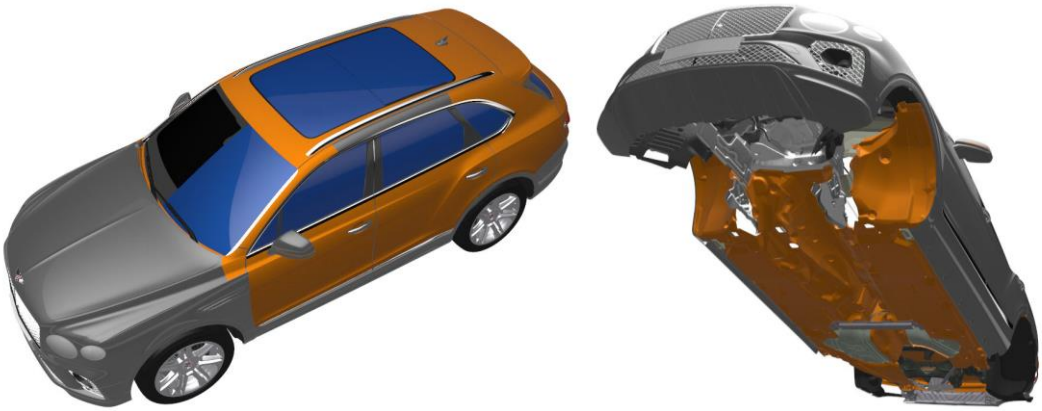

Figure 2: Pressure load measurement panels

Table A: Characteristic flow properties

| | |
|---|---|
| Wheels and Floor | Stationary |
| Flow Velocity, km/h (m/s) | 140 (38.89) |
| Incident Yaw Angle, ° | 0 |
| Flow Mach Number | 0.11 |
| Simulation Mach Number | 0.11 |
| Reynolds Number | 2.61e+06 |
| Incoming Turbulence Intensity | 1% |

Table B: Discretization, transient settings and computational effort

| Parameter | Upper Body | Underbody |
|---|---|---|
| Body Representation | Symmetry Model | Full Model |
| Frequency of Interest, kHz | 0.5 – 5 | 0.25 – 1 |
| Fine-Equivalent Surfel Count | 24,173,956 | 49,070,870 |
| Minimum Wall Cell Size, mm | 0.5 | 1 |
| Fine-Equivalent Voxel Count | 185,423,888 | 253,104,575 |
| Physical Time, s (past settling) | 0.6 (past settling) | 2 (incl. settling) |
| Timestep, s | 8.34e-7 | 2.10e-6 |
| Number of Time Steps | 719,390 | 713,332 |
| Measurement Interval, s | Last 0.5 | Last 1.5 |
| Number of Processor Cores | 431 | 479 |
| Total Clock Time, h | 75.75 | 116.6 |
| Total CPU Time, h | 32,648 | 55,851 |

Once solution is completed, the pressure excitation over 47 different panels and segments of panels are output in the form of standard transient surface measurement CGNS files (CFD General Notation System), totalling 87Gb of data once compressed. The surface mesh coordinates are also converted in uniform grids of 2 to 8mm depending on the panel. The CGNS files contain the pressure time history recorded at pre-defined sampling, at all mesh coordinates of each panel. Upper Body and Underbody measurement panels are illustrated in blue (glazing) and orange in Figure 2.

# 3 Aero-Vibroacoustic Modelling

## 3.1 Statistical Energy Analysis

Statistical Energy Analysis (SEA) is an established methodology to perform interior noise and vibration predictions to support both acoustic and structural package development. In the automotive industry, SEA is widely used for the interior airborne noise prediction from sources from 250Hz and includes the ability to model the energy contribution through various transmission paths as in an actual vehicle by the use of reference acoustic sources [5]. For this project, the SEA software VAOne® is used.

## 3.2 Model Description

The present SEA model was originally built for road and powertrain noise development. The model was defined to provide the best understanding of the energy flow around and within the vehicle, enabling a large variety of analyses. The exterior sound field was comprised of near and mid field cavities defined and connected to ensure the correct exterior acoustic power input at all locations. The mid field cavities were also connected to a semi-infinite fluid (Figure 3) to represent an unbounded exterior acoustic space. The Coupling Loss Factors (CLF) between SEA subsystems were analytically derived and calculated automatically by the software. The Damping Loss Factors (DLF) of subsystems are defined based on test data, and the SEA model considers both resonant and non-resonant propagation transfer paths, with the total contributions and energy flows being the sum of both. Previous validation cases have shown that in a typical vehicle cabin, the direct field contribution is negligible compared to the reverberant field response at the frequencies mostly contributing to the interior noise (above 250Hz, where the acoustic wavelength is less than a meter and the distance between side glasses and occupant ears is substantially less than a quarter wavelength).

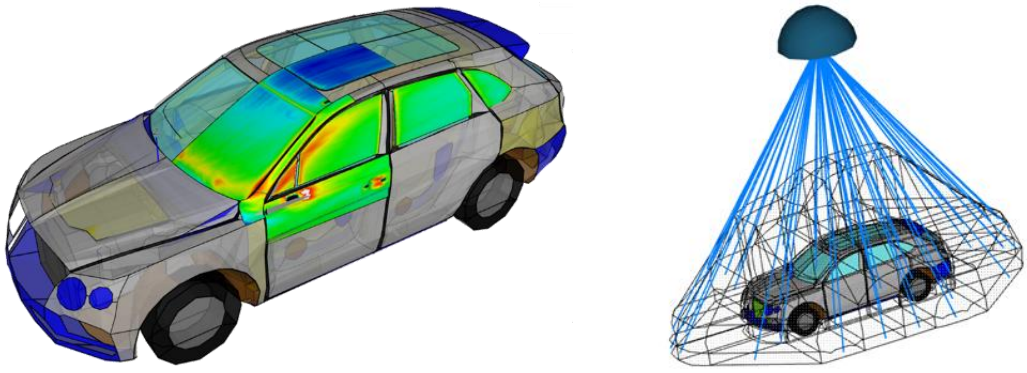

Figure 3: Visual representation of the whole-vehicle SEA model (left) & its exterior sound field (right)

### 3.3 Aero-Vibroacoustic (AVA) Data Import

To extract the excitations to be applied on the SEA model, the surface measurements from compressible CFD were post-processed by converting the total fluctuating surface pressure into a combination of a Turbulent Boundary Layer (TBL) representing the convective component, and a Diffuse Acoustic Field (DAF) representing the acoustic component. A visual overview of the end-to-end process from transient surface pressures to excitation loads applied on the SEA model is shown in Figure 4.

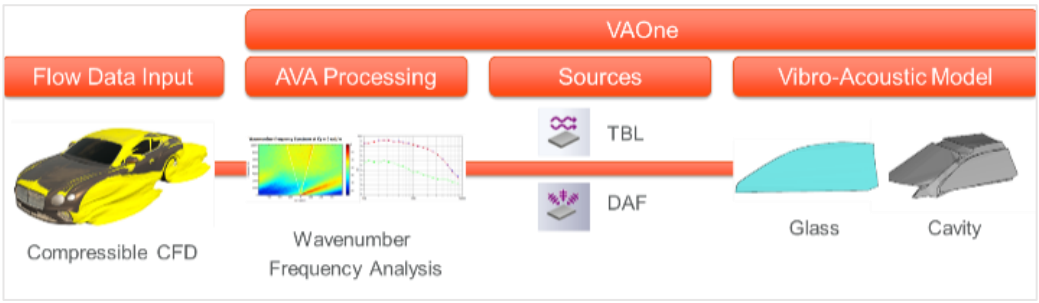


Figure 4: Data conversion process from CFD to SEA Vibroacoustic model

Initially, the fluctuating surface pressure results obtained from the CFD are processed into a two dimensional Wavenumber Frequency Spectrum (WFS). This wavenumber analysis allows movement from the time domain to the frequency domain, and from a two-dimensional physical space to a two-dimensional wavenumber space in the flow direction ($k_x$) and cross-flow direction ($k_y$). Although the glasses are slightly curved, a projection to a flat panel for the wavenumber transform is acceptable given the small scale of the acoustic wavelength for the frequencies of interest relative to the radius of curvature. Once the wavenumber frequency spectrum is obtained, it is possible to separate and extract the convective and acoustic components.

Equation (1) describes the Wavenumber Frequency Spectrum $S_{pp}(k, f)$, as a two-dimensional spatial Fourier Transform of the Pressure Correlation Spectrum $R_{pp}(r, f)$. The Pressure Correlation Spectrum is an average pressure at a given location, conjugated with a pressure at another location. $F[*]$ is the Fourier transform operator.

Equation (2) describes the power of the signal associated with the wavelengths inside the acoustic circle. The Wavenumber Frequency Spectrum $S_{pp}(k, f_i)$ is integrated from 0 to the acoustic wavenumber $a_{k0}$. Equation (3) is similar to Equation (2) but calculates the power of the signal associated with all other wavelengths outside of the acoustic circle, i.e. the convective component.

Along the $k_x$ axis of a Wavenumber Frequency Spectrum (Figure 5a), the convective component is identified as travelling downstream with an inclination equal to the flow speed. The acoustic cone, with an inclination equal to the speed of sound, is integrated to obtain the acoustic component.

The wavenumber analysis acoustic cone can be seen to be tilted slightly to the left of the theoretical acoustic cone (white lines in Figure 5a). This is the result of Doppler shift whereby the flow velocity affects the relative velocity of sound. The observation shows the convective component is in the flow direction only (positive $k_x$) centred around the convective wavenumber whereas the acoustic cone shows the acoustics having an upstream as well as a downstream direction with energy concentrated near the acoustic wavenumber in both upstream and downstream directions.

$$S_{pp}(k,f) = F\,[R_{pp}(r,f)] \tag{1}$$

$$P_{\mathrm{ac}}(f_i) = \int_0^{|a_{k0}|} S_{pp}(k,f_i)dk \tag{2}$$

$$P_{\mathrm{co}}(f_i) = \int_{|k|>a_{k0}}^{|k_{\max}|} S_{pp}(k,f_i)dk \tag{3}$$

Where,

| | | |
|---|---|---|
| $S_{pp}$ | = | Wavenumber Frequency Spectrum |
| $k$ | = | Wavenumber |
| $f$ | = | Frequency |
| $F$ | = | Fourier Transform Operator |
| $R_{pp}$ | = | Pressure Cross-correlation Spectrum |
| $r$ | = | Node position |
| $P_{\mathrm{ac}}$ | = | Acoustic Autopower Spectrum |
| $f_i$ | = | Frequency increment |
| $a_{k0}$ | = | Acoustic wavenumber |
| $P_{co}$ | = | Convective Power |
| $k_{max}$ | = | Maximum Wavenumber of interest |

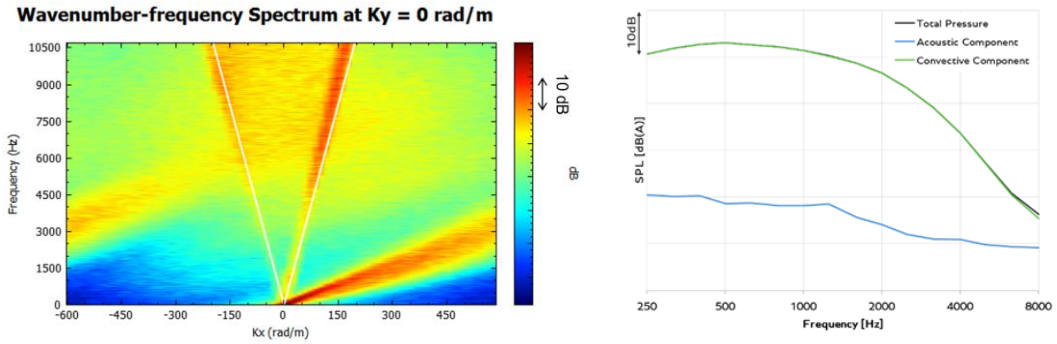


(a) (b)

Figure 5: (a) Wavenumber Frequency Spectrum on side glazing panel ($k_x$ direction); (b) Resulting 1/3 Octave acoustic & convective components.

The result of a wavenumber separation into acoustic and convective components can be seen in Figure 5b. The convective component is significantly greater in magnitude than the acoustic, but the acoustic component must not be omitted due to the broad frequency range of interest (250-8kHz). The stronger coupling between the acoustic component to interior noise due to resonant and non-resonant transmission of the energy, means that the acoustic component dominates over a substantial part of the frequency range, even though the excitation level is significantly lower [1].

Ultimately, the convective component is applied as a Turbulent Boundary Layer excitation to the SEA model on the vehicle panels. Where the spectrum is specified by that extracted from the wavenumber analysis, and the appropriate area modifier applied dependent upon the examination of specific turbulent zones. The acoustic component is applied as a Diffuse Acoustic Field, at the level of the acoustic component extracted from the wavenumber analysis, and applied to a face of the near field external cavities.

## 4 Validation Experiment

Previous validation experiments conducted in a sports coupé [2] proves the potential of achieving a correlation offset of 1 to 3dB in all 1/3 Octave bands from 250 to 5kHz. In the present project, interior noise correlation measurements replicating the CAE setup to its best are taken in the Full-Scale Aeroacoustic Wind Tunnel of FKFS© (Figure 6). Sealing shutlines and part matching interfaces are taped to prevent localized flow & noise phenomena not modelled in CFD, as well as residual aspiration. Binaural and multiple free-field recordings are taken in the driver's seating compartment. Given the nature of SEA, the energy of inner and outer ears was averaged for each head location in order to provide comparable results. The measurements are taken for 30s and data is sampled at 48kHz.

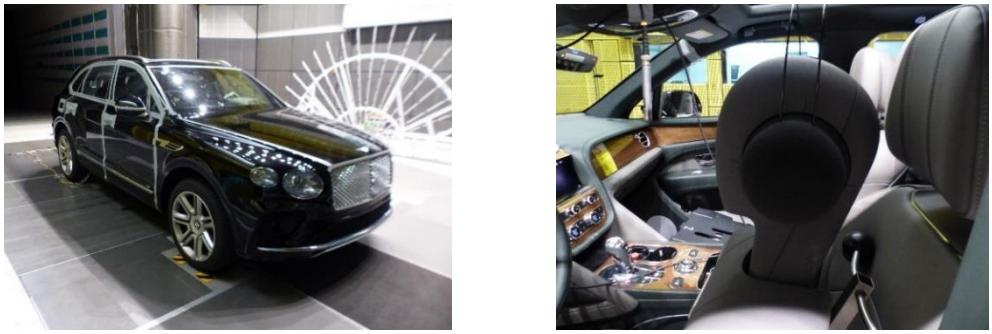

Figure 6: Validation test setup

### 4.1 Whole-Vehicle Interior Noise

Modelled and tested interior noise at the front head position are shown in Figure 7, along with the zonal contribution from Glazing, Body and Underbody Panels, bounded by the minima and maxima of each part group. “AAWT” stands for Aeroacoustic Wind Tunnel testing data. Below 1kHz, the methods are in good agreement with an offset from 1 to 3 dB. Above 1kHz, excellent agreement is met with a difference in decimal order in most 1/3 Octave bands. In the front driver location, windscreen and side glass panels are the top contributors above 500Hz, and body cavities such as A-Pillar and doors dominate over roof and rear glazing. Those findings indicate the modelling of body and trim components is relevant to predict the interior noise with due accuracy, in particular for this vehicle where glazing paths are highly damped for high frequency noise. Below 500Hz, noise from Underbody panels such as under trays and wheel arches dominate as expected (Figure 8).

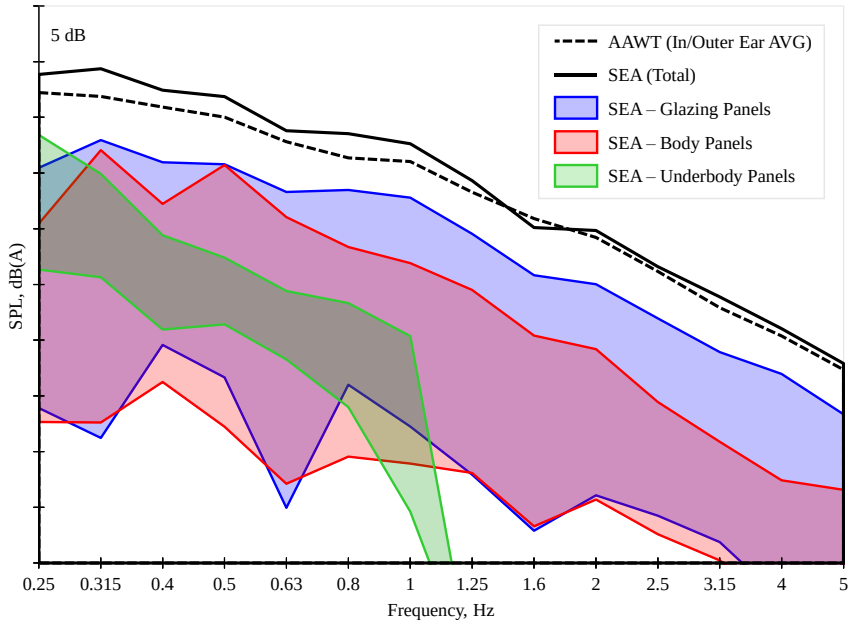


Figure 7: Interior noise at front right head location

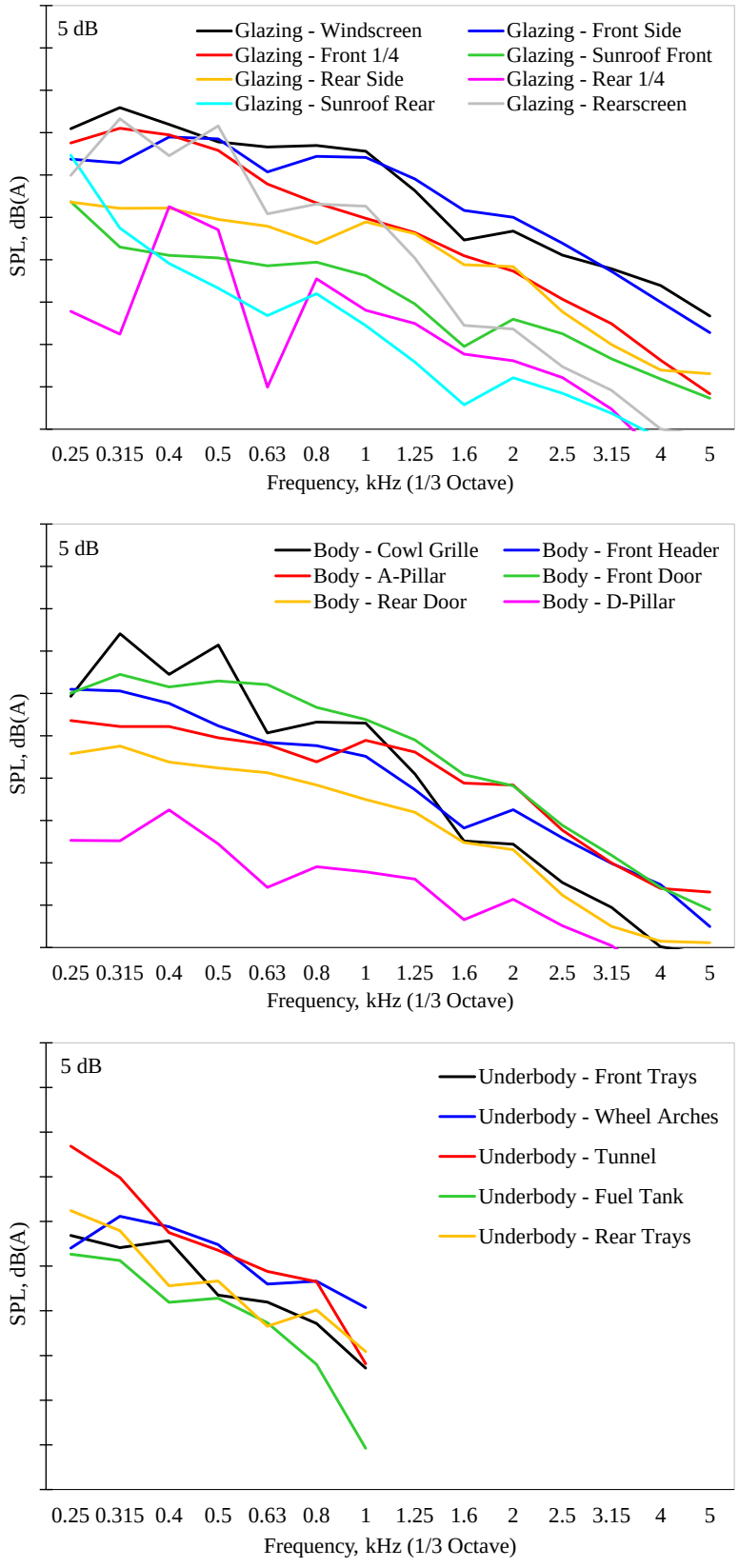


Figure 8: All panels contributions (Top: Glazing panels; Middle: Body panels; Bottom: Underbody panels)

## 4.2 Glazing & Body Panel Contributions

To investigate the accuracy of the method in predicting the relative contribution of the glazing panels, measurements of glazing blanking taken in the wind tunnel were compared to equivalent estimations from the numerical approach. In the test, A-B insulation material was applied to all panels, and the contribution from un-blanking each panel was measured separately (not cumulative). In the SEA model, the blanking pads were modelled by applying noise control treatment of equivalent specifications to each panel. Figure 9 shows a comparison of the physical test and numerical increments for the most relevant panels to the driver location (Windscreen and Front Side Glass). Contribution from the Windscreen correlates with an offset of 1 dB in lower frequencies, and 2 dB maximum in frequencies above 4kHz. The offset for the Front Side Glass is 2.5 dB maximum in both lower and higher frequencies. The trend between test and numerical data is in good agreement for both panels. Body panel contribution is validated by removing acoustic treatment from specific panels in the test and replicating the change in the SEA model. An example is demonstrated where the insulation from the front door trim is removed and the increment to baseline condition is plotted in Figure 10. The increments match significantly well except from 500 to 800Hz, which is subject for investigation.

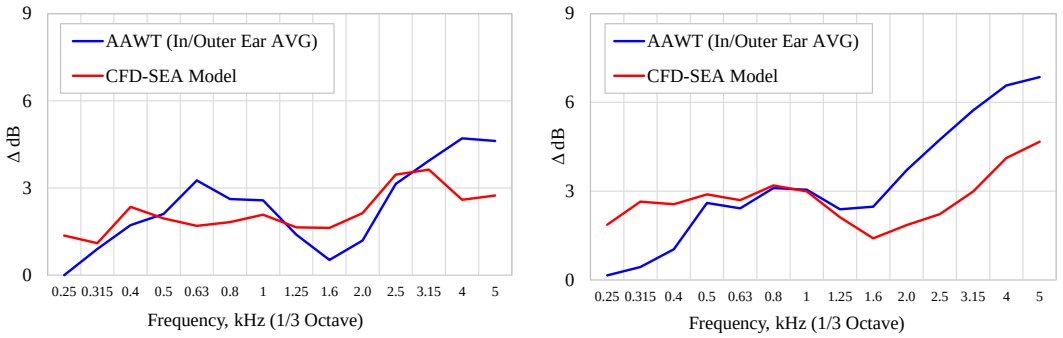


(a) Windscreen (b) Front Side Glass

Figure 9: Glazing blanking contribution analysis (Front Head location)

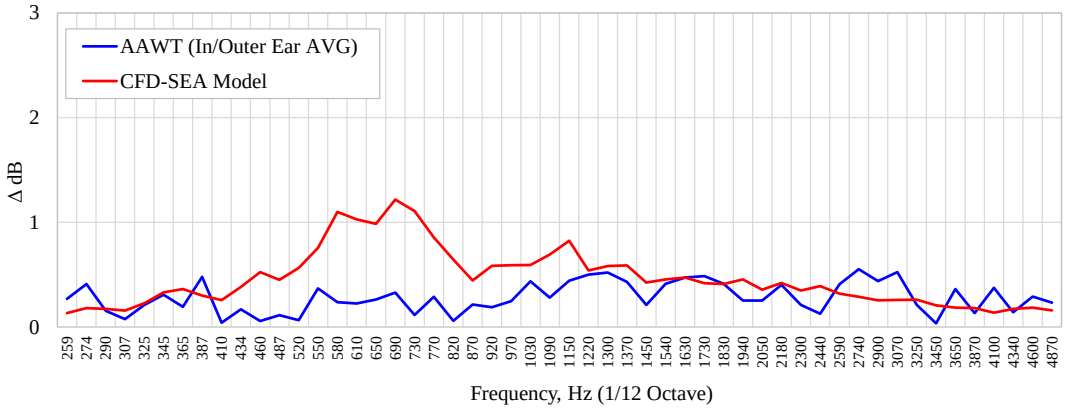


Figure 10: Body panel contribution analysis (Front Head location)

## 5 Conclusion

Coupling compressible CFD and SEA to support whole-vehicle Aeroacoustics development has been proven as a reliable and realistic methodology. The work undergone to optimize the CFD burden at no accuracy loss has significantly reduced turnaround, and the reuse of Road Noise whole-vehicle SEA models has been proven cost-effective. Correlation offsets are acceptable for whole-vehicle statusing in reference to validated targets, and A-B comparisons of multiple Upper Body and Underbody acoustic specifications have been made possible with the caveat of specific frequency bands under investigation for future projects.

## 6 Acknowledgements

The authors acknowledge Benjamin West and Holly Daniels for previous developments which ground the present work; as well as Christopher Shaw, Joseph Castle and Boris Fechner from Dassault Systèmes© for constructive partnership.

## 7 Bibliography

[1] Hartmann, M., Ocker, J., "Wind Noise Caused by the Side-Mirror and A-Pillar of a Generic Vehicle Model", AIAA 2012-2205, 18th AIAA/CEAS Aeroacoustics Conference, 2012, DOI:10.2514/6.2012-2205.

[2] West, B., Daniels, H., Venor, J., and Martin, S., "Development of a Process to Predict Whole Vehicle Aeroacoustic Interior Noise", SAE Technical Paper 2021-01-1047, 2021, DOI:10.4271/2021-01-1047.

[3] Manoha, E., Caruelle, B., "Summary of the LAGOON Solutions from the Benchmark problems for Airframe Noise Computations-III Workshop", AIAA 2015-2846, 21st AIAA/CEAS Aeroacoustics Conference, 2015, DOI:10.2514/6.2015-2846.

[4] Romani, G., Casalino, D., van der Velden, W., "Numerical Analysis of Airfoil Trailing-Edge Noise for Straight and Serrated Edges at Incidence", AIAA JOURNAL Vol. 59, No. 7, July 2021, DOI:10.2514/1.J059457.

[5] Venor, J., Caillet, A., Martin, S., Marz, C. et al., "Using Statistical Energy Analysis to Optimize Sound Package for Realistic Load Cases", SAE Technical Paper 2020-01-1525, 2020, DOI:10.4271/2020-01-1525.

[6] Venor, J., Zopp, A., "Using SEA to Model near Field External Sound Pressure Distributions Based on Automobile Geometry", Vibro-Acoustic Users' Conference, Köln, 2007.

# Physical & virtual assessment methods for simulating thermal propagation at cell and battery pack level.

Devyanshu Kumar, Miquel Planells, Enric Aramburu, Didac Casanellas, Charalampos Tsimis

Body Performance & Battery Lab
Applus+IDIADA
PO Box 20 L'Albornar
E-43710, Santa Oliva (Spain)
Charalampos.tsimis@idiada.com

**Abstract:** Battery cell thermal runaway and the resulting thermal propagation in battery packs pose a significant safety risk that needs to be addressed by OEMs. Moreover, since 2021 different thermal regulations, such as GB 38031 or UN ECE R100.03, require thermal runaway tests to be performed for vehicle type-approval. This paper outlines the experimental setup designed by Applus+IDIADA for conducting thermal runaway tests on individual battery cells. The experimental data gathered was used to validate the numerical methodology at the cell level. Subsequently, the paper outlines the methodology employed to simulate thermal propagation at the battery pack level.

## 1 Introduction & motivation

Li-ion cells operate properly in controlled temperature conditions, however, if due to external or internal heating cell temperature reaches a specific threshold, a thermal runaway (TR) process is triggered [1], which means highly exothermic chemical reactions occur internally and a large amount of energy and gasses are released rapidly. Moreover, besides overheating cases, other possible causes of Li-ion TR are internal shortcuts due to mechanical damage or manufacturing defects, which means that even avoiding impacts or external overheating, TR can happen spontaneously at any time in the vehicle lifetime. Thus, engineers must assume that thermal runaway may occur eventually, and concentrate on minimising the risk that it poses by studying it during the initial design stages of the battery pack.

It is well known that whenever TR happens, this can produce a cascade effect on neighbouring cells, the power released by the initiation cell can produce the overheating of the neighbour cells and then generate secondary TR, and so on. The goal of battery designers is twofold, first to provide sufficient cooling at the cell level to minimise the probabilities of a TR starting due to the formation of hot spots, and second to delay the heat transfer phenomena during a TR event by employing different mitigation strategies, such as proper thermal insulation or efficient extraction of TR gases.

Information regarding the chemical composition of battery cells can help engineers better estimate the energy and materials released during a TR event, by relying on the principles of theoretical chemical reaction kinetics. However, this information is not readily available as it typically forms part of the intellectual property of the cell manufacturer. An alternative path is conducting physical tests and measurements, in which the cell is deliberately induced into TR through various methods, and the thermodynamic behaviour of the cell is assessed with the help of sensors.

This paper will first describe a complete methodology for characterising cells in the test bench by a newly developed test rig at Applus+IDIADA. It will then detail the CFD methodology that was developed to replicate this test rig for fine tuning the battery cell model. Finally, it will present a CFD methodology for simulating battery packs with cell temperature dependent boundary conditions, to ultimately study the impact of different mitigation measures that can minimize thermal runaway and its propagation hazards.

## 2 Cell Characterization test rig.

A vertical cylindrical reactor with a lower air inlet and upper exhaust outlet was designed to test battery cell TR events in controlled conditions. The main goal of this test rig was to characterise cell TR by monitoring the temperature of the cell and measuring the gasses generated, along with their temperature.

### 2.1 Reactor design

The enclosure (reactor) to perform TR at cell level was selected to be a 40 L cylinder from a mechanically modified compressor.

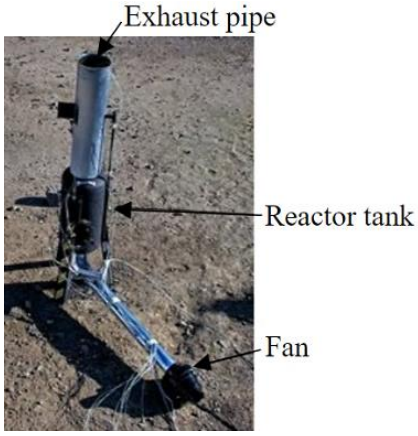


Figure 1: Reactor used for TR tests at cell level.

Both extremes of the cylinder were cut, and a ducting was attached before and after the reactor (Figure 1). At the bottom, a fan capable of circulating 200 m3/h was used to ensure continuous airflow; while at the top, an exhaust pipe of 20 cm diameter was

added, with a 10 mm diameter sampling point installed at 90 degrees. Several temperature sensors (Thermocouples Type K – fibre glass coated) were also added inside the reactor through a cable gland, as well as heating cables.

## 2.2 Cell selection

The cells used, as an example, in this paper to showcase the testing procedure and its subsequent replication in the CFD setup, were selected from a commercially available EV from 2022. The total energy of the battery pack was 52 kWh, with an individual cell energy of 440 Wh. Selected cells were prismatic and were recovered from a battery pack by dismantling the modules and accessing the individual cells. All plastic covers were removed, and cell walls were cleaned.

## 2.3 Cell assembly

Ceramic heaters were installed on the largest cell walls to trigger the cell thermal runaway. 4 heaters of 220 W were attached to the prismatic cell (2 on each face). Cell and heaters were assembled using metal grids (sandwich type configuration - Figure 2) and secured with springs. This let any potential cell expansion during TR to be allowed without putting stress on the cell. Thermocouples were added between the heater and the cells ($T_{heater}$) and on top of the larger cell wall, next to the heater ($T_{case}$).

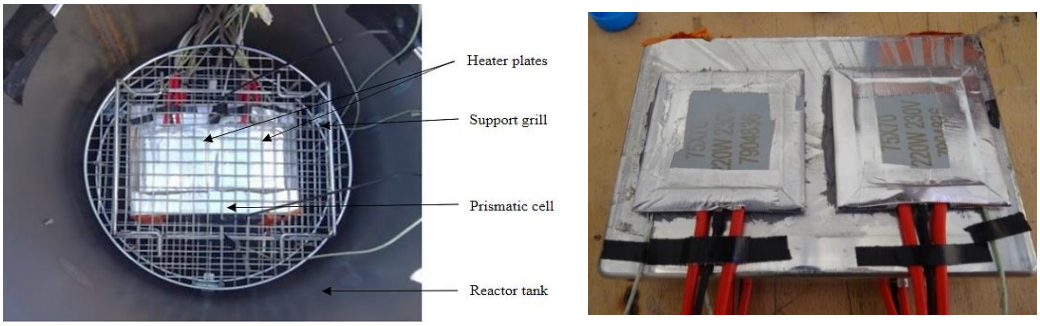


Figure 2: Cell assembly before TR tests, presented inside the reactor.

## 2.4 Data measurements

The gases released were estimated through the combination of three measurements. First the cell was weighted before and after the experiment to measure the total mass lost, second the exhaust gasses velocities were measured with the help of an anemometer positioned at the exit of the reactor tank, and third, the composition of the exhaust gasses was measured via the 10 mm diameter sampling point. Temperatures were monitored using thermocouples at key locations, including the

battery casing, heater plates, inlet and exit of reactor tank etc. In addition, a camera was installed to capture on video the detailed venting and runaway process. These measurements combined allowed to identify the TR onset temperature for cell-to-cell propagation and the venting phase.

On one hand the estimation of the gases released was used as an inlet boundary condition for the venting of hot gas in the simulations. On the other hand, the cell temperature measurements were used in an iterative, reverse engineering, process that helped determine the material properties (i.e. thermal conductivity & specific heat).

### 2.5 Test procedure

Constant heat flux was supplied to the battery cell through electric resistance, up to the point where smoke was detected. At that moment, the electric heaters were turned off and the ventilation fan was immediately activated to bring the cell back to ambient temperature.

## 3 CFD cell model

This section of the study focuses on finding key cell properties using an iterative CFD data-fitting approach. So, that further CFD thermal runaway analysis at battery module and/or pack level can be performed with greater accuracy. In the n*umerical model* of the physical experiment, a simplified, but full scale, model of the battery cell, heater-plates and reactor tank was considered (see figure 3). Thermocouples were placed at similar locations as they were in physical setup but the contact resistances between thermocouples, heater plates and cell casing were neglected (assumed zero thermal contact resistance). Also, the support grills and wiring connections were excluded in CFD modelling.

Commercial, STAR-CCM+ software was used as the CFD solver, with implicit unsteady modelling scheme. Turbulence was modelled with the K- ε, two-layer and All y+ model. Air was modelled as ideal gas and radiation was modelled with the surface-to-surface and gray thermal radiation models. Anisotropic thermal conductivity was assumed for the solid region representing the battery cell.

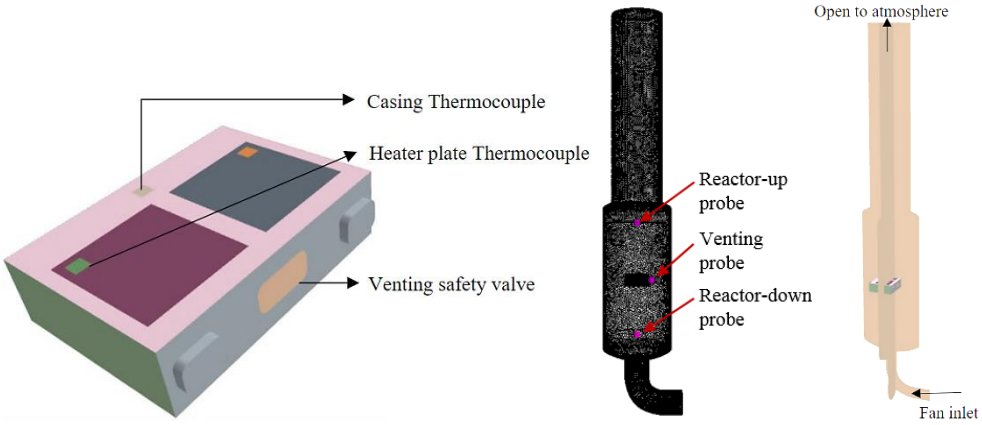


Figure 3: a) Cell geometry with heater plates and thermocouples; b) CFD simulation domain with surface mesh; c) Cut-section view highlighting the cell placement in the reactor tank.

### 3.1 Cell characterization methodology

In the current study, the actual prismatic cell was replaced by an equivalent lumped mass of same dimensions and attempts were made to find the equivalent thermal conductivity and specific-heat values for this rectangular mass.

In a usual CFD workflow the boundary conditions and material properties are provided, and with suitable modelling techniques, the desired flow field variables are obtained. In this study, initial simulation results were first obtained with some reference (/guessed) material properties of the battery cell. And then these characteristic properties were manually and iteratively adjusted to better match the experimental results.

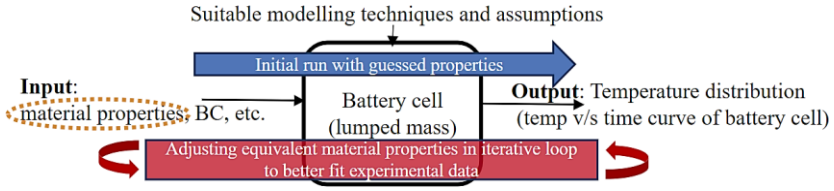


Figure 4: Illustration of CFD methodology for characterization of cell material properties.

The energy balance for this equivalent cell can be expressed as:

$$\rho_{eq}\, Cp_{eq} \left(\frac{\partial T}{\partial t}\right) = \nabla\left(K_{eq} \nabla T\right) + \phi$$

Where, $\phi$ is the additional source term accounting for the heat addition form heater plates and the internal heat generation during TR. The above equation also shows the relation between time rate of change of cell temperature and material properties,

which especially for low temperature ranges, becomes a strong function of thermal diffusivity, $\left(\frac{K_{eq}}{\rho Cp}\right)$; as radiation and natural convection currents are very small.

Due to the complexities in thermal runaway, the experimental data was analysed numerically in different phases, see figure 5.

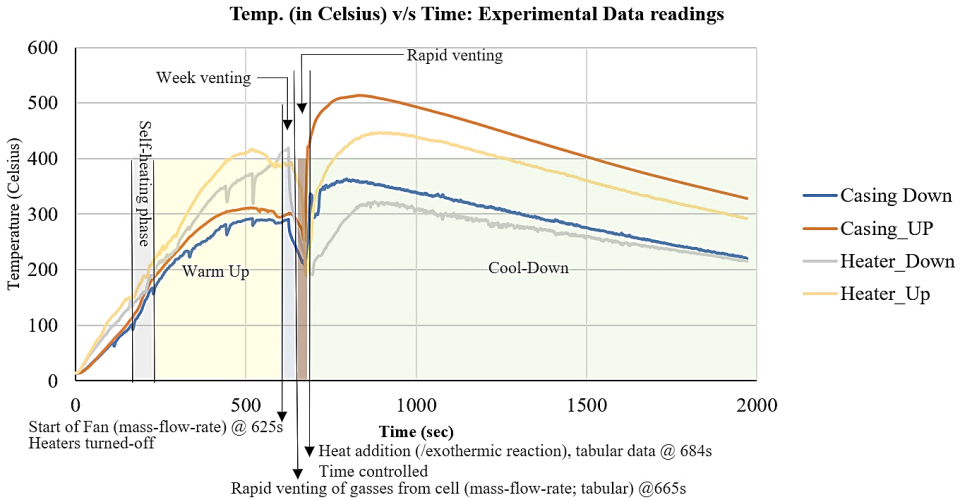


Figure 5: Breakdown of experimental data in multiple phases

### 3.1.1 Self-heating phase

A positive increase in the temperature gradient was observed (shown in fig. 5). Several literatures have identified the decomposition of SEI (Solid Electrolyte Interface) layer between temperature range of 90-120°C [2], resulting in exothermic reactions and hence the jump in the cell temperature. To depict this behaviour in simulation, a time-controlled total heat source was added to the cell region.

### 3.1.2 Warm-up phase

As the thermal abuse continued, cell underwent various physical and chemical changes. Polymer separator starts to melt (endothermic reaction) slowing down the rate of temperature increase. Moreover, as the temperature rises above 250°C decomposition of graphite anode with the electrolyte takes place [3], leading to exothermic chain reactions.

In this phase due to multiple reactions' (endo/exothermic) complexities, no additional heat generation was approximated, within the cell region. Cell temperature was allowed to increase solely due to the heater-plates.

### 3.1.3 Weak venting phase

Due to the continuous abnormal heating by the heater plates, separator layer vaporizes (endothermic), allowing the cathode and anode to make contact with each other, resulting in internal short circuit. This leads to highly exothermic Thermal runaway with the visible venting of smoke from the cell.

The instant smoke was detected, the heater plates were turned off and ventilating fan was started. This fan flow was modelled as velocity inlet in simulation, based on the experimental readings of air velocity entering the reactor tank. Similarly, to the warm-up phase, no additional heat generation was included due to multiple reactions' (endo/exothermic) complexities.

### 3.1.4 Rapid venting phase

Cell had undergone thermal runaway and about 460g of mass was lost as gas release. No actual combustion was detected. This venting of gas was modelled as an additional air mass-flow-inlet from venting safety valve surface of cell (shown in figure 3.) into the main air domain, at temperature equals to instantaneous cell average temperature. However, no actual reduction in lumped mass (representing the cell) was considered.

Additional time varying total heat source table was applied to the cell region for highly exothermic thermal runaway.

### 3.1.5 Cool down phase

Cell temperature started to decrease under the influence of forced convection, but still active internal reactions were slowing down the effect of cooling. For this reason, heat source was also introduced in this phase to better match the observed temperature trend.

However, it is very evident from the figure 6 that, simulations results (solid lines, in figure 6.) are offset by 40-50°C from experimental results (dotted lines). This could be because, in experimental analysis the contact between the cell casing, thermocouples and heater-plates was highly disturbed due to the high temperature and burning effects during thermal runaway process (see figure 7). Moreover, the thermal effects of TR were also observed to be non-homogenous in the actual cell experiment (figure 7, shows prominent burning effects on one side of the cell).

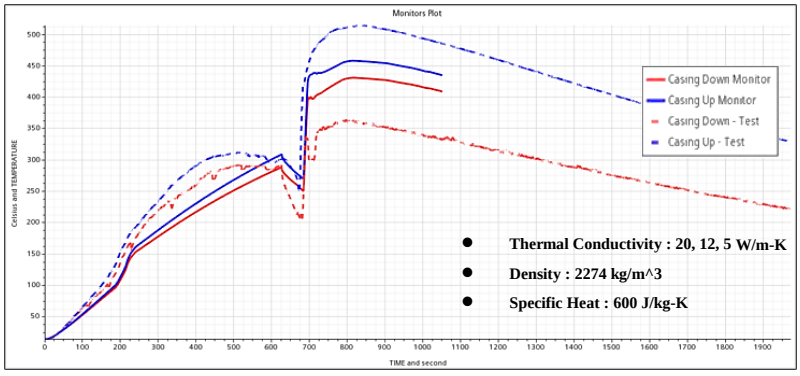


Figure 6: Experimental data of battery-casing temperature (up & down; dotted lines) v/s simulation results after iteratively correcting the material properties (solid lines)

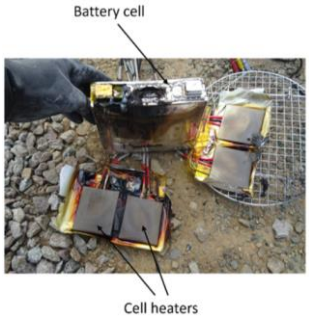


Figure 7: Battery cell and heaters after Thermal Runaway (TR) event.

As the current work shows, with suitable assumptions and proper analysis of experimental data this iterative approach has the potential to model virtually the battery cell as lumped mass and identify its equivalent material properties. The results from this method showed that an anisotropic thermal conductivity of 20, 12, 5 W/m-K ($K_{xx}$, $K_{yy}$, $K_{zz}$) and specific heat of 600 J/kg-K is better fitting the experimental data, for the cell tested, and the data fitting is within reasonable limits.

## 4 CFD battery model

Battery CFD models are used to study thermal propagation within the battery packs aiming to delay cell-to-cell propagation times by trying different materials, battery layouts, etc. In order to do so, the authors created a CFD model including a full module, composed by 6 prismatic cells and studied how adjacent cells are heated-up by convection, conduction and radiation, to identify the main energy exchange drivers. The battery pack example shown below (Figure 8) as proof of concept of the CFD methodology for thermal runaway simulation belongs to the Marbel EU project (https://marbel-project.eu/).

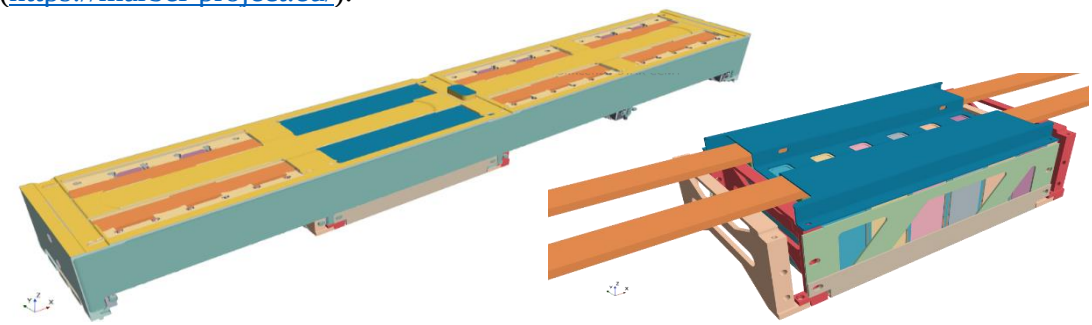

Figure 8: a) Battery pack (1 row), b) module (6 cells)

## 4.1 Case set-up

The cell characterization procedure described in chapters 2 and 3 is used to define the main cell parameters, regarding thermal conductivity, specific heat, energy and gas release. Energy and gas release are temperature- and time-dependent boundary conditions. The release of energy and gas happens when battery cells reach an onset temperature, which was identified in the cell characterization tests, and then follows a time-dependent curve. To mimic this behaviour in the CFD model, the authors used customized field functions to activate time-dependent tables (boundary conditions) instantaneously, as the monitor reaches threshold values. The maximum cell temperature is monitored cell-by-cell, individually, then when this temperature exceeds the onset temperature (150ºC), an inlet boundary condition, located on the cell burst membrane, is activated to inject hot venting gases (air) into the flow domain, along with a cell internal heat source with time-dependent definition.

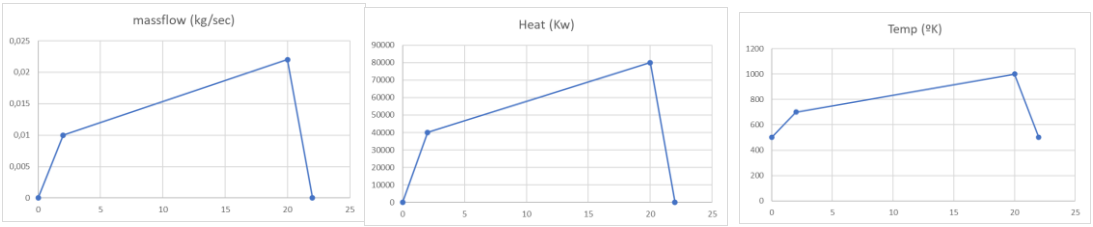


Figure 9: Cell time-dependent boundary conditions

Since the battery cell assumed in the Marbel battery pack was not available for testing using the procedure described in the first part of this paper, the internal heat generation and gas release quantities were initially set, based on the authors experience in testing similar chemistry batteries. Authors then amplified these theoretical values, reaching peak values to 80 kW of internal heat, 0,022 kg/s of gas release and 1.000º K for the gas temperature, in order to force thermal propagation within batteries and hence, to validate the methodology for simulating this propagation cascade effect. The time-dependent boundary conditions curves are presented in Figure 9.

The main material parameters of the module assembly were provided by the Marbel consortium and are shown in the figure 10, below.

As explained above, the first challenge was creating a temperature- and time-dependent cell set-up that leverages measurements obtained in the cell test rig. The second challenge was simulating a full battery test including a realistic battery pack capable to simulate up to 5’ of real time, with affordable computational resources. These challenges as well as the confidence level on the simulation depends very much on the spatial and temporal discretization, so the authors performed a sensitivity analysis regarding time-step and mesh refinement to ensure that CFD results do not depend on these model parameters.

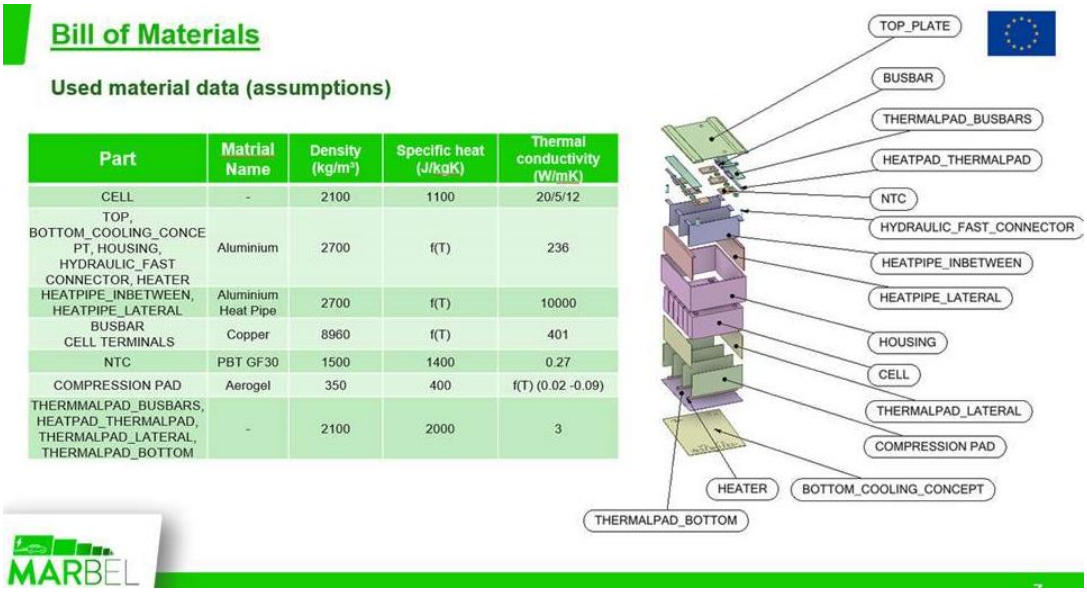


Figure 10: Material properties

## 4.2 CFD results

The authors monitored cell maximum temperatures in all the battery cells to compute cell-to-cell propagation time, which is deemed the main test KPI. The plots of these monitors are shown in the picture below (Figure 11). Looking at these results and checking when the onset temperature is reached, we can conclude that cell to cell propagation time of the example case is realized on average within 15 seconds. If the main venting period of this cell lasts 20" (fast venting), the authors understand that delaying the cell-to-cell propagation time to more than 20", for example 30", could help to contain TR to a single cell and interrupt thermal propagation to the entire battery.

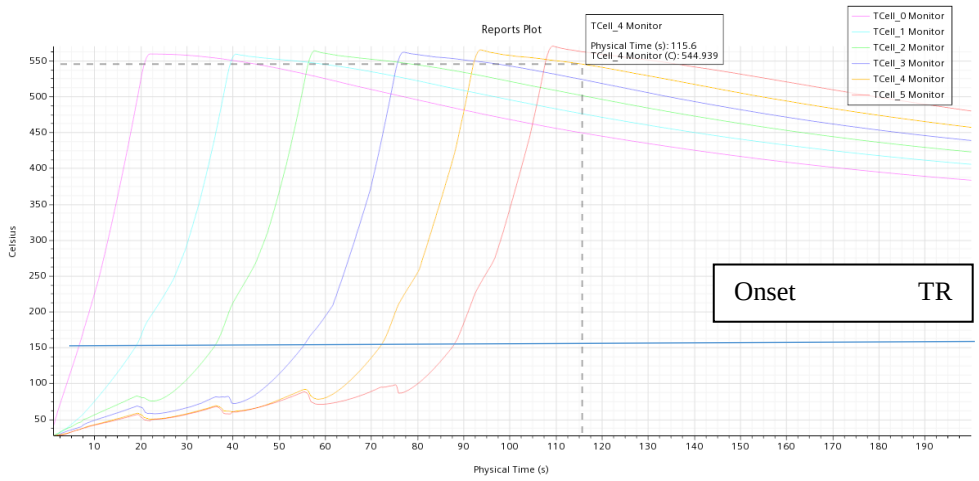


Figure 11: Maximum cell temperature plots

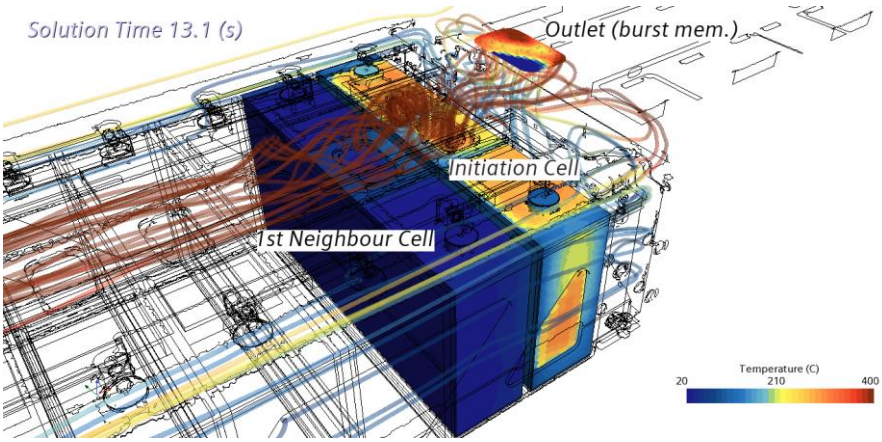


Figure 12: CFD results: cell temperature & streamlines

CFD analysis can be very useful to understand how batteries heat-up in TR tests. The energy exchange balance at the first cell next to the initiating cell can show how this cell heats-up and which are the main heat transfer paths (these results are presented in Table 1). Looking at this table, we can conclude that the main energy path is through the frame metal parts. Therefore, acting on that heat transfer path, we could delay the cell-to-cell propagation, for instance by adding a thermal insulation between the metal and the cell.

Table 1: Cell heat transfer paths

| Heat transfer breakdown (Time = 13.1) | % |
|---|---|
| Flow domain | 4% |
| Thermal pads | 34% |
| Metal frames | 62% |
| TOTAL | 100% |

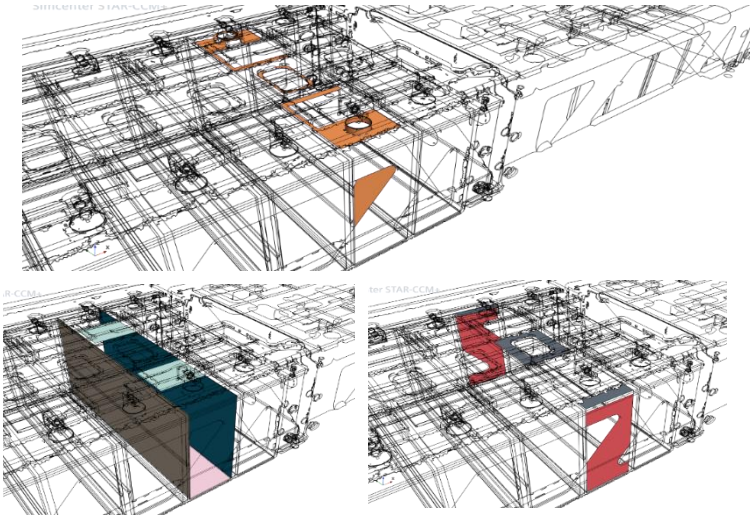

Figure 13: a) Flow domain patch, b) thermal pads patch, c) metal frames patches (grey & red)

## 5 Conclusions and future scope

The authors developed a complete methodology for simulating thermal propagation tests by means of CFD, which are helpful in the decision-making process at batteries design phases, furthermore the authors have proven its applicability at industrial level on a real test-case. This process includes a cell characterization test rig, a reverse engineering process for setting the cell parameters from test measurements, a CFD methodology for full battery pack thermal simulation and an analysis procedure to diagnose the neighbouring cell heating process during thermal propagation.

This CFD methodology is currently limited to fluid-dynamics and thermal analysis, further methodology developments could be introduced in the future for being more realistic, through adding more complexity in the CFD set-up, for instance: modelling of melting parts, deformation of structural parts, or secondary fire events and smoke modelling.

## 6 Bibliography

[1] V. Ruiz and A. Pfang, “JRC exploratory research: Safer Li-ion batteries by preventing thermal propagation,” European commision, 2018.

[2] H. Liu, Z. Wei, W. He and J. Zhao, Thermal issues about Li-ion batteries and recent progress in battery thermal; A review, Energy Conversion and Management, Elsevier, 2017.

[3] X. Feng, M. Ouyang, X. Liu, L. Lu, Y. Xia and X. He, Thermal runaway mechanism of lithium ion battery for electric vehicles: A reiew, Energy storage materials, Elsevier, 2017.

# External Thermal Management Concept for BEV fast charging

Marcus Auch, Timo Kuthada, Andreas Wagner

Institute of Automotive Engineering – University of Stuttgart
Pfaffenwaldring 12
70569 Stuttgart
marcus.auch@ifs.uni-stuttgart.de
timo.kuthada@fkfs.de
andreas.wagner@ifs.uni-stuttgart.de

**Abstract:** This study investigates the feasibility, conceptualization and thermal modeling of an external thermal management concept for battery electric vehicle (BEV) extreme fast charging (XFC) scenarios. Since BEV standard operating conditions are normally much less challenging from a thermal point of view compared to XFC an external thermal management system has been developed being able to remove the generated waste heat in the XFC process of the BEV. The system consists of an external cooling circuit including a thermal energy storage tank and an external refrigeration circuit removing the waste heat to the environment. The feasibility of the proposed concept has been shown by a developed 1D-simulation of the whole external thermal management concept, delivering insights into additional heat to be removed and sizing of the thermal energy storage tank, pumps, compressors and heat exchangers.

## 1 Introduction

With the ongoing demand of customers to recharge in a similar timeframe as internal combustion engine vehicles, extreme fast charging (XFC) is one of the most important research topics for battery electric vehicles (BEVs). While the maximum charging power depends on the maximum allowable continuous current applied of the individual cell, it also can be limited due to thermal safety reasons. Depending on the active cathode material used, an operating temperature range of 25 - 40 °C is desired [1]. If the temperature is further increased, there is a risk of thermal runaway of the LIB cell. Thermal runaway is an uncontrolled exothermic reaction inside the LIB cell resulting in big heat releases through the developing gases [2]. If one cell enters the state of thermal runaway there is the risk of thermal propagation, which can result in the explosion of the battery pack and dangerous lithium fires. To prevent those thermal safety issues adequate and reliable thermal management systems are of great importance for BEVs.

For most BEVs, XFC is the most challenging scenario from a thermal point of view. This can be seen by analysing the heat generation occurring inside a LIB. The heat generation in LIBs is dependent on the internal resistance and resulting voltage drop of the LIB cell. The heat generation can be calculated through the simplified Bernardi equation [3]

$$Q_{\text{loss}} = I\,(U_{\text{OCV}} - U_{\text{t}}) - I\,T\,\frac{\partial\,U_{\text{OCV}}}{\partial\,T} \tag{1}$$

whereas $U_{\text{OCV}}$ is the LIB open circuit voltage, $U_{\text{t}}$ is the LIB terminal voltage, $I$ is the applied current, $T$ is the temperature and $\partial\,U_{\text{OCV}}/\,\partial\,T$ is the entropic coefficient of the LIB cell. Replacing the voltage drop from the open circuit voltage to the terminal voltage with the product of the current $I$ and the internal resistance $R_{\text{i,cell}}$ of the LIB

$$U_{\text{OCV}} - U_{\text{t}} = R_{\text{i,cell}}\,I \tag{2}$$

and then substituting this term into equation (1)

$$Q_{\text{loss}} = I^2\,R_{\text{i,cell}} - I\,T\,\frac{\partial\,U_{\text{OCV}}}{\partial\,T} \tag{3}$$

shows that the first term of the heat generation is proportional to the square of the applied current. While the internal cell resistance is not entirely ohmic resistance, the ohmic resistance share of the total heat generation increases with increasing current applied to the cell. This makes XFC an extremely challenging task for a BEV thermal management system. The maximum temperature must not be exceeded throughout the XFC cycle despite the battery experiencing currents four or eight times higher than those typically applied in the standard driving cycles of the BEV. The aim of the CoolEV project is to explore the potential application of an external thermal management system for XFC of BEVs, with the goal of minimizing the size of the in-vehicle thermal management system to regular operating conditions. The CoolEV consortium consists of Dr. Ing. h.c. F. Porsche AG, Hydac Cooling Gmbh, University of Esslingen, the Zentrum für Sonnenenergie- und Wasserstoff-Forschung Baden-Württemberg (ZSW) and the University of Stuttgart, all contributing to the results of this study.

## 2 Fundamentals of 1D thermal modeling

The following section presents the fundamentals of modeling cooling circuit and refrigeration components. Furthermore, additional heat inputs by the required cooling circuit components are discussed.

## 2.1 Modeling of Cooling Circuits

In this study, the cooling circuit modeling approaches for a heat exchanger, a pump, pressure losses due to cooling circuit components and a thermal energy storage tank are necessary. To model heat exchangers, there are several methods available in 1D simulation tools. In this study two different methods are used. An experimental data-based effectiveness-number of transfer units method is utilized for a liquid to liquid heat exchanger and a macroscopic geometrical data method is used for a liquid to refrigerant fluid heat exchanger (also known as chiller). A thermal-hydraulic centrifugal pump is chosen to model the cooling circuit pump. Therefore, the pressure increase

$$\Delta p = f(\dot{m}, w, T) \tag{4}$$

as a function of mass flow rate $\dot{m}$, pump rotation speed $w$ and temperature $T$ can be calculated. Furthermore, an efficiency table also depending on the mentioned parameters

$$\eta_{\mathrm{pump}} = f(\dot{m}, w, T) \tag{5}$$

can be provided to include the losses of the chosen pump. To model the pressure losses occurring inside the cooling circuit two different approaches are used. A simple pipe pressure loss estimation of

$$\Delta p_{\mathrm{pipe}} = f(d_{\mathrm{pipe}}, l_{\mathrm{pipe}}) \tag{6}$$

depending on the diameter $d_{\mathrm{pipe}}$ and length $l_{\mathrm{pipe}}$ of the pipe can be taken. When experimental data of the pressure loss is available, an experimental based model approach can be used as

$$\Delta p_{\mathrm{coupling}} = f(\dot{m}, T) \tag{7}$$

at specific temperatures and mass flow rates. Lastly, thermal energy storage tanks can be modeled by a thermal-hydraulic capacity model. In this case, the tank requires an initial pressure and temperature as well as the total tank volume $V_{\mathrm{tank}}$. Furthermore, it is possible to include a heat transfer rate to the environment, considering heat losses of the chosen thermal energy storage tank. [4]

## 2.2 Modeling of Refrigeration Circuits

Refrigeration circuits are mostly vapor compression cycles [5]. One important aspect of vapor compression cycles is the saturation curve of the chosen fluid, which connects the evaporation/condensation saturation temperature with a saturation pressure. This means that additional or removed heat at this specific temperature and pressure will result in a phase change and not an increased or decreased temperature. Using a phase change in cooling systems results in significantly higher moved heats compared to liquid only cooling cycles through the evaporation enthalpy of the chosen fluid [6].

Figure 1 shows the most common refrigeration cycle architectures used. Both architectures consist of the same five components. These are an evaporator (heat exchanger (chiller)), a compressor, a condenser (heat exchanger), an expansion valve and an accumulator. Depending on the position of the accumulator the cycle definition can change.

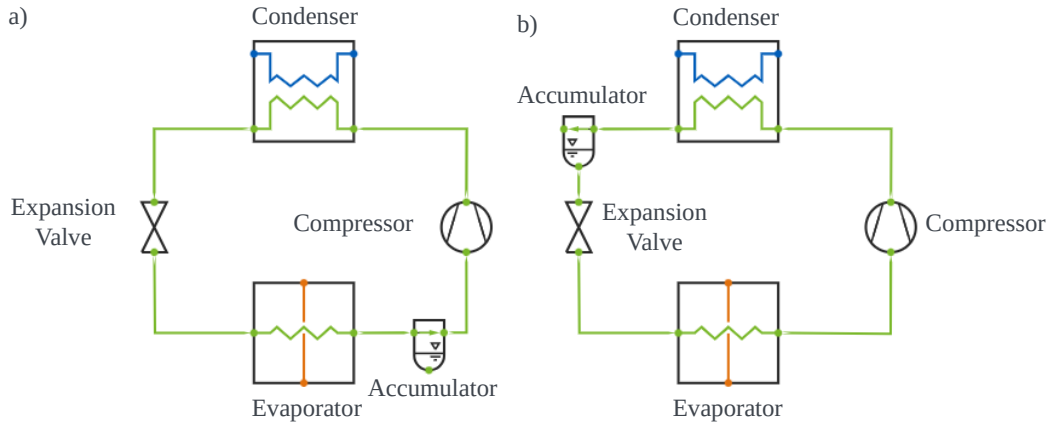


Figure 1: Refrigeration Cycle Designs when integrating an accumulator.
a) Accumulator sets superheat = 0 K, b) Accumulator sets subcooling = 0 K. [7]

However, the overall refrigeration cycle works the same for both architectures. Starting at the evaporator, the fluid enters in liquid (or mixed liquid and gas state) and evaporates completely at low pressure and low temperature while absorbing heat. Then, the resulting vapor is compressed isentropically inside the compressor to a higher pressure and temperature. The compressed vapor (high pressure and temperature) enters the condenser, where it condenses back to liquid while removing heat. The heat removed is the sum of the heat absorbed at the evaporator plus the added energy from the compressor. Lastly, the expansion valve expands the liquid fluid back to low pressure and temperature. The accumulator's function is to control the superheat after the evaporator (Figure 1 a)) or the subcooling after the condenser (Figure 1 b)), depending on the positioning inside the circuit. Both positions can define the thermodynamic cycle.

For the design of refrigeration cycles, the degrees of freedom are the compressor speed, the compressor efficiency, the expansion valve opening, the size of the evaporator and the size of the condenser. These degrees of freedom can be set by the determination of the unknowns, which consist of the evaporation pressure, the condensation pressure, the superheat before the compressor, the temperature after the compressor, the subcooling after the condenser and lastly, the mass flow rate of the refrigerant. While the first five unknown define the thermodynamic cycle, changing the mass flow rate scales the absorbed and removed heat. [7]

The evaporator is modeled by providing the simulation tool the geometrical parameters of a brazed plate heat exchanger. In the CoolEV project the evaporator can be designed by using the Kaori software [8]. The refrigeration compressor pressure increase can be modeled by

$$\Delta p = f(\dot{m}, w, T) \tag{8}$$

with the same parameters as the cooling circuit pump [4]. Furthermore, the isentropic and mechanical efficiency can be calculated with the pressure increase and rotating speed of the compressor

$$\eta_{\mathrm{is,me,compressor}} = f(\Delta p, w) \tag{9}$$

improving the ideal to a real refrigeration cycle. As mechanical efficiency a standard value of 0.99 can be used, while the isentropic efficiency can be calculated depending on the chosen refrigerant fluid [9].

The condenser in this study is modeled with its exact geometrical data. The 1D-simulation software AMESIM then calculates the heat transferred according to the mass flow rates of refrigerant and air with the documented Nusselt-correlations for a microchannel heat exchanger [4]. In the CoolEV project the condenser design software Climetal [10] has been used.

Accumulators are defined by their size and their initial percentage of liquid volume. Depending on the refrigerant chosen and total mass of the refrigerant, an adequate accumulator can be iteratively sized. The sizing should be done to ensure proper accumulator function but not unnecessarily increase the total refrigerant mass. In this study a thermostatic expansion valve is used to control the mass flow rate of the refrigeration cycle depending on the desired superheat after the evaporator.

## 2.3 Additional Heat inputs

In general, occurring losses result in additional heat inputs into the cooling circuit. Additional heat inputs caused by the pump can be calculated by

$$\dot{Q}_{\mathrm{pump}} = \left(1 - \eta_{\mathrm{pump}}\right) P_{\mathrm{mech}} \tag{10}$$

whereas $\eta_{\mathrm{pump}}$ represents the pump efficiency and $P_{\mathrm{mech}}$ the mechanical power of the pump. Additional heat inputs due to pressure losses are calculated by

$$\dot{Q}_{\Delta p} = \Delta p \, \dot{V} \tag{11}$$

whereas $\Delta p$ is the total pressure loss inside the circuit and $\dot{V}$ represents the volume flow rate in the circuit.

## 3 Methodology

This chapter presents the conceptualization of the external thermal management system to evaluate its feasibility. Additionally, it presents the design process and set boundary conditions.

### 3.1 Conceptualization of the external Thermal Management System

The concept for the external thermal management is developed in the CoolEV project [9] and shown in Figure 2. In total, there are three different circuits involved, connected by heat exchangers. The first circuit is the vehicle cooling circuit, in which the oil Opticool has been chosen as working fluid. This study assumes the loss behaviour of the LIB pack to be constant over the whole XFC scenario. Therefore, the battery can be presented as a boundary condition of waste heat that needs to be removed from the vehicle cooling circuit, without modeling its internals. However, should it be necessary to model a dynamic loss behaviour of a real LIB pack, it is also possible to implement an additional battery pack model. [9]

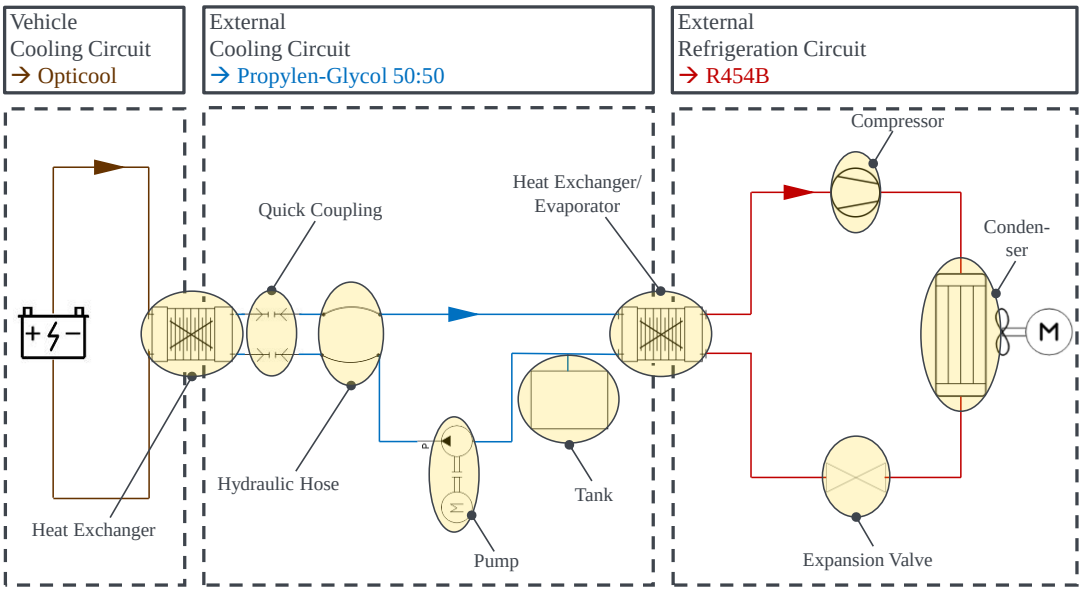


Figure 2: Conceptualization of the external thermal management concept for XFC of BEVs.

The second cycle is the external cooling circuit, running with HYDAC Coolant N50, which is Propylen-Glycol 50:50 (PGL). The external cooling circuit's purpose is to remove the total waste heat of the LIB pack. However, it is not required to

instantaneously remove the total battery waste heat. Therefore, a thermal energy storage tank integration is studied. This would allow to decrease the size of other components (especially in the refrigeration circuit) while still removing all the waste heat over an increased period. Furthermore, a cooling fluid coupling to the vehicle is necessary to connect the vehicle cooling and the external cooling circuit. Therefore, a quick coupling and hydraulic hoses are necessary to allow drivers to easily couple the external cooling system with the vehicle cooling circuit, similar to the electrical coupling systems. Lastly, as in all cooling circuit designs, a pump is needed to fulfill the requirements of the desired volume flow rate. This includes overcoming all pressure losses occurring inside the external cooling circuit. [9]

The last component, the heat exchanger/evaporator, connects the external cooling circuit to an external refrigeration circuit. The refrigeration circuit is responsible for removing the battery pack waste heat to the environment, with R454B as working fluid. Refrigeration circuits use the heat transfer characteristic benefits of phase changes inside the fluid to remove more heat with less power required compared to standard cooling circuits [6]. The refrigeration circuit consists of evaporator, compressor, condenser, accumulator and expansion valve and can be designed by using the thermodynamics fundamentals of a vapor compression cycle.

Figure 3 shows the design process for the external thermal management concept. The design starts with the parameters defined in the CoolEV project [9]. These consist of the inlet heat exchanger oil temperature, the battery waste heat, the oil volume flow rate and the maximum pressure loss allowed of the vehicle cooling circuit. By choosing an adequate heat exchanger that makes the removal of the heat possible, the PGL heat exchanger inlet temperature and the PGL volume flow rate can be determined. Choosing the quick coupling system and hydraulic hose lengths and diameters as well as the heat exchanger pressure losses enables a suitable pump design. The remaining parameters depend on the concept of the thermal energy storage tank. The tank design sets the amount of heat the evaporator must remove, which in turn determines the design of the refrigeration circuit components.

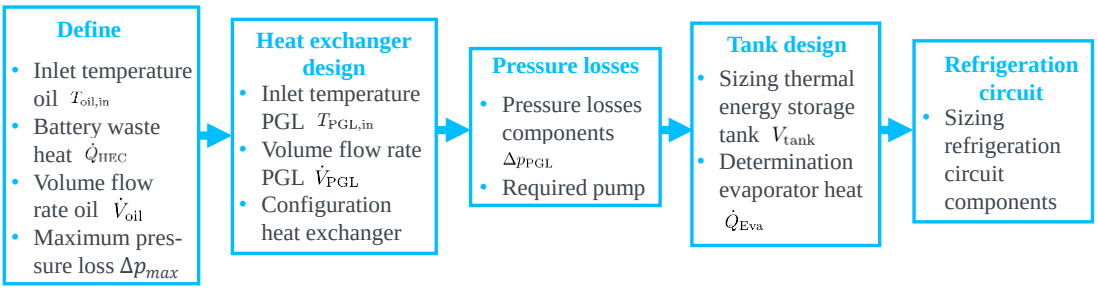


Figure 3: Design process of the external thermal management concept.

In total, four thermal energy storage tank integration concepts are studied and shown in Table 1. In general, the bigger the tank, the smaller the components of the refrigeration circuit can be. However, this benefit comes with a disadvantage of a longer rest time frame after every XFC, during which no other BEV can be charged. The final design is a trade-off between size of the refrigeration circuit, size of the thermal energy storage tank and necessary rest time after every XFC at the charging station.

Table 1: Design options for the thermal energy storage tank.

| **Concept** | **Phase 1: XFC time in min** | **Phase 2: Break time in min** | **Heat Evaporator in kW** | **Heat stored in tank per second in kJ** | **Tank size** |
|---|---|---|---|---|---|
| A) No tank | 10 | 0 | 27.5 | 0 | 0 |
| B) Big tank | 10 | 10 | 13.75 | 13.75 | 463 |
| C) Medium tank | 10 | 5 | 18.33 | 9.17 | 309 |
| D) Small tank | 10 | 3 | 21.1 | 6.4 | 215 |

The tank size can be calculated by taking the density $\rho$ and specific heat capacity $c_p$ of the chosen cooling fluid of the external cooling circuit. In this study, this is PGL, with a freezing point of $\mathrm{T} = -32\,°\mathrm{C}$ which enables a safety margin to the minimum temperature design point in the external cooling circuit of $-15°\mathrm{C}$. The tank size is estimated by

$$V_{\mathrm{tank}} = \frac{Qt}{\rho c_{\mathrm{p}} \Delta T} \tag{12}$$

whereas $Q$ represents the heat in J stored per second, $t$ the total storage time and $\Delta T$ the maximum temperature increase inside the thermal storage tank. As long as the maximum temperature increase is within 5 K for the studied cooling medium PGL, equation (12) is sufficient to calculate the tank volume. However, for higher temperature increases, the density and specific heat capacity would need to be adapted to the real start and end temperature values of the fluid inside the thermal storage tank.

Additionally, in appendix Figure A.1, the tank temperature ($T_{\mathrm{tank}}$) development of the studied concepts is shown. In the CoolEV project, option B) has been chosen [9]. This option provides a good trade-off between refrigeration circuit component size and maximum rest time. As a result, the external thermal management system is divided into two different phases. One phase is the XFC which takes 10 min and the second phase is the 10 min rest time after every XFC.

## 3.2 Boundary Conditions

This section will discuss the boundary conditions of the external thermal management system which result from the previously chosen thermal energy storage design. The boundary conditions as well as the built 1D thermal simulation model in Amesim are shown in Figure 4. The boundary conditions of the vehicle cooling circuit can be set according to the XFC. The XFC is defined as a constant battery waste heat loss of 27.5 kW, which has to be removed for 10 min. This represents an XFC from 10 to 80 % State of Charge (SOC) in 10 min. The second boundary condition of the vehicle cooling circuit is the maximum pressure loss resulting of the vehicle cooling circuit pump design. The maximum pressure loss on the vehicle cooling circuit inside the heat exchanger has been set to $\Delta p_{max} = 0.225$ bar resulting in an additional design requirement for the heat exchanger between vehicle and external cooling circuit [9].

To limit the cooling circuit pressure loss to $\Delta p_{max}$ on the vehicle cooling circuit, a configuration consisting of two heat exchangers have been chosen. This configuration enables to fulfill the pressure loss, inlet temperature of the vehicle circuit and volume flow rate requirements [9]. Therefore, the chosen heat exchanger design determines the external cooling circuit volume flow rate and heat exchanger inlet temperature. In order to remove the required amount of heat a volume flow rate on the external cooling circuit of 50 l/min is necessary with a heat exchanger inlet temperature on the external cooling circuit between -15 °C and -10 °C. The low required inlet temperatures necessitate PGL as the external cooling circuit fluid, because it freezes at lower temperatures than comparable fluids.

The required volume flow rate and the occurring pressure losses define the pump of the external cooling circuit. The pump needs to overcome the combined pressure losses of the heat exchangers, the hydraulic hose and the quick coupling system. The pressure increase and efficiency of the chosen pump are shown in appendix Figure A.2. The data is taken from a centrifugal pump by Grundfos [11]. Therefore, the pressure increase corresponding to the volume flow of the cooling fluid and the efficiency can be directly sourced from the provided data sheets.

The length of the hydraulic hose has been chosen as 5 m to allow the customer to easily plug and unplug the quick coupling system. As quick coupling system a liquid adapter solution by the company Stäubli [12] has been chosen, providing the pressure losses for all external cooling circuit components. The pressure losses depending on the volume flow rate for the chosen quick coupling CGO12 by Stäubli are shown in appendix Figure A.3.

Modeling refrigeration circuits is more complex than modeling cooling circuits. The main difference is the phase. However, several design points need to be fixed before addressing the components. One of the most important aspects is the choice of the refrigeration fluid. The refrigeration fluid needs to have adequate evaporation temperature and pressure to be able to absorb the heat at all desired operation points.

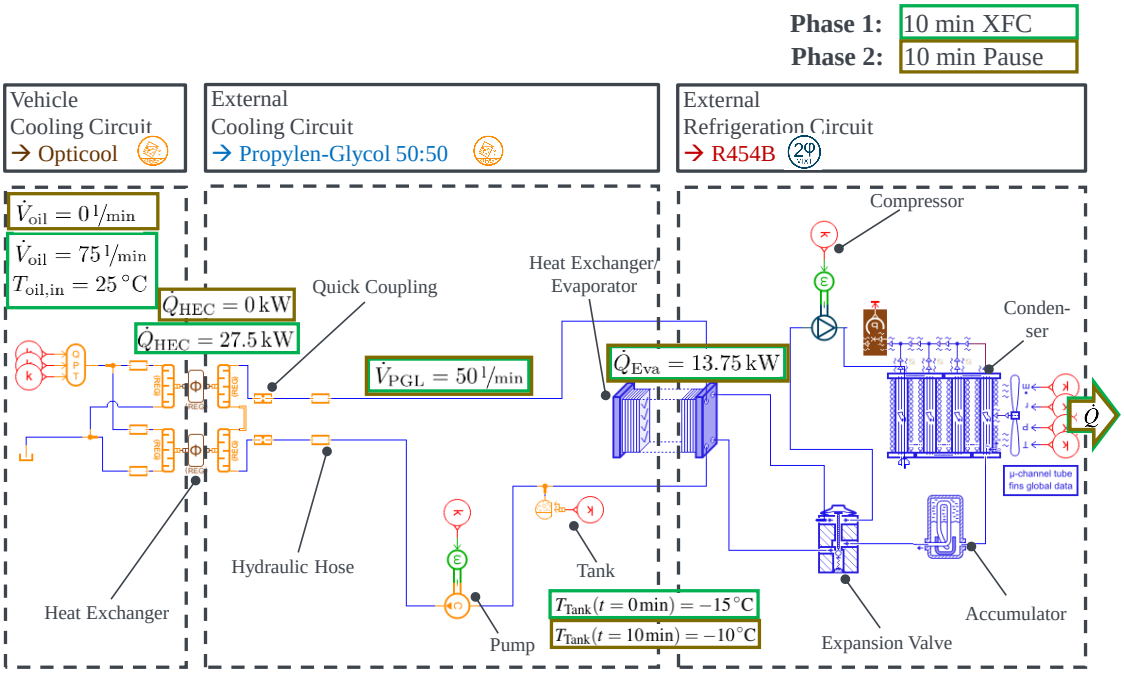


Figure 4: Defined boundary conditions of the external thermal management concept for XFC of BEVs.

The designed refrigeration cycle for the chosen refrigerant fluid R454B is shown in Figure 5 and consists of four steps. First, the vapored fluid is compressed in the compressor, Then, the refrigerant fluid condenses in the condenser until the fluid is at full liquid state. In this study, an accumulator is used after the condenser to ensure a subcooling of 0 K. After the accumulator, the liquid fluid goes through the expansion valve, which adjusts the mass flow rate so that the expanded liquid at lower pressure fully evaporates in the evaporator. If there is no full evaporation of the liquid, the compressor will suffer damage due to liquid ingestion. Therefore, an overheating of 5 K is set to be controlled by the expansion valve mass flow control unit. This guarantees full evaporation in all design points and dynamic profiles.

The refrigeration cycle design starts with the chosen refrigerant fluid R454B. Next, the evaporation and condensation temperature need to be determined. The evaporation process requires lower refrigerant temperatures than the external cooling circuit, while the condensation process requires higher refrigerant temperatures than the ambient temperature. Since the minimum cooling fluid temperature is −15 °C, the evaporation temperature has been set to −16 °C. Furthermore, the maximum ambient temperature defined in the project CoolEV is $T_{amb} = 30$ °C. To ensure a safe operation and limited condenser size, the condensation temperature has been set to 47 °C. The pressure levels of the refrigeration cycle are determined by the saturation curve of R454B, being $p_{Eva}$ = 4.22 bar and $p_{Con}$ = 26 bar. Lastly, the chosen compressor must be able to compress the refrigerant to the desired pressure, which is an isentropic compression process.

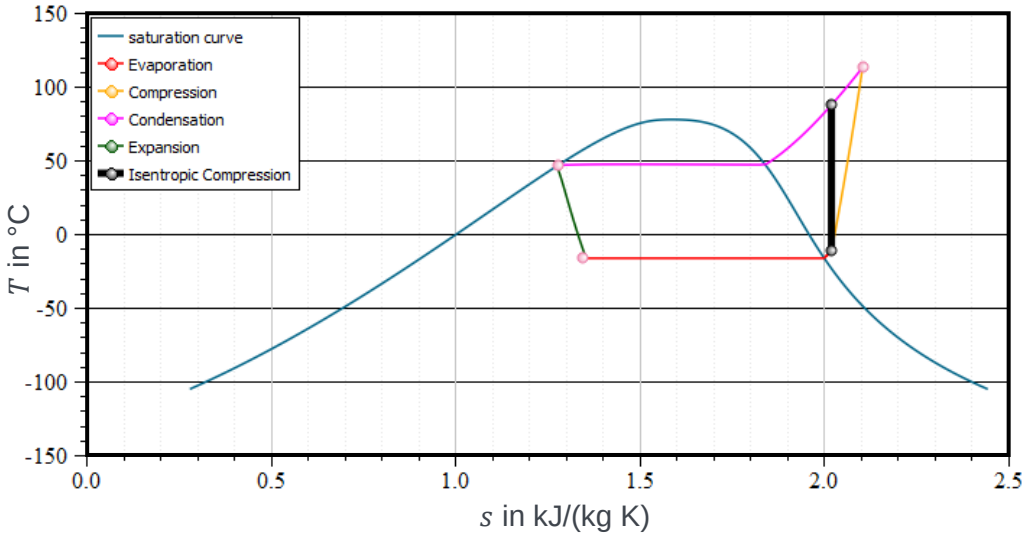


Figure 5: Wet steam region of the refrigerant R454B including the design points of the vapor compression cycle in a T-s diagram. [4]

The values for the compressor can be calculcated from the desired evaporation heat, the evaporation and condensation temperatures as well as the refrigerant fluid. A software tool by Bitzer [13] has been used for an adequate compressor design. The resulting necessary condensation heat and mass flow rate are shown in appendix Figure A.4. The expansion valve design is an iterative process, especially when using a thermostatic expansion valve, which controls the mass flow rate according to the desired superheat of the vapor after the evaporator. The heat transferred during all four processes are shown in Table 2 for the Bitzer design as well as for the 1D thermodynamic cycle in AMESIM. This results in a Coefficient of Performance (COP) of the refrigeration cycle of $\mathrm{COP} = Q_{\mathrm{Con}}/P_{\mathrm{Compressor}} = 2.84$.

Table 2: Powers of desinged vapor compression cycle processes in Amesim and Bitzer software.

| | **Transformation** | **Power Amesim in kW** | **Power Bitzer in kW** |
|---|---|---|---|
| 1 | Evaporation | 15.1 | 15.5 |
| 2 | Compression | 8.3 | 8.5 |
| 3 | Condensation | 23.6 | 24 |
| 4 | Expansion | 0.2 | - |
| 5 | Mass flow rate in kg/h | 313 | 314 |

## 4 Results

In total, three XFC/Pause cycles have been simulated resulting in a total simulated physical time of $t = 3600$ s with a simulation time step of $\Delta t = 2$ s. Additional heat inputs in the external cooling circuit have been considered, resulting in adjusted boundary conditions for the refrigeration circuit. The results of the heat exchangers and thermal energy storage tank temperature are presented to demonstrate the system's ability to meet the demands of the external thermal management system.

### 4.1 Heat exchanger Vehicle cooling circuit

Figure 6 shows the heat transferred over the first $Q_{\mathrm{HEC},1}$, second, $Q_{\mathrm{HEC},2}$, the sum of both $Q_{\mathrm{HEC,sum}}$ and the mean heat over all three XFC cycles $Q_{\mathrm{HEC,sum,mean}}$. While in the first XFC cycle the heat transferred differs by 10 % between Heat exchanger 1 (HEC1) and HEC2 for the second and third XFC, the removed heat is the same over both HECs. Hence, the temperature difference between external cooling circuit and vehicle cooling circuit is high enough, so that the higher inlet temperature of HEC2 compared to HEC1 does not influence the heat transfer. Additionally, during the rest time Phase 2, no heat is transferred between the vehicle and external cooling circuit. The average transferred heat in the XFC cycles is at $Q_{\mathrm{HEC,sum,mean}}$ = 27.56 kW, fulfilling the cooling requirements of the LIB pack during XFC of 27.5 kW.

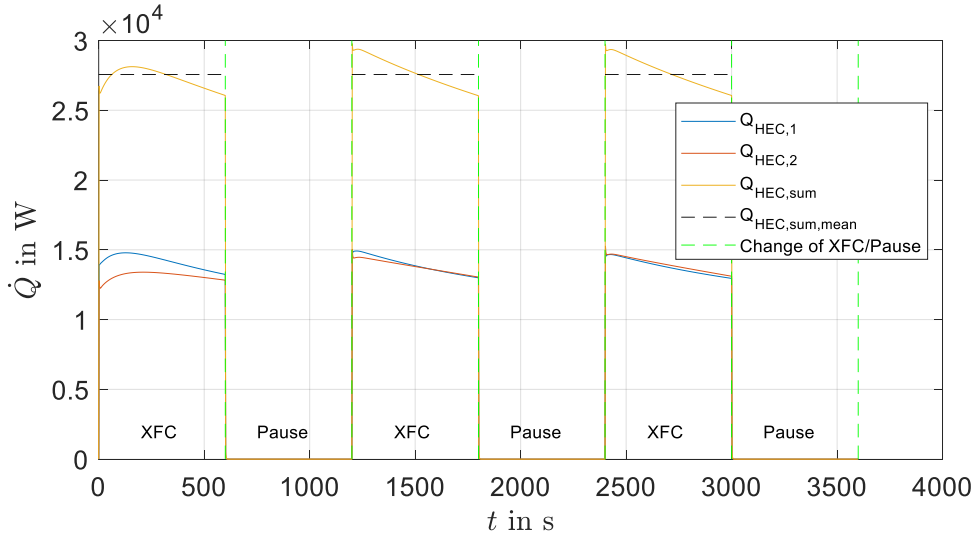


Figure 6: Heat transferred over three XFC/Pause cycles through both heat exchangers between vehicle and external cooling circuit.

## 4.2 Additional heat input

The simulation model reveals an additional heat input from the external cooling circuit. The additional heat input results from the combined effect of the pump efficiency and the pressure losses. By using equations (10) and (11), the additional heat inputs can be calculated. The external cooling circuit pump has an almost constant efficiency of $\eta_{\mathrm{pump}} = 0.269$ and a mechanical power of $P_{\mathrm{mech}} = 1.33$ kW. This equals an additional heat input due to the pump of $\dot{Q}_{\mathrm{pump}} = 0.97$ kW. A pressure loss of $\Delta p = 4.23$ bar inside the external cooling circuit results from the simulation. At a volume flow rate of $\dot{\mathrm{V}} = 50$ l/min this equals an additional heat input due to the pressure losses of $\dot{Q}_{\Delta p} = 0.35$ kW. Hence, the combined additional heat inputs, which need to be removed in both concept phases equal to 1.32 kW increasing the heat to be removed through the evaporator by 10 % to $\dot{Q}_{\mathrm{eva}} = 15.07$ kW. Therefore, the additional heat needs to be considered in the conceptualization of the refrigeration circuit.

## 4.3 Evaporator heat

The evaporator has been designed to remove $\dot{Q}_{\mathrm{eva}} = 15.07$ kW in average over the XFC/pause cycle. However, in the design process a constant removed heat over the evaporator has been assumed. This is not true for the real dynamic behavior of the external thermal management design. The reason is the changing boundary conditions of the vehicle and external cooling circuit.

Due to the XFC/pause design, the removed heat over the same evaporator cannot be kept constant. The external cooling circuit's evaporator inlet temperature changes depending on wheter it is in an XFC or pause phase. During XFC there is a large amount of battery waste heat (27.5 kW) delivered into the external cooling circuit. This increases the external cooling circuit fluid temperature and hence, the inlet temperature at the evaporator on the liquid side. Higher inlet temperatures result in higher temperature differences between external cooling fluid and refrigerant and hence, a higher heat transfer. However, during the pause phase, there is no heat delivered into the external cooling circuit. Therefore, the evaporator inlet temperature is lower in the pause phase compared to the XFC phase. To still be able to remove the constant heat of 15.07 kW over both cycles, a larger compressor is necessary. The larger compressor increases the heat transfer during XFC and thus, can compensate for the decreased heat transfer in the pause phase. This also influences the necessary thermal energy storage tank sizing. The final evaporation heat removal results can be seen in Figure 7. The average removed heat over the evaporator over three XFC/Pause cycles results in $\dot{Q}_{\mathrm{Eva,mean}} = 15.2\,kW$ and therefore, fulfills the requirement of removing 15.07 kW heat. However, the larger compressor decreases the COP of the refrigeration circuit.

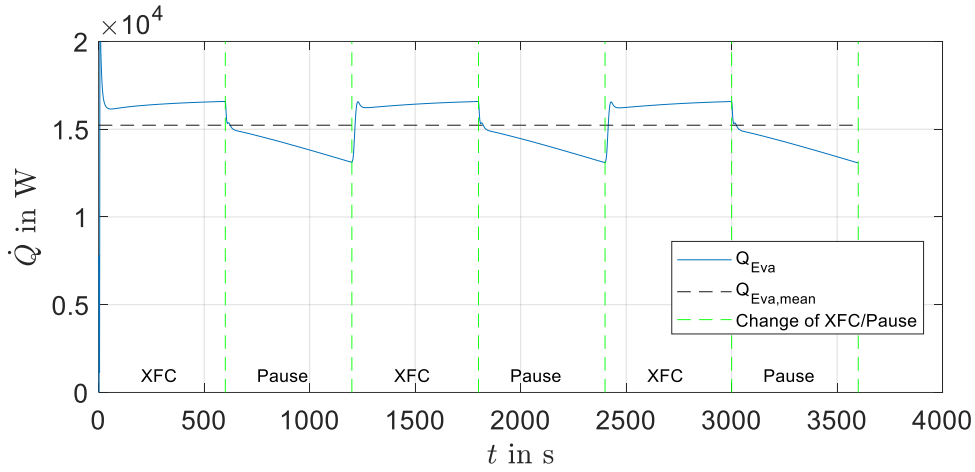


Figure 7: Heat transferred over three XFC/Pause cycles through the evaporator.

### 4.4 Condenser heat

The results for the heat removed to the environment by the condenser are shown in Figure 8. The higher the ambient temperature the more challenging the task is for the condenser, because the temperature difference between refrigerant fluid and environmental air decreases. Therefore, an ambient temperature of $T_{\mathrm{amb}} = 30$ °C has been chosen for the simulation to ensure operation over all environmental conditions. Because of the increased compressor size and the resulting increased losses, more heat must be removed by the condenser than designed. The chosen condenser is suitable for the increased heat loads and does not need to be replaced. The condenser heat follows the same trend as the evaporator heat regarding the XFC and pause phases. On average, the condenser removes $\dot{Q}_{\mathrm{Con,mean}} = 27.3$ kW and fulfills the requirements of the conceptualization.

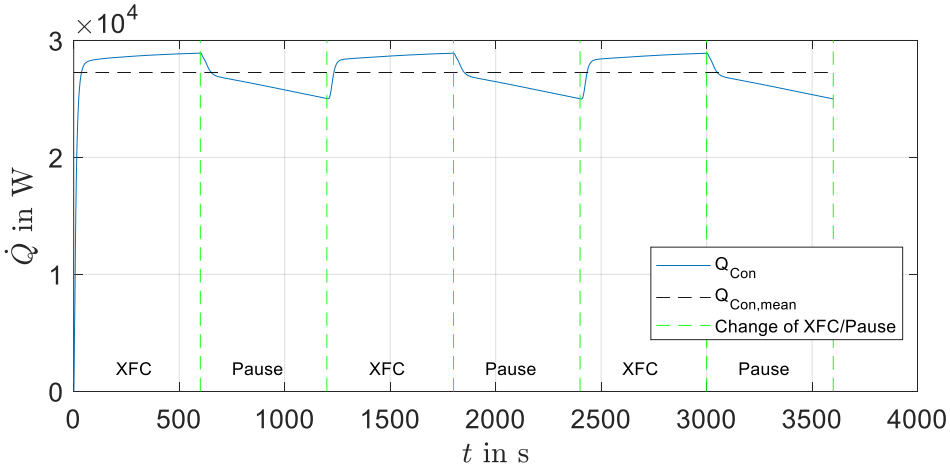


Figure 8: Heat transferred over three XFC/Pause cycles through the condenser to the environment.

### 4.5 Tank sizing

To determine the inital boundary conditions, the tank has been dimensioned with a simple heat balance equation (12) involving the start and end temperatures desired in the tank as well as the time frames for XFC and pause. However, the total system simulation is influenced by dynamic modeling and changing inlet temperatures at the evaporator. The enlarged compressor and hence, increased heat removal during the XFC phase allows a downsizing of the tank. This can be done iteratively after the refrigeration and external cooling circuit parameters are set. Compared to the initial calculated value of 463 l the tank can be decreased by 40 l (approx 10%) to 420 l. An additional effect allowing a smaller tank is that some of the liquid cooling fluid is spread out in the heat exchanger and pipes. The tank temperature over time over three XFC/pause cycles is shown in Figure 9. The set limits of an inlet temperature between $-15$ °C and $-10$ °C for the vehicle to external cooling circuit heat exchangers can be fulfilled.

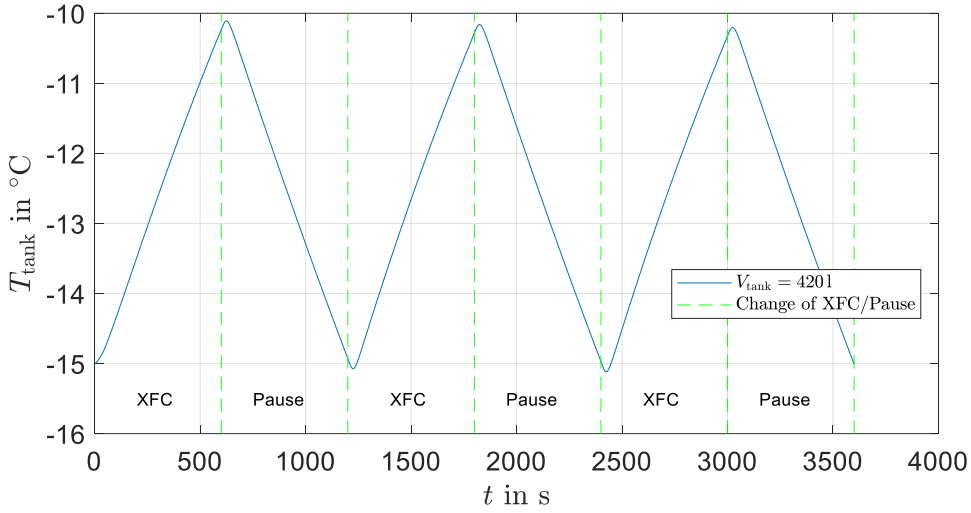


Figure 9: Tank temperature over three XFC/Pause cycles in the thermal energy storage tank of the external cooling circuit.

## 5 Conclusion

In this study, an external thermal management system for XFC scenarios of BEVs has been designed . The conceptualization and design process is presented. Furthermore, the boundary conditions set to fulfill the requirements for the removed heat are shown. In the 1D-simulation tool AMESIM, a simulation framework has been built, being able to model the external thermal management concept. The results have shown the feasibility of the designed system for the application of external thermal management systems in XFCs.

The developed simulation framework can further be used for sensivity and optimization studies. With changing heats to be removed or specifications of the cooling fluids inside the circuits, all other components can be scaled to fulfill new requirements for different BEV architectures and cells. However, this study uses a maximum heat to be removed scenario to be able to work for most BEV XFC cases. By developing an adequate control system, which could be a PID control between the desired vehicle cooling circuit heat exchanger outlet temperature and the condenser fan rotation speed (mass flow rate of the air) the developed concept should be suitable to all common BEVs.

## 6 Acknowledgments

This research is accomplished within the project “CoolEV”. We acknowledge the financial support for the project by the German Federal Ministry of Economic Affairs and Climate Action (BMWK) as part of the "Electric Mobility" funding program.

## 7 Bibliography

[1] Pesaran, Ahmad A. "Battery thermal models for hybrid vehicle simulations." Journal of power sources 110.2 (2002): 377-382.

[2] Feng, Xuning, et al. "Thermal runaway mechanism of lithium ion battery for electric vehicles: A review." Energy storage materials 10 (2018): 246-267.

[3] Bernardi, D., E. Pawlikowski, and John Newman. "A general energy balance for battery systems." Journal of the electrochemical society 132.1 (1985): 5.

[4] Siemens, "Simcenter Amesim User Manual." (2023).

[5] Sumeru, K., H. Nasution, and F. N. Ani. "A review on two-phase ejector as an expansion device in vapor compression refrigeration cycle." Renewable and Sustainable Energy Reviews 16.7 (2012): 4927-4937.

[6] Németh-Csóka, Mihály. Thermisches Management elektrischer Maschinen. Springer: Wiesbaden, Germany, 2018.

[7] Gräber, M., “Why receivers and accumulators in refrigeration cycles?” (2020) Accessed on 01/09/2023, url: https://tlk-energy.de/blog/warum-gibt-es-sammler-und-abscheider-im-kaeltekreislauf

[8] Kaori Heat Treatment Co., LTD., Accessed on 01/09/2023, url: https://www.kaori.com.tw/en/modules/nc_product/

[9] CoolEV Consortium, “Design and project requirements of the external thermal management system by the CoolEV consortium” (2022).

[10] Climetal, S.L., “Climetal Microchannel Simulation”, Accessed on 10/07/2023, url: http://webapp.climetal.com/Account/Login.aspx?ReturnUrl=%2f

[11] Grundfos GMBH, “MTH 4-6/6 A-W-A-AQQV”, Accessed on 01/09/2023, url: https://product-selection.grundfos.com/de/products/mt-tank-mounted-pumps/mth/mth-4-66-98993064?tab=variant-curves&pumpsystemid=2157052039

[12] Stäubli International AG, Accessed on 01/09/2023, url: https://www.staubli.com/de/de/corp.html

[13] Bitzer Kühlmaschinenbau GmbH, “Bitzer Software 6.18.0”, Accessed on 01/09/2023, url: https://www.bitzer.de/de/de/tools-archiv/software/software/versionen -software.jsp

## 8 Appendix

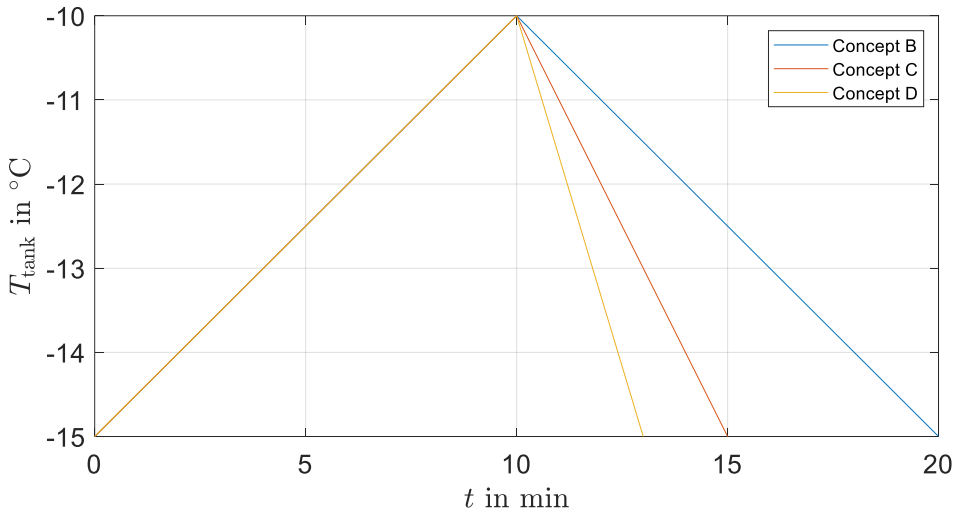


Figure A.1: Tank temperature development for three different thermal energy storage tank concepts.

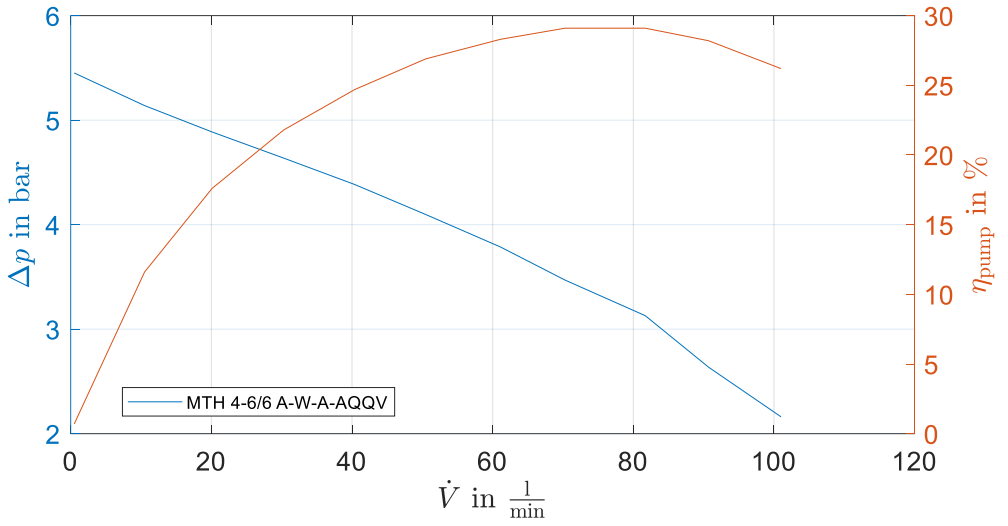


Figure A.2: Pressure increase and efficiency dependent on the volume flow rate for the chosen cooling pump by Grundfos [11].

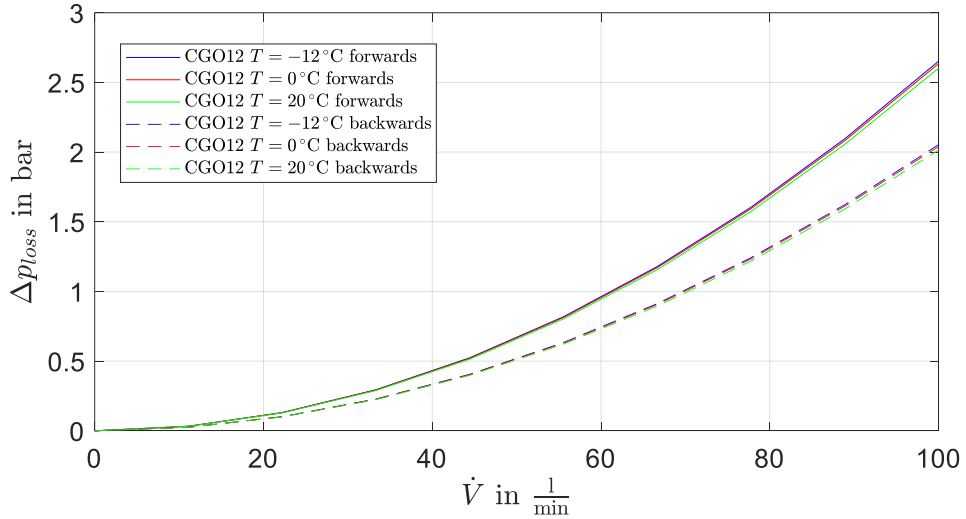


Figure A.3: Pressure losses of the chosen quick coupling configuration CGO12 by Stäubli [12]. Distinguished between forward and backward flow direction.

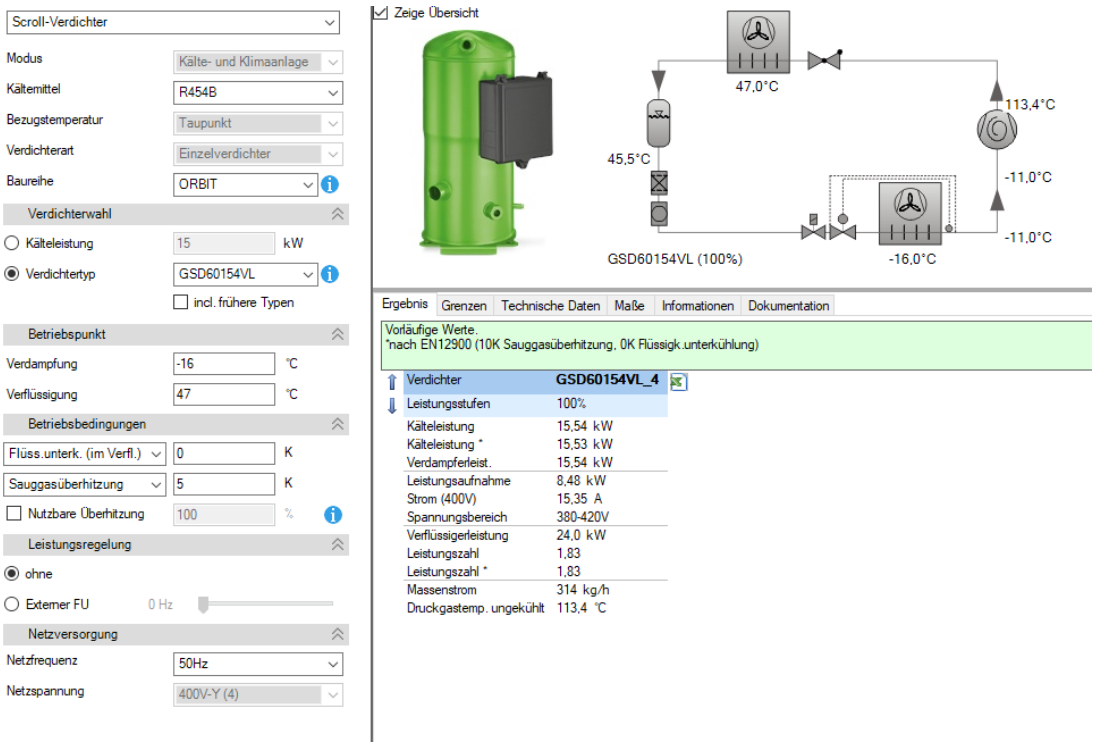


Figure A.4: Bitzer data of the designed compressor. [13]

# Stochastic noise sources for broadband CAA at geometrical variations of a vehicle

Philipp Uhl[1], Alexander Schell[1], Roland Ewert[2], Jan Delfs[2]

[1]: Aerodynamics and Aeroacoustics Department
Mercedes-Benz AG
Benz-Straße
71063 Sindelfingen

[2]: Institute of Aerodynamics and Flow Technology, Technical Acoustics
German Aerospace Center (DLR)
Lilienthalplatz 7
38108 Braunschweig

**Abstract:** The Fast Random Particle-Mesh method as member of the class of stochastic noise source methods for broadband aeroacoustic simulations is employed for two test cases and compared to scale-resolving simulations. A side mirror geometry and a full vehicle underbody test case are used to investigate the accuracy and robustness of the method as part of a hydrodynamic-acoustic splitting methodology for nearfield aeroacoustics. The acoustic Deltas of two geometrical configurations of the side mirror are computed with good agreement to reference simulations when choosing a physically agreeing RANS input. Taking minor input data leads to less accurate results. The underbody test case reveals a good performance of the method even for very low frequencies with robustness on three geometrical configurations. With a computational speed-up of a factor of up to 8, the stochastic method proves the capability to be used for broadband noise optimization cycles in very early development stages.

## 1 Introduction

The automotive industry is rapidly changing due to digital advancements, leading to shorter development cycles and heightened efficiency. A key focus in automotive engineering is reducing noise from aerodynamic sources, called aeroacoustics, which significantly improves passenger comfort. To meet faster development needs, the automotive sector is shifting towards virtual prototyping and simulation-based design. Digital simulations offer cost-effective and efficient ways to evaluate designs and optimize noise reduction before physical prototypes are made, reducing costs and time-to-market. Integrating computational fluid dynamics (CFD) with computational aeroacoustic (CAA) methods provides insights into noise sources and effective mitigation strategies. Advanced computing and numerical methods with e.g. Large

[1] Corresponding author: philipp.uhl@mercedes-benz.com

Eddy Simulations (LES) have transformed aeroacoustic prediction and analysis. However, computational capabilities struggle to match shortened development timelines, highlighting the need for fast yet accurate CAA methods. Stochastic noise source methods based on stationary Reynolds-averaged Navier Stokes (RANS) equations offer promising solutions. These include energy-based methods like Stochastic Noise Generation and Radiation (SNGR) and the correlation-based Fast Random Particle-Mesh (FRPM) method. Both methods realize turbulent velocity fluctuations, with SNGR using random Fourier modes and FRPM utilizing white-noise convolution with predetermined correlations and amplitudes. FRPM has aerospace origins and is yet to be applied in the automotive context.

This paper starts with theoretical remarks on the FRPM method for broadband nearfield aeroacoustics and is followed by two test cases showing the capability of FRPM to deliver consistent and robust noise source data with high accuracy. The last part deals with the computational advantage of the stochastic noise source method.

## 2 Theoretical remarks

In this section, some theoretical remarks on the used methods are given. The reference simulations are based on two different methods depending on the test case: (i) for the side mirror test case, a Hybrid-Temporal RANS-LES (HTLES) approach as in Duffal et al. [1] with a $k$-$\varepsilon$ Lag Elliptic Blending (LEB) for the sub-filter scales is used, whereas (ii) for the underbody test case, a LES with the WALE sub-gid scale model is chosen. The stochastic noise source method investigated in this work is the Fast Random Particle-Mesh method by Ewert et al. [2] which is explained in the following. A more detailed explanation of the workflow is given in Uhl et al. [3].

### 2.1 Fast Random Particle-Mesh method

The Fast Random Particle-Mesh (FRPM) method by Ewert et al. [2] used in this work synthesizes stochastic noise sources in the form of turbulent velocity fluctuations in time domain. Time-averaged data from e.g. RANS simulations like the vectorial velocity or scalar turbulent kinetic energy as well as turbulent length scale distribution are necessary as input. With the prescription of frozen turbulence, the method realizes two-point space-time correlations with Gaussian decay in space. The generation of turbulent velocity fluctuations relies on the spatial filtering of a white-noise field $\mathcal{U}_k$ with amplitude $\hat{A}$ with a filter kernel of Gaussian shape $G^0$:

$$\psi_k(\boldsymbol{x},t) = \int_{V_s} \hat{A}(\boldsymbol{x}) G^0\big(|\boldsymbol{x}-\boldsymbol{x}'|, l_s(\boldsymbol{x}')\big)\mathcal{U}_k(\boldsymbol{x}',t)d\boldsymbol{x}'$$

The curl of the vectorial stream function leads to solenoidal velocity fluctuations $u_i'(\boldsymbol{x},t) = \varepsilon_{ijk}\frac{\partial \psi_k}{\partial x_j}$ since the identity $\nabla \cdot \nabla \times \psi = 0$ holds. The white-noise fields $\mathcal{U}_k$ on the particles introduce the randomness and have zero mean, are mutually

uncorrelated and do not change their value along the streamline for frozen turbulence. The filter kernel $G^0$ depends on the turbulent length scale distribution $l_s$ which can be derived from RANS via $l_s = c_l \frac{k^{3/2}}{\varepsilon}$ for an $\varepsilon$-based model with $c_l = 0.54$. For an $\omega$-based model, the relation $\varepsilon = C_\mu k\omega$ with $C_\mu = 0.09$ can be used. Turbulence spectra of arbitray shape can be realized, such as Liepmann or von Karman spectra, by superposition of multiple stream functions with different length scale and amplitude. Further details can be found in Wohlbrandt et al. [4].

## 2.2 Conversion of velocity fluctuations to hydrodynamic pressure fluctuations

The turbulent velocity fluctuations provided by either the scale-resolving simulations like HTLES and LES or the stochastic noise source method FRPM are converted to hydrodynamic pressure fluctuations with the following Poisson equation

$$\frac{1}{\rho}\nabla^2 p_h' = -\frac{\partial^2}{\partial x_i \partial x_j}\left(u_i u_j - \overline{u_i u_j}\right) \quad (\text{with } u_i(\boldsymbol{x},t) = \overline{u}_i(\boldsymbol{x}) + u_i'(\boldsymbol{x},t))$$

which can be derived from the incompressible Navier-Stokes equations. At walls, a Neumann boundary condition $\frac{\partial p_h'}{\partial n} = 0$ and at farfield boundaries with large distance to the source region a Dirichlet boundary condition $p_h' = 0$ is prescribed. This provides a pure hydrodynamic pressure in the nearfield.

## 2.3 Aeroacoustic analogy

The hydrodynamic pressure field states the driving metric for the acoustic analogy used in this work which is based on a second-order Perturbed Convective Wave Equation (PCWE) derived by Piepiorka and Estorff [5] of the following form

$$\frac{D^2\phi_a}{Dt^2} - c_0^2\nabla^2\phi_a - \frac{1}{\rho}\nabla\phi_a \cdot \nabla p_h' = -\frac{1}{\rho}\frac{Dp_h'}{Dt} \quad \rightarrow \quad p_a' = \rho\frac{D\phi_a}{Dt}$$

which solves for the acoustic potential $\phi_a$. The acoustic pressure $p_a'$ is gained by taking the total derivative of the acoustic potential.

# 3 Side mirror test case

The side mirror is a fundamental noise source in vehicle aeroacoustics and calls a strong attention to itself by being located relatively close to the passenger ears. Due to materialistic coincidence effects of the side window glass, the acoustic pressure $p_a'$ plays the major role for frequencies larger than 1kHz. Therefore, specific experimental studies for validation of numerical methods exist which hold the

hydrodynamic footprint on the side window almost constant with very locally amplifying the acoustic pressure. Such a study is introduced in the following subsection.

### 3.1 Introduction to test case

In the work of Schell and Cotoni [6], a series side mirror was geometrically modified such that the acoustic footprint on the side window was elevated by approx. 5dB. This was achieved by mounting a forward-facing step with step height of 4mm on the inner, diffusor side of the side mirror. The two geometrical variants can be seen in Figure 1 and are abbreviated with 'plain' and 'step' in the following results.

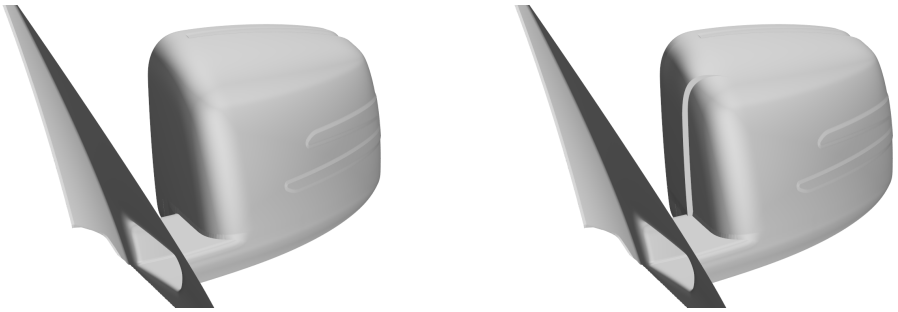

Figure 1: Geometrical variants of the side mirror; left: 'plain' variant, right: 'step' variant with step height 4mm

By experimental wind tunnel tests with artificial heads in the interior of the vehicle as well as beamforming algorithms for acoustic source localization, the acoustic Deltas were proven. Numerical simulations based on the scale-resolving Spalart-Allmaras IDDES approach revealed the acoustic Delta while not changing the hydrodynamic excitation on the side window. The frequency range of interest was 1-5kHz. In this work, the HTLES method with the $k$-$\varepsilon$ LEB model for the sub-filter scales is used. This model delivers identical results to the previously mentioned SA IDDES approach in Schell and Cotoni [6], but is better suited for cross-comparison with FRPM mainly for one reason: FRPM needs two turbulent scales ($k$ and $l_s$) which are only prescribed by at least a two-equation turbulence model so that for the instationary and stationary computations, a (sub-filtered) turbulence model of the same class is used.

Due to implementation reasons of FRPM, the whole side mirror and side window cannot be included in the source region. Therefore, the source region for FRPM and the HTLES method is only very locally concentrated around the step on the inner side of the mirror with isotropic 1mm cells for FRPM and 0.5mm cells for the HTLES method, see Figure 2. With this small source region, only a little underestimation of 3dB to acoustic results with the whole side mirror are computed showing the high concentration of the acoustic source around the step.

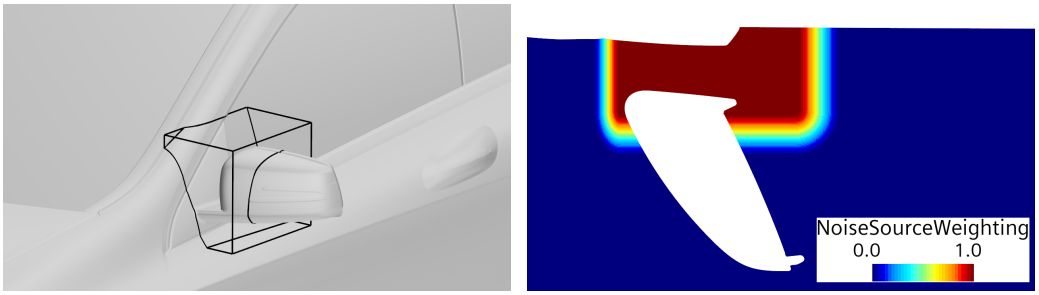


Figure 2: Geometry and source region (left) and noise source weighting function (right) of side mirror test case

### 3.2 Results of FRPM

This subsection presents broadband noise results by FRPM for both geometrical variants ‘plain’ and ‘step’. The spectra show the integrally averaged power spectral density (PSD) of the acoustic pressure $p'_a$ on the side window. Since the stochastic method does not get along without any empiricism in the form of constants in the turbulent length scale $l_s$, first the focus is set on the dependence on this parameter by introducing a factor $l_{fac}$ leading to $l'_s = l_{fac} l_s$. This result can be seen in Figure 3 at the geometrical variant with the step.

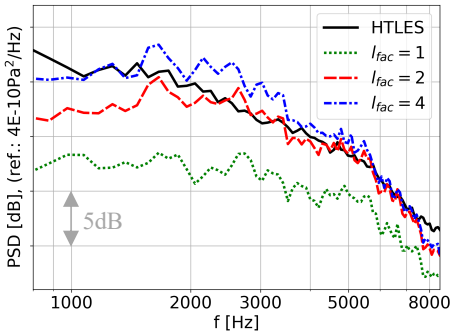


Figure 3: FRPM results of acoustic pressure $p'_a$ on side window based on $k$-$\varepsilon$ LEB for ‘step’ variant with different $l_{fac}$ compared to HTLES reference simulation

Choosing $l_{fac} = 1$, i.e. using the formula from literature, a massive underprediction is computed. Increasing the turbulent length scale to $l_{fac} = 2$ leads to a very good agreement from $f = 1.5$kHz on. The underprediction for lower frequencies stems from the chosen length scales to be realized by FRPM. In the current configuration, only length scales in 2mm $< l_s <$ 8mm are computed by means of 5 Gaussians leading to a Liepmann spectrum. The reason for the better agreement with higher $l_{fac}$ is that by increasing the length scale, the step is taken more into account since the length scales from RANS are then shifted in the length scale interval and the realized turbulent kinetic energy focusses more around the step. The FRPM spectra are in very good agreement up to 7kHz from where on a faster decay compared to the HTLES

method occurs. This can either have its reason in less numerical noise or in the grid size which amounts uniformly 1mm compared to 0.5mm in the volume mesh of the HTLES method. Increasing the length scale even more ($l_{fac} = 4$) leads to a slight overprediction in a mid-frequency range from 1.5-5kHz.

Choosing $l_{fac} = 2$ as default settings due to the agreement of absolute levels also for the 'plain' mirror variant results in the integrally averaged spectra on the side window in the left part of Figure 4.

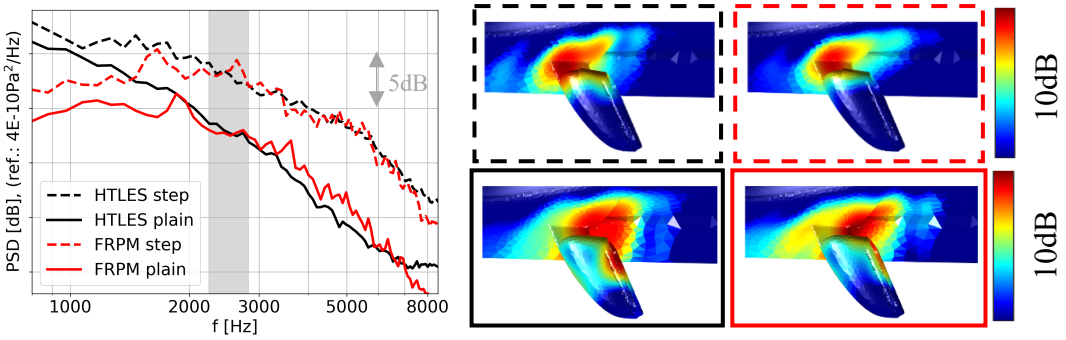


Figure 4: FRPM results of $p'_a$ on side window with $l_{fac} = 2$ based on $k$-$\varepsilon$ LEB for both geometrical variants (left) and beamforming results for third-octave band with center frequency $f_c = 2.5$kHz (right); colorbars with 10dB dynamic each apply rowwise (+7dB for the 'step' variant)

As can be seen, a good agreement for 1.5-7kHz can be achieved. The low-frequency underestimation can be traced back to the missing, larger length scales. Including these improves the agreement for $f < 1.5$kHz but introduces high-frequency noise from 5kHz on. These results are not shown here. Remarkable is the high-frequency behavior from the FRPM fluctuations as the decay is very uniformly whereas the HTLES method has a slight amount of numerical noise indicated by the stagnation in the spectra. This underlines the solenoidal and clean realization of turbulent velocity fluctuations by FRPM. In the gray area in Figure 4, the third-octave frequency band with center frequency $f_c = 2.5$kHz is shown. In this frequency band, a beamforming algorithm is applied with sampling of the acoustic pressure in a plane with top view on the side mirror. Experimental data in Schell and Cotoni [6] showed an upstream shift of the acoustic source from the trailing edge for the 'plain' variant to approx. the position the step with the 'step' variant. This can be reproduced by both approaches, HTLES and FRPM, shown in the right half of Figure 4 and verifies the high-quality stochastic sources of FRPM.

To further investigate the robustness of FRPM on the input data, the acoustic Deltas are also shown when starting with $l_{fac} = 1$, i.e. with an FRPM configuration that underpredicts the absolute levels. This can be seen in Figure 5 by visually comparing the shaded areas between the two FRPM variants to the HTLES spectra. The FRPM variants are artificially shifted downwards as indicated in the legend entries.

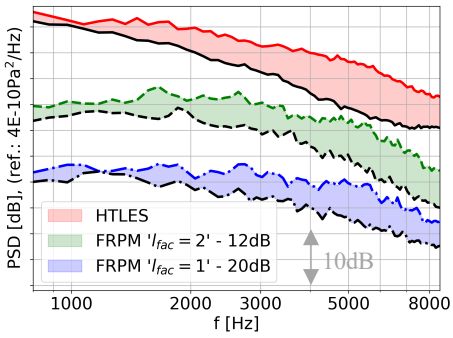


Figure 5: FRPM results of $p'_a$ on side window for both geometrical variants with $l_{fac} = 2$ and $l_{fac} = 1$ compared to reference HTLES

The spectra show the robustness of FRPM to react on geometrical variations. This performance is a fundamental key to the usage for optimization purposes since relative changes in the flow phenomena should lead to relative differences in the acoustic radiation even though the absolute agreement could not be given since a scale-resolving reference simulation may not exist.

The last open question to be answered is the performance of FRPM based on a RANS model that is not of the accuracy as the $k$-$\varepsilon$ LEB. Therefore, the $k$-$\varepsilon$ Realizable (Real.) is chosen. The derivation of the turbulent length scale is identical for both models. To be in touch with absolute HTLES results, the $k$-$\varepsilon$ Real. is calibrated with $l_{fac} = 2.2$. This leads to Figure 6 with acoustic Deltas on the left and with some insights into the flow phenomena on the right:

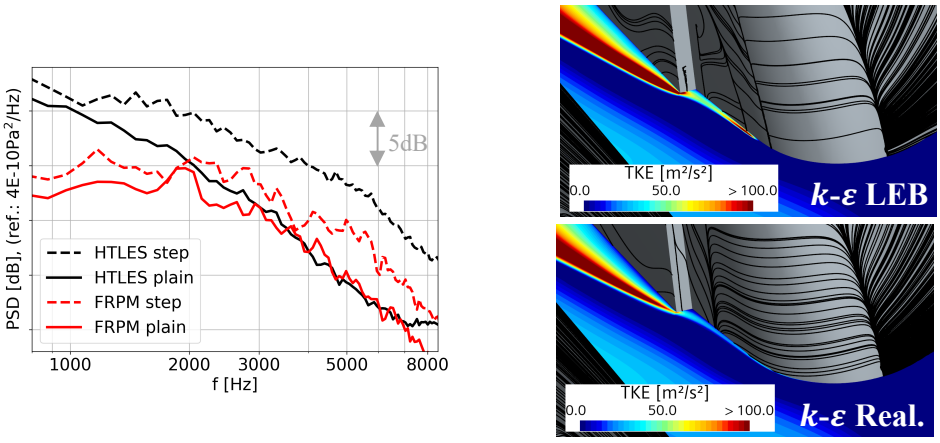


Figure 6: FRPM results of $p'_a$ on side window based on $k$-$\varepsilon$ Real. (left) and flow phenomena (right) with turbulent kinetic energy (TKE) and surface streamlines

Whereas the ‘plain’ variant might have an acceptable agreement to the reference simulation, the ‘step’ variant is massively underpredicted. This can be traced back to the flow phenomena. The $k$-$\varepsilon$ LEB computes a separation bubble on the inner side near the leading edge of the mirror with some high production of the turbulent kinetic energy close to the bubble. The $k$-$\varepsilon$ Real. starts with a turbulent boundary layer and does not exhibit this behavior. Although the separation bubble is acoustically not

relevant, and in FRPM due to the grid size not represented, it provides higher TKE values for downstream interaction with the step leading to higher acoustic amplifications close to this source region. This turbulence model study reveals the necessity for good input data to expect acoustic results with good agreement to high-fidelity simulations.

## 4 Underbody test case

In a next step, the focus is set on low frequencies in a range from 50-800Hz. This frequency range is mainly excited by the underbody flow between the car and the ground which can be best investigated with a very simplified yet realistic geometry.

### 4.1 Introduction to test case

The AeroSUV is a simplified car geometry developed by Zhang et al. [7] which has different geometrical variants in the underbody flow, the degree of detail of the underbody structure as well as engine bay flows. In a first step, the engine bay is closed and the variant with flat underbody is chosen. The source region is taken around the right front wheel due to symmetry effects of the vehicle. A visual representation of the test case and the size of the source region is given in Figure 7:

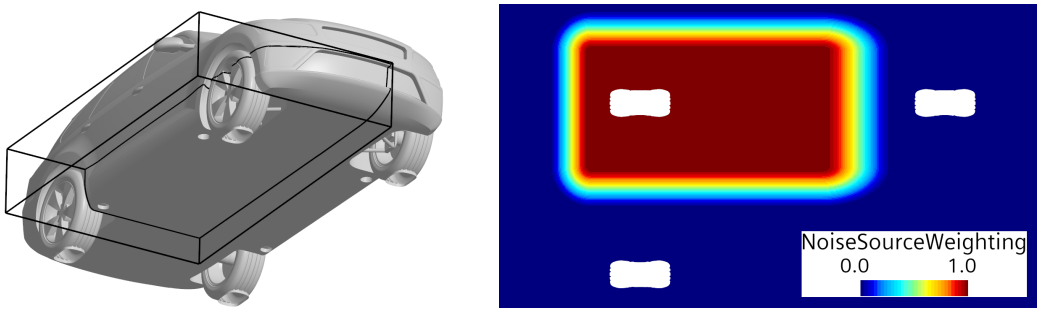


Figure 7: Geometry and source region (left) and noise source weighting function (right) of AeroSUV test case

The original investigation of the AeroSUV does not cover any aeroacoustic results and was performed in a model wind tunnel with a 1:4-scaled model geometry. Therefore, in this work, the geometry is scaled up by a factor of 4 to enable realistic frequency values.

### 4.2 Results of FRPM

It is especially emphasized here that the given results in this subsection on the AeroSUV are ongoing work. The results show promising agreement with scale-resolving simulations; however the open question will be answered in future works

why approaches like FRPM with isotropy in the Reynolds stresses as well as in the length scales are suitable for such kind of problems. The results shown in Figure 8 are achieved on an isotropic $\Delta x$=8mm grid.

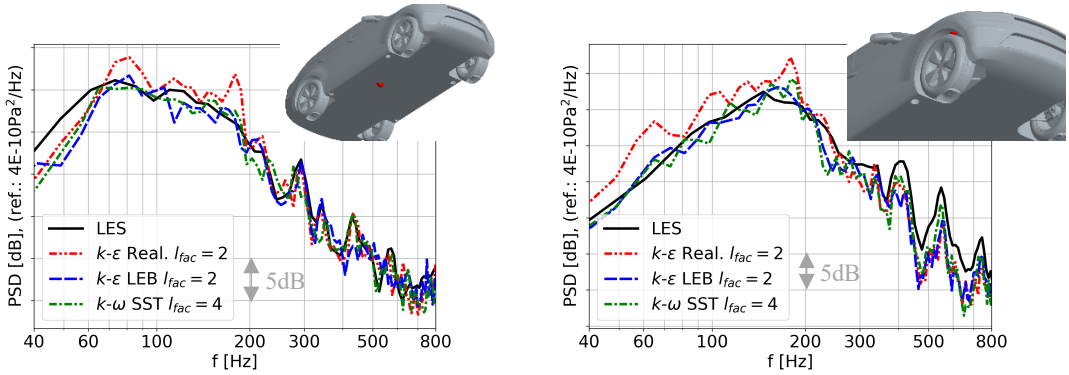


Figure 8: Point spectra of $p'_a$ for three different turbulence model inputs; points indicated with red dots; left: on underbody, right: in wheelhouse

Two different points are shown for the variant with the flat underbody – in the wake of the right front wheel inside the noise source region and in the top part of the wheelhouse covered mostly by the wheel outside the noise source region. Therefore, three RANS models are used: the $k$-$\varepsilon$ Real., the $k$-$\varepsilon$ LEB as well as the $k$-$\omega$ SST model. Both points show a very promising agreement over the whole frequency range of interest from 40 to 800Hz. The peaks in the spectrum indicating modes by geometric features are also captured. A further validity of the FRPM approach to deliver accurate source data for CAA can be seen in Figure 9 showing streamlines colored with the root-mean-square (RMS) of the acoustic source $-1/\rho\ Dp'_h/Dt$. The streamlines are generated on the (mean) velocity vector for the reference LES (left) and the $k$-$\varepsilon$ LEB variant (right).

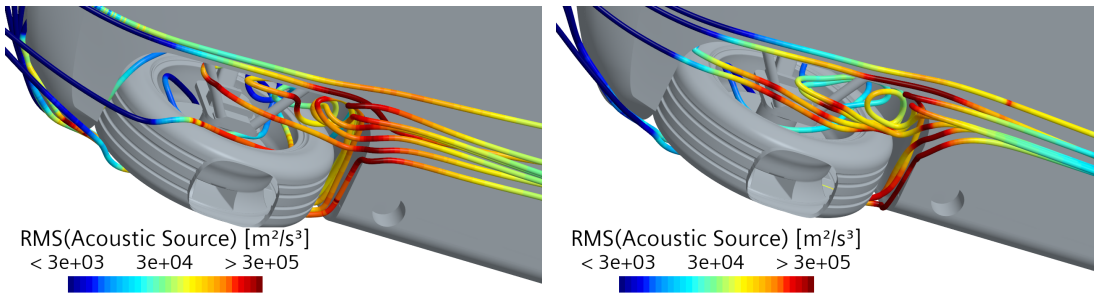


Figure 9: Root-mean-square of acoustic source for PCWE for LES (left) and FRPM based on RANS $k$-$\varepsilon$ LEB (right)

A conglomeration of high acoustic source values in the close wake of the wheel colliding with the downstream located edge of the flat underbody can be observed for both simulations. This region is not coinciding with the region of maximum turbulent kinetic energy which is far downstream of the front wheels at the downstream end of the source region.

Further investigating the Delta prediction capabilities of FRPM leads to slightly differing geometries for the flat underbody configuration shown in Figure 10. As a first simplification to the default (black frame), the wheels are closed with planar surfaces to prevent a flowthrough (red frame). In a second step, the wheelhouse is completely closed to remove this resonance volume and the downstream edge of the underbody at which high acoustic source values are observed (blue frame):

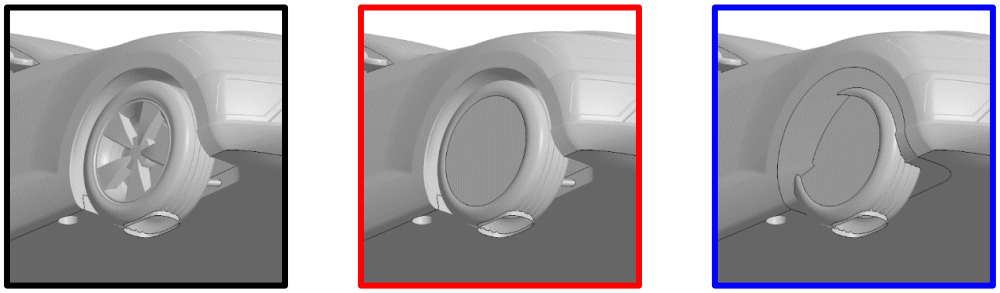

Figure 10: Geometrical modifications on front wheels (red) and wheelhouses (blue compared to default variant (black)

The results in the acoustic pressure for a point in the centerline at approximately the x-position of the wheel is given in Figure 11.

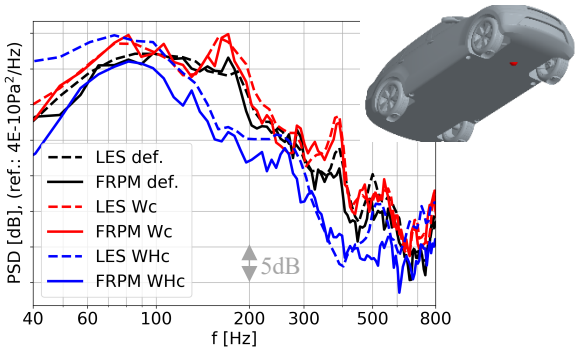


Figure 11: Point spectra of $p'_a$ for LES (dashed) and FRPM (solid) for three variants (see Figure 10); legend: *Wc* = wheels closed, *WHc* = wheelhouse closed

FRPM reacts correctly on both geometrical modifications. The slight elevation of the levels with the closed wheels compared to the open wheels in the default configuration especially at 180Hz and 380Hz is in very good agreement. For the entirely closed wheelhouses on the front axle, the trend is also computed although FRPM reacts a bit too strong by underestimating the overall levels slightly at mid frequencies of 100-300Hz and with stronger disagreement for lower than 100Hz and between 500Hz and 600Hz. However, the overall trend is captured.

As an outlook for future work regarding the underbody acoustics of the AeroSUV, more detailed and hence realistic underbody geometries are taken. These are also available in the package of geometry data provided for this vehicle test case.

## 5 Computational effort of methods

In this section, a short comparison of the computational efforts of the different methods is given with the CPU hours normalized to the reference simulation of each test case. The reference workflow consists of the stationary initialization with a RANS and the transient reference initialization followed by final reference CAA simulation. The stochastic workflow is based on the same RANS as the reference simulation but continues with the realization of fluctuations with the FRPM method with storing on the hard drive and ends with the CAA simulation induced by those FRPM fluctuations by importing from the hard drive.

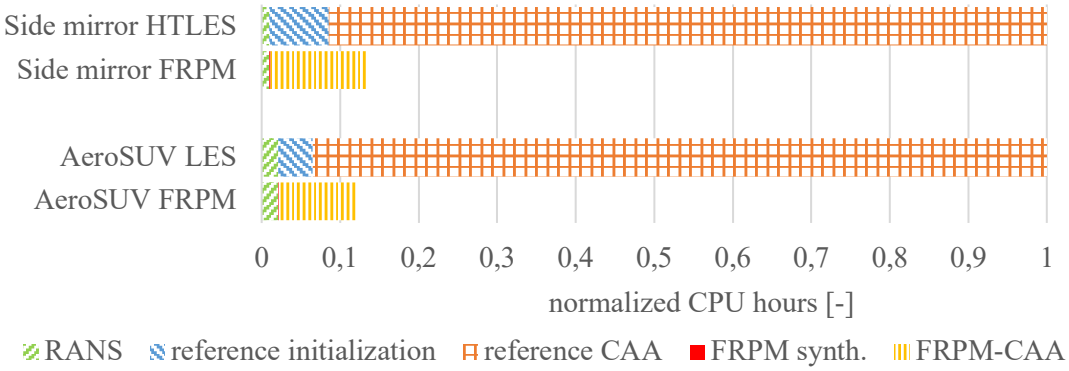


As one can see, for both test cases a similar picture is drawn in terms of computational advantage with a speed-up of approximately a factor of 8. The bottleneck in the simulation process so far is the import of the velocity fluctuations from the hard drive in the FRPM-CAA step. Removing this step with an on-the-fly implementation in one simulation environment is expected to lead to an additional speed-up of a factor of 2-3 in the FRPM-CAA step.

## 6 Conclusion and outlook

Stochastic noise source methods like the Fast Random Particle-Mesh method can be a significant enabler for optimization regarding broadband noise in the field of computational aeroacoustics. Therefore, several conditions need to be fulfilled: (i) accuracy of the results, (ii) robustness and (iii) consistency of the method. Accurate in the sense of only minor deteriorated results compared to existing scale-resolving reference simulation, robust by predicting trends of modified input data similarly to reference simulations (e.g. geometrical modifications) and consistent in the sense of the quality of input data (e.g. usage of different turbulence models). These three points are worked out in a different degree of detail for two test cases: a high-frequency side mirror test case and a low-frequency underbody test case by means of a Hydrodynamic-Acoustic Splitting approach based on a Poisson equation and a second order Perturbed Convective Wave Equation. For the side mirror test case, very accurate results for two different geometries of the mirror are achieved compared to a high-resolved Hybrid-Temporal RANS-LES approach. With a RANS simulation

capturing the important flow aspects, a good agreement is achieved whereas using a RANS without these phenomena leads to only partially good agreement. The underbody test case is still ongoing work but shows very promising results with less sensitivity on the used turbulence model. Geometrical variants are investigated with overall good agreement in the acoustics. The benefit of stochastic noise source methods with enhanced modelling assumptions comes across with an enormous computational speed-up of a factor of approx. 8.

## 7 References


[1] V. Duffal, B. de Laage de Meux and R. Manceau, "Development and Validation of a Hybrid RANS-LES Approach Based on Temporal Filtering," in *Proceedings of the ASME-JSME-KSME 2019 8th Joint Fluids Engineering Conference*, San Francisco, California, USA, 2019.

[2] R. Ewert, J. Dierke, J. Siebert, A. Neifeld, C. Appel, M. Siefert and O. Kornow, "CAA broadband noise prediction for aeroacoustic design," *Journal of Sound and Vibration,* vol. 330, no. 17, pp. 4139-4160, 2011.

[3] P. Uhl, A. Schell, R. Ewert and J. Delfs, "Validation of the Fast Random Particle-Mesh Method for Broadband CAA of a Forward-Facing Step and its prediction sensitivity for geometrical modifications," in *AIAA AVIATION 2023 Forum*, San Diego, California, USA, 2023.

[4] A. Wohlbrandt, N. Hu, S. Guérin and R. Ewert, "Analytical reconstruction of isotropic turbulence spectra based on the Gaussian transform," *Computers & Fluids,* vol. 132, pp. 46-50, 2016.

[5] J. Piepiorka and O. von Estorff, "Numerical investigation of hydrodynamic / acoustic splitting methods in finite volumes including rotating domains," in *23. International Congress on Acoustics*, Aachen, Germany, 2019.

[6] A. Schell and V. Cotoni, "Flow Induced Interior Noise Prediction of a Passenger Car," *SAE International Journal of Passenger Cars - Mechanical Systems,* vol. 9, 2016.

[7] C. Zhang, M. Tanneberger, T. Kuthada, F. Wittmeier, J. Wiedemann and J. Nies, "Introduction of the AeroSUV - A New Generic SUV Model for Aerodynamic Research," in *WCX SAE World Congress*, Detroit, Michigan, USA, 2019.

# Low Frequency Aerodynamic and Aeroacoustics Phenomena of Vehicles with Flat Underbody

Laura Breitenbücher, Prof. Dr.-Ing. Andreas Wagner, Dr.-Ing. Thomas Wiegand, Dr.-Ing. Maarten Brink
Dr. Ing. h.c. F. Porsche AG
Porschestraße 911
71287 Weissach
laura.breitenbuecher1@porsche.de
andreas.wagner@ifs.uni-stuttgart.de
thomas.wiegand@porsche.de
maarten.brink@porsche.de

**Abstract:** Due to the increasing importance of drag minimization and the absence of an exhaust system, battery electric vehicles (BEVs) typically feature a very streamlined underbody. While this shape of underbody is typically characterized by a low acoustic interference potential, significant flow resonance can be observed for certain vehicle configurations and frequencies below 30 Hz. The goal of this study is to identify the exact origin of the aforementioned low-frequency flow resonances at the vehicle underbody in order to subsequently develop stable and robust measures with which the flow phenomenon can be avoided while simultaneously meeting aerodynamic requirements. In order to isolate the flow phenomenon and to be independent of a specific vehicle configuration, an abstract model was developed with the help of which the flow phenomenon can be investigated in detail. Computational Fluid Dynamic (CFD) simulations were carried out on the one hand and wind tunnel experiments on the other. The investigations unanimously show that the flow around the front wheel spoilers has a decisive influence on the low-frequency resonance. Due to flow separation at the front-wheel spoilers and at the front wheels, vortices that are growing substantially while being transported with the flow downstream are generated. At the rear section of the vehicle, the separations caused by the front and rear components superimpose, which results in very high levels of pressure fluctuations. The excitation of the vehicle interior as a Helmholtz resonator then takes place by coupling the pressure fluctuations via an "air path" and leads to reduced comfort for the passengers.

# 1 Introduction

Since aeroacoustics considerably influences the passengers' comfort, it is increasingly gaining importance in the vehicle industry. Even small changes in flow around the vehicle can lead to significant sources of noise. It is a general goal to execute aeroacoustics investigations early in the vehicle development process.

Noise emissions of a vehicle which are important for the interior as well as for the exterior noise consist of engine noise, tire-road noise and flow noise. For a conventional combustion engine, the first two dominate at low speeds, whereas at high speeds from about 130 km/h onwards the flow noise dominates the overall noise emission. In contrast BEVs generate almost no drive noise. This is the reason why flow noise becomes more important at significantly lower speeds.

Due to the desired reduction of drag and lift, BEVs typically are characterised by a streamlined underbody. Although this shape of underbody is typically characterised by a low acoustic interference potential, significant flow resonance can be observed for certain vehicle configurations and frequencies below 30 Hz. As a consequence, the interior of the vehicle is excited as a Helmholtz resonator by coupling these low-frequency periodic pressure fluctuations via the forced ventilation in the rear of the vehicle.

The present frequency range of this flow phenomenon falls into the range of the human auditory threshold. The perception of the high levels of pressure fluctuations varies greatly from one individual to another. In addition to an audible impression, they are very often experienced as an unpleasant feeling of pressure on the ears, as a so-called "buffeting". Due to this way of perceiving the phenomenon, as well as the fact that the emergence of the pressure fluctuations can be attributed to the flow around the vehicle, the phenomenon is hereinafter referred to as "underbody buffeting".

The aim of this work is to investigate the flow phenomenon in detail. Based on previous investigations, the first step consists of the development of an abstract research model that is used to investigate the phenomenon using both CFD simulations and wind tunnel experiments [1, 2]. After the flow phenomenon is generated, variant studies are carried out to investigate the influencing parameters in order to identify the exact formation mechanism.

Subsequently, these findings will be used to identify stable and robust measures to prevent the phenomenon. The major challenge here is the interaction between aerodynamics and aeroacoustics because the geometric modification of aerodynamic add-on components on the underbody influences the aerodynamic performance of the vehicle.

## 2 Research Model

In order to identify the exact origin of the low-frequency pressure fluctuations it is necessary to isolate the flow phenomenon. Therefore, and to be independent of a specific vehicle configuration, an abstract model was developed. Moreover, simplification of the geometry features the possibility of a theoretical observation of the flow around the particular geometries.

The so-called SAE-Body represents the Basis for the research. It is a generic car reference model which is based on the Ahmed body, and which was developed by a consortium of German car developers [3]. It has an abstract vehicle shape with a smooth underbody and a diffusor. Due to the simple and well-defined shape it does not have many other interfering aeroacoustics noise sources. Hence, the flow phenomenon will be easier to isolate.

To generate the flow phenomenon on the SAE-Body, add-on components were mounted on the vehicle's underbody. Here, in addition to cut-off cylinders representing the wheels, rectangular plates were used to model the wheel spoilers. In developing the model, care was taken to represent the flow phenomenon as accurately as possible in terms of flow variables and acoustic quantities. Simultaneously, the geometry was kept as simple as possible in order to enable a theoretical analysis of the flow.

The geometry of the developed basic configuration of the research model is illustrated in Figure 1. Subsequently it was possible to investigate the flow phenomenon both, with CFD simulations and wind tunnel experiments.

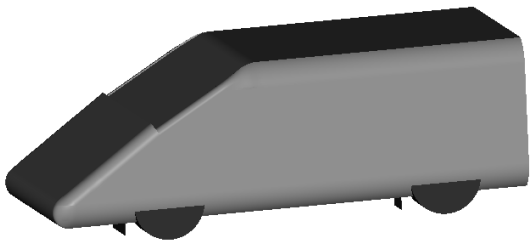

Figure 1: Geometry of the basic configuration of the research model with wheels and wheel spoilers

## 3 Simulation Setup

All simulations were carried out with the software PowerFLOW of 3DS Simulia. The research model described in Chapter 2 was used as simulation model. It was located in a virtual wind tunnel. The incoming flow velocity was 140 km/h. When performing the variant study, the calculation time was reduced by using a half model. The physical time of the transient simulation was 2.5 seconds.

The discretization in PowerFLOW was done using a cartesian grid. The individual grid cells were not all the same in size, but their size was defined by variable resolution areas. Since the focus of this work is mainly on the observation and analysis of the underbody flow, this area was discretized particularly finely.

In PowerFLOW, the flow is solved using the Lattice-Boltzmann method. A Very Large Eddy Simulation turbulence model and a wall law are also implemented to simulate high Reynolds numbers and flows near the wall. All simulations were performed with a moving floor configuration and with stationary wheels.

## 4 Simulation Results

Since very large amounts of data are generated during the transient simulation, evaluation planes were defined in advance on which the time data should be stored. For the images shown below, an evaluation plane is considered which is parallel and which is located 100 mm above the wind tunnel floor. In addition, virtual surface microphones were placed on the underbody of the SAE body, for which the particular pressure information is stored.

Frequency spectra were generated using this pressure information. In the following, spectra at a reference microphone in the rear area of the vehicle model are considered. The spectrum of the basic configuration of the research model is shown in Figure 2. Significantly increased pressure fluctuation levels are present in the low frequency range between 10 and 20 Hz. This important result shows that it is possible to model the flow phenomenon in CFD simulation on an abstract vehicle model, which provides the opportunity to study the flow phenomenon and its exact formation mechanism in more detail in the following.

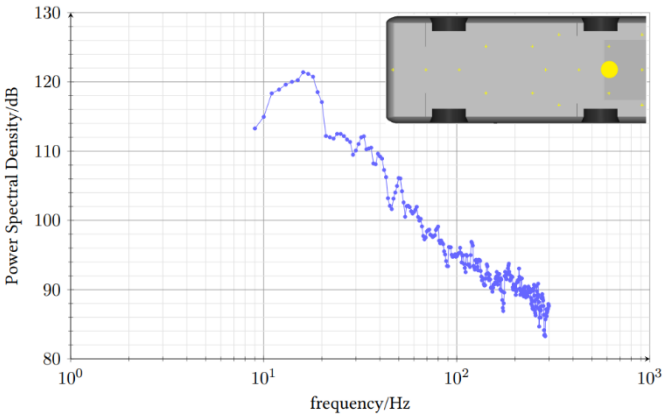


Figure 2: Frequency spectrum of the basic configuration of the research model at the reference microphone

Figure 3 (a) shows a dB-Map filtered by 16 Hz on the evaluation plane below the vehicle underbody. The map shows very clearly that the highest-pressure fluctuation levels occur in the rear area between and especially on the inside of the wheels. The averaged flow velocity on the same plane is shown in Figure 3 (b). The flow separates at the front wheel spoilers and at the front wheels. The wake behind this area extends until the rear wheels. Moreover, there is a shear layer with a strong gradient between the wake and the area of undisturbed flow.

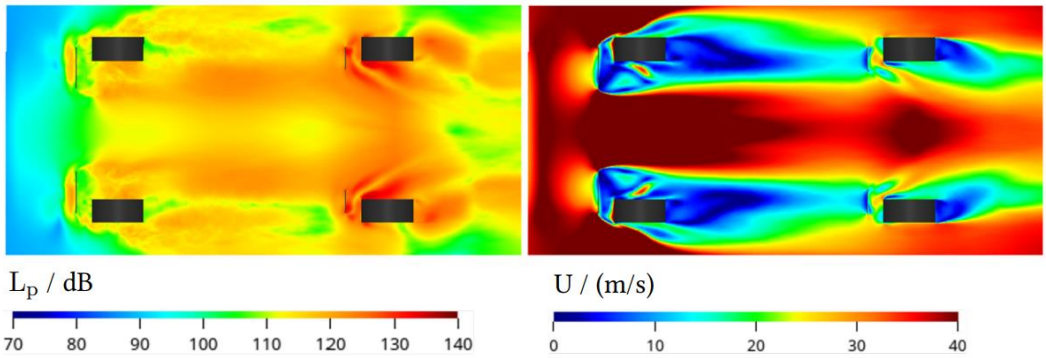


Figure 3: dB-Map of the pressure fluctuations filtered by 16 Hz (a) and averaged flow velocity (b) of the basic configuration of the research model - evaluation plane: 100 mm above the floor

In the following, some geometrical modifications were conducted in order to investigate the flow phenomenon and its origin in detail.

First, all cut-off cylinders and the rear wheel spoilers were removed, resulting in the SAE-body with only the front wheel spoilers as add-on components. The frequency spectra of this configuration in comparison to the basic configuration is illustrated in Figure 5. Significantly increased pressure fluctuation levels are present in the frequency range between 10 and 20 Hz. Hence, the front wheel spoilers seem to be decisive for the development of the underbody buffeting. The filtered dB-Map of this configuration is shown in Figure 4. Since a half model was simulated, only the driver's side is presented. In this case, the maximum levels occur behind the front wheel spoilers and no longer in the rear area. However, even there, the levels are still significantly increased.

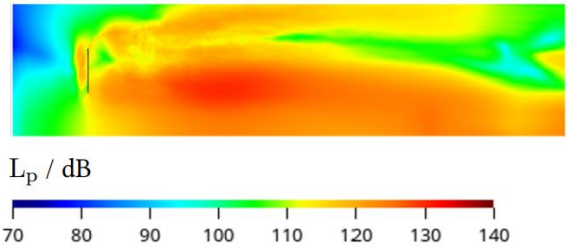


Figure 4: dB-Map of the pressure fluctuations filtered by 18 Hz of the configuration with front wheel spoilers - evaluation plane: 100 mm above the floor

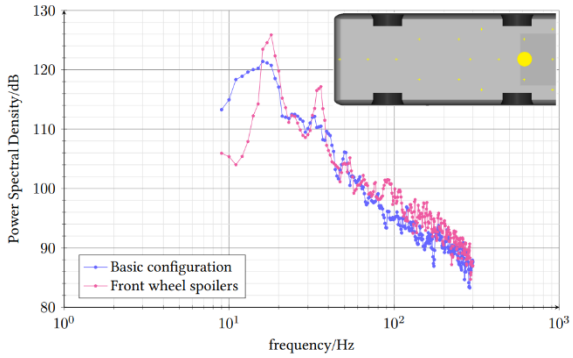


Figure 5: Comparison of the frequency spectra at the reference microphone - Basic configuration and configuration with only the front wheel spoilers

In a second version, the vehicle has the same wheel spoiler as the basic configuration, but instead of cylindrical wheels, splitter plates were attached behind the wheel spoilers. The splitter plates are rectangular plates mounted directly behind the wheel spoilers in streamwise direction. The frequency spectrum is illustrated in Figure 6 and shows 1 to 2 dB higher pressure fluctuation levels as the basic configuration. However, the curve progression as well as the values are comparable with it.

Figure 7 shows the dB-Map of this configuration. As same as for the basic configuration, the maximum pressure fluctuations are located in the rear area between the splitter plates. Interactions between the separations from both sides of the wheel spoilers are only possible behind the splitter plates in the front. In this region, there is a strong increase of pressure fluctuations. Therefore, the interaction between the two shear layers behind both sides of the front wheel spoiler seems to play a significant role for the development of the underbody buffeting. The similarity of dB-Maps and spectra of this configuration and the basic configuration hypothesise, that the wheels have the same effect as splitter plates: They suppress the interaction between the shear layers directly behind the front rear spoiler, which may lead to lower pressure fluctuations compared to the configuration without wheels.

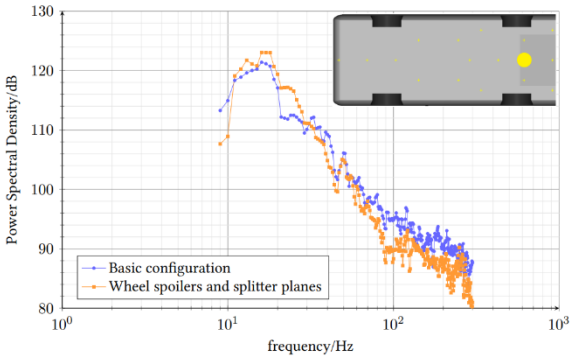


Figure 6: Comparison of the frequency spectra at the reference microphone – Basic configuration and configuration with wheel spoilers and splitter plates

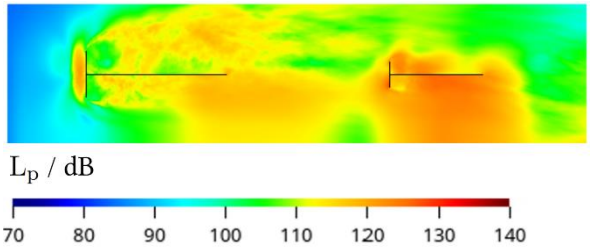


Figure 7: dB-Map of the pressure fluctuations filtered by 17 Hz of the configuration with wheel spoilers and splitter plates - evaluation plane: 100 mm above the floor

## 5 Formation Mechanism of the Underbody Buffeting

Subsequently the formation mechanism of the flow phenomenon is described. The variant study has shown the significance of the flow around the front wheel spoiler for the underbody buffeting. Therefore, it is discussed below.

The simplified wheel spoiler will be observed as a normal flat plate. This represents a simplification since the flow is affected by the underbody of the vehicle and by the wind tunnel floor. There are three tearing edges on which flow separation occurs. As a consequence, free shear layers develop. The velocity difference in the shear layer leads to the rotation of the fluid and its instability cause the formation of vortexes. The flow passing the lower edge of the wheel spoiler leads to a unilateral shear layer development. Consequently, a so-called "roof vortex" is generated. In contrast, the flow around the lateral edges causes a bilateral shear layer development. Due to the interaction between the two shear layers, a Kármán vortex street evolves. Its dimensionless frequency is around Str = 0.15. In the frequency spectra a dominating frequency $f$ was visible. It can be calculated with the inflow velocity $u$, the characteristic length $l$ and the dimensionless frequency $Str$ via

$$f = \frac{Str \cdot u}{l}. \qquad \text{(eq. 1)}$$

Besides, splitter plates can be used to suppress the development of a Kármán vortex street. For this configuration a significant reduction of the pressure fluctuation levels in the front area of the vehicle's underbody was visible. As a consequence, the bilateral shear layer development is the dominating mechanism for the underbody buffeting.

The generated vortexes are transported streamwise within the fluid flow. Thereby they grow in size, especially in regions with a strong gradient of the fluid velocity. This leads to the assumption of vortexes growing through the energy which they detract from the fast external flow. Flow separation occurs also at the rear wheel spoilers and at the rear wheels. In the rear part of the vehicle's underbody the separations of all spoilers and wheels superimpose. As a consequence, extremely high levels of pressure fluctuations arise in this area.

Furthermore, plots of the averaged velocity show that the rear add-on components are located inside the wake of the front add-on components. Therefore, the flow around the rear add-on components cannot be considered isolated from the front geometries. In [4], the flow around two cylinders in tandem configuration is investigated. The examination showed that the transient pressure fluctuations at the rear cylinder are 10 to 15 dB higher than the ones at the front cylinder if the rear cylinder is located inside the wake of the front cylinder. The wake interaction seems to be the reason for the strong pressure level increase. The wake of the add-on components in the front leads to a slower but higher turbulent inflow of the rear add-on components. The resulting pressure fluctuations at the geometries on the rear part of the underbody are therefore higher than the ones generated through vortex shedding in front of the underbody.

Figure 8 shows schematically the development of the flow phenomenon. Vortex shedding occurs at the front rear spoilers and at the front wheels. The vortexes are transported within the fluid flow. Thereby the grow in size and strength. Finally, the superposition of separations from front and rear add-on components together with wake interaction lead to extremely high levels of pressure fluctuations in the rear part of the vehicle's underbody.

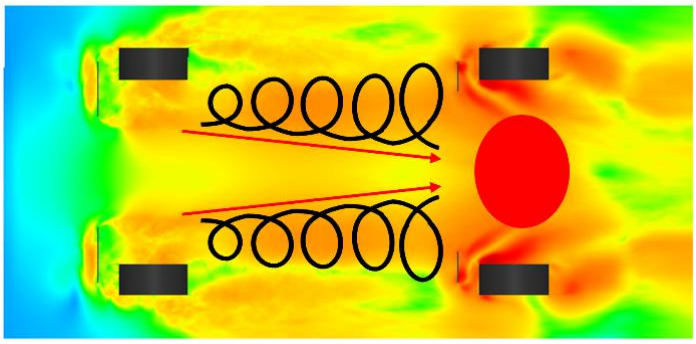

Figure 8: Schematic representation of the formation mechanism of the underbody buffeting

The SAE body was used to examine the external airflow and the external acoustics of the vehicle. For a real vehicle, the pressure fluctuations in the diffuser area are relevant for the resulting sound pressure levels in the vehicle’s interior. Finally, these are decisive for the evaluation of customer comfort. The transmission of pressure fluctuations from the underbody flow takes place via the air path of the forced ventilation. The excitation of the vehicle interior takes place when the low-frequency pressure fluctuations match the Helmholtz resonance frequency of the passenger cabin. Here, the air path represents the neck of the Helmholtz resonator, while the vehicle interior acts as a resonance volume. [5]

## 6 Experimental Setup

All experiments were conducted in the aeroacoustics wind tunnel of the Porsche AG. The same model geometry was used for CFD simulations and experiments. In order to ensure the closest possible matching in comparison to the CFD simulations, they were carried out with a moving center belt. All experiments were carried out at an inflow velocity of $U_\infty = 140 \frac{km}{h}$. Moreover, surface microphones were placed at the vehicle's underbody, consistently to the virtual microphones of the CFD-simulations. They served as quantification of the aeroacoustics performance of different vehicle configurations. Figure 9 shows the SAE-body in its basic configuration inside the wind tunnel.

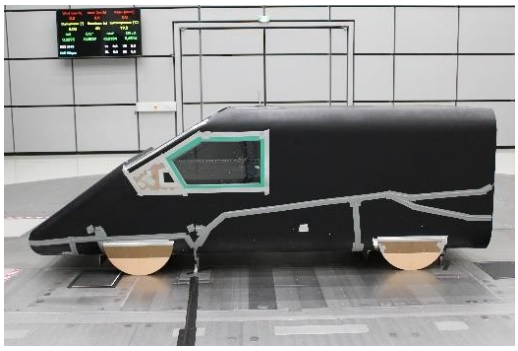

Figure 9: Basic configuration of the research model inside the wind tunnel

## 7 Experimental Results

The possibility of modelling the underbody buffeting with the software PowerFLOW was already shown. The next goal was to generate the flow phenomenon in the wind tunnel. Therefore, the research model described in Chapter 2 was designed and investigated.

Figure 10 shows the frequency spectra of the SAE-body on the reference microphone, which is located in the rear part of the vehicle, analogous to the CFD simulations. In the frequency range between 10 and 20 $Hz$, there are significantly increased pressure fluctuations, and the maximum is located at 15 $Hz$. Hence the flow phenomenon was successively generated in the wind tunnel at the SAE-body. This allows a detailed investigation of the underbody buffeting at the generic vehicle model.

The CFD simulations have already shown the significance of the front wheel spoilers for the underbody buffeting. The goal of the following variant study was therefore to investigate and evaluate different wheel spoiler geometries and their influence on the flow phenomenon.

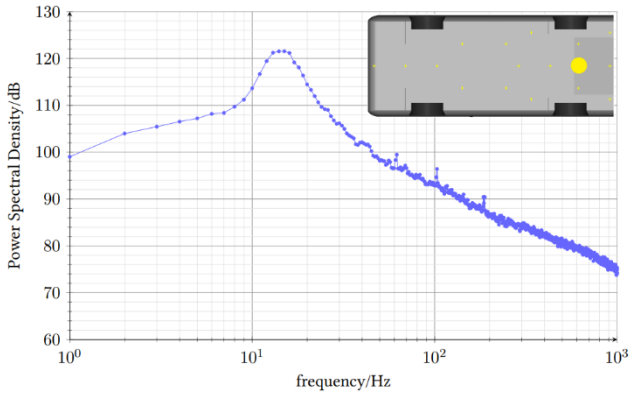


Figure 10: Frequency spectrum of the research model at the reference microphone

Firstly, the width of the front wheel spoiler is modified. The frequency spectra at the reference measuring point are illustrated in Figure 11. All curves show increased pressure levels in the lower frequency range. However, the frequency of the maximum pressure fluctuations as well as the pressure level varies with the wheel spoiler width. In general, the trend is that the maximum level increases with increasing wheel spoiler width, while the frequency at which this occurs decreases. The latter can be seen directly from eq. 1 if the wheel spoiler width is assumed to be the characteristic length. An exception to this trend is the variant with the highest wheel spoiler width. The frequency of the maximum level has also been reduced in this case, but the value of the maximum is reduced compared to the initial variant, in which the front wheel spoiler has a width of $b = 350\,mm$. The decrease in the maximum level may be related to the mutual influence of both wheel spoilers, since their distance is relatively small in this configuration. In addition, Kármán's vortex street may be weakened by the greater distance of the wheel spoiler side edges. In the case of very narrow wheel spoilers that do not protrude beyond the front wheel, the underbody buffeting does not exist since there are only slight level increases in the spectra. They can probably be traced back to detachments on the wheels and the rear wheel spoilers.

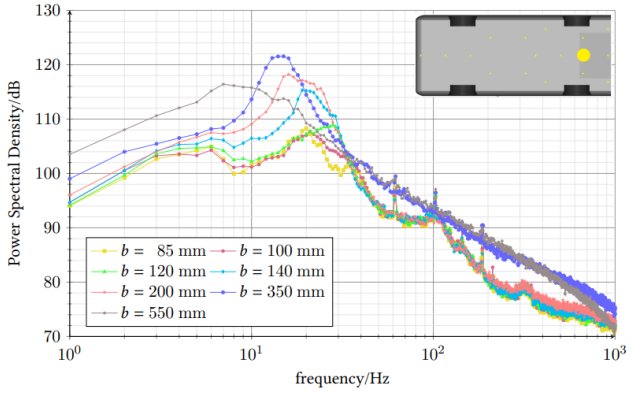


Figure 11: Comparison of the frequency spectra at the reference microphone by varying the width $b$ of the front wheel spoilers

Although the underbody buffeting could be prevented by a small wheel spoiler, this geometric modification is not possible for aerodynamic reasons however, since this wheel spoiler do not generate sufficient front axle lift. Subsequently, two further wheel spoiler geometries were examined. One wheel spoiler has a reduced height compared to the original wheel spoiler, while the wheel spoiler width of the second wheel spoiler has also been increased. The resulting frequency spectra are shown in Figure 12. All spectra show the level increase in the frequency range between 10 and 25 $Hz$, which is typical for the flow phenomenon. The level maximum and the frequency at which this occurs differs between the different versions. For the variant with a lower wheel spoiler, the maximum level is reduced by 8 $dB$ and the frequency shifts by 4 $Hz$ to higher frequencies compared to the basis variant. The latter could be attributed to the fact that the Strouhal number increases slightly with increasing ground clearance. Due to the greater distance between the lower edge of the wheel spoiler and the wind tunnel floor, the roof vortex described in the second paragraph of Chapter 5 can evolve more strongly. This could weaken the formation of the Kármán vortex street and thus be the cause of the level reduction. By additionally increasing the width of the wheel spoiler, the maximum level can be further reduced. In addition to the stronger roof vortex, this could also be due to the increased spacing of the wheel spoiler side edges and the resulting weakened Kármán vortex street. In addition, the aerodynamic performance of this wheel spoiler improves compared to the first modification, because a wider wheel spoiler generates more front axle lift.

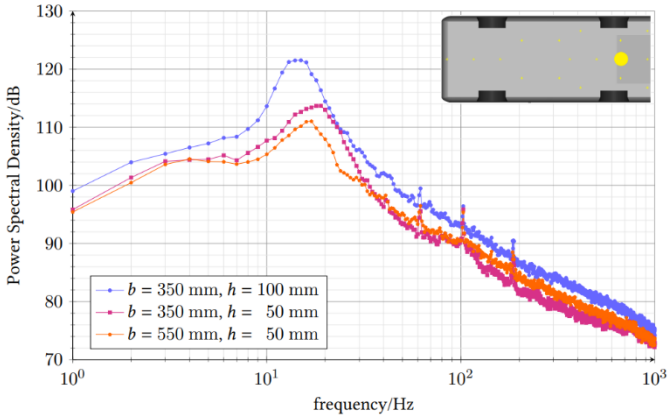


Figure 12: Comparison of the frequency spectra at the reference microphone by varying the height $h$ and width $b$ of the front wheel spoilers

## 8 Conclusion

In the present paper the flow phenomenon “underbody buffeting” was investigated. For this purpose, a research model was developed and used to generate the flow phenomenon both in CFD simulation and in the wind tunnel. Consecutively, the underbody buffeting was investigated by variant studies in order to subsequently identify the fluid mechanical mechanisms of the phenomenon.

The investigations have shown that the flow around the front wheel spoiler and the periodic vortex formation, evolved through the interaction of the bilateral shear layer development, cause the dominant separation frequency. The generated vortices are transported within the fluid flow, whereby they increase in strength and size. The high levels of pressure fluctuations in the rear part of the vehicle's underbody are decisive for the sound level in the vehicle's interior because they excite the interior Helmholtz resonator.

Future work will cover the development of measurements to suppress the underbody buffeting by simultaneously satisfy the aerodynamic requirements. These will first be designed on the research model and then transferred and optimised to real vehicles.

## 9 Acknowledgement

My special thanks go to Professor Wagner, my boss and supervisor Dr. Thomas Wiegand and my supervisor Dr. Maarten Brink for the professional exchange as well as the supervision and support in my doctoral thesis.

Furthermore, I would also like to thank all my aerodynamics and aeroacoustics colleagues as well as the concept building and wind tunnel team.

## 10 Bibliography

1. Benedikt Staudenmayer. „Analyse der tieffrequenten Strömungsphänomene bei Fahrzeugen mit geschlossenem Unterboden“. Master's thesis. University Stuttgart, 2021
2. Laura Breitenbücher. „Untersuchung von tieffrequenten Strömungsresonanzen am Fahrzeug-Unterboden“. Master's thesis. University Stuttgart, 2022
3. Hartmann, M., Ocker, J., Lemke, T., Mutzke, A., Schwarz, V., Tokuno, H., Toppinga R., Unterlecher P. and Wickern, G. Wind Noise caused by the Apillar and the Side Mirror flow of a Generic Vehicle Model. 18th AIAA/CEAS Aeroacoustic Conference, AIAA paper (2012), 2012-2205
4. Lockard, D., Khorrami, M., Choudhari, M., Hutcheson, F., Brooks, F. and Stead, D. „Tandem cylinder noise predictions“. 13th AIAA/CEAS Aeroacoustics Conference (28th AIAA Aeroacoustics Conference), S. 3450
5. Christian Weber. „Aufbau einer aeroakustischen Simulationsmethode zur Bewertung der Fahrzeug-Unterbodenströmung“. Master's thesis. University Stuttgart, 2018

# Automotive on-road flow quantification with a large-scale Stereo-PIV setup

S. Hüttig[1], T. Gericke[1], A. Sciacchitano[2], R.A.D. Akkermans[3]

[1] Volkswagen AG, Wolfsburg, Germany

[2] Delft University of Technology, Department of Aerospace Engineering – Aerodynamics, Delft, The Netherlands

[3] Hamburg University of Applied Sciences, Department of Automotive and Aeronautical Engineering, Hamburg, Germany

steffen.huettig2@volkswagen.de

**Abstract:** In this work the large-scale stereoscopic PIV setup for on road flow quantification, originally introduced by Sciacchitano et al. [1] under the name Ring of Fire, is adapted to automotive demands. The current study presents the experimental setup and results of the whole wake of the investigated test vehicle Volkswagen up!, travelling at a speed of 120 km/h. High-Speed measurements at a rate of 6000 Hz with a field of view of approximately 2.8 x 2.2 $m^2$ were performed and the time-resolved data was processed by means of cross correlation and the lagrangian particle tracking approaches. Resulting ensemble-averaged velocity fields of the wake show good accordance to literature and display the capabilities of the new measurement technique for on-road flow quantification.

## 1 Introduction

Beside the optimization of powertrain components the aerodynamic performance is a key development field to further increase the overall efficiency of future cars. Aero-acoustics, drag and also soiling are main goals for current and future developments, to increase the battery range, fulfil comfort demands and guarantee a functional sensor environment for autonomous driving. Current aerodynamic studies a mainly performed in large industrial wind tunnels, by means of pressure probes and in some cases by means of optical measurement techniques like Particle Image Velocimetry (PIV) or Particle Tracking Velocimetry (PTV) under laboratory conditions. Wind tunnels can guarantee high repeatability due to very controlled flow conditions, while no all flow conditions are represented as in on the road and need to be simulated by means of a conveyor belt for a moving ground and/or rotating wheels. Only single vehicle configurations can usually investigated, while in future platoon configurations can by of high interests due to the large drag reduction potential of vehicles in platoon.

The Ring of Fire measurement concept for on-road flow quantification for sport aerodynamics has been introduced by Sciacchitano et al. [1] and the capability of this experimental configuration to analyze flow fields of speed skater and road cyclists has been presented in recent studies (Terra et al. [2], Spoelstra [3], Terra et al. [4]). Furthermore, drag calculation by means of the momentum approach was introduced by Spoelstra et al. [5].

In this work the measurement system is adapted for on-road car aerodynamic investigations with a large-scale stereoscopic particle image velocimetry setup (Stereo-PIV). Flow quantification is performed by means of cross correlation and lagrangian particle tracking method Shake-The-Box (STB) originally introduced by Schanz et al. [6].

## 2 Experimental Setup

The experiment was carried out at the Volkswagen proving ground in Ehra-Lessien in August and September 2021. A tunnel-like construction was built of eight 20-foot shipping containers and a truss arrangement for a roof. The tunnel had a total length of 14 m and a width of 9.17 m and a height of 5 m and was placed at a straight track with a total length of 950 m, see Figure 1. The investigated vehicle was a Volkswagen up! with a frontal surface area of 2.07 $m^2$, leading to a tunnel blockage ratio of 4.5 %. For the reduction of light reflections, thus erroneous image data, the car was prepared with black matt foil, see Figure 2.

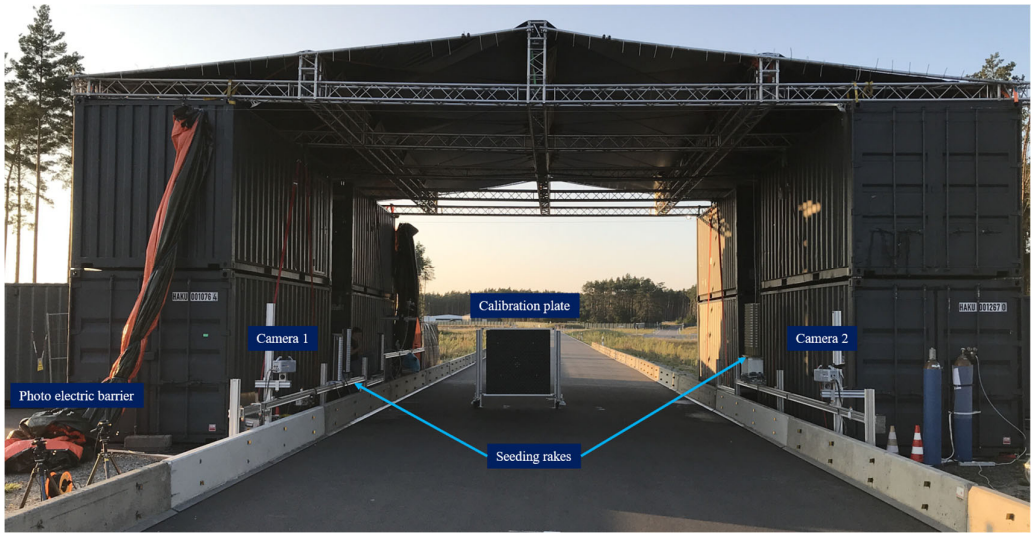


Figure 1: Experimental Setup at test track

For the presented wake analysis two Photron SA-X2 cameras (Camera 1 & 2 in Figure 1) were placed at the tunnel entrance, with a distance of 7.6 m to the light sheet. The cameras have a sensor size of 1024x1024 $px^2$, maximum acquisition frequency of 10 kHz, 12-bit digital output and 20 µm pixel pitch. They were equipped with Scheimpflug-Adaptors V3 from LaVision and Nikon Nikkor lenses with a focal length of f= 60 mm and the lens aperture was set to $f_{\#}$ = 4.0. The light sheet had a thickness of approximately 4 cm and was realized by the use of two high speed lasers Quantronix Hawk Pro & Quantronix Hawk II (Nd:YAG, 6 mJ pulser energy at 6 kHz, wavelength of 532 nm) and corresponding light sheet optics; positioned on each side of the road, in the longitudinal middle of the tunnel.

The tunnel volume was seeded with neutrally buoyant helium-filled soap bubbles (HFSB) with a diameter of 300 µm, produced by fourteen 20-nozzle LaVision seeding arrays and a 204-nozzle-generator seeding rake from TU Delft, producing in total up to 18 millions bubbles per second. The seeding rakes were placed on X95-beams on each side of the track, allowing a quick repositioning depending on the ambient flow conditions. Helium, soap liquid and air were provided and controlled by one fluid supply unit (FSU) from LaVision for each seeding rake. Two curtains were installed at the entrance and exit of the tunnel in order to accumulate a large number of particles inside the tunnel and depending on the wind conditions one curtain was closed during the seeding time of approx. 5 minutes before each measurement run.


Figure 2: Test vehicle Volkswagen up! – stationary positioned in light sheet.

In order to reduce the influence of ambient flow the experiments were conducted during the night times. The cameras were installed each day on the mounts and a geometrical pinhole calibration was performed using a custom 3D-calibration plate (size:1440 x 1440 mm2, 324 markers, 8 mm marker diameter, 80 mm spacing, 18 markers in y & x, 20 mm plane-to-plane distance), resulting in a RMS fit of 0.0342 and 0.0386 for cameras 1 & 2 and an image resolution of 0.38 pixel/mm.

The calibration and image acquisition was performed by LaVisions DaVis 10.2.0 and a Programmable Timing Unit (PTU-X) controlled the timing of the lasers and the cameras. The start of the measurement was triggered by photo electric barrier which was placed before the entrance of the tunnel. Time-resolved data was acquired at 6000 Hz resulting in a longitudinal shift of $\Delta x = 5.55$ mm between consecutive frames at a vehicle velocity of $u = 33.33$ m/s (120 km/h). A constant vehicle speed for all measurements was realized by the vehicles cruise control and a digital GPS-speedometer, to accurately set the cruise control speed once each day. The whole flow field around the car was captured during the passage through the tunnel, with approximately 10 m before and 20 m behind the car. After each run the data was transferred from internal camera memory to the computer while the car resumed to the starting position and the tunnel volume was seeded with HFSB again.

The raw images were processed with several processing steps, in order to reduce background reflections. First a background subtraction of an average of 100 images from the freestream in front of the car is performed, second step was a geometric masking for the image region below the light sheet and third step a sliding minimum subtraction over a filter length of L=5 pixels. The flow field quantification was performed by the two approaches: Particle Image Velocimetry (PIV) and a 2 Camera Shake-The-Box (STB) [6].

For the PIV-approach a total of 100 images of the non-disturbed freestream flow in front of the car were used the perform a planar self-calibration [7]. Vector calculation was subsequently performed with the sliding sum of correlation approach Sciacchitano et al. [8], followed by universal outlier detection [9] and linear interpolation to fill empty spaces.

A distinct marker on the car allowed the lateral correction of the vector fields of each run since the car passed the test section in slightly different y-position. Finally, a total of 22 PIV runs were averaged.

As a LPT approach, the STB-algorithm has widely been used to deliver time-resolved 3D velocity fields of experimental setups with a high seeding density of up to N = 0.2 particle per pixel with multi camera configurations of usually 4 to 8 cameras. In this work a 2-Camera STB-evaluation could be applied due to the relatively small light sheet thickness. Thus, the disadvantages of a low seeding density for a cross-correlation approach were beneficial for this 2-Camera LPT-evaluation, leading to good particle reconstruction and very little ghost particles. A volume self-calibration [10] of 1000 images of the far wake was performed for each run, followed by a multi-pass STB for the whole wake of the car.

Particle fields of in total 52 runs were merged into one particle set, considering the lateral correction of the cars coordinate systems of each run similar to PIV averaging. The relatively sparse particle concentration of a single run $C_{single}$ = 0.000306 particles/voxel could be increased to $C_{avg}$ = 0.0132 particles/voxel for all runs. A total of 14.7 million particle tracks are then averaged in a Gaussian weighted bins of 32 x 32 x 32 $mm^3$ resulting in one vector field for each time step, which were afterwards merged into a single 3D velocity field considering the longitudinal separation of $\Delta x$= 5.55 mm for each time step. A single particle field in the wake and resulting bin averaged 3D-velocity field are illustrated in Figure 3.

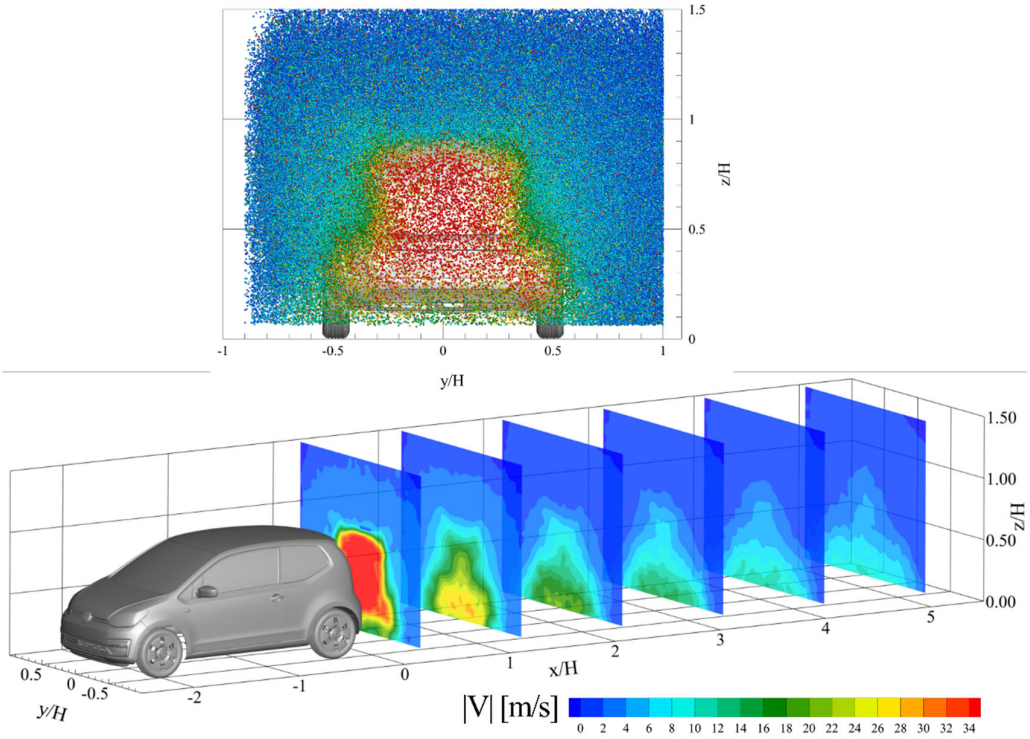


Figure 3: Single particle field in the wake color coded by velocity magnitude (top); resulting bin averaged 3D velocity field in the wake (bottom)

## 3 Results

The averaged flow field results are normalized to the vehicle speed of 33.33 m/s and the coordinate system is normalized to the vehicles height with the origin at the back/ground position of the car. The flow field of the PTV-evaluation in y-plane y/H = 0, thus corresponding to the symmetry plane is shown on Figure 4. The near-wake topology is dominated by a distinct recirculation core (A), located around z/H = 0.25, fed by the high velocity under the car and in good accordance to square-back vehicle results from Pavia et al. [11]. The low pressure region in the wake with negative streamwise velocity is present up to x/H = 0.7 illustrated by the stagnation point S. Further downstream streamlines coming from the top meet those coming from the bottom at around x/H = 1.1. A distinct upwash from the bottom of the car is clearly noted at the near wake x/H = 0.5 and are comparable to investigation from Ahmed [12] and the analyzed wake structure of an estate back car model.

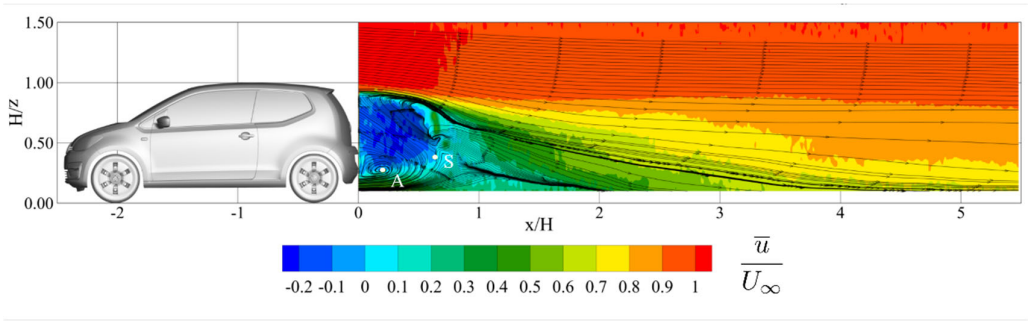


Figure 4: Non-dimensional, ensemble-averaged streamwise velocity in y/H = 0 plane in the wake of the Volkswagen up! from PTV-Data

Wake slices of the y/z-plane of the LPT and the PIV approach are illustrated in Figure 5. Below of z/H = 0.1 no particles were captured and the average signal to noise ratio was below 1.5 and thus no valid data is available close to the ground. The PIV results are limited at the negative y/H direction at y/H < 0.9 due to less available runs where sufficient seeding was present in this region.
The low pressure region at x/H = 0.34 with a negative normalized velocity match the results of Placzek [13]. It can be noted, that the in the near wake the area of negative streamwise velocity from PIV data is slightly larger compared to the results from the LPT approach. As mentioned before the seeding density in the near wake is relatively low, thus a single particle influences the cross-correlation calculation of a single time step significantly, leading to an overall lower velocity after averaging all PIV runs.
Moving further downstream the beforementioned upwash meets the flow from over the car leading to an overall downwash. At z/H = 0.65 two counter rotating vortices are generated by the upwash in the wake. Because of the pressure difference between the flow coming from the sides and over the rear window, the shear layer rolls up about the side edge of the curved surface and forms the C-pillar vortices. The upper vortices start to shrink further downstream and two counter-rotating trailing vortices are formed at the bottom of the flow field at z/H = 0.3. The PIV as well as the LPT-approach resolve those flow phenomena equally good.

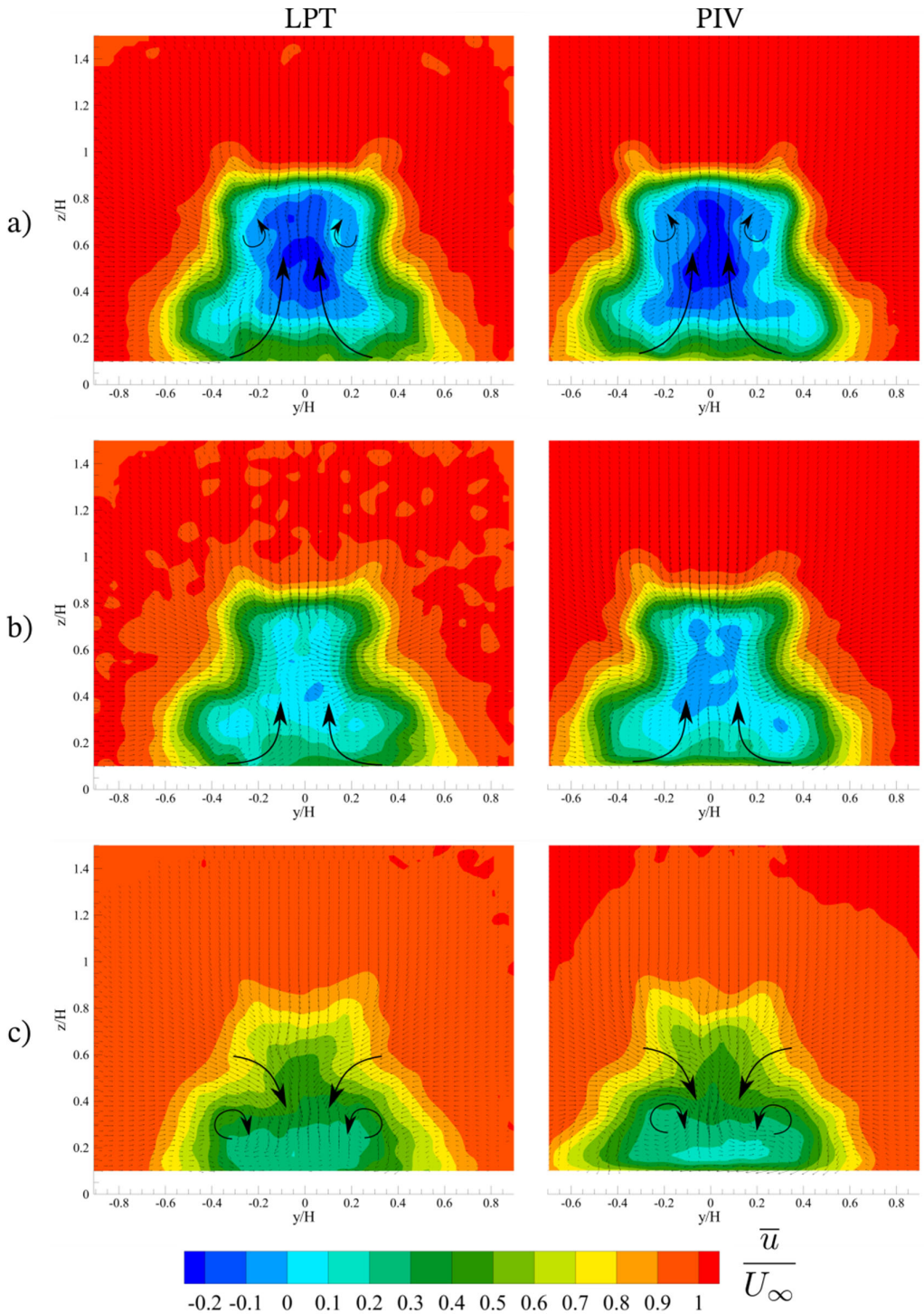


Figure 5: Non-dimensional, ensemble-averaged streamwise velocity slice in the y/z-Plane in the wake of the Volkswagen up! from LPT-Data (left) and PIV-data (right) at a) x/H = 0.34, b) x/H = 0.68, c) x/H = 1.36

## 4 Conclusion

The large-scale Stereo-PIV setup Ring of Fire is adapted to automotive applications to investigate flow topologies under real driving condition. The wake flow of a square back Volkswagen up! is investigated by means of the sliding-sum of correlation approach and furthermore two-camera lagrangian particle tracking was implemented on the same data. Results prove the capability of the Ring of Fire concept to resolve the flow topology of car aerodynamics at high speeds. LPT was successfully applied due to the small light sheet thickness and relative sparse seeding density. In particular the recirculation in the near wake with a strong upwash is noted and vortices formed by the flow reattachment at the C-Pillar and counter-rotation ground vortices are resolved equally good by both evaluation approaches. Ambient flow conditions had a big influence on the available seeding concentration as well distribution within the test section. For future investigations this could be improved by a longer tunnel and industrial air curtains at the entrance and exit of the tunnel. For a more efficient use of the large amount of generated seeding particles the authors recommend for future experiments the LPT-approach with volumetric illumination and a multi-camera setup. The capability of pressure field calculation from three-dimensional time resolved LPT-data from these experiments will be discussed in future work.

The results, opinions and conclusions expressed in this publication are not necessarily those of Volkswagen Aktiengesellschaft.

## 5 Bibliography


[1] Sciacchitano, A.; Caridi, G.C.A and Scarano F. (2015) A quantitative flow visualization technique for on-site sport aerodynamics optimization. Procedia Engineering 112:412–417. 'The Impact of Technology on Sport VI' 7th Asia-Pacific Congress on Sports Technology, APCST2015

[2] Terra, W.; Sciacchitano, A. and Scarano F. (2017) Aerodynamic drag of a transiting sphere by large-scale tomographic-piv. Experiments in Fluids 58:1–14

[3] Spoelstra, A. (2022) Ring of fire as a novel approach to study cycling aerodynamics. Ph.D. thesis. Delft University of Technology

[4] Terra, W.; Spoelstra, A. and Sciacchitano, A. (2023): Aerodynamic benefits of drafting in speed skating: Estimates from in-field skater's wakes and wind tunnel measurements. Journal of Wind Engineering and Industrial Aerodynamics 233:105329

[5] Spoelstra, A.; de Martino Norante, L.; Terra, W.; Sciacchitano, A. and Scarano, F. (2019) On-site cycling drag analysis with the ring of fire. Experiments in Fluids 60:1–16

[6] Schanz, D.; Gesemann, S. and Schröder, A. (2016): Shake-The-Box: Lagrangian particle tracking at high particle image densities. Experiments in Fluids 57, 70 (2016)

[7] Wieneke, B. (2005): Stereo-piv using self-calibration on particle images. Experiments in Fluids 39:267–280

[8] Sciacchitano, A.; Scarano, F. and Wieneke, B. (2012): Multi-frame pyramid correlation for time-resolved PIV. Experiments in Fluids 53:1087–1105

[9] Westerweel, J. and Scarano, F. (2005): Universal outlier detection for PIV data. Experiments in Fluids 39:1096–1100

[10] Wieneke, B. (2005): Volume self-calibration for 3D particle image velocimetry. Experiments in Fluids 45:549–556

[11] Pavia, G.; Passmore, M.A.; Varney, M. and Hodgson, G. (2020) Salient three-dimensional features of the turbulent wake of a simplified square-back vehicle. Journal of Fluid Mechanics 888

[12] Ahmed, S.R. (1981): Wake structure of typical automobile shapes. Journal of Fluids Engineering 103:162–169

[13] Placzek, R. (2018) Active Flow Control for Drag Reduction of a Square-back Car Model. Ph.D. thesis. Technische Universität Braunschweig

# A Hybrid Approach to the Evaluation of Thermal Comfort in Passenger Vehicles

Daniel Gehringer[1,*], Timo Kuthada[2], Andreas Wagner[1]

[1] Institute of Automotive Engineering (IFS), University of Stuttgart
[2] Research Institute for Automotive Engineering and Powertrain Systems Stuttgart (FKFS)
Pfaffenwaldring 12
70569 Stuttgart
* Correspondence: daniel.gehringer@ifs.uni-stuttgart.de

**Abstract:** Occupant thermal comfort is an important aspect of passenger vehicles. With powertrain electrification and autonomous vehicle operation, interior comfort is gaining increasing importance. The thermal comfort of the cabin must be evaluated during all stages of vehicle development. This study presents a method that enables the digital assessment of thermal comfort during the early development stages using computer-aided design (CAD) geometry of the vehicle, and later in prototypes or production vehicles using a thermal comfort manikin. The thermal comfort manikin equipped with various sensors, along with the corresponding simulation approach, is described. Validation measurements conducted under a controlled environment in a climatic test chamber demonstrate a strong agreement between the measurement and simulation results. Both evaluation methods yield comparable results, thereby allowing for comparisons of measures during different development stages of the vehicle.

## 1 Introduction

Satisfying the thermal comfort of passengers is an important aspect of modern road vehicles. It influences the overall perceived comfort within a vehicle cabin and, consequently, impacts customers' purchasing decisions. This is especially critical with the growing demand for battery electric vehicles (BEVs), where the energy required to maintain a comfortable interior climate can affect the vehicle's range, making it a decisive factor. Moreover, maintaining occupants in a thermally neutral state also contributes to driving safety [1]. Recent research indicates that thermal sensation can influence the immune levels of the human body [2]. Consequently, thermal comfort within the vehicle cabin must be considered throughout the development process.

One approach to evaluate thermal comfort is through subject trials involving humans. However, conducting such trials during the early stages of development is often

impractical. This can be due to the unavailability of a functional prototype or because the prototype's details are still confidential. In such cases, a standardized process with objective comfort ratings is essential.

The thermal comfort of humans is influenced by various factors, which can be categorized into external factors stemming from the environment and internal factors arising from physiological processes within the human body. Primary environmental influences on thermal comfort include air temperature, the temperature of surrounding surfaces, airflow velocity, and relative humidity [3]. The clothing worn by an individual significantly impacts heat dissipation from the body by acting as an insulating layer against the skin. The metabolic rate accounts for the internal heat generated by metabolic processes within the human body, with the person's activity level predominantly affecting it.

Acclimatization to the ambient climate also plays a role in determining thermal comfort. Research indicates that occupants' expectations concerning indoor climate are influenced by the external climate and their ability to regulate the indoor environment [4]. The external climate largely determines occupants' clothing choices, thus affecting clothing insulation.

This paper will present the development of a thermal comfort manikin (TCM) capable of providing a thermal comfort rating for the entire body, while also assessing factors such as airflow velocity, draught, and temperature on specific body parts. Another aim is to create a digital twin of the manikin that yields comparable results between measurements and simulations. This approach will facilitate a comprehensive evaluation of thermal comfort across all stages of vehicle development. The present work describes the thermal comfort manikin along with its associated software. Experimental measurements are conducted within a climate test chamber to showcase the functionalities of the manikin. The measurement setup is subsequently replicated within a simulation and a comparison between simulation and measurement results is presented.

## 2 State of the Art

To quantify thermal comfort within an occupied space, it is essential to measure the ambient conditions using appropriate sensors. This encompasses variables such as air temperature, air velocity, relative humidity, and the temperature of surrounding surfaces. Alongside the direct measurement of these parameters, various indices exist to objectively evaluate thermal comfort. Among these is the Predicted Mean Vote (PMV) model, introduced by Fanger [5]. This comfort index is widely used and established in the standard DIN EN ISO 7730 [6] as well as ASHRAE 55 [7]. With its foundation in the principles of heat balance and human physiology, the PMV model calculates an index that represents the average thermal sensation of a group of occupants. It is defined on a scale ranging from -3 to 3, with the corresponding ratings: cold, cool, slightly cool, neutral, slightly warm, warm and hot. An optimal thermal comfort level is attained at a value of 0 on this scale. Its widespread adoption in

research and practice is attributed to its simplicity, applicability, and empirical validation. PMV is defined as

$$PMV = [0.303\, e^{-0.036\, M} + 0.028] \left\{ \begin{array}{c} (M - W) - 3.05 \cdot 10^{-3}[5733 - 6.99(M - W) - p_a] \\ -0.42[(M - W) - 58.15] - 1.7 \cdot 10^{-5} M(5867 - p_a) - 0.0014M(34 - \vartheta_a) \\ -3.96 \cdot 10^{-8} f_{cl}[(\vartheta_{cl} + 273)^4 - (\bar{\vartheta}_r + 273)^4] - f_{cl} h_c(\vartheta_{cl} - \vartheta_a) \end{array} \right\} \quad (1)$$

where $M$ is the metabolic rate, $W$ the external work, $p_a$ the water vapor pressure, $\vartheta_a$ the air temperature, $f_{cl}$ the clothing area factor, $\vartheta_{cl}$ the clothing temperature, $\bar{\vartheta}_r$ the mean radiant temperature and $h_c$ the convective heat transfer coefficient. Using the PMV value the Projected Percentage of Dissatisfied (PPD) can be calculated as

$$PPD = 100 - 95\, e^{-0.03353\, PMV^4 - 0.2179\, PMV^2}. \quad (2)$$

Details on how each of the parameters used to calculate PMV are obtained with suitable measurement equipment will be described in section 3.1. Figure 1 shows the PMV models scale with all input parameters on the left and the PPD over PMV values according to equation (2).

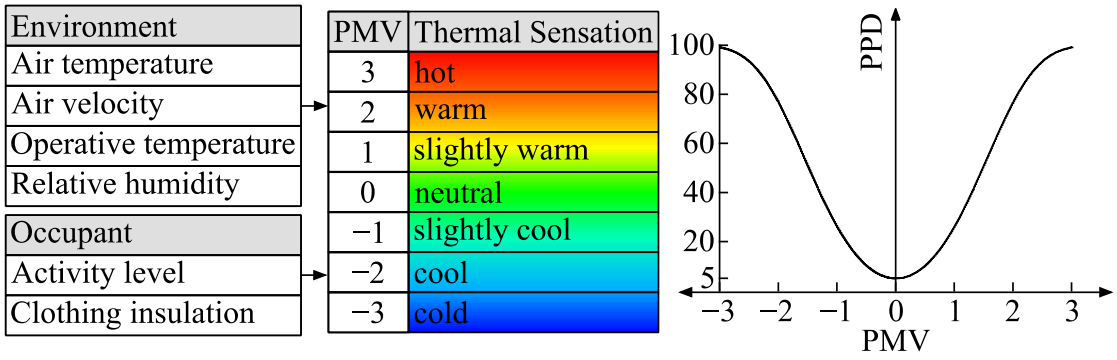


Figure 1: PMV/PPD model scale and its input parameters.

When assessing thermal comfort, it is important to account for the turbulence intensity of the airflow around an occupant. Elevated turbulence levels can result in a sensation of air draught. This can be quantified by the so called draught rate. It describes the percentage of people that would rate a given flow condition as unpleasant due to draught. The draught rate is calculated as

$$DR = \left(34 - \vartheta_{a,l}\right)\left(\bar{v}_{a,l} - 0.05\right)^{0.62}\left(0.37\, \bar{v}_{a,l}\, Tu + 3.14\right), \quad (3)$$

using the local air temperature $\vartheta_{a,l}$, the local mean air velocity $\bar{v}_{a,l}$ and the local turbulence intensity $Tu$ [6]. The Thermal Comfort Manikin calculates this draught rate for the head, neck, chest, hip and lower legs. The turbulence intensity is calculated in percent

$$Tu = \frac{\sigma}{\bar{v}_a}\, 100, \quad (4)$$

where $\bar{v}_a$ is the mean air velocity in the measuring interval and $\sigma$ the standard deviation of the air velocity

$$\sigma = \sqrt{\frac{1}{n-1}\sum_{i=1}^{n}\left(v_{a,i} - \bar{v}_a\right)^2} \tag{5}$$

using the air velocity at the time $i$ in a measurement interval $v_{a,i}$ [8].

Another source of thermal dissatisfaction in occupant comfort is the presence of a vertical temperature difference in the cabin. The manikin computes the vertical temperature difference $\Delta\vartheta_{a,v}$ between the head and the ankles. With this, the resulting percent dissatisfied for $\Delta\vartheta_{a,v} < 8\,°C$ can be calculated after

$$PD = \frac{100}{1 + e^{5.76 - 0.856\,\Delta\vartheta_{a,v}}} \text{ [6].} \tag{6}$$

The standard DIN 7730 imposes certain limitations on the application of the PMV model under transient ambient conditions. These limitations are categorized into temperature cycles, temperature drifts or drops, and transitions. Peak-to-peak deviations in a temperature cycle that fall below 1 K do not impact the comfort value. Deviations beyond this threshold can lead to reduced comfort. Temperature drifts or drops occurring at rates of change below 2 K/h are considered permissible for using the method. The standard also provides insights into temperature transitions. Immediate effects are observed for significant changes in operative temperature. PMV can be employed to predict comfort when the operative temperature increases. Conversely, when the operative temperature decreases, PMV predicts values that are higher than the perceived thermal sensation. After approximately 30 minutes in stationary conditions, the PMV value becomes applicable once again.

Ekici [9] has shown that the mean radiant temperature significantly affects the calculated PMV values. Some measurement systems take the assumption that the mean radiant temperature is equivalent to the measured air temperature, thus avoiding the need for a separate sensor for mean radiant temperature. However, Chaudhuri et al. [10] showed that this simplification leads to increased uncertainties in PMV predictions. Other studies have indicated that these uncertainties in PMV calculations can be minimized by directly measuring the operative temperature [11]. This can be accomplished using either a globe thermometer or an ellipsoid-shaped probe.

The diameter of a globe thermometer primarily impacts the uncertainty of the measured mean radiant temperature [12], and the use of globe thermometers can introduce significant systematic errors [13,14]. ISO 7726 [8] states that an ellipsoid sensor is more suitable and provides design specifications for an operative temperature probe. In research conducted by Simone et al. [15], which compared various operative temperature sensor types, an ellipsoid-shaped sensor was employed as a reference. The study also concluded that a black sensor tends to overestimate the influence of short-wave radiation, while a white or reflective sensor tends to underestimate it. As a result, the use of a flat gray sensor color is recommended [15], aligning with the specifications in ISO 7726 [8]. An ellipsoid-shaped sensor offers a

projected area factor that better corresponds to that of a human, affecting the relationship between convection and radiation heat transfer on the sensor.

The metabolic rate and clothing factor exert a significant influence on the PMV value. The calculated PMV index becomes more sensitive to the mean radiant temperature during light metabolic rates. Conversely, at higher metabolic rates, the impact of other parameters diminishes [16]. Tables to determine the activity level and clothing index are available in the standards ISO 7730 [6] and ASHREA 55 [7] for example.

## 3 Methodology

This chapter will highlight the technical background of the developed thermal comfort manikin. Firstly, the hardware manikin buildup, sensor equipment, and measurement software are described. A corresponding simulation approach with a digital twin of the TCM is presented in the second section of this chapter.

### 3.1 Thermal Comfort Manikin

The manikin's geometry is derived from that of a $50^{th}$ percentile western male human, with a total height of 1.78 m [17,18]. The base frame comprises 30 x 30 mm aluminum profiles connected by various joints. These joints allow for the adaptation of the manikin to different body positions. The potential degrees of freedom for each joint are outlined in Table 1. All exterior shell components of the manikin are manufactured using a fused deposition modeling (FDM) printer. The outer shell parts include apertures for sensor mounting and slots for routing cables through the manikin.

Table 1: Degrees of freedom of base frame joints.

| | Joint Type | Range of Motion in ° |
|---|---|---|
| Neck | Revolute | ±10 |
| Shoulder | Ball | 180 |
| Lower Torso | Revolute | ±5 |
| Hips | Revolute | 90 |
| Elbows | Revolute | 90 |
| Knee | Revolute | 90 |

Sensors are incorporated into the external shell of the manikin. The measurement system comprises four distinct sensor types: eight air velocity and temperature probes, one operative temperature probe, 32 thermocouples, and one relative humidity probe. The placement of the probes is determined based on the distribution of thermoreceptors on the human body. Thermoreceptors enable humans to perceive alterations in skin temperature [3]. Locations with a high concentration of

thermoreceptors are selected for sensor placement. Figure 2 shows the thermoreceptor density on the human skin and the chosen sensor positions for the manikin.

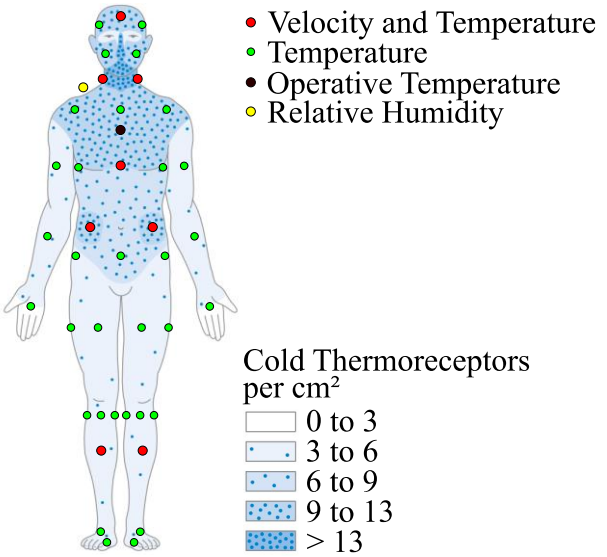


Figure 2: Thermoreceptor density on the human body and sensor placement, based on [3].

The velocity probes are mounted to a laser-cut steel plate, which is fastened to the outer shell of the manikin. Steel cages are positioned over the probes to shield them during handling, minimally obstructing airflow to the sensing surfaces. Thermo-couples are affixed to small carbon tubes within the shell. This arrangement allows for protective covers to be added when transporting or handling the manikin.

The operative temperature probe is a gray ellipsoid measuring 156 mm in length and 55 mm in diameter. The sensor's surface is influenced by both convection and radiation, possessing an emissivity coefficient of 0.95. Various body postures can be simulated by adjusting the sensor angle. The ellipsoidal shape ensures that the projected area ratio on the surrounding surfaces matches that of a human body. For instance, a standing individual is simulated with an upright orientation, while a seated person is represented at a 30° angle between the floor and the sensor. Horizontally positioning the sensor models a person lying down [8]. Employing such an operative temperature probe can reduce uncertainties in PMV calculation when compared to individual measurements of air temperature and mean radiant temperature. The probe's uncertainty is required to be below 0.2 °C [11]. The probe utilized in the manikin achieves this level of accuracy within the temperature range of 10 to 40 °C [19]. Figure 3 shows the TCM on a vehicle seat with all sensors attached.

Figure 3: Thermal comfort manikin with sensors on a vehicle seat.

A LabVIEW program featuring a graphical user interface (GUI) was developed for the purpose of acquiring measurement data. LabVIEW is a software package that employs a visual programming language, designed by National Instruments. Within the program, measurement signals undergo processing to reach their final format, and additional values are computed. The resulting measurement file encompasses all sensor measurements alongside the computed comfort evaluation parameters. The program allows real-time display of both measurement and comfort values, thereby enabling the assessment of the effects of configuration changes during a measurement session. The sensors allow for ambient pressure and humidity correction of flow velocity measurements. These corrections can be enabled in the measurement program. The measured humidity values of the manikin's sensor is directly used. Pressure values must be specified through the GUI.

Physical quantities measured by the comfort manikin include flow velocity $v_a$, air temperature $\vartheta_a$, operative temperature $\vartheta_o$ and relative humidity $\varphi$. The proposed measurement manikin enables the assessment of thermal comfort through direct interpretation of sensor data or via computed comfort values. The sensor data can be employed for comparing different setups or vehicles. While interpreting the measurement results requires expertise in the field, additional comfort values are subsequently derived due to the challenging nature of directly interpreting these measured values.

The instrumentation used on the TCM measures the operative temperature. It describes the temperature of an imaginary black enclosure where the human would exchange the same amount of heat due to radiation and convection as in the measured environment. For the computation of the PMV, the mean radiant temperature becomes necessary. It is defined in a manner analogous to the operative temperature, but only takes into account the heat exchange due to radiation excluding convection. The mean radiant temperature is calculated as

$$\bar{\vartheta_r} = \sqrt[4]{(273.15 + \vartheta_o)^4 + \frac{h_{c,o}}{\varepsilon_o\, \sigma}(\vartheta_o - \vartheta_a)} - 273.15, \tag{7}$$

using the measured operative temperature $\vartheta_o$, air temperature $\vartheta_a$, Stefan-Boltzmann constant $\sigma$, emission coefficient of the operative temperature probe $\varepsilon_o$ and the convective heat transfer coefficient

$$h_{c,o} = \max\left(18\ {v_a}^{0.55}, 3\ \sqrt[4]{|\vartheta_o - \vartheta_a|}\right). \quad (8)$$

The correlation calculates the convective heat transfer coefficient for both forced and free convection, selecting the higher value for the computation of the mean radiant temperature.

### 3.2 Simulation Approach

To allow thermal comfort prediction during the early development process when no prototype is available, a simulation approach is required. Results should be comparable to the measurement results conducted with the thermal comfort manikin. This comparability enables the validation of simulation models employed in the development process, possibly with the final prototype. For the computational fluid dynamics (CFD) simulation, Dassault Systèmes' PowerFLOW software package with its Lattice-Boltzmann Method (LBM) based solver is employed. The proposed simulation workflow comprises five distinct steps, outlined in Figure 4. The discretized manikin model can be positioned in the cabin with the pre-processing tool ANSA. The model is set up as a LS-DYNA dummy, which allows translation of the digital manikin and articulation of the joints in accordance with the degrees of freedom of the hardware manikin. Sensors are modeled as rigid body nodes connected to the surface mesh of the manikin. The resulting Nastran file is processed using a python script to extract sensor positions, which are then compiled into a text file containing all necessary probe data. This text file can be seamlessly imported into PowerFLOW by the python script. This script automates the generation of fluid and surface measurement probes at the relevant locations within the CFD model. Following the simulation run, results for all probe locations can be exported using a post-processing script. This script employs the PowerACOUSTICS software to extract the results and transfers the resultant text files to an output directory. These text files contain all physical quantities described earlier. In the final step, the output files are read by the LabVIEW program, which computes the thermal comfort values and outputs these values to a TDMS file. The structure of this output file replicates that of the measurement files generated through thermal comfort dummy measurements.

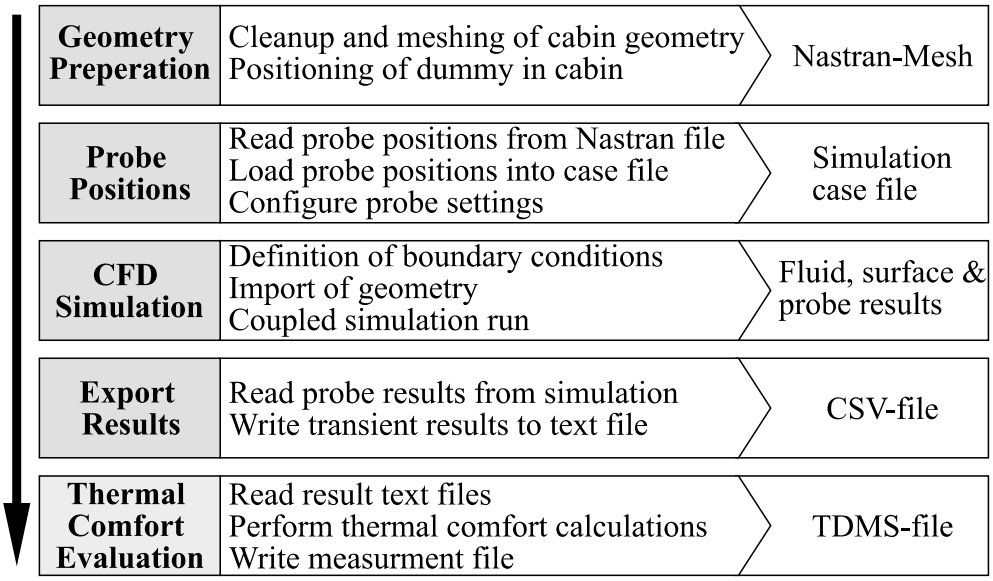


Figure 4: Thermal Comfort Manikin simulation workflow.

Velocity, humidity sensors and thermocouples are modeled as probes without geometry in the CFD simulation. However, the operative temperature probes' geometry is discretized. This is necessary to incorporate radiation effects on the sensor surface, which in turn impact the measured temperature. The temperatures of all surface nodes of the operative temperature sensor are exported to the result file. Subsequently, in the LabVIEW evaluation program, these temperatures are averaged, defining the operative temperature.

To simulate heat-up or cool-down cases spanning over several minutes, a computationally efficient transient approach is needed. Such cases require distinct methods and entail some simplifying assumptions. In case of transient heat up or cool down measurements, an initial flow development simulation is followed with a velocity freeze simulation [20]. The first 3 to 10 seconds are simulated to establish the flow field within the cabin. During this transient simulation, the draught rates and comfort values are calculated using the result data of the fluid file. In the subsequent step, the averaged flow field obtained from the first simulation is frozen. The computational grid is coarsened, and only the surface and fluid temperatures are simulated, while all other flow parameters are kept constant. The humidity can vary during this simulation step. If there are changes in the inlet mass flow rate, further flow development simulations are run. Subsequently, another velocity freeze simulation ensues at the new mass flow rate, as illustrated in Figure 5.

During velocity freeze simulations, where the velocity field is held constant, the air velocity remains unchanged over time. As a consequence, calculating the turbulence intensity and draught rate becomes impractical. In these scenarios, a workaround is implemented: the turbulence intensity and mean air velocity from the previous flow development simulation are averaged over time and treated as constants throughout the simulation cycle. This, combined with the evolution of air temperature, allows for the computation of the draught rate in accordance with equation (3).

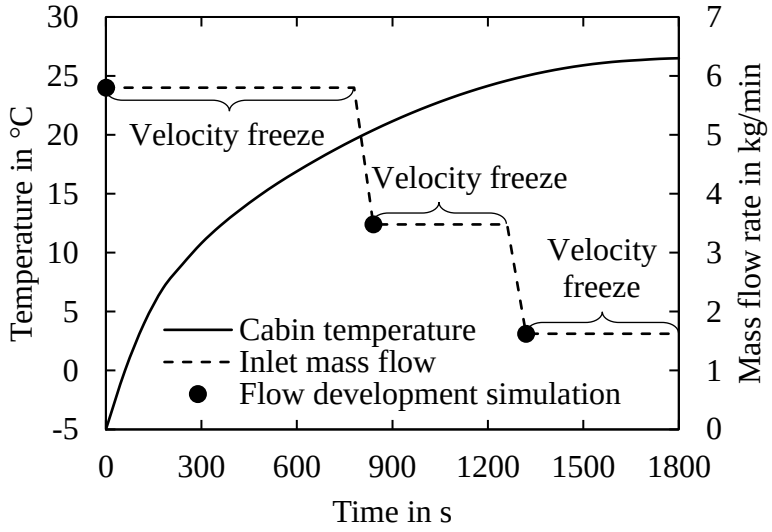


Figure 5: Simulation approach for transient heat up cases.

During transient simulations, accurate modeling of the manikin's specific heat capacity is crucial for achieving realistic temperature changes over time. To streamline the simulation process, a single specific heat capacity value $c_{p,manikin}$ is calculated for the manikin. This calculation employs a mass-weighted average method, incorporating the individual materials' mass $m_i$ and their respective specific heat capacities $c_{p,i}$, as well as the overall mass of the manikin $m_{manikin}$:

$$c_{p,manikin} = \frac{1}{m_{manikin}} \sum_{i=1}^{n} m_i c_{p,i}. \tag{9}$$

### 3.3 Experimental Setup

Measurements were conducted in a climate test chamber to validate the presented approach. The specific chamber used was the Weiss Umwelttechnik GmbH WT 8'/40-60, with a usable interior space of 2 x 2 x 2 m. This chamber offers a temperature range of -30 to 60 °C, with a heating and cooling rate of 1 K per minute and a time consistency of ≤ ± 1 K. Utilizing a climate test chamber guarantees a controlled environment with well-defined boundary conditions. A box is positioned in the climate test chamber, it can be supplied with a controlled airflow through a connected pipe with integrated fan. This pipe is supplied directly with air from the climate chamber conditioning system, which houses both air heater and evaporator. The box has an interior volume of 1.25 m³; which corresponds to the interior volume per person typically found in autonomous people mover concepts [21,22]. Due to this correspondence, it is referred to as "ThermoCab" in the subsequent discussion. To simulate a heated wall and account for the influence of uneven wall temperatures on the mean radiant temperature, a heating foil with a total power output of 190 W is

affixed to the interior rear wall. The comfort manikin is positioned on a chair in the center of the ThermoCab in a seated position. The operative temperature probe angle is set to 30° to represent a seated human. Stationary measurements over 30 seconds at different temperature levels with isothermal air injection were conducted. Each measurement was preceded by a soak duration of at least one hour to ensure stable and uniform temperature distribution, thus adhering to the requirements for consistent ambient conditions as outlined in EN ISO 7730 [6]. To assess the reproducibility of the results, all measurements were repeated three times. Clothing values were adjusted to match the ambient temperature conditions, aiming to achieve a PMV value close to neutral. The metabolism value was maintained constant at 1.1 to represent a seated individual.

The measurement setup is modeled using the simulation workflow described in section 3.2. The experiment is shown in the left and the corresponding simulation model in the right side of Figure 6. Radiation has a large influence on the operative temperature probe. Consequently, accurately modeling the radiation effect in the simulation becomes crucial. Apart from its absolute surface temperature $T$ and surface area $A$, the Stefan-Bolzmann constant $\sigma$, as well as the thermal emissivity $\varepsilon$ of a body determines its radiative heat flow

$$\dot{Q} = \varepsilon \, \sigma \, A \, T^4. \tag{10}$$

Figure 6: Climate chamber measurement setup (left) and simulation model (right).

The thermal emissivity values for both the interior walls of the test chamber, ThermoCab and the surface of the manikin were measured and incorporated into the simulation setup. A hand-held measurement device (Inglas TIR 100-2) that employs the total internal reflection (TIR) principle, as described in DIN EN 15976 and 16012 [23,24], was used to measure the thermal emissivity. It has a measurement range of 0.02 to 0.98, a repeatability accuracy of ± 0.005 for low and ± 0.01 for high emissivity specimens [25,26]. All interior measurements within the test chamber were integrated

into the simulation. The temperatures of the ThermoCab walls were monitored throughout all tests. These measured temperatures are used as prescribed boundary conditions within the simulation. Further, the mass flow rate, temperature and humidity of the supply air into the ThermoCab are also recorded during the measurement.

## 4 Results

In the following, a heat-up case from 5 to 30 °C is presented. The Climate chamber, including the ThermoCab and manikin, was pre conditioned to 5 °C. At measurement start, the inlet mass flow rate was set to 2.11 kg/s, with the inlet temperature gradually rising to 30 °C over the course of 60 minutes. Figure 7 illustrates the measurement data collected at the ThermoCab inlet during this heat-up process. To promote a more uniform vertical temperature distribution due to natural convection and buoyancy caused by the injection of warmer air into the ThermoCab, the air outlets were oriented downward at a 45° angle.

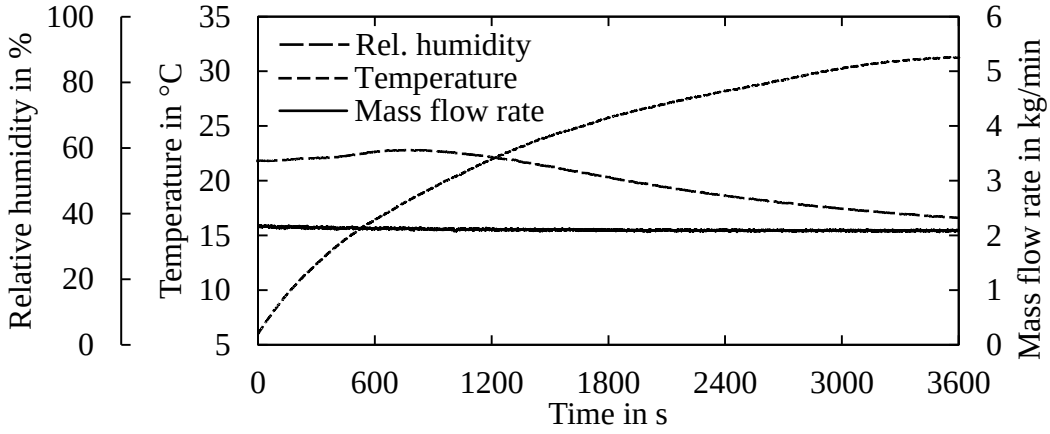


Figure 7: Measured inlet conditions of heat-up case.

Because the inlet mass flow rate remained approximately constant, only one cycle of flow development, followed by a velocity freeze simulation, was used. The flow development simulation was run for 10 seconds. The fluid domain was initialized with a flow velocity of 0 and a temperature of 5.5 °C, corresponding to the measured values. Inlet boundary conditions, including the inlet mass flow rate, temperature, and humidity, were derived from the measurements. Figure 8 depicts a y-aligned velocity cross-section positioned in the middle of the right air outlet after 10 seconds of simulation time. The flow has fully developed throughout the entire ThermoCab.

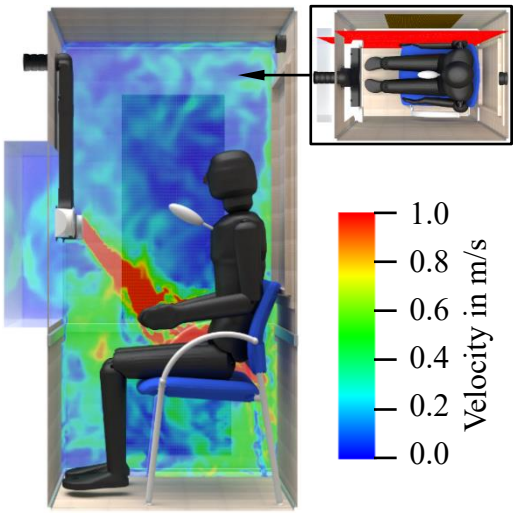


Figure 8: Y-aligned slice of the developed flow inside the ThermoCab.

In Figure 9, the flow velocities during the initial 10 seconds are compared to the measurement values over time for each probe. The comparison of probe data reveals a strong agreement between the measurement and simulation results. Specifically, for the left abdomen probe, the simulation shows slightly higher values in comparison to the measured data. Conversely, both lower leg probes exhibit slightly lower values in the simulation results. To facilitate this comparison further, Table 2 presents additional calculated statistical values for the air velocities. The table compares mean velocities, standard deviations $\sigma$, turbulence intensity $Tu$, and draught rate $DR$ for each probe. Once again, these values indicate a good correlation, with the left abdomen probe exhibiting slightly higher mean and maximum values, while the lower leg probes show lower mean and maximum values when compared to the measurements. The protective cage fitted to the probes on the manikin can potentially influence the incident flow and introduce some turbulence. However, in the simulation, this cage is not modeled, which could lead to discrepancies in the results.

The air temperature values from all probes on the manikin exhibit a root mean square error (RMSE) of 0.8 K or less during the flow development simulation. Consequently, these values are not presented in detail here. The operative temperature, averaged over the 10-second interval, is 5.4 °C in both experiment and simulation. The transient temperature evolution leads to a RMSE of 0.1 K. The average relative humidity in the measurement is 52.3 %, compared to 50.4 % in the simulation, or a RMSE of 2.0 % between the two datasets.

Following the ten-second flow development simulation, the fluid domain is averaged over the last second of simulation time. This averaged flow field serves as the initial condition for the subsequent velocity freeze simulation. During this phase, velocities do not vary over time, and only the temperature evolution within the fluid domain is computed through the coupled simulation with a coarsened mesh, as outlined in section 3.2.

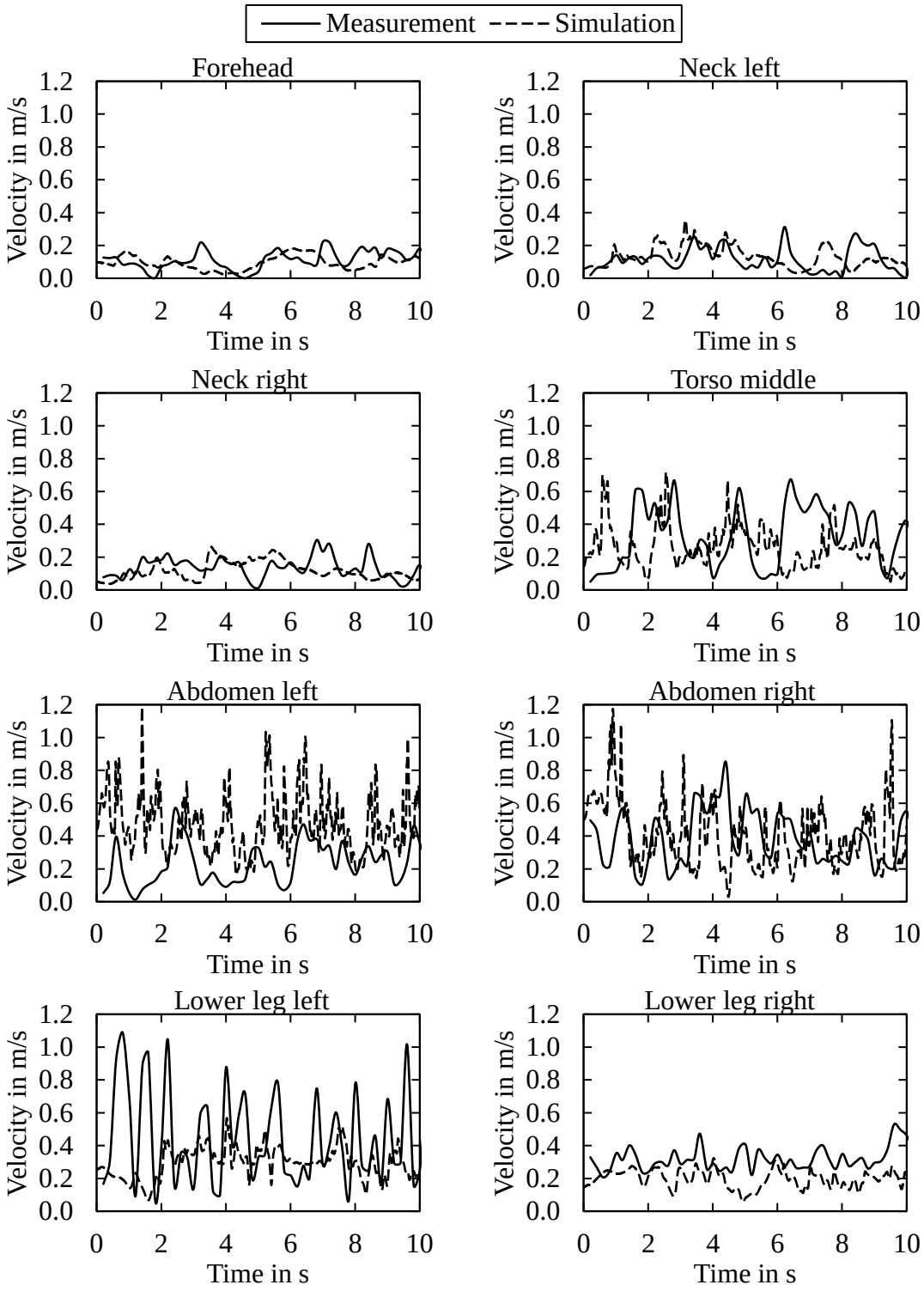


Figure 9: Comparison of velocity probe data between measurement and simulation.

Table 2: Statistical comparison of velocities between measurement and simulation.

| | Measurement | | | | Simulation | | | |
|---|---|---|---|---|---|---|---|---|
| | $\bar{v}_a$ m/s | $\sigma$ m/s | $Tu$ % | $DR$ % | $\bar{v}_a$ m/s | $\sigma$ m/s | $Tu$ % | $DR$ % |
| Forehead | 0.11 | 0.06 | 49.5 | 26.6 | 0.10 | 0.04 | 44.6 | 19.8 |
| Neck left | 0.12 | 0.07 | 63.2 | 30.1 | 0.13 | 0.06 | 47.4 | 33.0 |
| Neck right | 0.14 | 0.06 | 47.0 | 34.1 | 0.12 | 0.06 | 46.4 | 28.2 |
| Torso middle | 0.33 | 0.19 | 56.2 | 100.0 | 0.26 | 0.13 | 48.9 | 83.9 |
| Abdomen left | 0.23 | 0.13 | 56.6 | 79.1 | 0.47 | 0.18 | 37.2 | 100.0 |
| Abdomen right | 0.39 | 0.17 | 43.6 | 100.0 | 0.41 | 0.19 | 47.9 | 100.0 |
| Lower leg left | 0.45 | 0.29 | 65.6 | 100.0 | 0.30 | 0.09 | 31.1 | 78.2 |
| Lower leg right | 0.32 | 0.07 | 22.2 | 73.7 | 0.20 | 0.05 | 27.2 | 44.6 |

A comparison of PMV values derived from measurement and simulation of the heat-up case is illustrated in Figure 10. In the simulation, surface temperatures are updated after every coupling interval between the CFD and thermal solver. Since surface temperatures have a direct impact on the operative temperature, the PMV is calculated at the same interval when the surface temperatures are updated. The comfort value obtained from measurements exhibits slight fluctuations due to changes in flow velocity. Initially, when average air and surface temperatures are below 6 °C, the PMV value in both measurement and simulation is -3. However, as the air and surface temperatures within the ThermoCab increase, the PMV value also rises. A neutral thermal state, represented by a PMV of 0, is attained after 2984 seconds in the experiment and 3060 seconds in simulation.

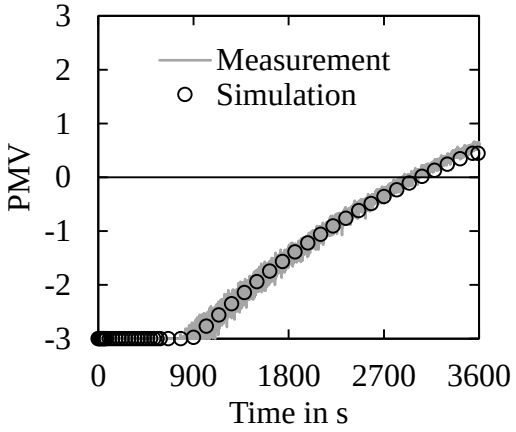


Figure 10: Comparison of calculated PMV values for heat-up case.

The air temperature averages over all probes at the end of the heat-up cycle (t=3600 s) is only 0.9 K higher in the simulation results. This deviation lies within the measurement accuracy of the thermocouples used in the TCM.

## 5 Conclusions and Outlook

The proposed thermal comfort manikin enables the measurement and real-time examination of velocity and temperature fields within a vehicle cabin. It takes radiation as well as relative humidity into account. Together with the clothing and metabolism factors defined in the measurement GUI, an objective rating of the thermal comfort is possible. The simulation approach presented, utilizing a digital twin of the TCM, provides results that are comparable to measurements. Both the velocity field obtained from the initial flow development simulations and the temperature evolution over time derived from subsequent frozen velocity field simulations as well as the calculated PMV align well with measurement values.

In the future, an approach to weigh temperatures and velocities at different locations of the body according to the thermal sensitivity of the body part will be implemented into the software. This enhancement will enable a more precise evaluation of temperature distributions across the body, recognizing that not all regions contribute equally to the overall thermal sensation. Furthermore, the TCM will be applied to a vehicle cabin, and its results will be compared to those obtained from other comfort models in simulations.

## 6 Acknowledgements

This research is accomplished within the project “UNICARagil” (FKZ 16EMO0289). We acknowledge the financial support for the project by the Federal Ministry of Education and Research of Germany (BMBF).

## 7 Abbreviations

| | |
|---|---|
| BEV | Battery Electric Vehicle |
| CAD | Computer-Aided Design |
| CFD | Computational Fluid Dynamics |
| FDM | Fused Deposition Modeling |
| GUI | Graphical User Interface |
| LBM | Lattice-Boltzmann Method |
| PMV | Predicted Mean Vote |
| PPD | Projected Percentage of Dissatisfied |
| TCM | Thermal Comfort Manikin |
| TIR | Total Internal Reflection |

## 8 Bibliography


1. Daanen, H. A.M.; van de Vliert, E.; Huang, X.: Driving performance in cold, warm, and thermoneutral environments. Applied Ergonomics 34 (2003), p. 597-602.
2. Cheng, X.; Zhou, Z.; Yang, C.; Zheng, X.; Liu, C.; Huang, W.; Yang, Z.; Qian, H.: Effects of draught on thermal comfort and respiratory immunity. Building and Environment 224 (2022), p. 109537.
3. Brandes, R.; Lang, F.; Schmidt, R. F.: Physiologie des Menschen: mit Pathophysiologie, Springer Lehrbuch, 32. Auflage, Berlin, Heidelberg: Springer, 2019.
4. Brager, G. S. u. Dear, R. J. de: Thermal adaptation in the built environment: a literature review. Energy and Buildings 27 (1998) 1, p. 83–96.
5. Fanger, P. O.: Thermal comfort analysis and applications in environmental engineering. Analysis and applications in environmental engineering. New York: McGraw-Hill, 1970.
6. Deutsches Institut für Normung e.V.: DIN EN ISO 7730:2006-05, Ergonomie der thermischen Umgebung – Analytische Bestimmung und Interpretation der thermischen Behaglichkeit durch Berechnung des PMV- und des PPD-Indexes und Kriterien der lokalen thermischen Behaglichkeit. Berlin: Beuth Verlag GmbH, 2006.
7. American Society of Heating, Refrigerating and Air-Conditioning Engineers: ANSI/ASHRAE Standard 55-2017: Thermal Environmental Conditions for Human Occupancy. Atlanta: ASHRAE, 2017.
8. Deutsches Institut für Normung e.V.: DIN EN ISO 7726:2021-03, Umgebungsklima - Instrumente zur Messung physikalischer Größen. Deutsche Norm. Berlin: Beuth Verlag GmbH, 2021.
9. Ekici, C.: Measurement Uncertainty Budget of the PMV Thermal Comfort Equation. International Journal of Thermophysics 37, Issue 5, 2016.
10. Chaudhuri, T.; Soh, Y. C.; Bose, S.; Xie, L.; Li, H.: On assuming Mean Radiant Temperature equal to air temperature during PMV-based thermal comfort study in air-conditioned buildings. IECON 2016 - 42nd Annual Conference of the IEEE Industrial Electronics Society. IEEE 2016, p. 7065–7070.
11. Broday, E. E.; Ruivo, C. R.; Gameiro da Silva, M.: The use of Monte Carlo method to assess the uncertainty of thermal comfort indices PMV and PPD: Benefits of using a measuring set with an operative temperature probe. Journal of Building Engineering 35 (2021) 4, p. 101961.
12. Da Silva, M. G.; Santana, M. M.; Alves e Sousa, J.: Uncertainty Analysis of the Mean Radiant Temperature Measurement based on Globe Temperature Probes. Journal of Physics: Conference Series 1065 (2018), p. 72036.

13. Teitelbaum, E.; Chen, K. W.; Meggers, F.; Guo, H.; Houchois, N.; Pantelic, J.; Rysanek, A.: Globe thermometer free convection error potentials. Scientific reports 10 (2020) 1, p. 2652.
14. Teitelbaum, E.; Alsaad, H.; Aviv, D.; Kim, A.; Voelker, C.; Meggers, F.; Pantelic, J.: Addressing a systematic error correcting for free and mixed convection when measuring mean radiant temperature with globe thermometers. Scientific reports 12 (2022) 1, p. 6473.
15. Simone, A; Babiak, J.; Bullo, M.; Landkilde, G.; Olesen, B. W.: Operative temperature control of radiant surface heating and cooling systems. In: Proceedings of Clima 2007 Wellbeing Indoors.
16. Dyvia, H. A.; Arif, C.: Analysis of thermal comfort with predicted mean vote (PMV) index using artificial neural network. IOP Conference Series: Earth and Environmental Science 622, 2021, p. 12019.
17. Deutsches Institut für Normung e.V.: DIN EN ISO 7250-1:2017-12, Wesentliche Maße des menschlichen Körpers für die technische Gestaltung – Teil 1: Körpermaßdefinitionen und –messpunkte. Berlin: Beuth Verlag GmbH, 2017.
18. Deutsches Institut für Normung e.V.: DIN CEN ISO/TR 7250-2:2013-08, Wesentliche Maße des menschlichen Körpers für die technische Gestaltung – Teil 2: Anthropometrische Datenbanken einzelner nationaler Bevölkerungen. Berlin: Beuth Verlag GmbH, 2013.
19. Dantec Dynamics A/S: ComfortSense – Installation and User Guide. Publication No.: 9040U4652, Skovlunde, 2016.
20. Dassault Systèmes: PowerFLOW – Climate Control Best Practices Guide PF5.5BP, DS Simulia, 2019.
21. Wisser, M.: Konstruktion einer generischen und anpassbaren Peoplemover-Kabine zur Simulation verschiedener Klimatisierungkonzepte. Masterarbeit, Universität Stuttgart, 2022.
22. Gehringer, D.; Kuthada, T.; Wagner, A. Thermal Management System of the UNICARagil Vehicles—A Comprehensive Overview. World Electr. Veh. J. 2023, 14, 6.
23. Deutsches Institut für Normung e.V.: DIN EN 15976:2011-07, Abdichtungsbahnen – Bestimmung des Emissionsgrades. Berlin: Beuth Verlag GmbH, 2011.
24. Deutsches Institut für Normung e.V.: DIN EN 16012:2015-05, Wärmedämmstoffe für Gebäude – Reflektierende Wärmedämm-Produkte – Bestimmung der Nennwerte der wärmetechnischen Eigenschaften. Berlin: Beuth Verlag GmbH, 2015.
25. INGLAS GmbH & Co. KG: TIR 100-2: Measuring of thermal emissivity within seconds. Stand 2/2010.
26. Kononogova, E.; Adibekyan, A.; Monte, C.; Hollandt, J.: Characterization, calibration and validation of an industrial emissometer. Journal of Sensors and Sensor Systems 8 (2019) 1, p. 233–242.

# A 1D model for zonal comfort estimation and control in a passenger car cabin

Anandh Ramesh Babu, Simone Sebben

Mechanics and Maritime Sciences
Chalmers University of Technology
Gothenburg
Sweden
anandh.rameshbabu@chalmers.se
simone.sebben@chalmers.se

**Abstract:** Cabin acclimatization in electric vehicles requires a large fraction of the energy from the battery, and as such, they play an important part in optimizing the driving range while still maintaining good passenger comfort. To study cabin conditions, zonal climate models have been commonly used. In this paper, a 4-zone cabin model has been modelled with the transport of temperature, CO2 and humidity. This model was verified using a CHT simulation of a passenger vehicle with about 5% variation for temperature estimation, and under 3% for the heat losses from the cabin. The JOS-3 thermoregulation model was used in conjunction with the zonal model to study the evolution of skin and core temperatures, and the UCB-Zhang thermal comfort model was later used to compute thermal sensation and comfort.

## 1 Introduction

Customer expectations for improved comfort in vehicles have increased over the past decades that excellent thermal comfort is a requirement for automobile OEMs. Heating ventilation air conditioning (HVAC) systems ensure that each occupant has the necessary thermal comfort. This means that these systems must take quick and robust measures to achieve the required targets. Typically, subjective assessments and calibration are performed for this purpose, which means that the process takes place at the late phase of vehicle development.

To mitigate this, and to investigate energy-efficient solutions for the HVAC, numerous cabin modeling strategies have been developed, each with respective advantages and disadvantages. A classification can be made depending on their levels of fidelity into low (Poovendran et al., 2020; Torregrosa-Jaime et al., 2015) and high-fidelity models (Chang et al., 2018; Lorenz et al., 2014; Ramesh Babu et al., 2023). The low fidelity methods typically include a lumped thermal, and zonal model that

are characterized by simplified physical representations of the systems. They are grey-box, meaning their behavior can be influenced by fundamental principles with some calibration based on existing datasets. Recently, low-fidelity black-box models in the form of neural networks have been suggested (Bandi et al., 2023; Warey et al., 2021). However, more research is required to ensure that these models perform adequately well under cases with transient conditions. The high-fidelity models include computational fluid dynamics (CFD) simulations which numerically solve the transport equations in space and time. These simulations are the most representative of the real world but are extremely expensive to solve. Hence, the grey-box models are usually preferred to study the cabin and its interactions with the climate systems.

In this study, a 4-zone cabin model was developed based on the principles of mass and heat conservation and was verified using a heat-up test with the results of a validated CFD model from previous work. The JOS-3 thermoregulation (Takahashi et al., 2021 was then used in the zones of the cabin to investigate thermal comfort metrics based on the UCB-Zhang scale (Zhang H., 2002) and PMV-PPD models. This was coded in Python and the package of the model was released in https://github.com/anandhSRB/fourZoneVehicleCab.git.

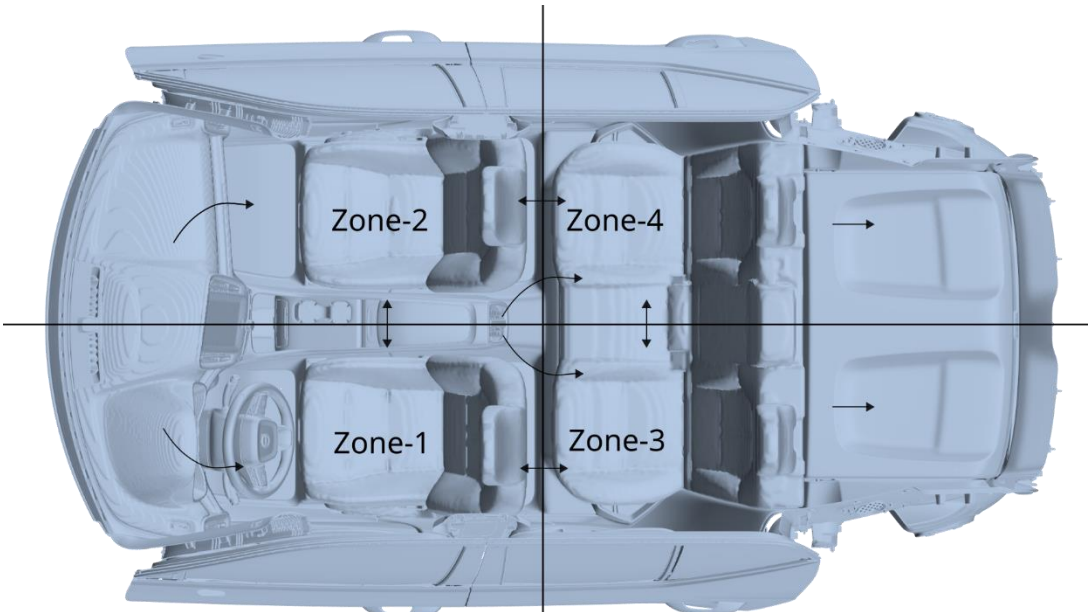


Figure 1. Schematic of the four zones in the vehicle cabin.

## 2 Cabin modelling

In this work, the cabin was developed using the work of (Poovendran et al., 2020). A schematic of the four-zone cabin model has been illustrated in Figure 1. The air was modeled as incompressible air with each zone conserving mass and energy. The mass entering zones 1 and 2, is carried into zones 3 and 4, respectively with, lateral mass flow being neglected.

The energy balance in each zone $i$ can be represented as,

$$C_i \frac{dT_i}{dt} = Q_{HVAC,i} + Q_{conv,int,i} + Q_{conv,ext,i} + \Sigma_j Q_{exch,ij} + Q_{occ,i} \quad (1)$$

where $C$ is the total capacitance of air in each zone, T is the temperature, $Q_{hVAC}$ is the energy from the HVAC, $Q_{conv,int}$ and $Q_{conv,ext}$ are the convective losses to the internal solids and external ambient, respectively, $Q_{exch,j}$ is the heat loss to the neighboring zones, $Q_{occ}$ is the heat from the occupants.

The formulations for terms $Q_{exch,j}$ and $Q_{HVAC}$ are in (Poovendran et al., 2020). The heat loss through convection from each zone is taken as,

$$Q_{conv,int,i} = h_{int,i}\, A_i\, (T_{s,i} - T_i) \quad (2)$$

Where $h_{int,i}$ is the internal heat transfer coefficient, $A$ is the area of contact with the solids inside the zone and $T_s$ is the temperature of the solids. The internal heat transfer coefficient has been computed based on the empirical expressions of the Nusselt number (Ghiaasiaan, 2018),

$$Nu = \begin{cases} A.Re^{0.5}, Bo > 10 \\ B.Gr^{0.25}, Bo < 0.1 \\ \frac{A}{Re^{-0.5}}\left(1 + \left(\frac{B}{A}\, Bo^{0.25}\right)^3\right)^{\frac{1}{3}}, \text{otherwise} \end{cases} \quad (3)$$

Where $A$ and $B$ are functions of Prandtl number ($Pr$), and are equal to 0.579, and 0.526, respectively assuming that air has a $Pr$=0.7.

The buoyancy number (Bo) is defined as $Bo = \frac{Gr}{Re^2}$, where $Gr$ is the Grashof number and $Re$ is the Reynold's number. The length scale ($L$) for these terms was taken as the square root of the zonal area. Using these expressions, the internal heat transfer coefficient was computed as,

$$Nu_i = \frac{h_{conv,int,i} L_i}{k} \quad (4)$$

and $k$ is the thermal conductivity of air. Similarly, the heat transfer to the ambient was computed as,

$$Q_{conv,ext,i} = \frac{T_i - T_\infty}{R_{t,i}} \quad (5)$$

Where $T_\infty$ is the ambient temperature and $R_{t,i}$ is the resistance to heat transfer. The resistance was computed in three parts: the internal convection resistance ($1/h_{int}$) as shown above with a representative length for the windows, the thermal resistance of the windshield and windows ($t/k$), and external heat transfer resistance ($1/h_{ext}$), where $h_{ext}$ is the external heat transfer coefficient defined as (Zhang et al., 2009),

$$h_{ext} = 1.163\left(4 + 10\sqrt{v}\right) \quad (6)$$

The temperature of the solids inside the cabin was computed similar to eqn. (1), with energy from internal convection, and solar radiation. The reader can refer the original work (Poovendran et al., 2020) for more information on the formulations.

In addition to temperature, two transport equations, $CO_2$ and specific humidity were solved in each zone as,

$$M_i \frac{d\alpha_i}{dt} = \dot{m}_{in}\left(\alpha_i - \alpha_{in,i}\right) + \mathrm{A_{s,i}} + \Sigma_{\mathrm{j}} \mathrm{A}_{exch,ij} \tag{7}$$

Where $M_i$ is the mass of the cabin, $\dot{m}_{in}$ is the inlet mass flow rate, $\alpha_{in}$ is the concentration of the transport quantity ($CO_2$ or specific humidity), $\mathrm{A}_s$ is the source term from the human, and $\mathrm{A}_{exch}$is the species exchange across zones (computed similarly to $Q_{exch}$).

The JOS-3 thermoregulation model was included in the model with one occupant in each zone. The zonal conditions, i.e., air temperature, solid temperature, relative humidity (RH), and air velocity were taken into the JOS-3 model to simulate each time step. The heat produced by the occupant ($Q_{occ}$ in eqn. (1)) was estimated from the JOS-3 as the total sensible heat loss from the human, which was computed as,

$$Q_{occ,i} = \Sigma_j \frac{\left(T_{sk_j} - T_{o,i}\right)}{R_{th,j}} \tag{8}$$

Where j represents individual segments of the JOS-3 model such as the head, neck, back, pelvis, left and right arms, and so on, $T_{sk_j}$ is the skin temperature of each segment, $T_o$ is the operative temperature computed based on the air and radiation temperatures, and air velocity. $R_{th}$is the thermal resistance between the zone and the skin which includes clothing resistances, and convective and radiation resistances.

The source term in eqn. (7) for CO2 was due to respiration from the human at 9l/min at 40,000 ppm (Chang et al., 2018) while the source term for humidity was considered at 90% relative humidity (RH) at the core temperature of the head (Mansour et al., 2020).

Thus, using this model, the temperature transport, heat losses to the solids, concentration of CO2, and specific humidity were simulated with appropriate boundary and initial conditions explicitly in time.

## 2.1 Control model

As (Poovendran et al., 2020) showed that the model was robust for control, a simplified control for the cabin model was created where the HVAC heating and cooling were modeled using a PI controller. The target was set to 22°C in the cabin.

Thus, the HVAC rate was defined as,

$$Q_{HVAC} = k_p \epsilon + \Sigma k_i \epsilon \Delta t \tag{9}$$

Where $\epsilon$ is defined as the difference between the mean cabin and the target temperature. The inlet temperature at each time step was then defined as,

$$T_{in} = T_{\infty} + \frac{Q_{HVAC}}{\dot{m}_{in} c_p} \tag{10}$$

The inlet temperatures were limited to a minimum of 2°C and a maximum of 60°C. Several ambient conditions ranging from temperatures between -10 to 20°C were simulated with a driver using the JOS-3 model as described above.

# 3 Model Validation

The model was first simulated without any passengers and verified with the data published in (Ramesh Babu et al., 2023). The scenario considered was a passenger car being heated up from -7°C while driving at 50 km/h. The definitions of the cabin are described in Table 1. Note that the internal area represents the area where the cabin air is in contact with the solids, and the external area represents the area where the windows are in contact with the ambient.

| **Parameters** | **Values** |
|---|---|
| Dimensions | 2.5m x 1.2m x 0.85m |
| Solid thermal capacitance | 2.4 x $10^6$ kJ/K |
| Inlet mass flow rate | 0.0461 kg/s |
| Internal area | 18.8 $m^2$ |
| External area | 3.5 $m^2$ |

The inlet temperatures in the cabin were taken from (Ramesh Babu et al., 2023). Figure 2a displays the average cabin temperature over 40 min of simulation time comparing the zonal model and CFD. The zonal model overpredicts the temperature during the initial heat-up phase until about 10 min as compared to the CFD model. This is believed to be because the convective jets from the inlets contribute to local heating effects while this energy from the HVAC is diffused into the control volumes in the zonal model. This is supported by the fact that in Figure 2b, which illustrates the energy lost from the cabin air to all solids, the zonal model estimates the energy losses quite well throughout the simulation with marginal over-prediction towards the end of the simulation. The deviation was found to be within 2.5% in the net energy expenditure as compared to the CFD simulation. Another reason for the discrepancy in the temperature during the heat-up period can be attributed to the effect of buoyancy as the majority of the hot air into the cabin is directed at the floor and defrosters, which the zonal model could not account for. The biggest advantage of this model was the quick run-time as it took under a second to simulate 40 minutes while the CFD simulation required over 60 hours on a high-performance cluster with 1000 cores. Thus, the model provided reasonably accurate and quick results.

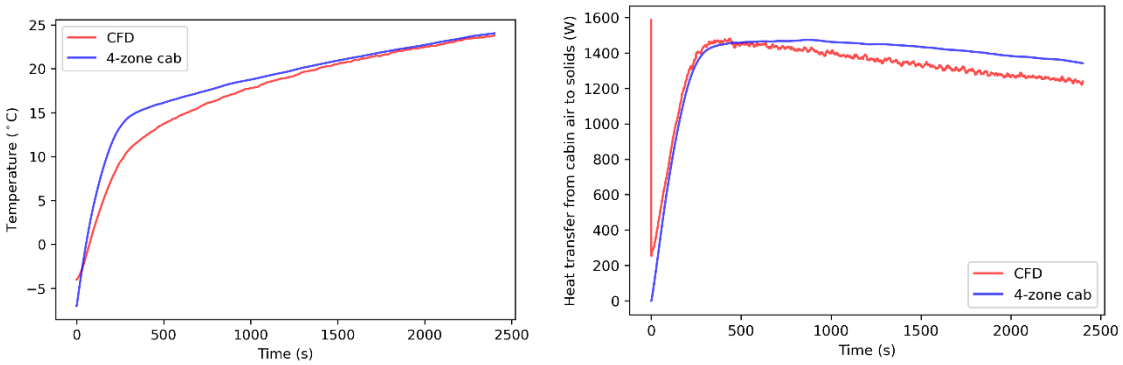


Figure 2. Comparison between CFD and four zone cabin model: (a) Mean cabin temperature, (b) Heat transfer to the interior cabin solids from the cabin air.

# 4 Results and discussions

## 4.1 Effect of the number of occupants

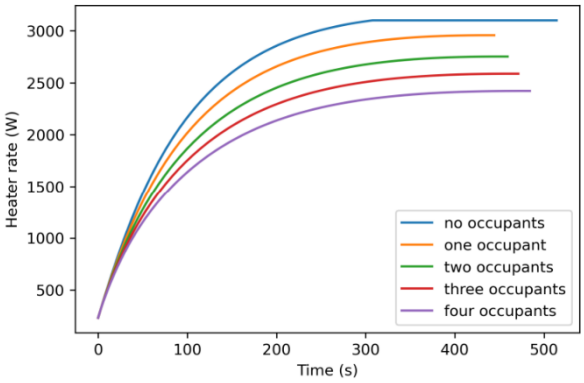


Figure 3. Comparison of heater control strategy with number of occupants until the cabin achieves 22°C.

The cabin was simulated with no passengers to establish a reference value for the heat generated. In this condition, the cabin has no heat or contaminant sources. The total energy required to heat the cabin to 22°C from -7°C is about 1.35MJ. The total energy required to heat the cabin decreases with the increasing number of occupants. The JOS-3 model rejects heat based on the boundary conditions and the sensible heat loss function provides the heat rejected from the skin to the air in the cabin. For the conditions simulated, about 170W was rejected on average. The mean cabin temperature, which was used in the control model, increases rapidly with more occupants and, hence, a less aggressive control strategy was employed. Thus, the time required to achieve the target set point increased slightly with more occupants present in the cabin. The energy required to heat the cabin decreased linearly at approximately 2.5% with from 1 to 4 occupants relative to no occupants.

Four cases with increasing number of occupants were simulated and the mean concentration of CO2 was monitored for 30 min. The mean CO2 levels increased with the number of occupants in the cabin, as expected. The CO2 levels for fresh air per

passenger shown below are in agreement with the trends presented by (Chang et al., 2018; Royo Bareng, 2023).

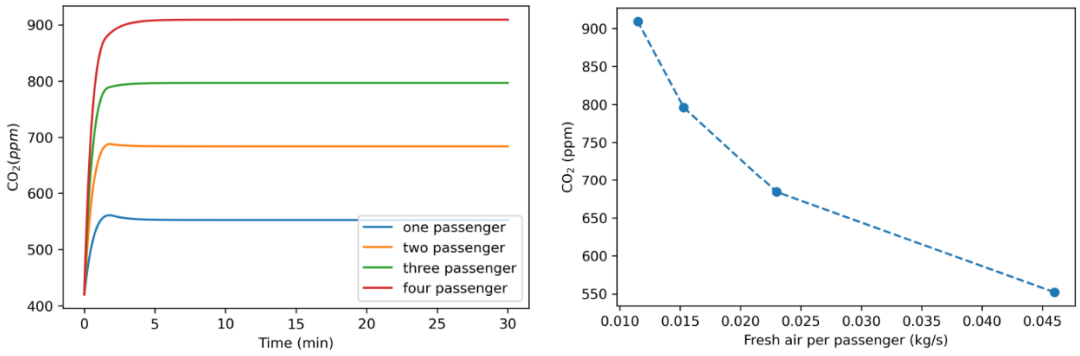


Figure 4. (a) Concentration of CO2 with varying number of passengers in the cabin. (b) CO2 concentration as a function of fresh air per passenger in the cabin.

The specific humidity increases similarly to $CO_2$. Due to the cabin heating up, the relative humidity decreases in time with increasing cabin temperatures as shown below. A marginal increase in relative humidity is noted with a higher number of occupants.

## 4.2 Thermal comfort metrics

Two scenarios were considered for the purpose of assessing thermal comfort: a cold (heating from 0°C) and a warm scenario (cooling from 35°C). Only one occupant in the driver position was considered for the analysis of the two scenarios and later the variations in sensations are presented for the cold scenario with two passengers. The JOS-3 model in combination with the UCB-Zhang was used to estimate the overall thermal sensation and comfort. Additionally, the PMV-PPD metrics were obtained using the Python package 'pythermalcomfort' (Tartarini and Schiavon, 2020). Since the minimum and maximum temperatures for this model were 10°C and 40°C, respectively, any temperature outside this range was set to -3 or +3, which corresponds to too cold or too warm.

The Figure 5 below compares the predicted mean vote (PMV) from the Fanger model and the overall thermal sensation from the UCB-Zhang model. Both models capture heating and cooling effects but from different perspectives. The Fanger model is relatively simple where it estimates PMV based on the environmental variations for a defined clothing resistance and metabolic rate. The UCB-Zhang model, on the other hand, uses the variations in temperatures from the skin and core nodes of the JOS-3 model and estimates local and overall sensations and comfort. In the context of thermal comfort, both models can be used to quantify if a certain condition is comfortable.

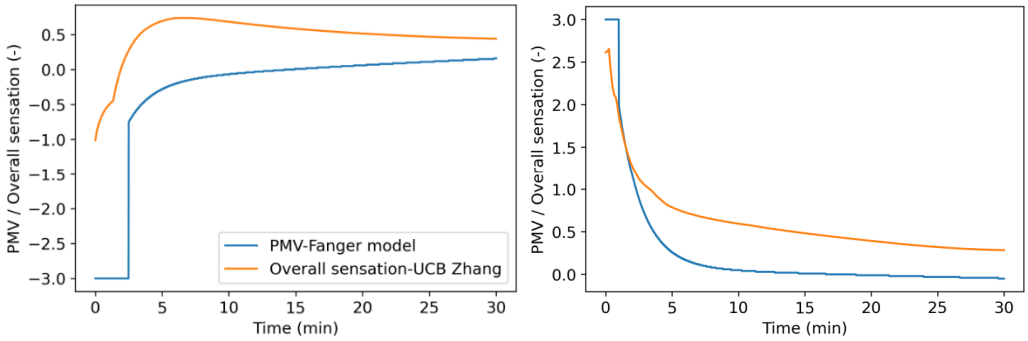


Figure 5. Comparison between PMV-Fanger and overall sensation-UCB Zhang metrics under: (a) Cold scenario; (b) Hot scenario.

Figure 6 compares the overall sensations between occupants in Zone-1 and Zone-2. The variations in the mass flow and temperatures to each zone result in differences in the heat loss from the JOS-3 model. This results in variations in the skin temperatures and thus, overall sensation.

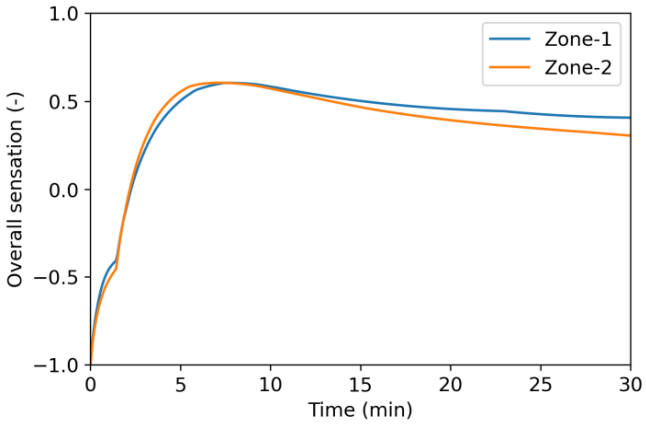


Figure 6. Comparison between overall sensations of occupants in Zone-1 and Zone-2 in the cold scenario.

## 5 Conclusions

A four-zone cabin model was developed where the transport equations for temperature, $CO_2$, and humidity were solved. The model was validated with a high-fidelity CFD simulation, which in turn was tested for accuracy against physical testing. The zonal cabin model produced almost the same mean cabin temperature at steady-state and the net heat transferred to the solids within 2.5% as compared to CFD, with little computational resources. The JOS-3 thermoregulation model was employed in each zone to simulate the presence of a manikin. The concentration of $CO_2$ and humidity in the cabin increased with the number of occupants in accordance with the literature. The PMV-PPD and UCB-Zhang comfort models were employed to estimate the thermal sensations under various conditions and showed good correlation

indicating that either of the models could be used for this purpose. In conclusion, the model described in the paper can be used for quick computations for the purpose of cabin temperature estimation under various operating conditions and for thermal comfort estimations.

# 6 Bibliography


Bandi, P., Manelil, N.P., Maiya, M.P., Tiwari, S., Arunvel, T., 2023. CFD driven prediction of mean radiant temperature inside an automobile cabin using machine learning. Thermal Science and Engineering Progress 37, 101619. https://doi.org/10.1016/j.tsep.2022.101619

Chang, T.-B., Sheu, J.-J., Huang, J.-W., Lin, Y.-S., Chang, C.-C., 2018. Development of a CFD model for simulating vehicle cabin indoor air quality. Transportation Research Part D: Transport and Environment 62, 433–440. https://doi.org/10.1016/j.trd.2018.03.018

Ghiaasiaan, S.M., 2018. Convective Heat and Mass Transfer. CRC Press.

Lorenz, M., Fiala, D., Spinnler, M., Sattelmayer, T., 2014. A Coupled Numerical Model to Predict Heat Transfer and Passenger Thermal Comfort in Vehicle Cabins. Presented at the SAE 2014 World Congress & Exhibition, pp. 2014-01–0664. https://doi.org/10.4271/2014-01-0664

Mansour, E., Vishinkin, R., Rihet, S., Saliba, W., Fish, F., Sarfati, P., Haick, H., 2020. Measurement of temperature and relative humidity in exhaled breath. Sensors and Actuators B: Chemical 304, 127371. https://doi.org/10.1016/j.snb.2019.127371

Poovendran, K., Abel, D., Reuscher, T., Govender, V., 2020. Vehicle Cabin Thermal Multi-Zone Modelling for Control, in: 2020 2nd International Conference on Control Systems, Mathematical Modeling, Automation and Energy Efficiency (SUMMA). Presented at the 2020 2nd International Conference on Control Systems, Mathematical Modeling, Automation and Energy Efficiency (SUMMA), pp. 489–495. https://doi.org/10.1109/SUMMA50634.2020.9280673

Ramesh Babu, A., Sebben, S., Bark, T., 2023. Effect of Cabin Insulation on the Heating Performance in EVs at Low Temperatures. Presented at the WCX SAE World Congress Experience, Detroit, Michigan, United States, pp. 2023-01–0763. https://doi.org/10.4271/2023-01-0763

Royo Bareng, R., 2023. Analysis of heat losses from the cabin of a battery electric vehicle.

Takahashi, Y., Nomoto, A., Yoda, S., Hisayama, R., Ogata, M., Ozeki, Y., Tanabe, S., 2021. Thermoregulation model JOS-3 with new open source code. Energy and Buildings 231, 110575. https://doi.org/10.1016/j.enbuild.2020.110575

Tartarini, F., Schiavon, S., 2020. pythermalcomfort: A Python package for thermal comfort research. SoftwareX 12, 100578. https://doi.org/10.1016/j.softx.2020.100578

Torregrosa-Jaime, B., Bjurling, F., Corberán, J.M., Di Sciullo, F., Payá, J., 2015. Transient thermal model of a vehicle's cabin validated under variable ambient conditions. Applied Thermal Engineering 75, 45–53. https://doi.org/10.1016/j.applthermaleng.2014.05.074

Warey, A., Kaushik, S., Khalighi, B., Cruse, M., Venkatesan, G., 2021. Prediction of Vehicle Cabin Occupant Thermal Comfort Using Deep Learning and Computational Fluid Dynamics. SAE Intl. J CAV 4, 12-04-03–0022. https://doi.org/10.4271/12-04-03-0022

Zhang, H., n.d. Human Thermal Sensation and Comfort in Transient and Non-Uniform Thermal Environments.

Zhang, H., Dai, L., Xu, G., Li, Y., Chen, W., Tao, W., 2009. Studies of air-flow and temperature fields inside a passenger compartment for improving thermal comfort and saving energy. Part II: Simulation results and discussion. Applied Thermal Engineering 29, 2028–2036. https://doi.org/10.1016/j.applthermaleng.2008.10.006

# Generating Tyre Geometries Incorporating Real Tyre Deformation for Aerodynamic CFD Analysis

Johannes Burgbacher, Leander Reichhart, Victor Mappes, Timo Kuthada, Felix Wittmeier, Andreas Wagner

Institute of Automotive Engineering (IFS)
Pfaffenwaldring 12
70569 Stuttgart
johannes.burgbacher@ifs.uni-stuttgart.de
leander.reichhart@fkfs.de
victor.mappes@ifs.uni-stuttgart.de
timo.kuthada@fkfs.de
felix.wittmeier@fkfs.de
andreas.wagner@ifs.uni-stuttgart.de

**Abstract:** For optimal flow predictions via computational fluid dynamics (CFD), a geometric representation that is as realistic as possible is necessary. Consequently, a process was developed as part of a research project, funded by the Forschungsvereinigung Automobiltechnik (FAT) with the aim to generate tyre geometries that accurately reflect real tyre deformation. The process involves a combination of structural light scanning and a newly designed and built tyre deformation test bench. Additionally, a parameter study was conducted on the tyre deformation test bench, to evaluate the influence of vertical tyre load, tyre pressure and rotational speed on the tyre deformation.

## 1 Motivation

Up to 25% of the vehicle aerodynamic drag is contributed by the wheels and the wheel arches [1]. This section of the car represents significant optimization potential for aerodynamic development. Aerodynamic optimizations mainly rely on wind tunnel testing and CFD. Wind tunnel testing is widely regarded as a highly accurate method for evaluating aerodynamic properties. However, during the initial stages of aerodynamic development, vehicle models are often unavailable. As a result, decisions regarding aerodynamic optimizations are primarily based on CFD simulations. Consequently, it is imperative that CFD models are highly accurate. The basis of all CFD applications is an accurate representation of the geometry being analysed. Supposedly, small geometrical changes of the tyre geometry have an influence on the flow around the tyre [2]. With respect to the geometric change due to tyre deformation, a multitude of studies with FEM generated tyre deformations have demonstrated the significant impact of tyre deformations on the wheel flow [3] [4].

When validating flow phenomena with FEM generated geometries, discrepancies between experimental and simulation results may arise due to errors in either the FEM or CFD. To address this issue, a process has been established to generate tyre geometries by combining a static, high-definition structural light tyre scan with the results from a new testing bench, that has been designed and built at the Institute for Automotive Engineering University of Stuttgart (IFS). This new tyre deformation testing bench enables to physically measure tyre deformations on rotating and loaded tyres, that can later be used for CFD studies.

This study is part of a research project funded by the Forschungsvereinigung Automobiltechnik (FAT) with the goal to investigate the effects of tyre deformation on vehicle aerodynamics and validate and improve CFD accuracy regarding this area.

## 2 Prerequisites

In automotive wind tunnel testing the road and the rotation of the wheels has to be represented accurately. This can be achieved using one or multiple belts to enable wheel rotation and simulate boundary layers on the ground. In typical 5-belt systems, the vehicle is constrained by rocker panel mounts. By restricting the body motion in some or all degrees of freedom, the vehicle can either be held in a fixed or a floating mounting configuration. In the floating configuration, only the longitudinal and lateral components of the forces are restricted. In the fixed configuration, the weight force from the vehicle is transferred both trough the rocker panel mounts and the tyre. Additional aerodynamic loads from the vehicle body are mainly transferred through the rocker panels, while radial tyre expansion creates additional forces that impact the tyre position in the wheel house and the vertical load of the tyre. In the floating setup, vertical aerodynamic load results directly in vertical tyre load. Because the vehicle model is not vertically restricted in floating mode, additional forces from expanding rotating tyres result in a change in vehicle ride height and are therefore not additional vertical tyre loads.

## 3 Tyre Deformation Test Bench

Regardless of the vehicle mounting configuration during wind tunnel measurements, the overall tyre load condition on the tyre deformation test bench must match the overall tyre load condition from the wind tunnel measurement. To accurately represent the same tyre deformation in CFD as in wind tunnel testing and open road driving the tyre test bench must be a flat belt system. Additionally, the tyre pressure, track, camber, rotational speed, temperature, and tyre vertical load must be identical to generate the same tyre deformation in both the wind tunnel and the tyre test bench. Since measuring vertical tyre load in the wind tunnel is not easily accomplished, the vertical tyre load is represented as the static tyre radius $r_{stat}$, which represents the standing height of the tyre. It is measured or calculated as the z-normal distance between the wheel axis and the floor. Since measurement positions on the wheel axis with tyre camber can generate varying $r_{stat}$ values, the measurement position is defined as the intersection of the wheel hub cover and the wheel axis.

Acquiring the geometry of a rotating tyre presents a significant challenge. The high rotational speeds and non-rotationally symmetric tyre geometries make mechanical scanning methods unsuitable. Optical measurement methods are possible, but the black, shiny surface of the tyre and its fast surface velocity present challenges for these methods as well. Preliminary investigations have shown that measurement methods such as high-speed photogrammetry are not cost- or time-effective. Structured light scanning methods were unable to accurately capture the rotating tyre geometry near the flat belt. The preliminary investigations indicated that laser line profile scanners are the most suitable optical measurement method in terms of accuracy and feasibility.

### 3.1 Tyre Deformation Test Bench Layout

The IFS Handling Roadway test bench (HRW) provides an ideal foundation for the tyre deformation test bench. In its original purpose, it is used for full vehicle dynamic research under laboratory conditions [5]. It consists of four independent flat belt units and a vehicle constraint, as shown in Figure 1. Each flat belt unit is capable of reaching speeds up to 220 km/h and can be hydraulically steered up to ± 20° and vertically actuated up to ± 75 mm. [5].

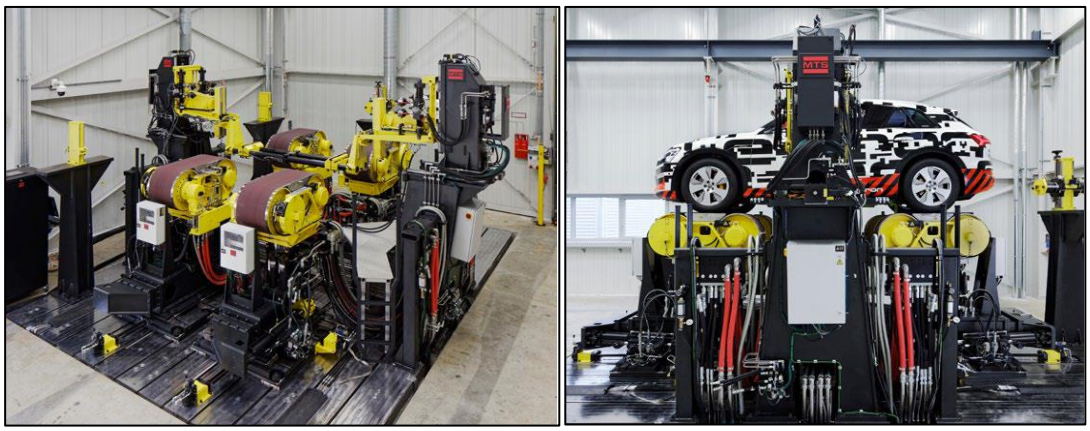

Figure 1: IFS Handling Roadway Test Bench [5]

To measure tyre deformations, the front left flat belt unit (relative to the vehicle) was augmented with a tyre measurement attachment, as shown in Figure 2. This attachment is mounted on two steel pillars. Prior to measurements, the flat belt is lowered to its minimum vertical position to facilitate tyre changes and accessibility.

Figure 2: Tyre Deformation Test Bench

During measurements, the wheel bearing remains fixed in position. A vertical tyre load is generated by hydraulically lifting the flat belt unit vertically, allowing for adjustment of the chosen static tyre radius $r_{stat}$ as in wind tunnel measurements. The tyre velocity is provided by the movement of the flat belt unit. Five optical laser profile scanners are mounted on a pivot arm. During measurements, this pivot arm is rotated ± 100° from the vertical arm position around the wheel by a stepper motor combined with a worm drive. For each pivot arm position, 100 profiles are recorded and afterwards averaged to produce a point cloud representing the average deformation of the tyre.

Both the main frame and the camber frame are constructed from 10 mm thick welded steel profiles and are connected by two radial spherical plain bearings and two manually adjustable camber actuators, as shown in Figure 3. A vertical sledge with a linear bearing is installed to enable vertical load measurements. The wheel bearing is installed in distance to the camber frame, to provide the appropriate measurement distance for laser scanner sensors. The main frame, camber frame and vertical sledge need to withstand all forces acting on the tyre.

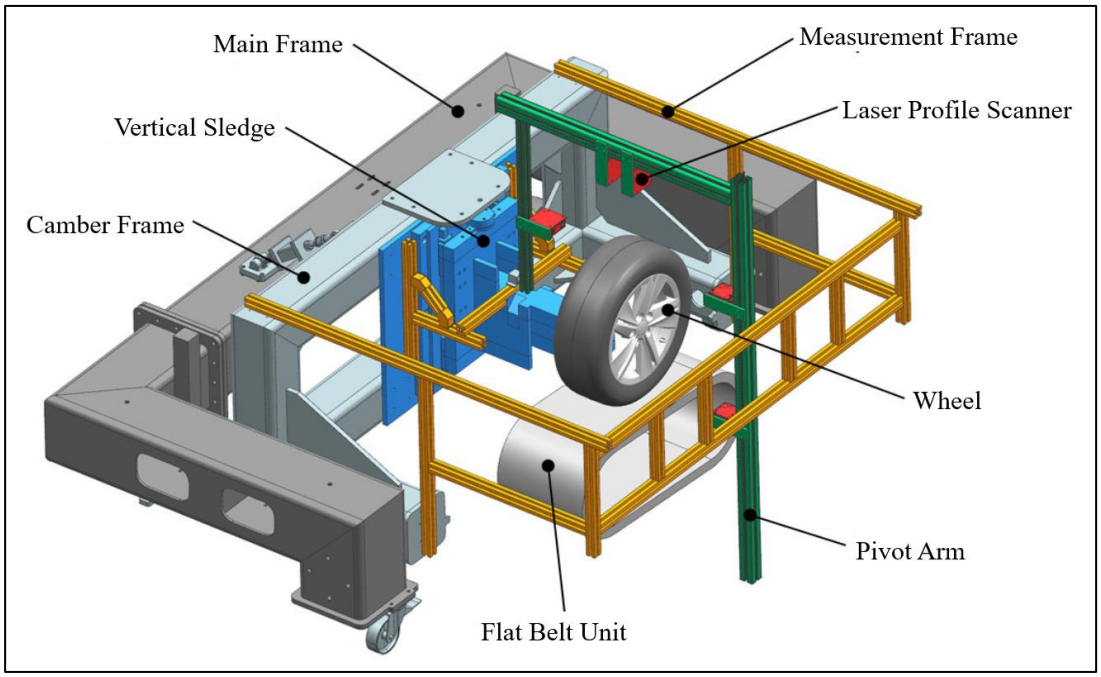


Figure 3: Tyre Deformation Attachment Layout

The measurement frame is positioned to align the wheel bearing and pivot arm bearing axis, as shown Figure 4. This layout satisfies the optimal laser scanner measurement distance for all pivot arm angle angles.

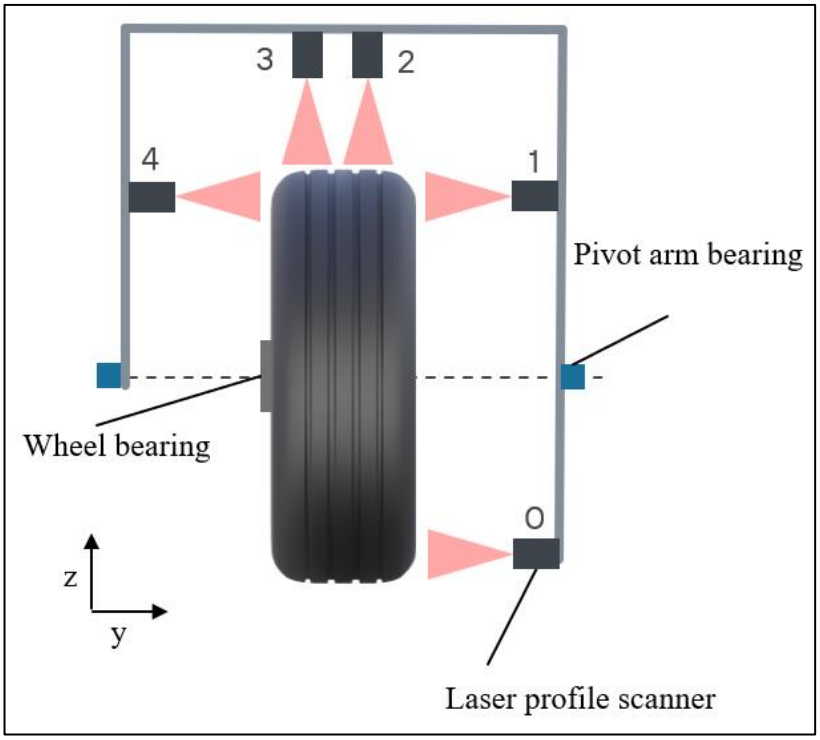


Figure 4: Sensor Layout

### 3.2 Tyre Deformation Test Bench Sensors and Data Acquisition

The software for recording measurements and controlling actuators has been implemented using LabVIEW code. Optical measurements are conducted via laser profile scanners, which operate on the principle of triangulation. Unlike distance sensors, which are equipped with a 1D line sensor to measure distances, laser profile scanners have a 2D sensor that can measure both height and distance coordinates [6]. The test bench is equipped with 5 laser scanners from micro epsilon. The sensors have a line linearity of 12 µm and are connected to the measurement computer via Ethernet port.


Figure 5: Laser Scanner: micro epsilon scanCONTROL [8]

To rotate the sensors around the wheel, a stepper motor combined with a worm drive is installed, allowing the sensors to be positioned with an accuracy better than 1°. For scanning of a rotating tyre, a 2° step was chosen for giving good results in radial direction.

The HRW flat belt unit serves both as an actuator and sensor for speed, vertical tyre load and steering angle. It can be rotated hydraulically around its vertical axis to set tyre slip angles. The vertical tyre load is adjusted by vertical positioning of the flat belt unit using a hydraulic actuator.

A laser height sensor is mounted on the vertical sledge to measure the distance to the flat belt and is used to set up the flat belt vertical position in correspondence to the predefined $r_{stat}$ values.

The vertical sledge and camber frame are connected by a load cell, allowing for the measurement of vertical tyre loads. A potentiometer is used to determine the absolute pivot arm angle and a tyre pressure monitoring system (TPMS) is used to track tyre air temperature and pressure.

### 3.3 Tyre Deformation Test Bench Measurement Procedure

Prior to a tyre deformation measurement the following parameters have to be defined: $r_{stat}$, the rotational speed and tyre pressure. Generally, adjusting one or more of these parameters results in a time relative temperature change of the tyre. This change in temperature impacts the tyre pressure. By keeping $r_{stat}$ constant, this change in temperature results in a change in tyre vertical load and tyre deformation. Therefore, a state of equilibrium tyre temperature and pressure has to be set prior to each tyre deformation measurement.

During measurements, the tyre rotates at a constant speed and under constant vertical load. The following measurement process is automatized. First, a vertical load measurement is performed, then each pivot arm angle is traversed stepwise. At each pivot arm angle, measurements are performed for each laser profile scanner. In order to get a time averaged measurement result, each laser scanner records 100 samples for every measurement.

Two approaches of tyre deformation measurements are implemented: full measuring mode and single cut mode. In full measurement mode, the pivot arm is rotated in 2° steps ± 100° relative to the vertical position. On Figure 6 right, the measurement result of this mode is shown. This setup is used to measure tyre deformation for CFD studies.

In single cut capturing mode, only the vertical position of the pivot arm is measured, allowing for fast measurement of multiple tyre deformation parameters and tyre models and determining their deformation behaviour. Its result is shown on the left in Figure 6.

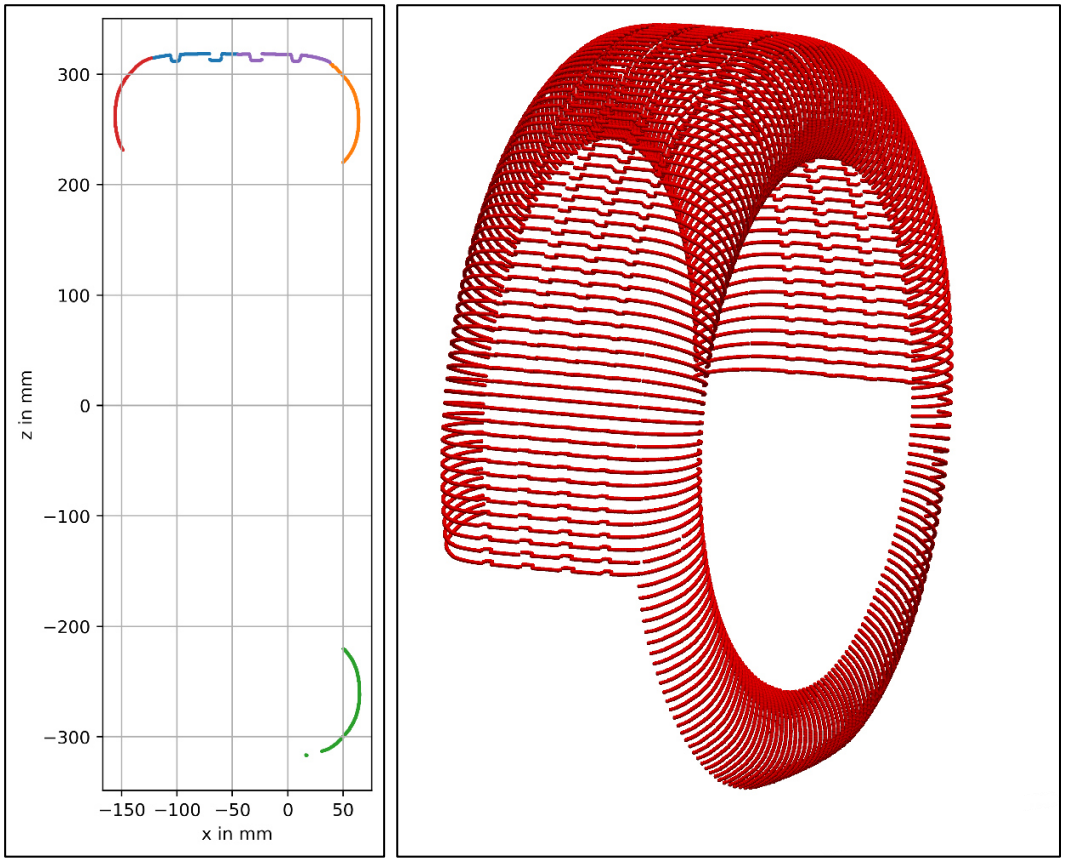


Figure 6: Left: Single Cut Deformation Capturing for rapid assessment of multiple parameters and tyres, with vertical pivot arm. Right: Full Deformation Measurement for the generation of CFD geometries with rotated pivot arm

### 3.4 Tyre Test Bench Post Processing

Post Processing is implemented using python code and is fed with the measurement raw data and a corresponding configuration file. The configuration file contains all additional data and instructions in order to average and coordinate transform the input data.

All sensor data must be coordinate transformed from the sensor coordinate system, to the wheel coordinate system using the sensor position on the pivot arm and the pivot arm angle. Then, the sensor data for each sensor is time averaged. Overlapping sensor areas must be automatically cut in a later step, and areas such as the floor and rims are deleted. The final result of the post processing routine can be seen in Figure 6 on the right and contains a point cloud of either a planar vertical section or a point cloud of the full tyre, depending on the measurement mode.

## 4 Process for Generating Tyre Geometries with Real Tyre Deformation

The process of generating tyre geometries with real tyre deformation involves combining a static tyre structural light scan with the results from the tyre deformation test bench measurement using a morphing function.

### 4.1 Static Structural Light Scanning

The structural light scan is performed on a static unloaded tyre and produces a high-resolution tessellated geometry representation of the tyre that captures fine details such as the tyre markings. Structural light scans rely on a projector and a camera positioned at a relative distance to each other, so they can only capture areas visible to both devices. Fine grooves or undercuts that cannot be captured result in holes, as illustrated by the white area in Figure 7 “Scan”. To overcome this issue, manual repairing, wrapping or reverse engineering the tyre as a cad model are options. The wrapped, reconstructed or a hybrid geometry and all defeatured versions thereof serve as a CFD geometries, as shown in Figure 7.

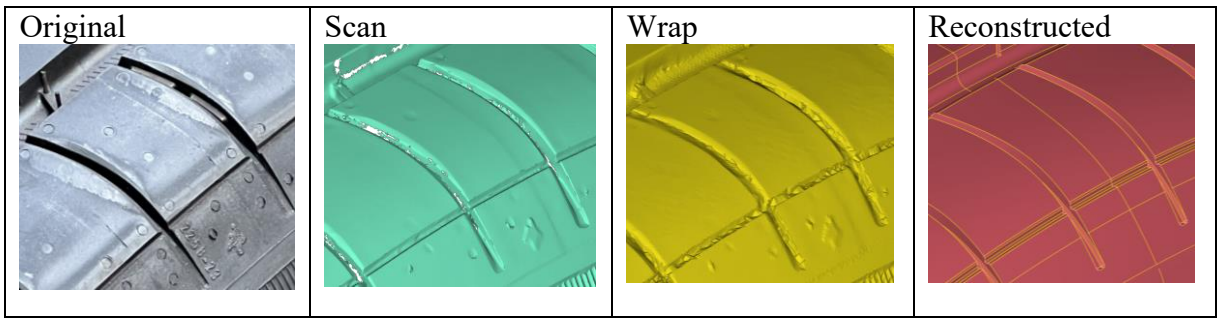


Figure 7: Static Tyre Scanning and CFD geometry generation

## 4.2 Morphing Process

The input to the morphing process is based on two inputs: The structural light scan or a defeatured version of it and a point cloud derived from the tyre deformation test bench measurement. The morphing process is implemented in ANSA. It is implemented in such a way that the same morphing function can be applied to multiple versions of the same tyre geometry regardless of its level of detail.

Prior to morphing, the input data must be pre-processed: based on the static tyre scan, a simplified slick tyre geometry is generated (as shown in Figure 8 a)) to serve as a construction basis for multiple Morphing Boxes. If not already tessellated, the undeformed tyre resulting from the tyre scan must be meshed and loaded into the morphing boxes. The point cloud derived from the deformation measurement is then reconstructed as a deformed slick tyre geometry using either manual CAD reconstruction or surface reconstruction.

By fitting the morphing boxes onto the deformed slick geometry, the loaded tyre geometry is deformed based on the deformation measurement. As a result, real deformed tyre scans or real deformed geometry derivatives of the tyre scans with a lower level of detail can be generated based on the real measured tyre deformation.

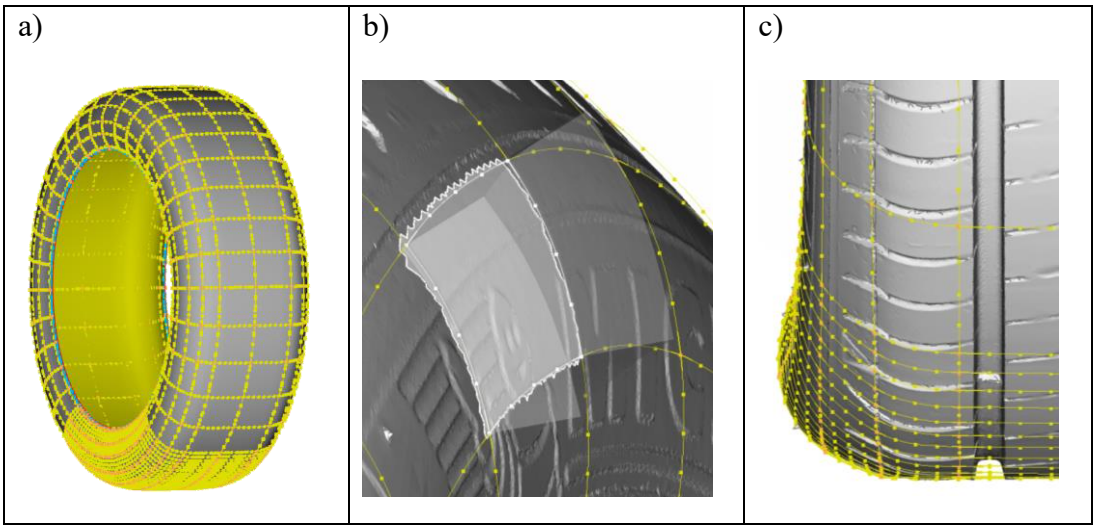


Figure 8: Tyre Morphing process. a) Fitting morphing boxes onto a slick tyre geometry b) Loading the tyre geometry into the morphing boxes c) Morphing the input tyre geometry by fitting the morphing boxes on the deformed slick tyre geometry deriving from the tyre deformation measurement

## 5 Results

A study was conducted to investigate the effects of tyre vertical load, rotational speed, and tyre pressure on tyre deformation using single cut measuring mode with the pivot arm in a vertical position. The tyre related parameters were selected based on a parallel wind tunnel campaign. The baseline configuration, from which each parameter was altered included an unloaded $r_{stat}$ value at standstill, a tyre pressure of 2.5 bar, and a rotational speed of 140 km/h. Figure 9 illustrates the differences of the tyre deformation at three positions for five tyre models:

- $\Delta z$: represents the difference in radial expansion at the top center position
- $\Delta y_{top}$: represents the difference in axial expansion at the most outward y position at the top half
- $\Delta y_{bottom}$: represents the difference in axial expansion at the most outward y position at the bottom

The Goodyear 19" tyre side wall shape features an exposed rim guard and $\Delta y_{top}$ and $\Delta y_{bottom}$ are calculated at this position.

The results indicate that an increase in rotational speed causes radial expansion and axial contraction of the tyres at both the bottom and top. Near to the flat belt, the tyre is unable to escape the flat belt. This inhibits axial contraction at the bottom compared to the top. In this study tyres with lower heights tend to exhibit lower axial contraction.

A decrease in tyre pressure results in radial contraction, with this effect being more pronounced for wider tyres. An increase in vertical load has the biggest impact on the change of shape, particularly on the tyre sidewall. Wider tyres have a larger contact area and can distribute the vertical load over a larger area, resulting in comparatively lower change in $r_{stat}$ and lower axial expansion at the contact area for the same vertical load.

When comparing the 16" and 19" tyres with equivalent tyre dimensions, it is observed that the change in shape in response to a configuration change is dependent on the specific tyre model and cannot be generalized.

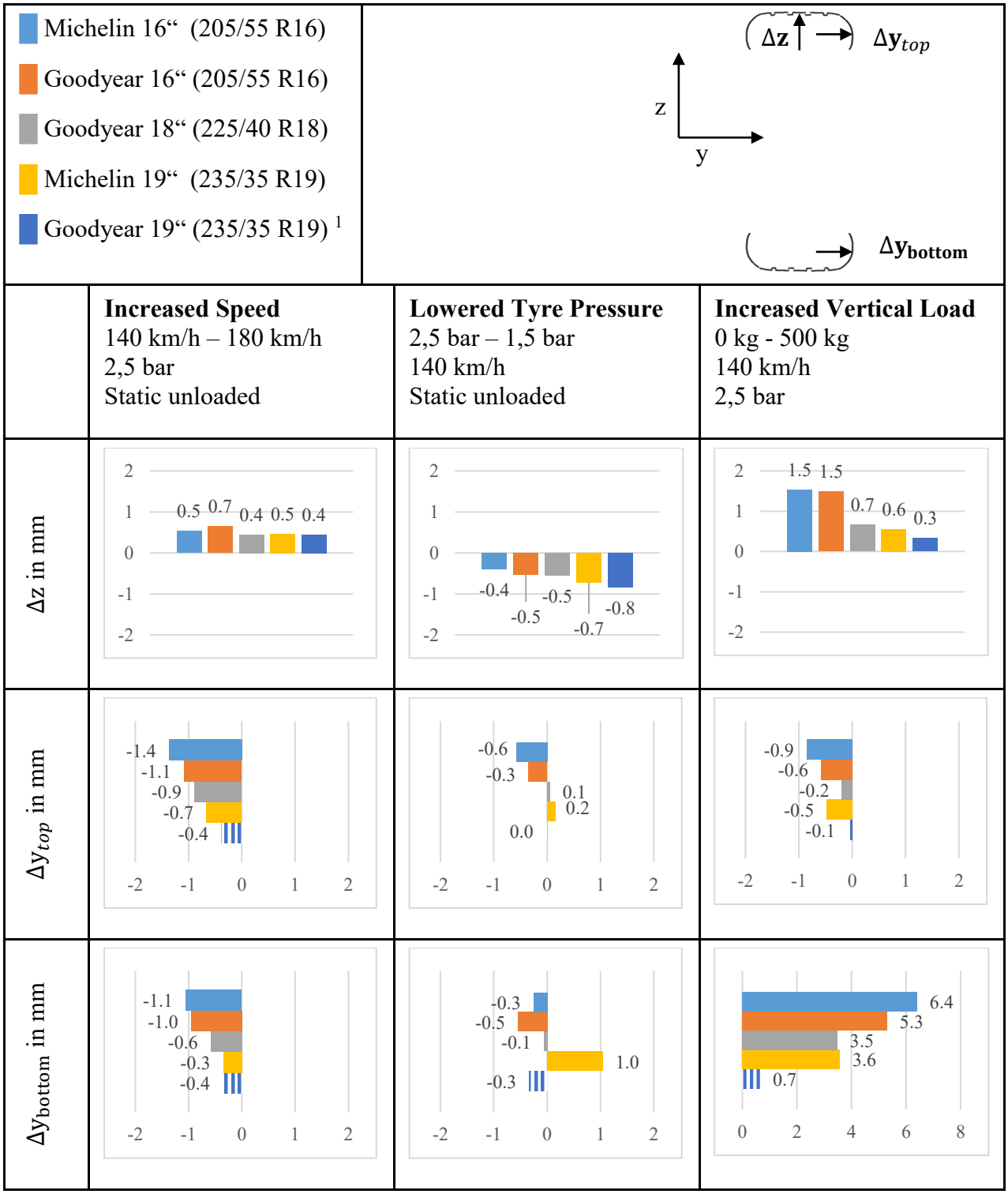


Figure 9: Parameter study results regarding tyre deformation parameters

[1] For the Goodyear 19” tyre, the widest position in y corresponds to the rim protection edge.

The combination of detailed, high-density structural light scanning and real tyre deformation provides an ideal basis for CFD studies. Figure 10 shows a comparison between experiment and geometry for a detailed tyre wrap. As previously mentioned, the process is not restricted to the wrapped tyre geometry and can be applied to all forms of tessellated tyre geometry.

a) Experiment:
Tyre not subject to load and rotation

b) Tyre geometry wrap without deformation

c) Experiment:
Tyre subject to load and rotation
(140 km/h, 2.5 bar, $\Delta r_{stat} = -20\ mm$)

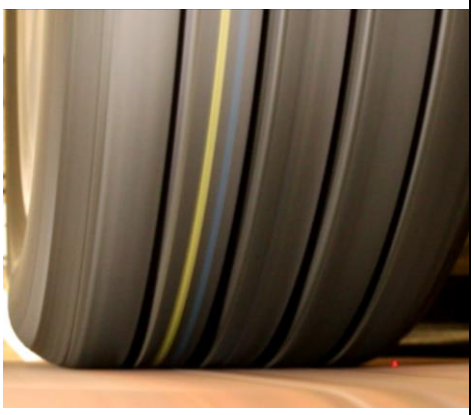

d) Tyre geometry wrap:
applied with real deformation
(140 km/h, 2.5 bar, $\Delta r_{stat} = -20\ mm$)

Figure 10: Undeformed tyre (top) and deformed tyre (bottom). Comparison between photographical image from the experiment (left) and geometry rendering (right)

## 6 Summary and Outlook

An accurate geometric representation is essential for all CFD studies, as even minor geometric changes to the tyre geometry can impact the aerodynamics of a vehicle. When driving a vehicle on the road, tyres are subject to rotation and load, resulting in changes to their shape compared to an undeformed, stationary tyre. To improve future CFD flow prediction for vehicle aerodynamics, a process has been established to generate high-quality tyre geometries that accurately reflect tyre deformation.

A tyre deformation test bench has been built, to reproduce and measure tyre deformation under conditions similar to those encountered during open road driving and wind tunnel measurements. A morphing process has been established, to combine structural light scans and tyre deformation measurements. Additionally, a parameter study was conducted to investigate the effects of vertical tyre load, tyre pressure and rotational speed on tyre deformation. Changes in tyre pressure have comparably lower effects on overall tyre shape, while rotational speed and vertical tyre load have a larger impact on the tyre deformation. The tyre deformation is dependent on both the tyre type and dimensions of the tyre.

The geometries generated using this process serve as the basis for future CFD studies. As part of this research project an extensive wind tunnel measurement campaign at the IFS Vehicle Aeroacoustics Wind Tunnel was already conducted using a DrivAer Model from Volkswagen to serve as a validation basis for this CFD study.

## 7 Bibliography


[1] Pfadenhauer, M.; Wickern, G.;Zwicker, K.: On the Influence of Wheels and Tyres on the Aerodyamic Drag of Vehicles. MIRA International Conference on Vehicle Aerodynamics, Birmingham, 1996

[2] Wittmeier, F.: Ein Beitrag zur aerodynamischen Optimierung von Pkw Reifen, Springer Vieweg Wiesbaden , 2014, https://doi.org/10.1007/978-3-658-08807-1

[3] Eder P.; Gerstorfer, T.; Lex, C.; Amhofer, T.: Tyre Deformation Modelling for High-Speed Open-Wheel Aerodynamic Investigations. In: SAE International Journal of Vehicle Dynamics Stability and NVH, 5 (2021), no. 3, article 10-05-03-0016

[4] Semeraro, F.F.; Schito, P.: Numerical Investigation of the Influence of Tyre Deformation and Vehicle Ride Height on the Aerodynamics of Passenger Cars. Online: https://www.mdpi.com/2311-5521/7/2/47#, accessed: 17. August 2023

[5] FKFS: Stuttgart Handling Roadway 3D Vehicle dynamics under laboratory conditions. https://www.fkfs.de/fileadmin/FKFS/4_Aktuelles/Pressebilder/Flyer_HRW.pdf, (accessed Aug. 30, 2023)

[6] Beyerer, J., Puente Léon, F., Frese C.: Automatische Sichtprüfung, Heidelberg 2016, https://doi.org/10.1007/978-3-662-47786-1

[7] MICRO EPSILON: Laser-Scanner für industrielle Anwendung scanCONTROL 25x0 https://www.micro-epsilon.de/download/products/cat-scancontrol/dax--scanCONTROL-25x0--de.html#page=2&zoom=Fit, (accessed Aug. 28, 2023)

[8] Blum F.: 2D/3D-Laserscanner mit roter und blauer Laserdiode von Micro-Epsilon https://www.ke-next.de/automation/sensorik-messtechnik/id-2d3d-laserscanner-mit-roter-und-blauer-laserdiode-von-micro-epsilon-306.html, (accessed Sept. 04, 2023)

# Transient thermal simulation process for cabin-electronic components

Gabor Matulik, Rakesh Dontham

SIMULIA
Dassault Systemes Deutschland GmbH
Meitnerstraße 8, 70563 Stuttgart-Vaihingen

gabor.matulik@3ds.com
rakesh.dontham@3ds.com

**Abstract:** The present work introduces a transient coupled aero-thermal simulation process focusing on the temperature of the electronic components inside the cabin of a vehicle. The simulations are carried out with the PowerFLOW Lattice-Boltzmann solver for the fluid domain coupled with the PowerTHERM finite element solver for the solid domain. The process represents a two-hour transient measurement (one-hour hot soak and one-hour cooldown). The validation is ongoing, the process was running on the Dassault Systemes' Car Bleu.

## 1 Introduction

The transportation and mobility industry is going under major changes due to the electrification. The topic of cabin-electronic components however can arise in cars with internal combustion engine as well as in electric vehicles. The number of electrical components connected for example to driver assistance, autonomous driving, and infotainment systems in passenger vehicles is growing. These systems' control units consume more and more power as they become more complex and are installed into smaller and smaller spaces inside the cabin. To determine whether adequate cooling is provided in various transient scenarios requires a streamlined simulation process.

With the PowerFLOW/PowerTHERM coupled approach, the current work presents a highly automated transient thermal simulation process for cabin-electronic components. The sample procedure deals with a measurement situation that includes two stages: first, the car is turned off, parked under the sun for an hour, then all the systems are turned on and the HVAC system is cooling down the cabin for an hour. The PowerTHERM/PowerFLOW Time Ratio and the Adaptive Coupling, two recently added elements of the PowerFLOW program, are crucial to reduce the turnaround time of the modeling process. In the case of a quasi-static flow field, the former makes it possible to calculate extended thermal transients; the latter permits the chosen adaptive scheme to automatically modify the time ratio in dependence on the rate of temperature change between thermal solutions. The flow field is in a quasi-static state aside from the first two to three seconds of the second stage, so the three steps of the introduced simulation process are as follows:

- hot-soak under the sun (1 h) - adaptive coupling
- initial flow development after starting HVAC (3 s) – high resolution transient
- transient cooldown (1 h) – adaptive coupling

## 2 Methodology

The simulation process is highly automatized from case preparation until post-processing. The base of automation is the folder structure (see Figure 1.), and a naming convention of the parts, which enables an organized workflow. The user is required to place the surface mesh files, the boundary condition data for the HVAC, the csv file with measurement probe locations and the PowerTHERM model into the corresponding folders. It is possible to introduce new parts (for example a mobile phone) between Soak and Flow Development phases, hence the different Mesh folders for them. A Shell script governs the three steps of the process, and the communication with the PowerCASE API is done in Python. Reducing the user interaction was a high priority goal during the development of this process. We achieved the automatic importing of mesh files, probe locations, PowerTHERM Model and Boundary conditions. When the naming convention requirements are met, then the template of the PowerCASE sets the parameters automatically. The Initial coupling between PowerFLOW parts and PowerTHERM parts are set on name-to-name basis, user interaction is needed, when special coupling settings are required.

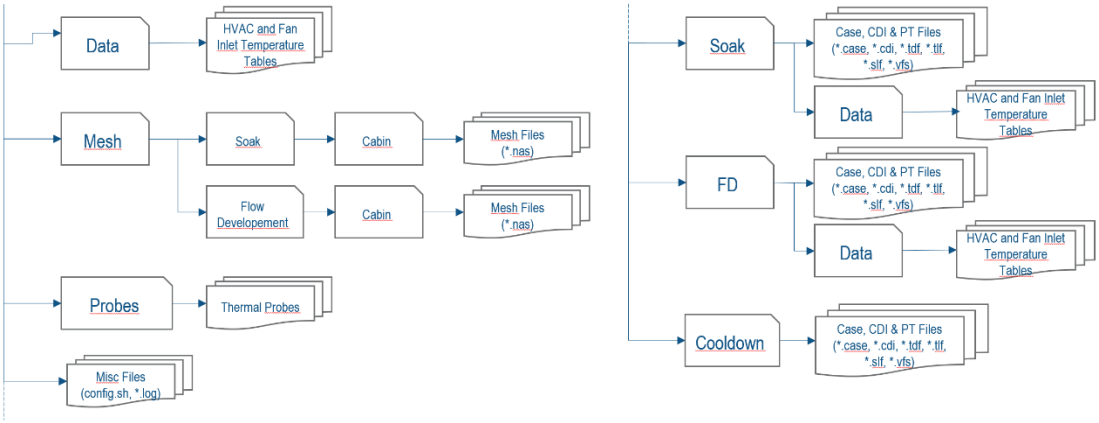


Figure 1: Folder structure of the process

## 2.1 Hot-Soak

In this simulation step the vehicle is standing under the sun for (at least) one hour. Goal of this step is to calculate the surface temperatures of the parts, and to get the thermal layering effect of the air inside the cabin. We represent the sun with a Solar Lamp in PowerTHERM. For its setup we use pyranometer(s). With this approach we can mimic the solar lamp parameters of a thermal wind tunnel measurement, in case the customer has such data. On the outer surfaces of the cabin we assume natural convection with $T_{env}$=45°C and h=5W/(m$^2$K). In this phase natural convection develops inside the cabin, the velocities are very low, the heat transfer coefficient is around 2-5 W/(m$^2$K). After 1-2 minutes the flow field reaches a quasi-static state, so in order to allow its development the starting PowerTHERM/PowerFLOW time ratio is set to 1. In order to reduce the simulation time, the PowerTHERM/PowerFLOW time ratio will be gradually increased with the help of adaptive coupling, when the temperature gradients are below a certain limit.

## 2.2 Flow Development - Cooldown

In the second simulation step the HVAC system and the board electronics are starting. This phase aims to calculate the transient flow field until it reaches a quasi-static state. This takes 2-3 seconds depending on the size of the cabin. Since the flow field is highly transient, the PowerTHERM/PowerFLOW time ratio is fixed to 1. The method uses velocity inlet boundary conditions with transient temperature field for the HVAC inlets. Some electronic components have active cooling via fans. In order to save on the computational effort, those fans are represented by Inlet-Outlet boundary condition pairs, where the average temperature of the outlet face is applied onto the inlet face. Heat generation of electronic devices is modelled on chip level in PowerTHERM. Starting from this phase until the end of cooldown we assume a 15 km/h head wind for the car (this comes as a customer request, the parameter is flexible). A standard external aerodynamic simulation provides the heat transfer coefficient data to be mapped on the cabin's outer surfaces.

In the third simulation step the flow field is already quasi-static, the PowerFLOW/PowerTHERM time ratio starts from 40, and with adaptive coupling it can gradually reach maximum of 180. The rest of the settings are same or very similar to the flow development phase.

## 2.3 Meshing strategy

The PowerFLOW surface mesh is triangle based, we recommend to follow the Best Practices Guideline: using tesselation for flow-critical components (Coarse – Very fine; Surface Tolerance: 0.5 mm – 0.01 mm; Normal Vector Tolerance: 30° - 20°) and using wrap for non-flow-critical components (mesh size between 5 mm – 25 mm).

The volume mesh is built up from voxels (hexahedrons), created automatically by the discretizer. The refinement region's parameters are set in PowerCASE. The soak simulation uses the coarsest mesh in the process, the minimum voxel size is 13 mm. In order to avoid excessive surface mesh count in a voxel, it is recommended to coarsen the very fine mesh parts. That is another reason why the folder structure offers different Mesh folders for Soak and Flow Development. Due to its highly transient nature, the Flow Development phase has the finest mesh, the minimum voxel size is 0.25 mm or 0.5 mm, depending on the required minimum gap size (1.25 mm and 2.5 mm respectively) to be resolved. In order to reach a reasonable runtime for the long transient, the cooldown phase is one level coarser then the Flow Development, i.e: 0.5 mm or 1 mm minimum voxel size.

PowerTHERM allows hybrid meshes, consisting of shell and solid parts. A balanced approach is to use triangle surface and tetrahedron solid elements on the important electronic components, and mixed quad+tria surface elements on the rest of the geometry.

## 3 Bleu car - cabin simulations

The Dassault Systemes' Bleu car is a car model, on which we can display our processes. Albeit in a simplified manner, but the cabin of the Bleu car contains everything, which usually occurs in a customer case (e.g. monitor on the middle console, electronics with and without cooling fan, HVAC system, etc.). Figure 2. shows the cabin of car Bleu from the outside, and Figure 3. from the inside.

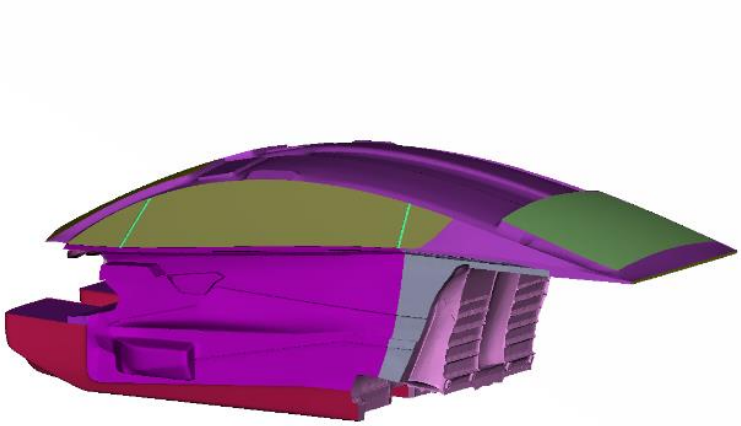

Figure 2: Bleu Car cabin outside

Figure 3: Bleu Car cabin inside

On Figure 4. we can see the surface temperature-, and on Figure 5. the air temperature distribution after one hour of soak. The hottest faces are the ones which are parallel to the solar lamp (below the windshield), hence higher solar irradiation. The thermal layering effect is clearly visible on the air temperatures. Altough one hour seems a very long time, it is not enough time to reach saturation temperature for all the parts. The dashboard probe is almost there, but the probe on the middle console monitor shows a positive temperature gradient by the end of the simulation (Figure 6. and Figure 7. respectively). This is the reason why we need to run a transient simulation for this phase, and cannot have a cheap steady-state solution.

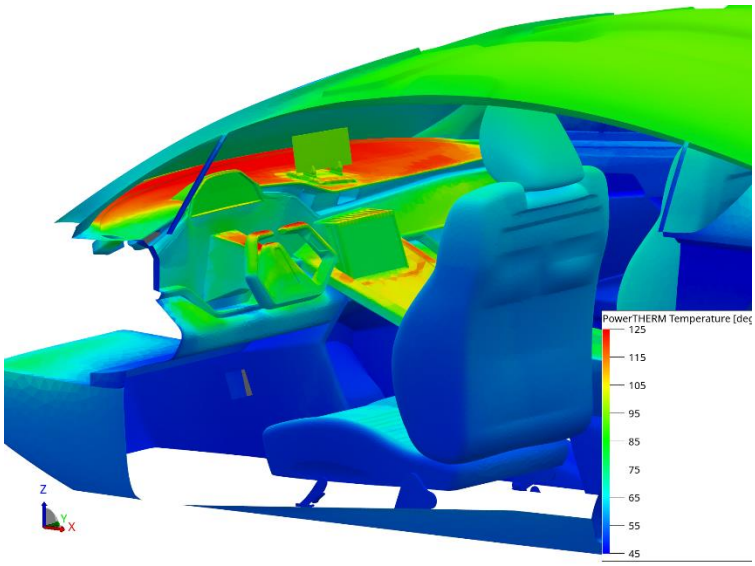


Figure 4: Surface temperature distribution after the soak

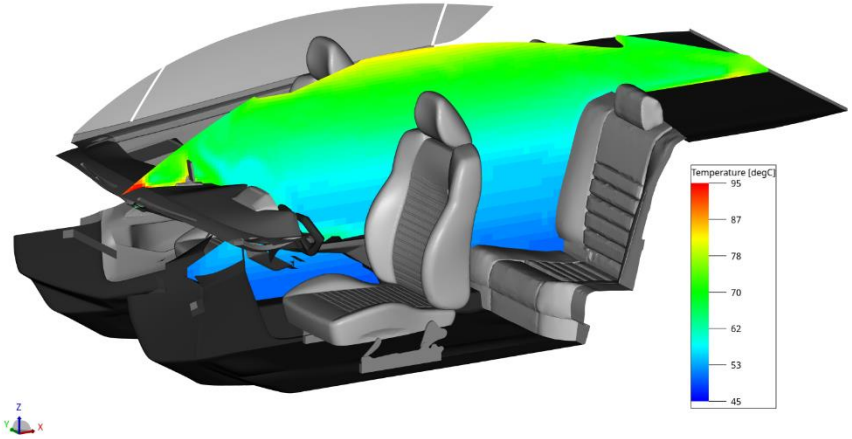


Figure 5: Air temperature distribution after the soak

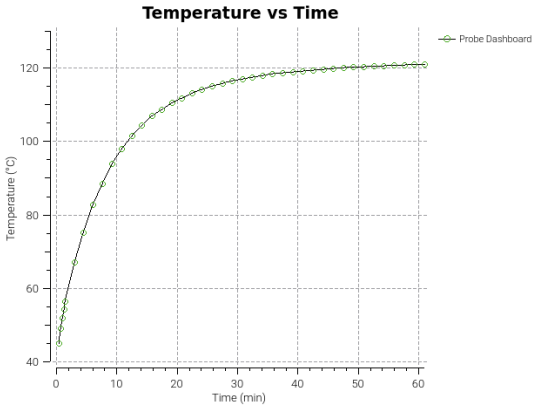


Figure 6: Probe temperature on dashboard

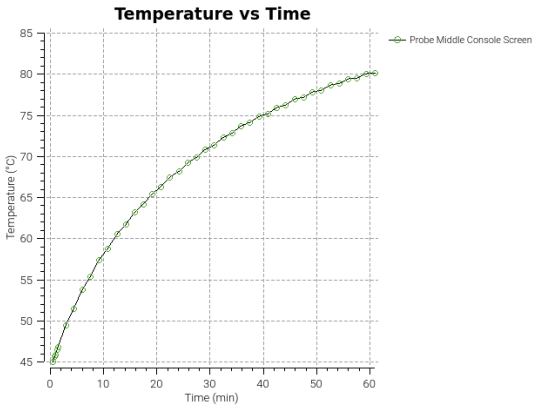


Figure 7: Probe temperature on middle console display

Figure 8. and Figure 9. shows the quasi-static velocity field in the cooldown simulation in a vertical and in a horizontal plane respectively. On Figure 10. we see the surface temperature distribution at the beginning and at the end of the cooldown phase.

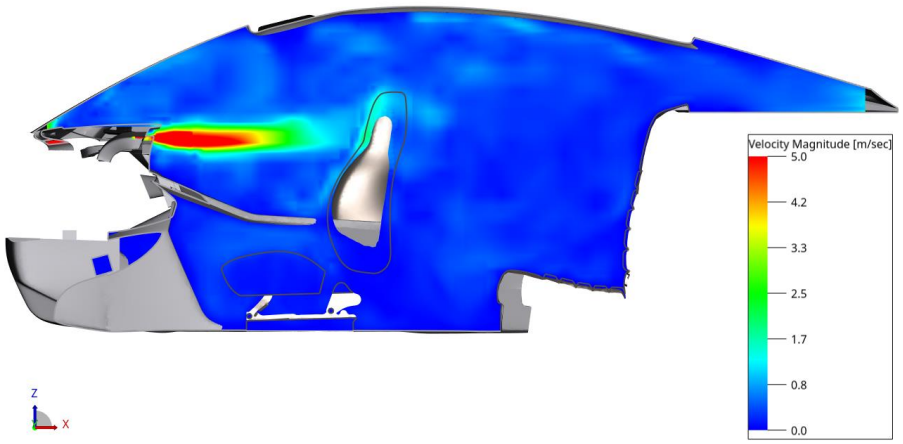


Figure 8: Velocity distribution in a vertical plane (cooldown phase)

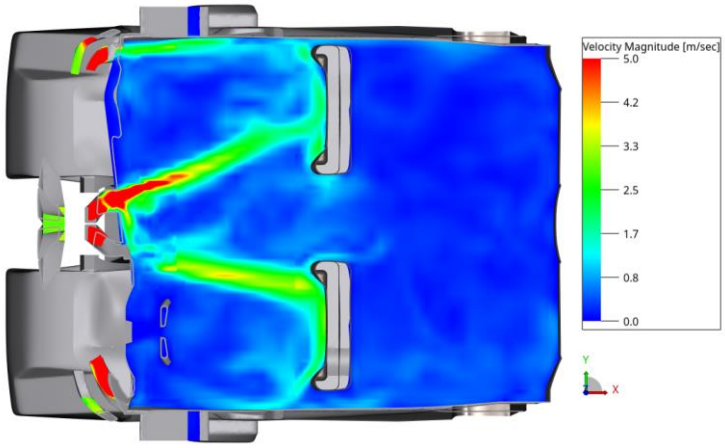


Figure 9: Velocity distribution in a horizontal plane (cooldown phase)

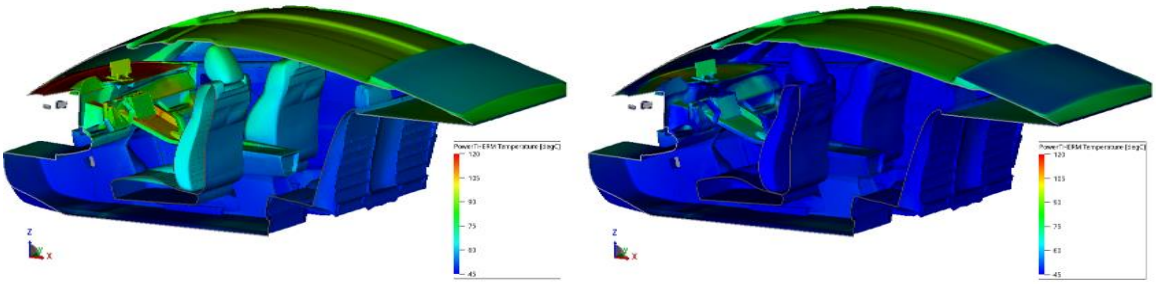

Figure 10: Surface temperature distribution in the beginning (left) and in the end (right) of the cooldown phase

## 4 Summary and future points

We have introduced an automated transient thermal simulation process, which aims for calculating the temperature of cabin electronic components. The process is not yet validated, this task will be carried out, when we can get access to detailed customer measurement data. Nevertheless, the expected physical phenomena are appearing in the simulation results, and other SIMULIA PowerFLOW/PowerTHERM coupled transient simulation processes are showing good agreement with the measurements.

A possible improvement of the methodology is to replace the inlet-outlet boundary condition pairs in electronic cooling fan models. With a small calculation expense, the use of transient boundary seeding would allow the flow field around those fans to be much closer to the real one.

# Empowering Engineering Organizations with Deep Learning: Applications to a faster transition towards electrification for Automotive OEMs and Suppliers - Heat Exchanger optimization

Pierre Baqué, Kosmas Kritikos, Thomas Von Tschammer

Neural Concept, Switzerland

pierre.baque@neuralconcept.com
kosmas.kritikos@neuralconcept.com
thomas.vontschammer@neuralconcept.com

## 1. Frontloading simulation with Deep Learning

In the evolving landscape of engineering, there's a growing need for enhanced capabilities, especially in optimizing the use of computational resources.

Traditional simulation tools, owing to their historical development, may sometimes face challenges in rapidly changing design and production environments. However, these tools have been instrumental in providing foundational insights for design teams.Integrating Deep Learning technologies can offer a way to seamlessly combine the strengths of simulation and design optimization tools, facilitating a more collaborative approach between design engineers and simulation experts.

While traditional design tools have been pivotal in shaping engineering solutions, there's room for further innovation. These tools have often been employed to select optimal configurations based on predefined parameters or to make incremental adjustments to existing designs. The future of engineering design could benefit from a more expansive, computer-driven exploration approach. In this context, Deep Learning can play a complementary role, enhancing the capabilities of traditional simulations and broadening the horizons of design possibilities.

In this talk, we explain how recent algorithms based on Geometric Deep Learning, allow shortcutting any simulation chain through a predictive model that outputs post processed simulation results and optimization suggestions, right from the CAD design. These models are being used in engineering companies to simplify processes and to emulate the expertise of simulation engineers in the hands of product or design engineers early in the development process. Thus, the number of iterations between teams are reduced while accelerating the design activities.

These new capabilities are being adopted by a growing number of leading players, especially in the Automotive industry, who have achieved:

- 2x reduction of lead time to deliver new vehicle or parts programs
- Product performance improvement resulting in 50% more successes in tender processes.

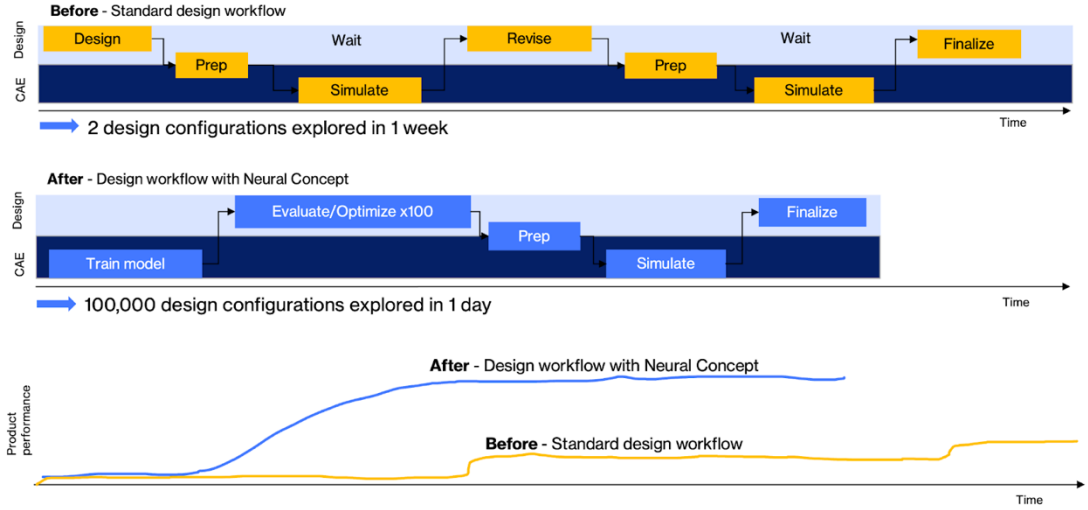


Figure 1: design workflows comparison

## 2. Geometric Convolutional Neural Networks

With traditional approaches, the models are trained on a specific parametric representation of the design space. Thus, any modification in the design space or in the boundary conditions will require generating a new dataset of simulations and training an independent model. In many industries, including automotive and aerospace sectors, each project involves many changes in the description of the parametric space or in the external conditions. Moreover, most engineering teams work on improving or redesigning variants of the same class of devices. Either way, the necessity to generate a completely new dataset at each iteration, without being able to leverage simulations collected during previous iterations, is underwhelming for the engineer.

At the same time, Geometric Convolutional Neural Networks can be used to build surrogate models of numerical solvers, like other learning-based methods, while also being agnostic to the shape parameters as it directly processes the mesh representation of the design. Hence, a single predictor can be trained with a large amount of data and can be used for numerous optimization tasks and the engineer does not have to choose and stick to a specific parametrization from the beginning to the end of experiments. Furthermore, it can leverage on transfer learning abilities of Deep models to blend simulations from multiple sources and with multiple fidelities.

Geometric Neural Networks can also provide more decisive accuracy gains by learning based on multiple data outputs and using the correlations between quantities to obtain the best result. Secondly, the convolutions used in Geometric Neural Networks are particularly suited to the accurate prediction of complex local field quantities, such as deformation, temperature, or pressure. Moreover, using the physical space as a reference for learning makes it possible to exploit any raw, unprocessed data source for training a model. Therefore, one can exploit an existing database of simulations or reuse data across design iterations, across projects or across multiple teams. This is a key enabler to improve performance of approximation models, while generating an order of magnitude fewer simulations in the long term. This new approach is breaking silos between projects to allow a unified model to be built and used once and for all.

Therefore, new methods are creating a conceptual merge and closing the gap between Kriging-type of techniques and Adjoint-based methods - or topology optimization - on the other hand.

With traditional approaches, the models are trained on a specific parametric representation of the design space. Thus, any modification in the design space or in the boundary conditions will require generating a new dataset of simulations and training an independent model. In many industries, including automotive and aerospace sectors, each project involves many changes in the description of the parametric space or in the external conditions. Moreover, most engineering teams work on improving or redesigning variants of the same class of devices. Either way, the necessity to generate a completely new dataset at each iteration, without being able to leverage simulations collected during previous iterations, is underwhelming for the engineer.

At the same time, Geometric Convolutional Neural Networks can be used to build surrogate models of numerical solvers, like other learning-based methods, while also being agnostic to the shape parameters as it directly processes the mesh representation of the design. Hence, a single predictor can be trained with a large amount of data and can be used for numerous optimization tasks and the engineer does not have to choose and stick to a specific parametrization from the beginning to the end of experiments. Furthermore, it can leverage on transfer learning abilities of Deep models to blend simulations from multiple sources and with multiple fidelities.

Geometric Neural Networks can also provide more decisive accuracy gains by learning based on multiple data outputs and using the correlations between quantities to obtain the best result. Secondly, the convolutions used in Geometric Neural Networks are particularly suited to the accurate prediction of complex local field quantities, such as deformation, temperature, or pressure. Moreover, using the physical space as a reference for learning makes it possible to exploit any raw, unprocessed data source for training a model. Therefore, one can exploit an existing database of simulations or reuse data across design iterations, across projects or across multiple teams. This is a key enabler to improve performance of approximation models, while generating an order of magnitude fewer simulations in the long term. This new approach is breaking silos between projects to allow a unified model to be built and used once and for all.

Therefore, new methods are creating a conceptual merge and closing the gap between Kriging-type of techniques and Adjoint-based methods - or topology optimization - on the other hand.

## 3. Deployment on HPC systems

Practical solutions are already available for teams who want to access such tools. For instance, Neural Concept Shape (NCS) is a software platform that allows engineers, at all levels of expertise, to implement the latest Deep Learning based engineering practices into their development processes. Using Neural Networks, simulation engineers and the design engineers can collaborate more efficiently and save costly iterations between teams.

Since NCS exploits directly the results of traditional simulations, the integration of HPC clusters with Kubernetes distributed training on multiple GPUs and the efficient exchange of large volumes of data is a force-multiplier for AI. Therefore, NCS has been built to leverage the flexibility and power of cloud HPC services (such as Microsoft Azure) that provide seamless integration with large volumes of simulation results, access to heterogeneous computing platforms and the ability to deploy trained models in a secure environment for remote engineering and design teams working in different locations. In short, the association of GCNNs with cloud-based HPC is breaking a new barrier in terms of possibilities, performance and convenience for deploying AI-based design optimization at large organizations and provides significant reduction of design times thanks to high performance in simulation, training and inference.

## 4. Heat exchanger application case

To illustrate the practical capabilities of Deep Learning, we use an example in Heat Exchanger design optimization. Heat Exchanger design and optimization is a critical topic with the electrification of vehicles, and more specifically for battery cooling applications, but also for other electronic components inside the vehicle. It is a major driver in the vehicle efficiency and its durability. Hence, a well established and efficient design process is a key competitive advantage within the automotive industry.

Heat Exchanger design is a complex task: the engineer has to make a lot of important design decisions to select the right concept (fins/pins heat exchanger, plate with dimples, channel structure…). Most of these decisions are based on best practices and rely on the experience of the team in charge of the development of the product. Moreover, within a single heat exchanger concept, the design freedom is significant, and small design changes could lead to drastic performance variations. Most of the time, the engineers and design teams can only afford to explore a few variations from a given concept, due to the complexity of the CAD/CFD workflow.

We conducted a study using Heat Exchanger internal CFD simulations, where we show how the AI model can be used to run a non-parametric optimization, leading to drastic performance improvements compared to a standard parametric study. Moreover, the predictive model can be made accessible to the design team through a simplified graphical interface. Ultimately, this leads to shorter lead times, especially critical for the RFQ phase in the automotive industry, together with better product performances.

In this application, we used the generative design capabilities of NCS models (NC Design Module) to create an initial, non-parametric dataset, used to train the predictive model. An integration with Ansys Fluent is then available, allowing to automatically simulate the created designs. Over a couple of days, a dataset of 100 geometries and corresponding simulations was created.

Leveraging this dataset, a predictive model was trained. The predictive model has proven to be highly accurate, capturing complex flow phenomenon such as recirculation, across different topologies.

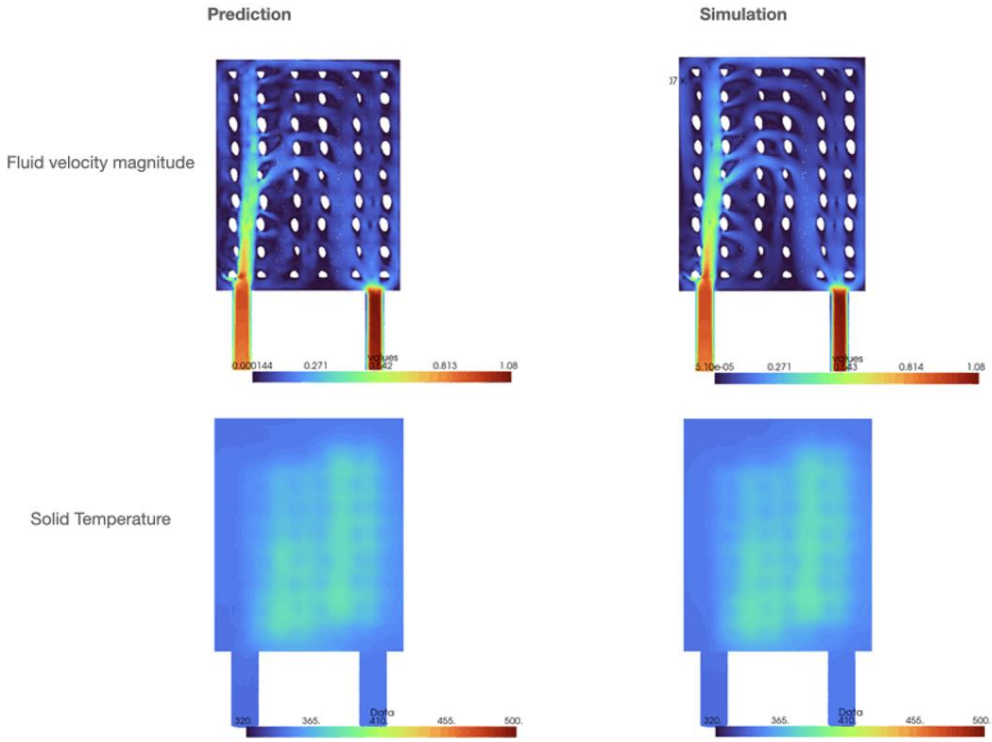


Figure 2: Comparison between a NCS model prediction (left), and the corresponding Ansys Fluent CFD simulation (right)

Once the predictive model was validated, it allowed to run a large optimization campaign, leveraging both the NC Design module for geometry generation, and the predictive model. With the goal to minimize pressure drop and maximum temperature, the optimization loop allows to explore hundreds of innovative designs very rapidly, ultimately converging to designs outperforming the original baseline. Validation through CFD simulation showed a 20% improvement of pressure drop at constant max temperature and manufacturing costs. These results largely outperform any parametric optimization, which could be started from a given heat exchanger topology.

As a summary, this end-to-end workflow shows how we can leverage Geometric Deep Learning based predictive models, coupled with the corresponding design generation capabilities, even without any historical data. The non-parametric nature of this optimization workflow allows the exploration of innovative design and concepts, across topologies, removing some key limitations of standard CAD/CAE based workflows.

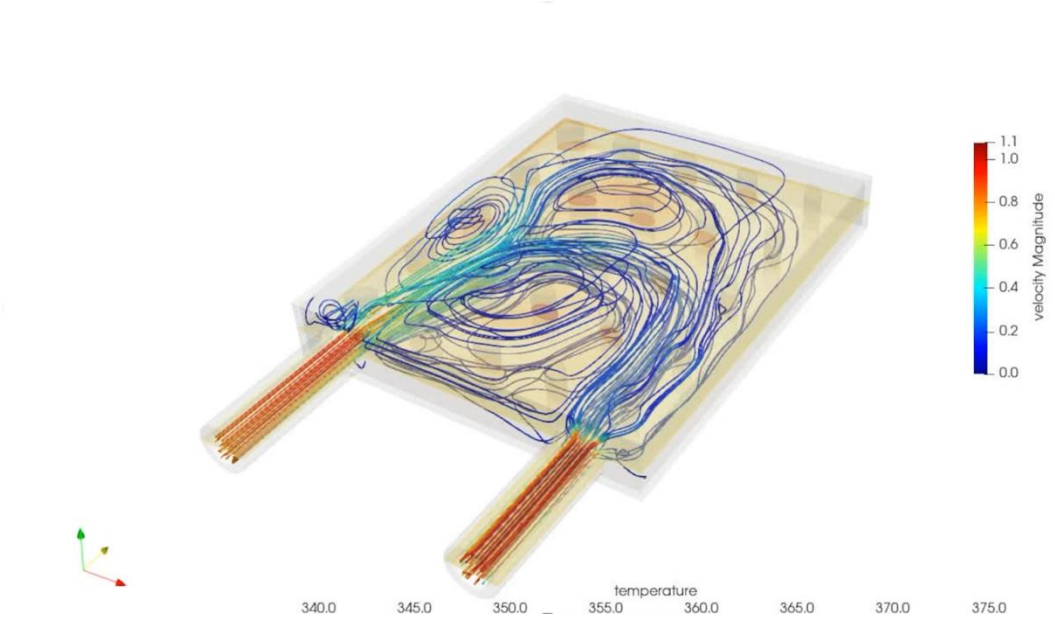


Figure 3: Example of a design explored during the optimization process, with the corresponding performance prediction from the AI model

# Upgrade on CAERI Automotive Full-Scale Aero-acoustic Wind Tunnel Intoduction

*ZHU Xijia*[1], *QIAO xin*[1], *XU lei*[1], *WANG Qingyang*[1*], *Feng Jinyang*[1], *HUANG tao*[1], *PENG chao*[1], *YANG hong*[2], *LAN peng*[3]

(1. Wind Tunnel Center, China Automotive Engineering Research Institute Co., Ltd. Chongqing 401122, China;

2. Data Information Center, China Automotive Engineering Research Institute Co., Ltd. Chongqing 401122, China;

3. Industrial Internet Department, Chongqing CAERI Robot Technology Co., Ltd. Chongqing 401122, China)

Email: wangqingyang@caeri.com.cn

**Abstract:** Automotive full-scale aero-acoustic wind tunnel is a crucial piece of equipment for the vehicle aerodynamics development. In this paper, CAERI wind tunnel upgrades, such as database and intelligent prediction, digital wind tunnel (DWT) and life time smart health management platform, are introduced. 1. Based on extensive data and industry expert experience, the CAERI wind tunnel platform has been developed, which is the leading one in China, with the largest amount of wind tunnel tests. It provides data viewing, comparison, and analysis. Neural network and artificial intelligence are used to deeply analyze the massive data, and the intelligent prediction model of the aerodynamic drag coefficient of a vehicle model is achieved with high accuracy and correlation. 2. Based on the geometric characteristics and flow parameters, the DWT highly reproduces the test environment of CAERI Aero-Acoustic Wind Tunnel, by which the accuracy of CFD simulation is significantly improved and contributes to the shorteness of the development phase durance for a vehicel model. 3. Based on the Internet of Things (IOT) technology, the smart wind tunnel system of the CAERI wind tunnel has been built with six management systems, which can effectively improve operating efficiency and reduce equipment maintenance duration and cost, enables CAERI wind tunnel to achieve operation management refinement, equipment information digitization, and health monitoring intellectualization.

**Key words:** aerodynamics； automotive wind tunnel; database; drag coefficient prediction; digital wind tunnel; internet of things; health management

## 1 Introduction

The Chinese government officially set strategic goals in 2020, aiming to achieve "carbon peak" by 2030 and "carbon neutrality" by 2060. These objectives are intended to enhance the global competitiveness of industries and the economy while continuously promoting adjustments in industrial and energy structures. Among these goals, energy efficiency and emission reduction in the automotive sector are crucial components of China's "dual carbon" strategy and vital measures for advancing national economic development and rejuvenation.

Aerodynamics play a significant role in achieving energy efficiency and emission reduction in automobiles, and the pursuit of low aerodynamic drag designs has become an industry trend. In the 20th CPC national congress report released in 2022, China introduced the strategic goal of "Digital China," elevating digital transformation to a national strategy from an economic perspective. Currently, most automotive performance development relies on physical equipment for testing and validation. Therefore, promoting the digital transformation of automotive development is a critical step in reducing development costs and improving development efficiency.

The development of digital economy has been defined as a crucial thematic during the 14th Five-Year Plan Period of China, and the car R&D and manufacture industry has been applying digital tools to increase the efficiency, especially for the new-energy car manufacturers. As a result of the fierce competition of the new-energy car industry, the development period of new model has been compressed to 2 years, and will still be compressing in the future, so the digital tools who can help to increase the quality and efficiency of the R&D phase of a vehicle model are favoured by the OEMs.

The CAERI Wind Tunnel Center has been in commercial operation for over 3 years since 2019. Based on the experience accumulated during the operational process and in response to the national "Dual Carbon" and the "Digital China" strategy, aimed to better support the high-quality development of the new energy vehicle industry, the CAERI Wind Tunnel Center has leveraged its proprietary wind tunnel hardware resources and accumulated experience in vehicle development to create a series of digital products. Chapter 2 introduces the wind tunnel database and the rapid prediction tool of the aerodynamic drag, the digital wind tunnel is introduced in chapter3, and chapter 4 introduces the smart wind tunnel system.

## 2 Database and Intelligent prediction model of the aerodynamic drag

To guide OEMs in formulating more reasonable and efficient vehicle aerodynamic and wind noise development targets and plans, leveraging the extensive full-scale wind tunnel test data from CAERI Wind Tunnel Center, we have established a wind tunnel database system. The main components of this system are as follows:

1. Summarizing wind tunnel test big data along dimensions such as vehicle classification, powertrain type, market launch date, price range, test status, and key macro-level design parameters of the vehicles.
2. Building a comprehensive wind tunnel database system based on the data compiled in step 1, which encompasses multiple dimensions for classification, reference, comparison, and evaluation.
3. Developing sound security strategies and measures to ensure data security during the construction, transmission, and utilization phases. Incorporating a real-time update mechanism into the database to maintain its timeliness.

## 2.1 Database

The database is divided into 3 components: the Intelligent Query of which can search and autosuggest target vehicle model and exam its aerodynamic and aero-acoustic performance parameters, the Pressure Measurement results of which can study the pressure distribution around the target vehicle model, and the Wind Noise Test results of which can compare and study the wind noise performance for different target vehicle models in aspect of SPL, AI, Loudness and Sharpness. The interface of the functions above is shown in figure 1.

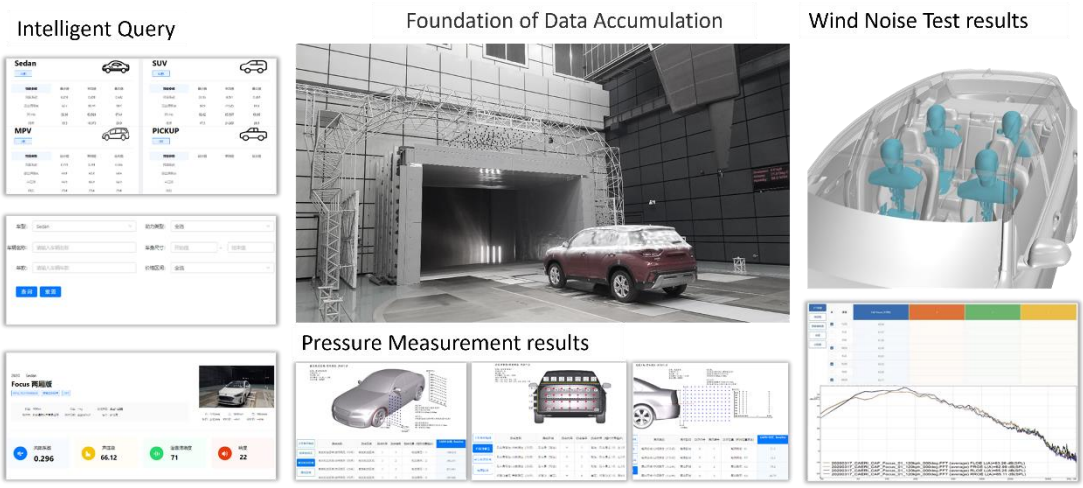


Figure 1: The interface of the database

## 2.2 Intelligent prediction model of the aerodynamic drag

By integrating aerodynamic performance test data and long-term accumulation of aerodynamic performance optimization design experience, we establish an intelligent predictive model for aerodynamic drag coefficients. This model enables us to set development goals at the project conceptual design stage, propose reasonable requirements for macro design, and provide quantitative support for rapidly assessing the impact of design changes on aerodynamic drag performance.

The ensemble machine learning algorithm Random Forest is used to train the intelligent predictive model, based on 24 macro design inputs and related wind tunnel test results for more than 80 production cars, the model can predict the aerodynamic drag coefficient for a certain vehicle model with prediction error less than 6%, compared to CAERI Wind Tunnel Center test results. The logic of the intelligent predictive model is shown in figure 2.

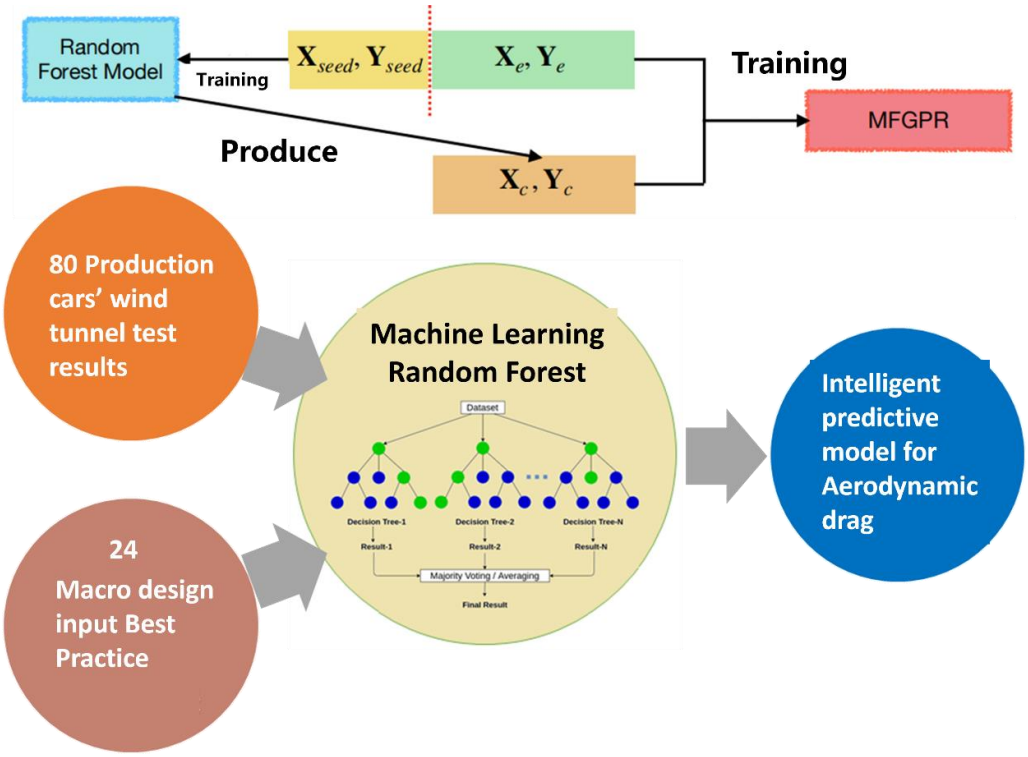


Figure 2: The logic of the Intelligent prediction model

## 3 Digital wind tunnel

Based on the geometric dimensions and physical conditions of the physical wind tunnel, with the flow field calibration in the empty wind tunnel as the basis and the flow field calibration around the vehicle as the core, the aerodynamic and flow field coupling calibration of the standard vehicle model was carried out, taking into account the influence of the moving belt of the physical wind tunnel balance, and combined with the wheel aerodynamic optimization plan, a set of automotive aerodynamics simulation calibration and correction method was proposed, and a digital wind tunnel software tool was finally developed.

### 3.1 Boundaries of computational domain

A calculation domain with the same size as the CAERI full-scale wind tunnel was established and used for digital wind tunnel simulation. The DWT geometry includes nozzle contraction, nozzle, plenum room, collector, diffuser and the first corner behind the collector (see Figure 3a).

Moreover, in order to be consistent with the test scenario, pivotal boundary layer suction system and balance five-belt system with the same positions and operating parameters as the wind tunnel are considered (Figure 3b).

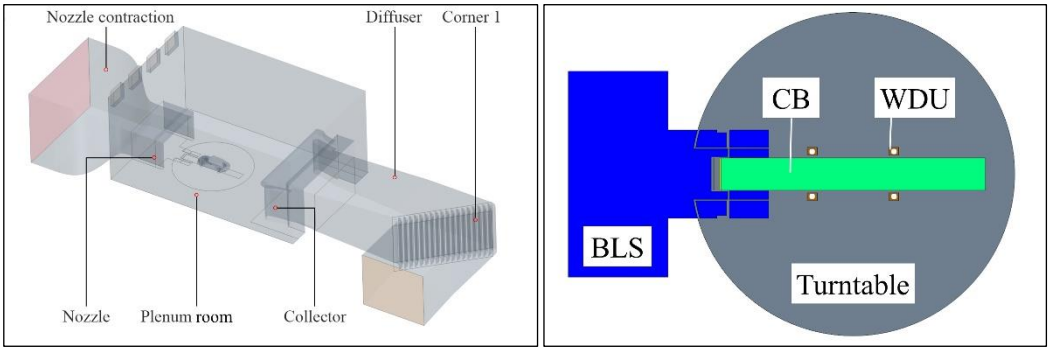


a b

Figure 3: The geometry of the digital wind tunnel (a); Boundary layer suction system and balance five-belt system of the digital wind tunnel (b)

### 3.2 Calibration results

Boundary layer thickness and longitudinal static pressure gradient are selected as the key indexes for empty wind tunnel flow field calibration. After fully considering the simulation of key wind tunnel wall systems and their operation parameters, such as the suction system, driving belt system and pressure balance system, the error of the boundary layer thickness between digital wind tunnel simulation results and the wind tunnel test results is less than 3%. For the longitudinal static pressure gradient, the maximum local error between the simulation results and the test results is less than 0.001dcp/dx. As shown in Figure 4a and Figure 4b.

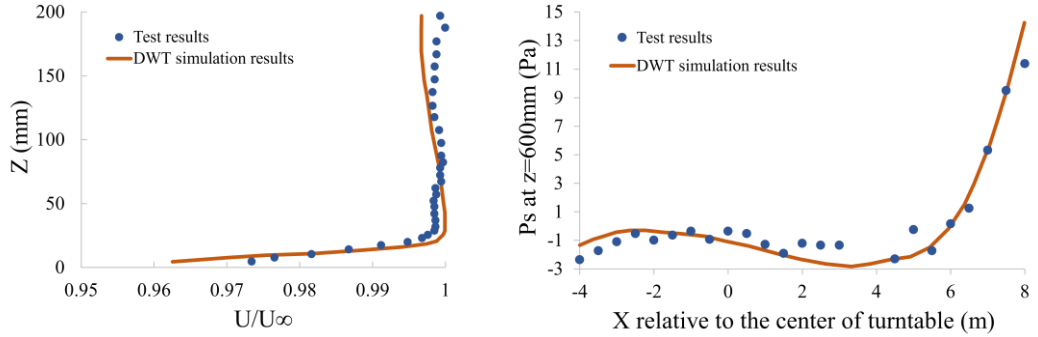


a b

Figure 4: Comparison of digital wind tunnel simulation results and test results: boundary layer thickness (a), longitudinal static pressure gradient (b)

Commissioning work with vehicle is carried out after the calculated metrics for the empty wind tunnel have been met. The vehicle used for the calculations is an expanded model of the DrivAer Model, as it possesses the ability to easily change rear back styling as well as multiple configuration states.

The benchmarking calculation vehicle model contains four kinds of back shapes and five kinds of key component states, and the flow field measurement results (surface and space pressure/velocity distributions) and force measurement results (aerodynamic drag, aerodynamic lift, etc.) are the key basis for evaluating the accuracy of numerical wind tunnel calculations.

The development studies of mesh delineation methods and dimensions, turbulence models and their parameter settings, and wheel rotation simulation methods were completed. The CFD simulation results obtained were in high agreement with the test results, both in terms of flow field measurements and force measurements. In particular, the average error for aerodynamic drag value, which is of highest concern in vehicle aerodynamic develop, is less than 1.5%. Some of the comparison results are showed in Figures 5 and 6.

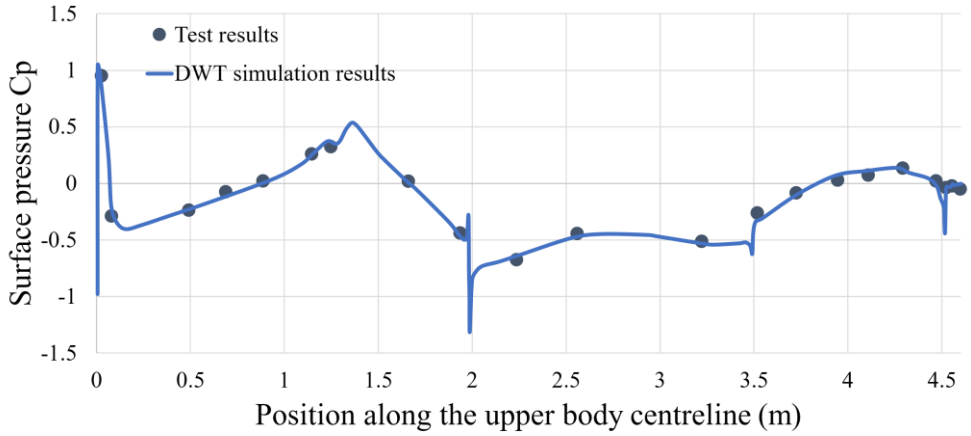


Figure 5: Comparison of surface pressure coefficients

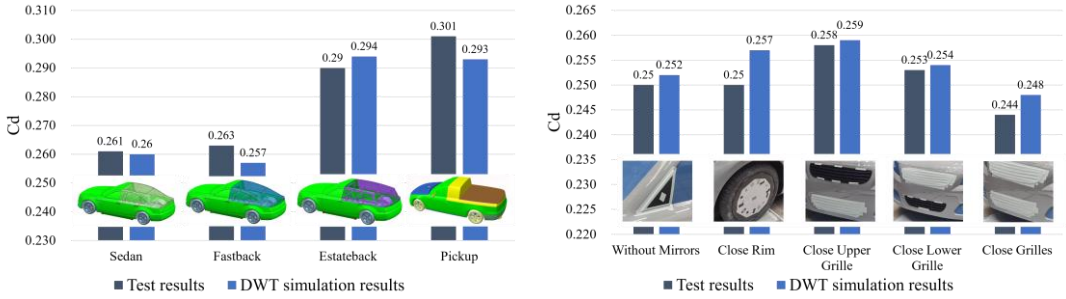


Figure 6: Comparison of aerodynamic drag coefficients for various working conditions

## 3.3 Digital platform deployment

The digital wind tunnel software is deployed on the digital platform of the Wind Tunnel Centre in CAERI, which has a high-speed data transfer rate and a huge amount of supercomputer resources. The digital wind tunnel software deployed based on the cloud platform is able to automate the execution of operations such as mesh generation, calculation parameter setting, simulating on cloud-high-performance-solver, post-processing, and analysis report compilation. The CFD simulation process has been standardised, which improves the accuracy of the simulation calculation and at the same time brings great convenience to the development of the aerodynamic performance of vehicles.

# 4 Smart wind tunnel system

It is an intelligent system based on the Internet of Things (IoT) that enables transparency of wind tunnel test process data, streamlines management, and brings intelligence to conduction of experiments.

## 4.1 Framework

Smart wind tunnel system is built using a microservice framework, which focuses on fully decoupling the business system, based on the independence of business functions. The original single business system is split into multiple small applications that can be independently developed, designed, operated, and maintained, and ultimately provide services to users. The specific technical architecture is shown in the figure below:

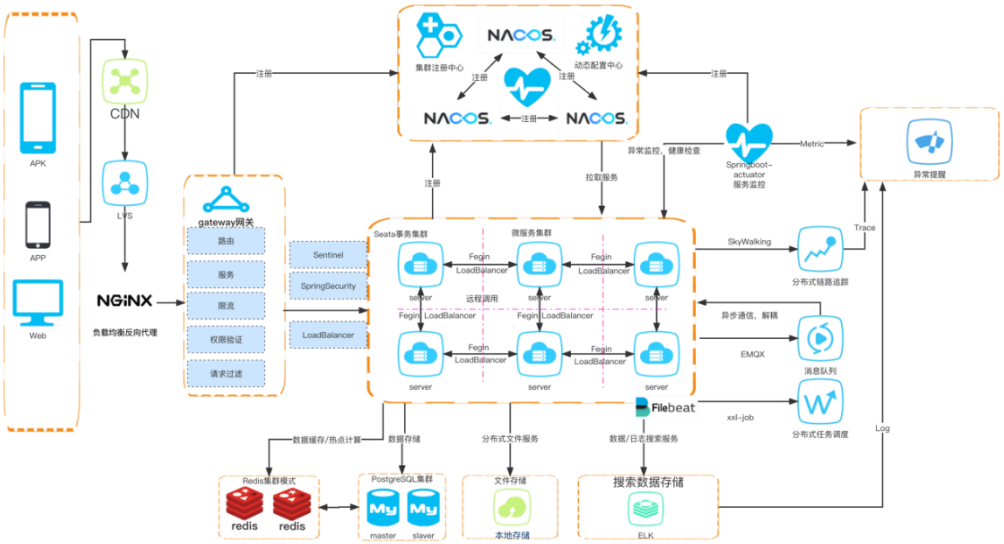


Figure 5: Technical Framework of Smart Wind Tunnel System

## 4.2 Components

The smart wind tunnel system consists of a management platform and six sub-applications and can be linked to the outside world through three interactive processes, while ensuring the security of the system.

Management platform is the central brain of the system and can receive and store equipment monitoring data and user test information. Using artificial intelligence to assist management, these data and information will be standardized and can be viewed and managed efficiently.

The application level including equipment health management, safety management, artificial intelligence assistance, test data analysis, customer experience management and energy management is the classification and value-added utilization of the data stored on the platform.

The smart wind tunnel system allows users to operate and interact through mobile terminals, web pages, and large-screen terminals to achieve full-time, anywhere monitoring and management of wind tunnel equipment and experiments.

### 4.3 Objectives

The smart wind tunnel system will be constructed and completed with the following objectives:

1. Based on the equipment internet, establish a set of intelligent wind tunnel system to achieve digital and intelligent test and lean management

2. Build a new system of safe, intelligent, and efficient digital management of wind tunnel test, using big data and artificial intelligence technology.

3. The real-time online monitoring rate of equipment working conditions reaches 80%, the real-time automatic warning rate of safety events reaches 85%, and the health prediction and maintenance rate of key components of core equipment reaches 50%.

4. For one year, reduce equipment downtime due to maintenance by about 100 hours, reduce equipment ineffective operation time due to ineffective testing by about 150 hours, and reduce test cancellation time due to unplanned downtime by 200 hours.

## 5 Conclusion

Wind tunnel database and intelligent prediction model, digital wind tunnel, smart wind tunnel system are products of the digital work of CAERI Wind Tunnel Center. These digital products greatly enhance the value of physical equipment and test data and are an important step towards intelligent operation of the CAERI Wind Tunnel Center.

Through the wind tunnel database and intelligent prediction models, it is possible to digitize experiments, label data, and realize intelligent aerodynamic drag prediction, achieving reasonable, accurate and efficient formulation of development goals in the concept development stage.

Committed to improving the correlation between CFD simulation results and wind tunnel test results, the digital wind tunnel was developed as a "virtual test" product for accurately representing test scenarios. The application of CAERI Digital wind tunnel can significantly improve the correlation between CFD simulation and CAERI wind tunnel test, compared with the traditional simulation using open rectangular solution domain.

The operation and maintenance of wind tunnel equipment currently seems to be a major and cumbersome task. Smart wind tunnel system can realize digital equipment operation, intelligent test management, and lean operation and maintenance, which can greatly improve the efficiency and economy of wind tunnel management.

## 6 Reference list

Huang, T., Liu, J., He, X., Bu, H., Wang, Q., Xu, S., & Zhu, X. (2022). Extended Study of Full-Scale Wind Tunnel Test and Simulation Analysis Based on DrivAer Model. Proceedings of the Institution of Mechanical Engineers, Part D: Journal of Automobile Engineering, 236(10-11), 2433-2447.

# Reduction of Flow Fluctuation with Vortex Generating System

Ju Yeol You*, Hyung-il Kwon, Sunghyun Jeon, Jungsik Cho and Yong Su Shin

Aerodynamic Development Team
Hyundai Motor Group
150, Hyundaiyeonguso-ro, Namyang-eup
18280, Hwaseong-si, Gyeonggi-do, Korea
aerodoctor@hyundai.com
hyungil.kwon@hyundai.com
Sunghyun0906@hyundai.com
Jungsik.Cho@hyundai.com
Shin.yongsu@hyundai.com

**Abstract:** The retractable vortex generating system has been employed in HAWT(Hyundai Aero-acoustic Wind Tunnel) to reduce the data fluctuation. Due to the high fluctuation of the aerodynamic data, large data measurement time has been required. Several experiments have been conducted to investigate the physical cause of the data fluctuation. The experimental results showed that the reflected shear layer from the collector flap caused the data fluctuation. The vortex generating system on the nozzle lip was proposed by FKFS. The plenum pressure and drag force were compared to illustrate the improvement in the data quality. The vortex generating system reduced the data measurement time by more than 50%. As a result, the data recording time was reduced from 200 seconds to less than 100 seconds. However, the axial static pressure distribution in the plenum changed and the drag coefficient increased. In addition, the aerodynamic contribution of each part of a vehicle also changed. Further research will be conducted to compensate for the increase of the drag coefficient.

## 1 Introduction

Flow uniformity and stability are very important features in open-jet wind tunnels. In order to obtain uniform and stable flow in the test section, it is very important to minimize pressure pulsation in the plenum. For a long time, a lot of studies have been conducted to find out the mechanism of pressure fluctuation [1-7]. The Hyundai Aero-acoustic Wind Tunnel(HAWT) was built in 1999. It had static pressure fluctuation at that time. In addition, the level of fluctuation at certain wind speed was larger than acceptable value. The vortex generator attached to the nozzle lip had been investigated to reduce the pressure fluctuation in the test section. However, due to the increase of aero-acoustic noise and negative static pressure gradient, the use of the vortex generators was considered unacceptable. The edge-tone feedback was found to be the main source of the pressure fluctuation and a slot between the trailing edge of the collector and the entrance of the test section diffuser was proposed [5]. As a result, location of the collector was modified to make a slot between the collector end and entrance of the test section diffuser. Although the structural modifications were made in 2001, there is still aerodynamic data fluctuation and it takes relatively long time to obtain the averaged value. In this study, in cooperation with FKFS, the source of the data fluctuation and the way to increase the quality of the measurement were investigated. Plenum pressure and drag force were analysed to explain the data quality improvement.

## 2 Experimental Analysis

Fig. 1 shows the wind tunnel test result of a mini-van recorded at 1Hz for 400 seconds at 140km/h. Because the drag coefficient is fluctuating more than 10 counts, a relatively large number of data is required at least 200 to obtain the averaged value.

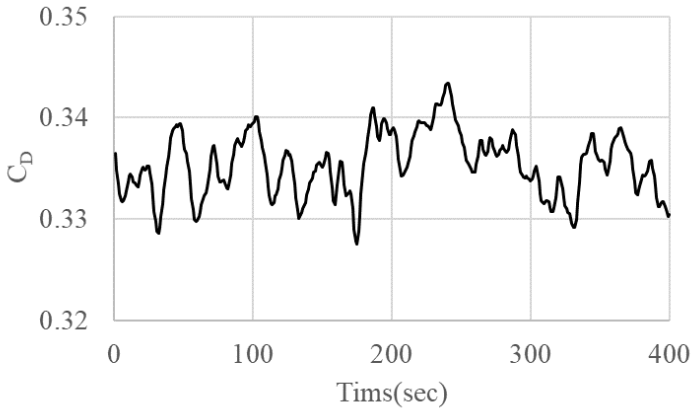


Figure 1. Drag coeffiecient of a mini-van

In order to determine the source of the data fluctuation, several experiments were conducted. A Pitot tube was installed 1.2m above the center of the turntable to compare the pressure fluctuation at 140km/h(reference wind speed) as shown in Fig. 2. The pressure data were recorded at 5Hz for 15 minutes after the wind speed achieved.

Figure 2. Pitot tube set-up

Fig. 3 and Fig. 4 show total and static pressure distributions according to time and their frequencies respectively. The edge-tone feedback loop frequencies are shown in Tab. 1. The frequency of the edge-tone feedback loop is[5]:

$$f_e = \frac{1}{\left(\frac{1}{m}\right)\frac{L_{jet}}{0.65U} + \frac{L_{jet}}{c-U}}$$

For the HAWT, $L_{jet}$ = 14.47m and U=38.9m/s.

The dominant frequencies of pressure pulsations were observed near 1.5Hz and 2.5Hz. In Tab. 1, the edge-tone feedback frequencies are similar to the dominant frequencies of pressure fluctuations. In particular, at m=2, the edge-tone feedback frequency is equal to the dominant frequency of the static pressure fluctuation. It means that the reflected shear layer from the collector can be a source of the aerodynamic data fluctuation.

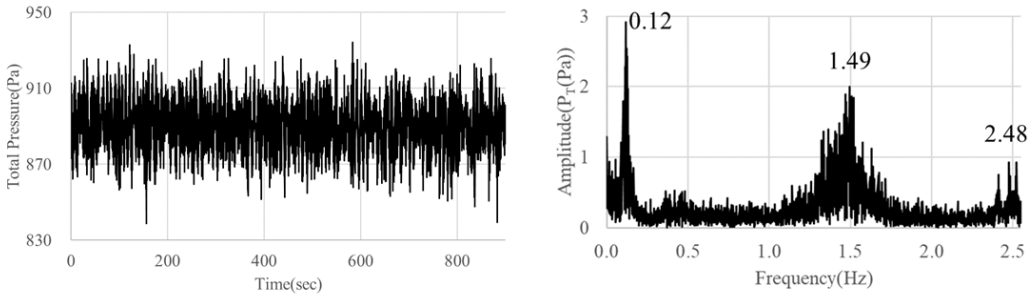


Figure 3. Total pressure distribution and dominant frequencies

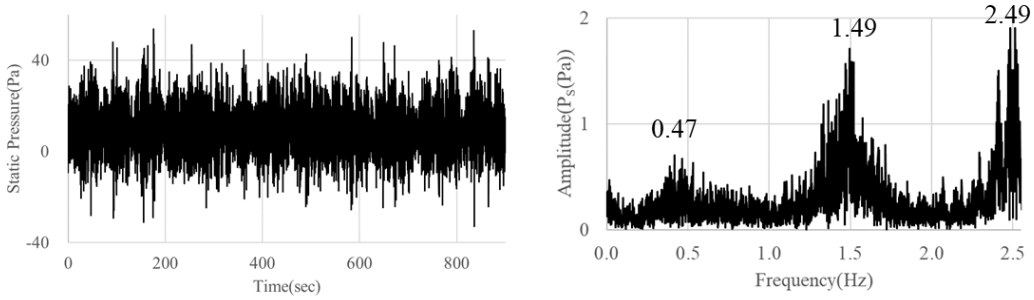


Figure 4. Static pressure distribution and dominant frequencies

| Mode(m) | $F_{edge\text{-}tone}$ |
|---|---|
| 1 | 1.336 Hz |
| 2 | 2.482 HZ |
| 3 | 3.475 Hz |

Table 1 Edge-tone feedback loop frequencies

A simple experiment was conducted to see if the reflected shear layer caused the fluctuation in aerodynamic data. Since HAWT has a traversing system with a large structure near the height of the jet shear layer, so it was assumed that the traversing system might lessen the shear layer reflection and the reduce pressure fluctuation. The traversing system was moved to the collector to prove the assumption as shown in Fig. 5. Fig. 6, Fig. 7 and Fig 8 show the changes in total and static pressure distributions, their frequencies and drag coefficient according to the location of the traversing system respectively. Tab. 2 shows the change in the standard deviation of pressure and drag coefficient of a mini-van. The results show that the data fluctuation reduces when the traversing system is above the end of the turntable. Although the movement of the traversing system is not a permanent solution, it shows that the reflected flow from the collector is manipulating the flow fields around a vehicle.

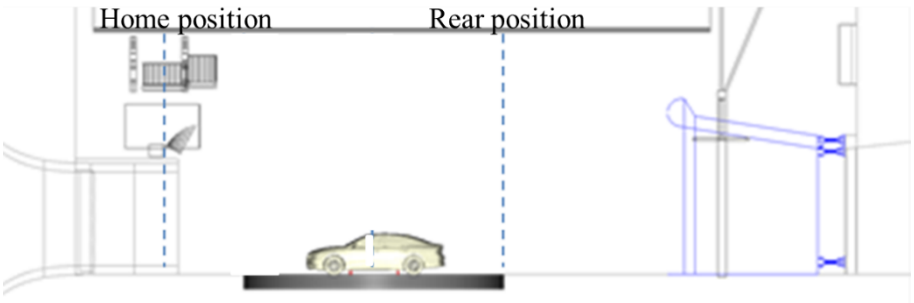


Figure 5. Position of traversing system

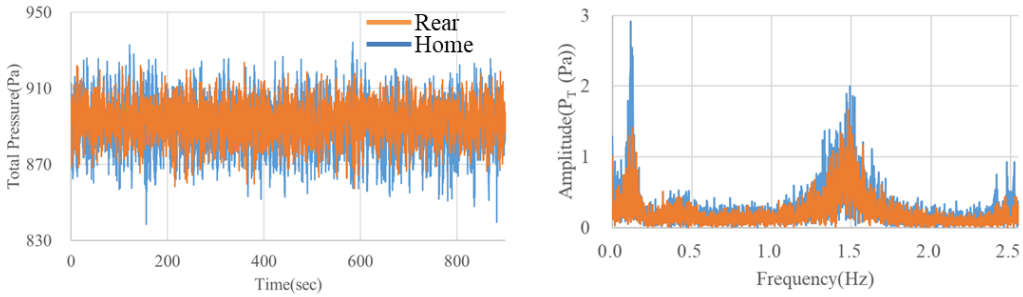


Figure 6. Change in total pressure distribution and frequencies

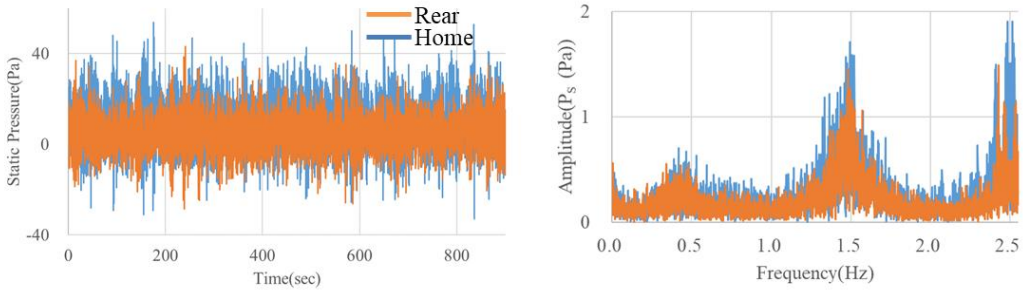


Figure 7. Change in static pressure distribution and frequencies

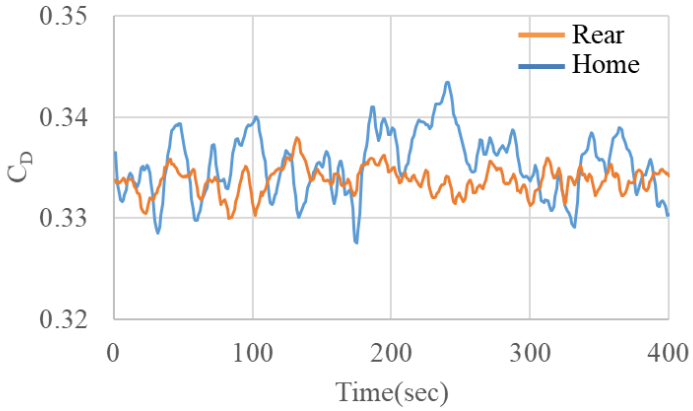


Figure 8. Change in drag coefficient of a mini-van

| | Traverse Home | Traverse Rear |
|---|---|---|
| STDEV of $P_T$ | 13.0 | 9.6(26% ↓) |
| STDEV of $P_S$ | 11.5 | 8.6(25% ↓) |
| STDEV of $C_D$ | 0.0031 | 0.0013(57% ↓) |

Table 2. Standard deviation of data

## 3 Application of Vortex Generators on Nozzle Lip

FKFS suggested vortex generators on the nozzle lip to prevent the formation of the coherent shear layer vortices and reduce the aerodynamic data fluctuation. Previous researches [6,7] applied vortex generators on the upper edge of the nozzle. In this study, vortex generators were also applied on the side edges of the nozzle to increase the stability of the flow. The vortex generator was designed to be retractable considering the aero-acoustic side effects as shown in Fig. 9. The length of the vortex generator is 100mm and the width is set to be placed equally spaced. The angle of flap is 10 degrees towards the nozzle outlet.

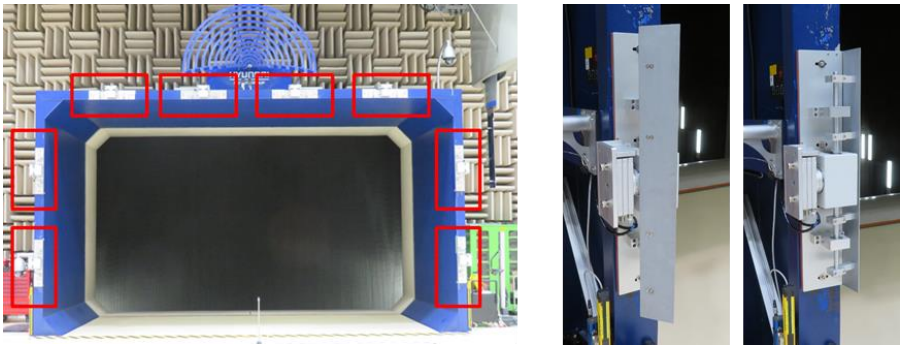

Figure 9. Retractable vortex generators on the nozzle lip

The static pressure at the center of the turntable was measured according to the wind speed. Fig. 10 shows the dominant frequencies of the static pressure fluctuation are depending on the state of the vortex generators. It is observed that all dominant peaks reduce for all wind speeds when the vortex generators are deployed. Especially, the reduction of the magnitude of dominant frequencies at 140km/h is noticeable. The axial static pressure was also measured along the longitudinal direction at 140km/h, and the dominant frequencies are shown in Fig. 11. The peaks of dominant frequencies reduce at all locations with the vortex generators on.

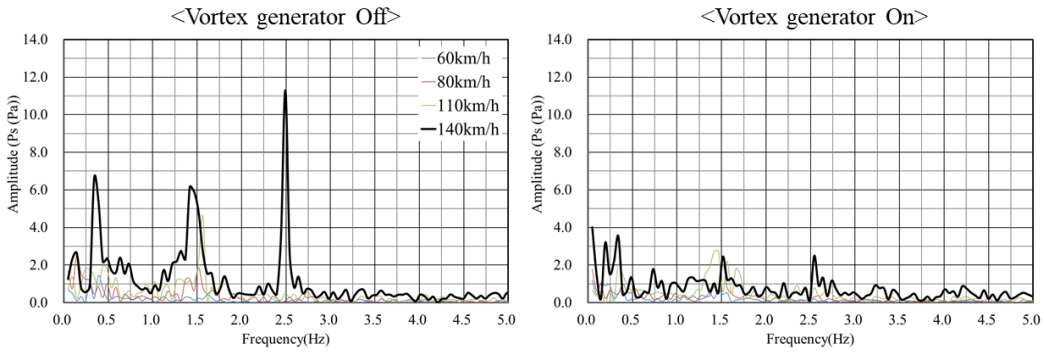


Figure 10. FFT of static pressure accoriding to wind speed

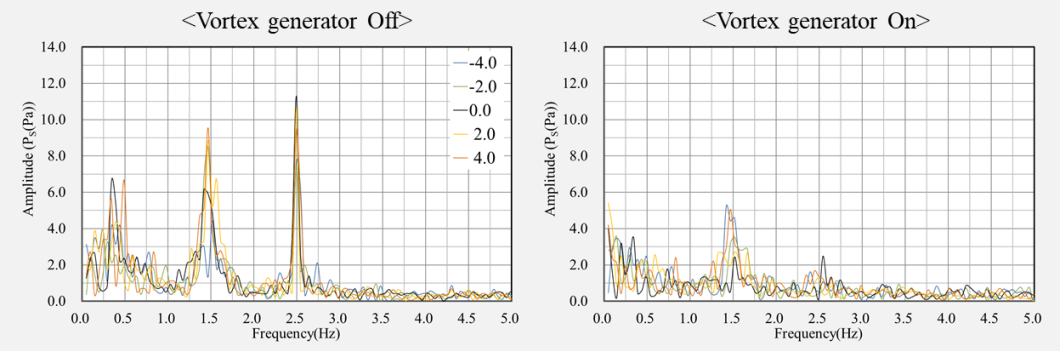


Figure 11. FFT of static pressure accoriding to axial position

The plenum axial static pressure gradient is shown in Fig. 12. The slope of the data varies according to the state of the vortex generators. When the vortex generators are deployed, the difference in static pressure data between fore-body and rear-body of a vehicle increases. It contributes to increasing the horizontal buoyancy effect and increasing the drag coefficient of a vehicle.

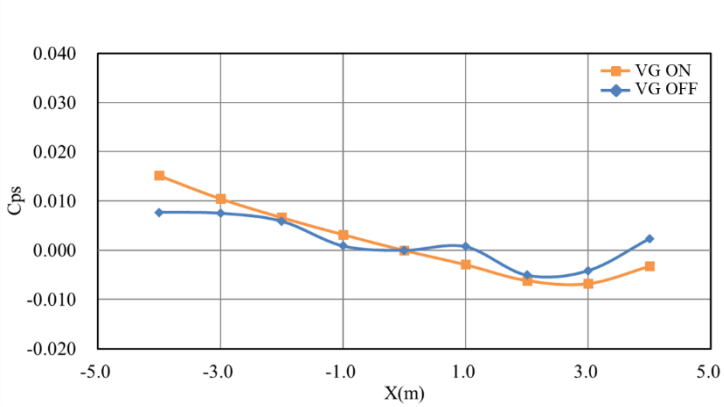


Figure 12. Axial static pressure gradient in plenum

The wind tunnel test of DrivAer notchback model was conducted. Fig. 13 shows the change in the drag coefficient. The standard deviation of the data is reduced by 67% and averaging time can be reduced to less than 100 seconds when the vortex generators are deployed. However, the averaged drag coefficient shows increase as explained in the axial static pressure gradient in Fig. 12. In Fig. 14, the difference in the static pressure along the 0L line shows the same tendency as the difference in axial static pressure gradient in Fig. 12. At the front of the model, the static pressure with vortex generators on is greater than one with vortex generators off, and it appears in reverse at the back of the model. Fig. 15 shows the variation of the drag coefficient according to the wind speed. When the vortex generators are opened, the values of the drag coefficient increase and the tendency of the variation changes similarly to the result of FKFS wind tunnel.

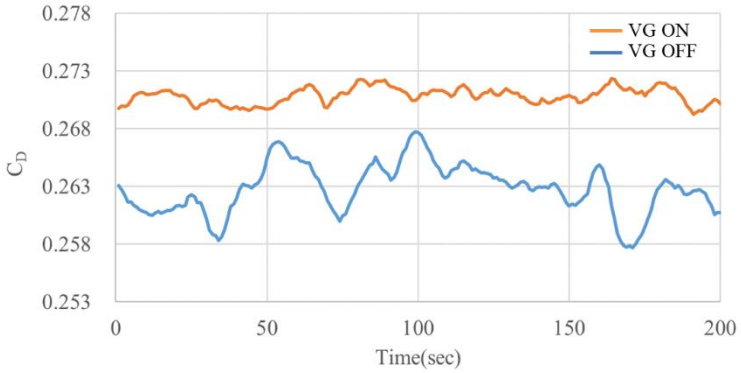


Figure 13. Drag coefficient of DrivAer notchback model

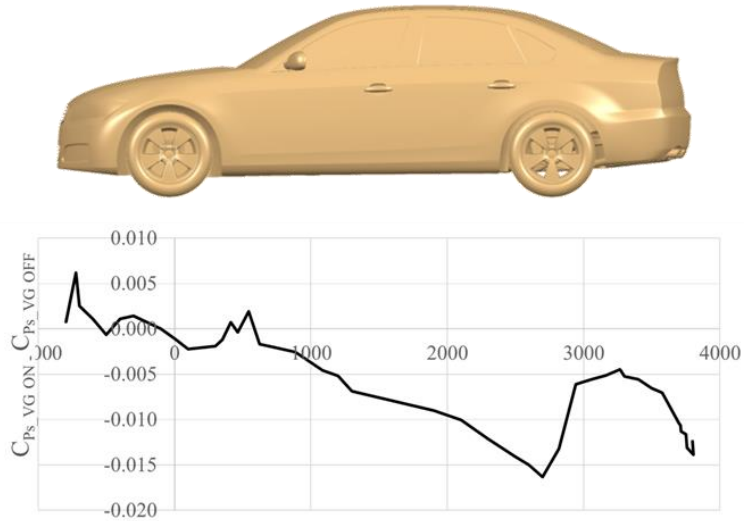


Figure 14. Static pressure distribution on upper body(0L)

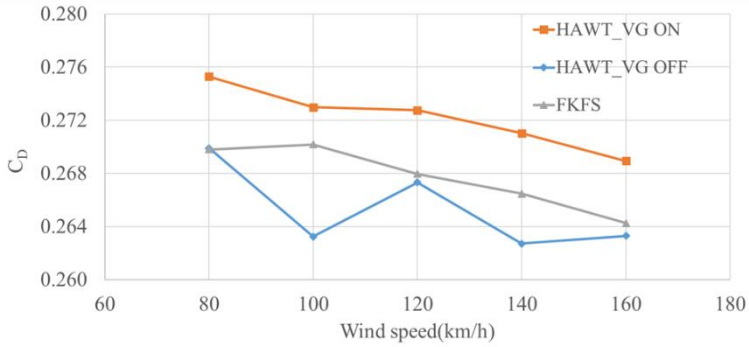


Figure 15. Variation of drag coefficient according to wind speed

Fig. 16 shows changes in the aerodynamic properties of each part of a vehicle, indicating the aerodynamic contributions of wheel, cooling, undercover and posture of a vehicle vary depending on the state of vortex generators.

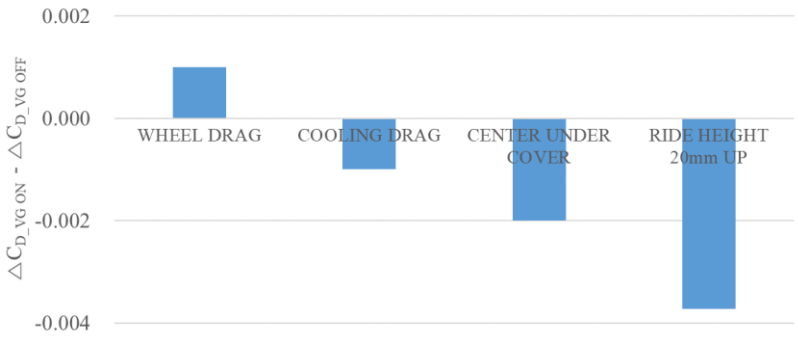


Figure 16. Change in aerodynamic contribution of each part

## 4 Conclusions

In this study, several experiments were conducted to reduce the fluctuation in the aerodynamic data, and improve the quality of measurement. The reflected shear layer from the collector has been found to be a source of the data fluctuation. Finally, the retractable vortex generators were installed on the nozzle lip not only to solve the problem but also to minimize the aero-acoustic side effect. The fluctuations of the plenum pressure and drag coefficient reduced dramatically when the retractable vortex generators were deployed. However, the vortex generators changed axial static pressure gradient in the plenum and increased the drag coefficient. In addition, the aerodynamic contribution of each part of a vehicle also changed. More researches will be conducted on the various types and positions of vehicles to find out how to compensate for the changes in the aerodynamic forces, and aero-acoustic tests with vortex generators will be conducted as well.

## 5 Bibliography


1. Wickern, G.; von Heesen, W.; Wallmann, S.: Wind Tunnel Pulsations and their Active Suppression. SAE 2000-01-0869, 2000.

2. Arnette, Stephen A.; Buchanan, Tony D.: On Low-Frequency Pressure Pulsations and Static Pressure Distribution in Open Jet Automotive Wind Tunnels. SAE Paper 1999-01-0813, 1999.

3. Lacey, John: A Study of the Pulsations in a 3/4 Open Jet Wind Tunnel. SAE Paper 2002-01-0251, 2002.

4. Manuel, G. S.; Molly, J. K.; Barna, P. S: Effect of Collector Configuration on Test Section Turbulence Levels in an Open-Jet Wind Tunnel. NASA TM-4333,1992.

5. Rennie, M.; Kim, M. S; Lee, J. H; Kee, J. D: Suppression of Open-Jet Pressure Fluctuations in the Hyundai Aeroacoustic Wind Tunnel. SAE Technical Paper 2004-01-0803, 2004.

6. Amandoles, X.; Vartanian, C.: Reduction of 3/4 Open Jet Low-frequency Fluctuations in the S2A Wind Tunnel. J. Wind Eng. and Industrial Aerodyn. 98(2010) 568-574, 2010.

7. Bao, D.; Jia, Qing; Yang, Z.: Effect of Vortex Generator on Flow Field Quality in 3/4 Open Jet Automotive Wind Tunnel. SAE Int. J. 2017-01-1530, 2017.

# The new DNW-LLF Automotive Test Section

Wilhelmi, H.; Hegen, S.; Melber, S.[1]; Bergmann, A.

German-Dutch Wind Tunnels (DNW)
Voosterweg 31
8316 PR Marknesse
The Netherlands
henning.wilhelmi@dnw.aero
sinus.hegen@dnw.aero
stefan.melber@dlr.de
andreas.bergmann@dnw.aero

Abstract: In recent years, the industrial wind tunnel requirements for automotive tests were largely shaped by the introduction of the Worldwide Harmonized Light Vehicle Test Procedure (WLTP). These regulations posed not only a challenge for existing wind tunnels infrastructures, but also for tests with long vehicles with large frontal surface areas (AF), such as vans or vehicles with box-bodies. The lack of a wind tunnel facility to cover all vehicles sizes in accordance to WLTP motived the German-Dutch Wind Tunnels (DNW) to modernize its Large Low-Speed Facility (LLF). Together with HORIBA an automotive test section (ATS) was developed and build to allow for tests with vehicles from a small form factor up to large, high roofed vans with dual tire configurations at wheelbases of up to 4.7 m and weights of up to 6000 kg. The facility not only allows for aerodynamic tests, but also for the determination of the road loads for energy cycles. In the following sections, the requirements, the development process in CFD and experimental research as well as the first results of the ATS will be presented.

## 1 Introduction

With the increasing pressure to reduce vehicle emissions (e.g. due EU regulation to combat climate change [1] and customer needs [2]) and to increase their reach, in particular for electrical vehicles, the need to reduce the driving resistances increased. The driving resistance is the sum of three main elements (see also Figure 1):

- The nearly constant rolling resistance,
- The power train resistance, which increases linear with the vehicle speed
- The aerodynamic drag, which increases quadratic with the flow velocity.

[1] German Aerospace Center (DLR), Lilienthalplatz 7, 38108 Braunschweig, Germany

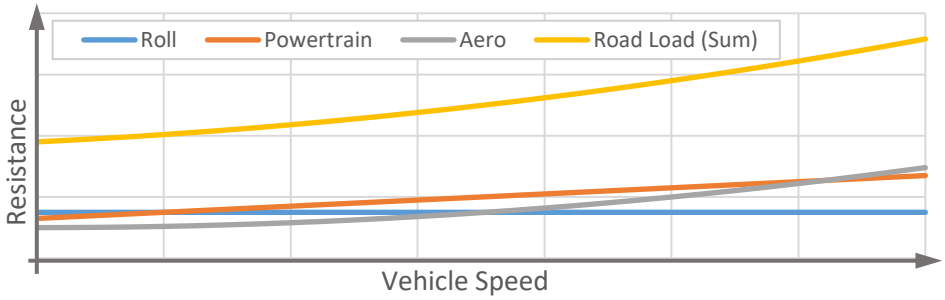


*Figure 1: Schematic development of the different resistances with the vehicle speed*

These relations indicate that the aerodynamic resistance becomes dominant at higher speeds. According to Hucho [3], the aerodynamic drag equals the roll resistance already at 60 km/h for a Mercedes-Benz B-Class and is almost 5 times the resistance at 120 km/h. Thus, determining the aerodynamic resistance is one of the main factors to determine the economy of a vehicle. However, the other forces – in particular at lower speeds – should not be neglected in the calculations.

To determine the resistances, usually a combination of wind tunnel and roller/flat track test benches or separate coast-down tests are performed. While the coast-down tests allow for determination of all combined forces, this test method lacks in accuracy and repeatability as it is sensitive to weather effects and it can only be conducted late in the development process. Furthermore, it is quite time consuming. Thus, an alternative approach in form of a wind tunnel test combined with roller / flat track tests exists. In an approach for more defined, harmonized testing procedures, a WLTP [4] (for latest iteration) was introduced in 2017. Over the last few years the introduction of the WLTP has led to modernized testing facilities. While most vehicles can be tested in the manufacturer's facilities in accordance to the procedures, in particular larger sized vehicles still provide a significant challenge for wind tunnel tests. The blockage effects are the most prominent challenges, but also the size and range of the wheel drive units (wheel base and track width) as well as the support mechanisms are prominent factors limiting the possible range of vehicles. Thus, there is a need in the market for wind tunnel and rolling resistance tests with larger vehicles as an alternative to the cumbersome coast-down tests.

## 2 The new automotive test section at DNW LLF

DNW's LLF – due to its large cross-sectional areas of up to 90 $m^2$ – is able to tests these larger vehicles. In the past, most tests from 1:4 to full-scale automotives and trucks were conducted in closed test sections. While the DNW has experience with moving belt tests, in particular in aeronautical tests, the application of a large, single belt for automotive testing required a high effort at was not feasible for most applications. Thus, most tests were conducted with a static ground in a closed test section. To fill the void of facilities supporting the WLTP certification particularly for larger vehicles – while keeping the blockage effects at a minimum during the measurements – DNW decided to modernize its LLF for automotive tests.

The LLF has various options to change its test section to adapt the system to the customer's request. The options for closed test sections go from a cross-section of

9.5 m by 9.5 m (e.g. for truck tests) over a 8 m by 6 m test sections to a test section with a cross-section of 6 m by 6 m (for tests at up to 465 km/h). The fully open test section has a cross-section of 8 m by 6 m and commonly for acoustic aeronautical tests in an anechoic chamber.

To be in accordance with quasi industry standard of a ¾ open test section, it was decided to develop a modification to the 20 m long, open test section together with HORIBA as supplier of the hardware. The modification consists for a movable test section floor, containing a 5-belt system, an active boundary layer control, a 6-component balance with additional measurement of each wheel force in x-direction as well as a turntable with 12 m diameter (see *Figure 2*). The cross section of the automotive test section (ATS) is 5.9 m by 8 m and thus results in a cross-sectional area of 47.2 $m^2$. This cross-sectional area results in blockages of around 12 % for vans with high roofs.

Special focus is on the boundary layer treatment for proper ground simulation. The floor length without any extension into the nozzle and collector is 20 m and the width is 14 m with a linear broadening at the aft section to 15 m. It is provided with a scoop, which extends 3 m upstream into the nozzle and a re-entry plate that extends 3 m into the collector. Thus, the total length its about 25 m. The primary boundary layer is removed from the main tunnel flow by the upstream scoop that has a height of 0.08 m with respect to the nozzle floor. Two controllable suction pumps are placed below the tunnel to generate the required volume flow (of up to 42 $m^3/s$) for different wind speeds. The sucked air can be re-injected into the tunnel flow at the collector or (partly) be released into the tunnel hall.

A secondary boundary layer control system is incorporated in the turntable just ahead of the rolling road. It removes (suction) and reenergizes (blowing), the newly formed boundary layer between primary scoop and the rolling road system. It consists of three independent elements: One system in front of the center belt over its full width of 1.1 m and two systems adjacent to the central device in front of the wheel drive units with a width of 1 m. Each of the three secondary boundary layer control systems is independently controllable

The 5 rolling road belts are made of stainless steel and run at wind tunnel speed up to its maximum of 250 km/h. The standard center belt is 9 m long and 1.1 m wide, while the wheel drive units are typically 0.36 m wide. However, optional a 0.9 m wide center belt is possible. The belts of the wheel drive units are also available in widths 0.28 m and 0.48 m. In combination with wheelbases between 1.9 m and 4.7 m at track widths between 1.43 m to 1.84 m, this allows for a wide range of vehicles from small compact vehicles to long, high roofed vans with twin-tire configurations.

The 6 component balance is integrated in the turntable. The balance rotates around a common vertical axis combined with the turntable. The maximum load range for all components and their accuracy is given in **Fehler! Verweisquelle konnte nicht gefunden werden.**.

Since the test section is around 6 m above the floor of the test hall (see *Figure 2*), the vehicles are loaded via an elevator over a bridge, allowing the next vehicle to be fully prepared in place during a vehicle change.

*Table 1: Requested ranges and accuracies for the balance system of the ATS*

| Component | Range | Accuracy | |
|---|---|---|---|
| $F_x$ | ± 6000 N | ± 0.015 % FS | ± 1.00 N |
| $F_y$ | ± 7500 N | ± 0.03 % FS | ± 1.25 N |
| $F_z$ | ± 6000 N | ± 0.03 % FS | ± 1.80 N |
| $M_x$ | ± 7500 Nm | ± 0.03 % FS | ± 2.25 Nm |
| $M_y$ | ± 7500 Nm | ± 0.03 % FS | ± 2.25 Nm |
| $M_z$ | ± 5000 Nm | ± 0.03 % FS | ± 1.80 Nm |

*Figure 2: View of the ATS in postion in the background with test vehicles in front (courtesy of Volkwagen)*

## 3. Experimental investigations on scale

Exploratory test campaigns were performed in the NLR-AWT (Acoustic Wind Tunnel). For this the overall elements of the ¾ open ATS were duplicated on 1:10 scale. The setup included the tunnel contraction, test floor with primary suction/re-injection and collector. One suction pump (not scaled) was located below the test floor. The suction pump setting was optimized at a wind tunnel reference velocity of 140 km/h by checking on any flow separation on the scoop and the boundary layer development along the test floor.

Several test campaigns were performed with the application of some of the following measurement instrumentation/ equipment:

- Tufts on the test floor to verify whether flow separation occurs at the scoop
- Long static pressure tube at tunnel center-line for axial static pressure development. The tube was supported in the collector and wire suspended to the contraction.
- Pressure taps in the floor from scoop up to the re-entry plate for static pressure distribution on the floor
- Traversing mechanism with pitot-static tube for axial static pressure development at different heights (amongst others 7 cm and tunnel centre) or total pressure tube for boundary layer measurement above the test floor

Fore reference measurements were also performed in the 0.8 m by 0.6 m fully open jet configuration. The tunnel characteristics in terms of axial static pressure $C_p$ distribution (see figure 3) and wind tunnel resonances turned out to be similar to the ¾ open ATS. Also the test floor pressures of the ATS (not shown) collapse with the pressures at tunnel centre line. Tunnel modifications for improvement on the $C_p$ distribution were also investigated. The $C_p$ rise could indeed be delayed with an acceptable penalty of a vertical $C_p$ gradient which does not exist for the standard configuration. However, the methods have not been tested in the LLF yet.

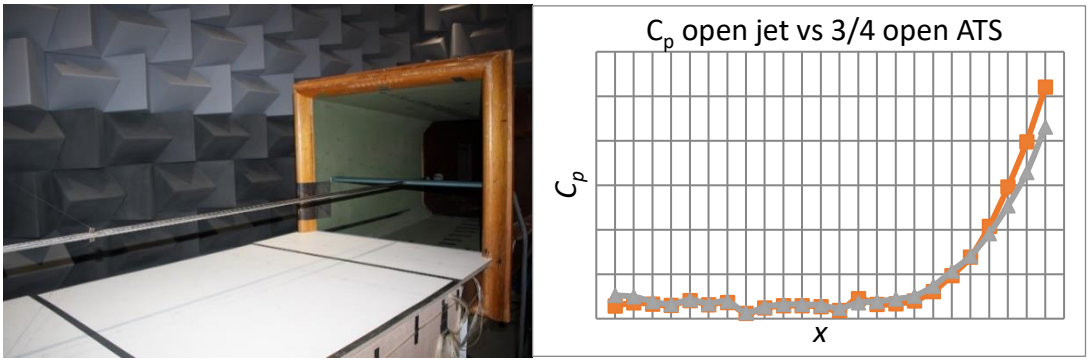


Figure 3: *Long static pressure tube installed in the NLR-AWT (left) and the $C_p$ distributions at tunnel centre line for the open jet (grey) and ¾ open ATS (orange) configurations at reference velocity v = 140 km/h*

The impact of tunnel blockage on the tunnel reference system, as introduced by representative scaled car(s), is investigated by variation of the car distance from the tunnel contraction (distances on scale conformal to car locations in the LLF). At closer car distance the static pressures of the tunnel reference system (located in the contraction end) are clearly disturbed indicating that the plenum method instead of nozzle method should be preferred for determination of the tunnel reference data. Smoke visualizations and $C_p$ distributions behind the car show that the big wake is closed before it enters the collector.

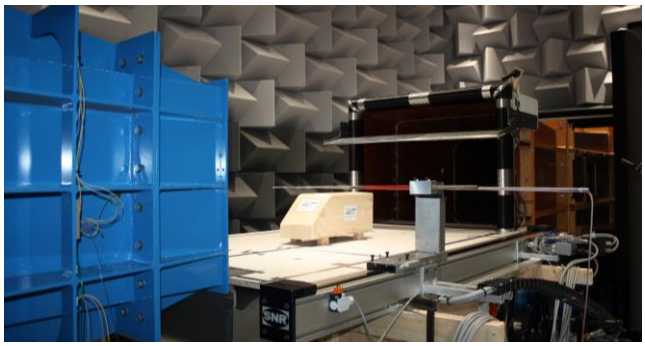

*Figure 4: Wooden car model on ATS test floor of the NLR-AWT with pitot-static tube on the traversing mechanism*

## 3 CFD Based Simulation & Optimization

To find the optimal shape and mass flow rates for the boundary layer treatments (in front of the centerbelt and to its sides), numerical flow simulation based on the Reynolds averaged Navier-Stokes equations were used. This was done in a

cooperation between DNW and DLR's institute for Aerodynamics and Flow Technology. The aim is a constant velocity profile in height without crossflow at the center of the belt for the empty test section. For the optimization, a reference velocity of 140 km/h was chosen and the simulation domain consisted of a 2D cut. The domain included the scoop in the nozzle of the wind tunnel (Figure 5 left, green), the suction and blowing re-injection devices itself (right, yellow) and the rolling belt (right, orange; treated by special "moving wall" boundary condition). Based on the optimized geometry found for this reference velocity, the mass flow rates for suction and re-injection at other velocities are optimized in a second step.

The complete shape and mass flow optimization for the center and the side boundary layer treatment systems took place independently, because of different geometrical constraints. This application is based on a numerical optimization chain developed and first applied for the shape optimization of aero acoustic turning vanes in the wind tunnel DNW-NWB [5].

To check the geometry and mass flow rates resulting from the 2D design, the complete center and side parts were simulated in 3D in the next step. With these simulations it can be verified, whether span-wise flow structures over the width, including the outer edges, of the boundary layer control elements occur. Furthermore, possible flow separations in the nozzle/re-injection as well as time depended fluctuations of the flow can be identified. Consequently, the local geometry could be adapted to improve the flow behavior. Though not presented in this paper, the 3D-simulations were also used to identify effects on the pressure distribution of the tunnel with simplified reference configurations as well as with a more detailed model of a car. Finally, these simulations gave a more detailed insight in the flow field and possible optimizations of supply pipes, screens (which are fully resolved in the CFD-Simulations) as well as the feeding of the suction/blowing system.

### 3.1 Parametric Geometry & Grid Generation

The basis of any kind of optimization is the determination of the free parameters and the parameterization of the geometry. In the case at hand, Figure 5 (right) presents the free parameters in different colours: Red/blue - the mass flow rates of the secondary suction/re-injection, yellow – the inner contours of these elements as well as the shape of the center element.

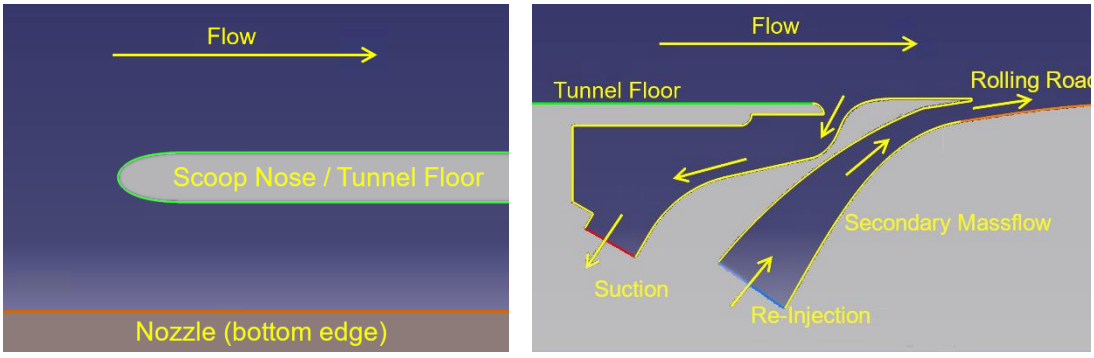


*Figure 5: Domain optimizations of primary suction and secondary mass-flow for suction/re-injection*

The design was build up as a parametric CAD design. The discretisation of the flow domain in 2D (optimization) and in 3D (verification) took part in the mesh generator SOLAR [6]. It was used due to the overall short runtime and high grid quality. Because topological constraints for 2D meshes in SOLAR the optimization meshes have a finite width of a few cells.

The mesh generator SOLAR consists of a surface mesh generator based on a novel advancing front technique to produce mainly quadrilaterals elements and works on a CAD-patch basis in parametric space. Volume meshing is achieved through a two-stage process. Firstly, the mesh is grown away from the solid surfaces captured in the surface mesh to form a structured mesh of hexahedra for the resolution of the boundary layer. The remaining computational domain is filled with tetrahedral elements in a second step.

A mesh convergence study was performed to minimize the number of grid points on the one hand and on the other the maximize the quality of the flow solution. Overall the mesh results in a n extensive, costly boundary layer discretization and a relatively fine discretization of the suction / re-injection (see Figure 6).

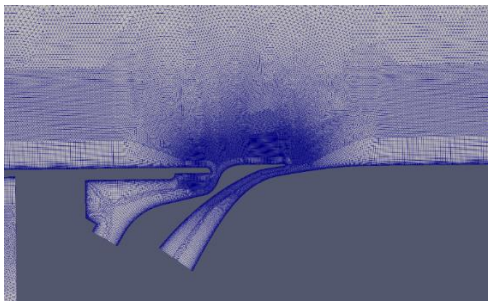

*Figure 6: Mesh for optimization in the region of secondary suction / blowing.*

### 3.2 Flow Solver & Optimizer

The solution of the RANS equations is carried out using the hybrid unstructured DLR TAU code [7]. For the closure of the Reynolds-averaged equations the RSM turbulence model [8] is used, which allows for robustness results at a good quality. Due to the low Mach numbers and the resulting stiffness of the RANS equations, low Mach number preconditioning is inevitable. The central JST-scheme in combination with 80% matrix dissipation assures numerical flow solutions with low numerical dissipation. Finally, implicit time-integration is utilized in the TAU code.

The optimization system CHAeOPS (Computational High-Lift Aerodynamics Optimization System) [9] is designed as a modular system. The optimization strategy chosen is the downhill-simplex algorithm SUBPLEX [10]. Previous investigations had shown that the simplex method provides the best compromise of robustness, efficiency and globality when applied to aerodynamic design by RANS simulations. For optimization, the objective function was generated by integrating the (absolute) deviation of the velocity profile at three meters down the second blowing (position of the car bumper) from the reference velocity over a height of 5 meters.

### 3.3 Results

One distinct result of the optimization runs is the stronger dependence of the resulting velocity profile from the mass flow rates, while the dependence from the geometry itself is smaller. This gives some flexibility for the fine-tuning in the wind tunnel by modifying the suction & blowing rates instead of having to redesign the system.

Another clear result of the optimizations is the centerpiece between the suction and re-injection (which sticks up from the tunnel floor in Figure 7). This fixes the stagnation point of the suction on the rounded nose and reduces the influence of the suction mass flow rate on the resulting velocity profile in front of the car. Other geometries with a bigger nose at a level with the tunnel floor showed a larger movement of the stagnation point at different suction rates and thus, changed the resulting velocity profile.

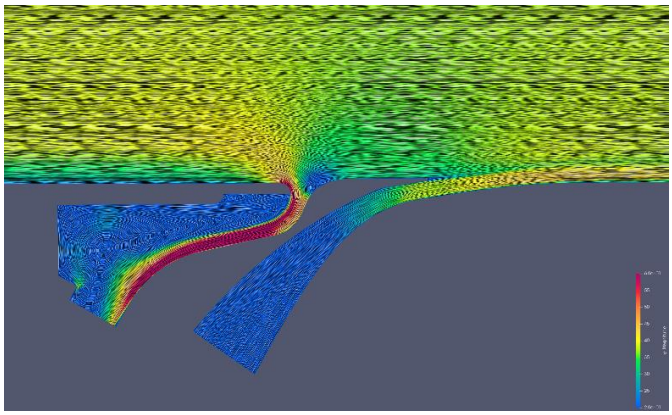

*Figure 7: Optimized geometry for center part (absolute velocities and streamlines)*

The off-design impact on the boundary layer over the belt was tested with 2D simulations of the optimized geometry by varying the suction- and re-injection mass flows. Overall, changing the suction mass flow has a smaller impact on the velocity profile ("Objective") than varying the mass flow of the re-injection part (Figure 8, left). Further on, in the optimized cases, both mass flows differ by about 10-30 % (with the higher mass flow being at the suction element).

The 3D-simulations show a quite good comparison of mass flow rates in 2D and 3D (determined by the static pressures in the in- and outlet sections). The span wise variation of the flow is quite small even with the split of the center and outer parts.

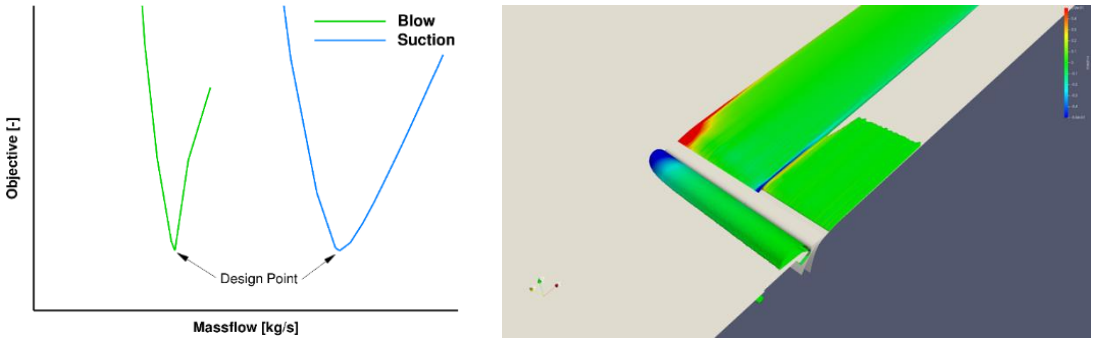


*Figure 8: The systems off-design behaviour on the block profile of the boundary layer ("Objective") with varying mass flows at the suction and blowing elements (left) & the iso-contours (39 m/s, span-wise velocity colouring) for a half-model of the suction/blowing in a 3D-simulation (right).*

## 4 WLTP requirement measurements

To show compliance with the WLTP requirements, various tests were conducted. These consisted of aerodynamic tests, belt tests as well as tests of the balance, including measurements with the flat belt system.

### 4.1 Flow velocities

The flow velocities were measured with pitot static probes in the tunnel centerline (TCL) above the balance center as well as in nine distinct points in the nozzle exit plane (NEP). The nine measurement positions are illustrated in Figure 9. The probe in the tunnel center line was held by 2 symmetric airfoils over the belt. (see Figure 10, left). The measurements in the NEP were conducted with 3 pitot static probes measuring parallel at the 3 required heights (see Figure, right). After each measurement, the system was shifted to a position in the width of the NEP.

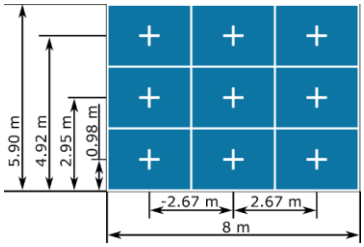


*Figure 9: Position of the measurement probes in the NEP*

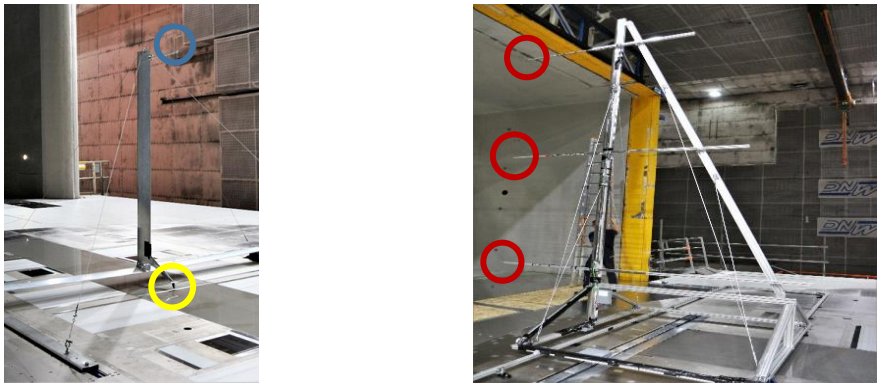

*Figure 10: Measurement setup for measurements at the TCL (left, blue circle), at the boundary layer (yellow circle) and at the NEP (right, red circle)*

The measurements were conducted with at a targeted air velocity of 140 km/h. In the tunnel centerline the velocity was measured over 600 s (see Figure 11). The velocity was between 139.8 km/h and 140.8 km/h with an average of 140.3 km/h and shows a stable behavior. In the NEP the measurement was over 60 s and averaged at 140.0 km/h over the nine measurement points with a maximum difference of ±0.8 km/h between those points. Both results are well below the WLTP requirements.

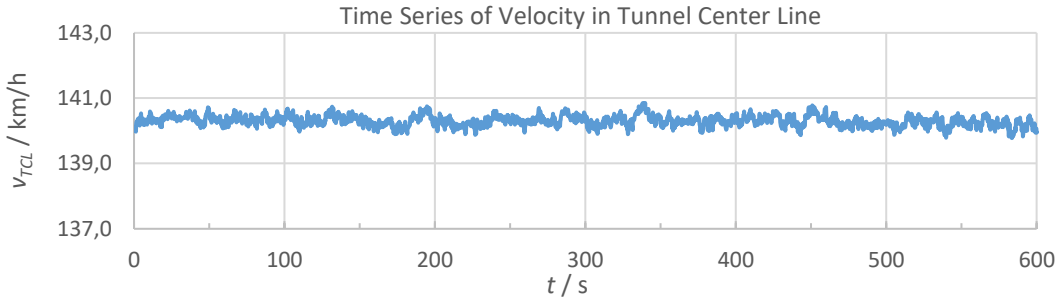


*Figure 11: Time resolved velocity data over 10 minutes in the tunnel centerline*

## 4.2 Pressures

Since the pitot static tubes allow for the measurement of the total and static pressures, the previous setups were used for the measure measurements as well (see paragraph 4.1 and Figure 10). In the NEP the standard deviation over all nine measurement points for the total pressure deviation from the mean total pressure divided by the dynamic pressure was determined, while in the TCL the change of the static pressure in form of the pressure coefficient $C_p$ in the region between ±3 m was measured. For the ladder, the holding mechanism for the probe was shifted back and forth in 1 m steps from the balance center and after each shift, the pressure was measured. Since the setup allowed for it, an additional measurement was taken at 4.5 m. The integration time for the measurements was 60 s and the wind tunnel velocity was set to 140 km/h.

The normalized pressures coefficients along the tunnel centerline increase by 0.0056 between -3 m and 3 m, which is well below the WLTP requirement of 0.02. The linearized trend line shows an increase of 0.0007 per meter (see Figure 12). Even when extending the distance to +4.5 m, the linear factor remains at this value. A low crease of the static pressure over a long distance reduced the induced horizontal buoyancy effect during wind tunnel measurements.

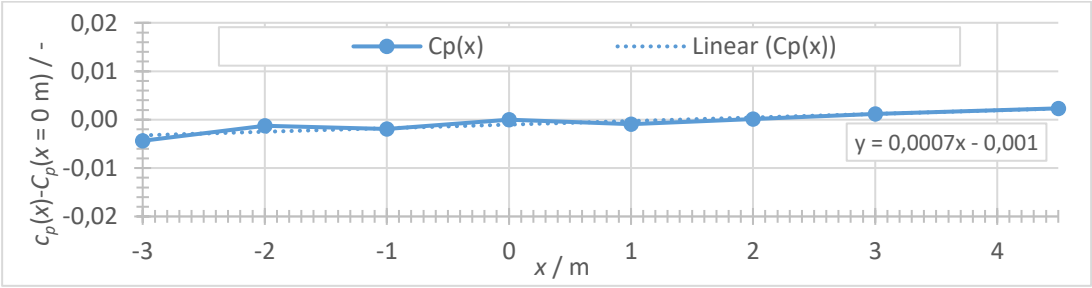


*Figure 12: Normalized pressure coefficient distribution along the TCL -3 m to +4.5 m from the balance center in flow direction and the linear trend line with its calculated equation.*

The standard deviation of the total pressures in the NEP indicate a slow pressure fluctuation in the NEP of 0.002 or 0.2 % of the dynamic pressure. This also is well within the WLTP requirement of 2 %.

## 4.3 Turbulence Intensity

The turbulence intensity was measured in the NEP by means of x-wire hot-wire measurements. The holding mechanism was modified for the hot-wires probes in a way that allowed for a 90° turning of the probes to measure the fluctuations in all three flow directions. The data was acquired at 60 kHz over 30 s and an aliasing filter was applied at 30 kHz. In post-processing the data was high pass filtered at 1Hz to prevent non-physical disturbances from entering the turbulent data. Above 3kHz the data is filtered with a linear filter to avoid electrical noise to enter the hotwire data. Additionally a filter was used around 260 Hz to reduce the frequencies by around 3 magnitudes, since mechanical vibrations of the holding system were affecting the results. In particular at the highest positions, mechanical noise, in particular in the y- and z-direction remained an issue, but were too broad to filter out to be separable from the aerodynamic results. The resulting average total turbulence intensities for the wind tunnel at 140 km/h are 0.13 % overall, with 0.05 % in x-, 0.17 % in y- and 0.13 % in z-direction. Despite the mechanical vibrations, this is well below the required 1 % turbulence intensity for WLTP.

With the x-wire hot-wire setup, the flow angles $\alpha$ and $\beta$ were measured simultaneously. The standard deviation over the nine points was 0.41° and 0.42° respectively. This is also within the regulations.

### 4.4 Boundary Layer Thickness

The boundary thickness was measured with a boundary layer rake above the center belt in the center of the balance system (see Figure 10, yellow circle). The rake measured the pressures between 16 mm and 66 mm above the moving belt. Due to safety concerns, lower heights were avoided. Together with the aforementioned systems to control the boundary layer thickness (see section 3), the boundary layer at 140 km/h resulted in the distribution presented in Figure 13.

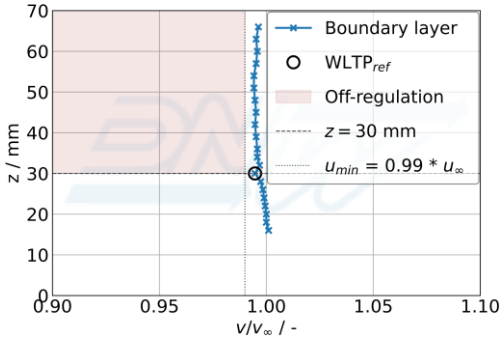


*Figure 13: Measured boundary layer with primary and secondary boundary layer treatment in the balance center above the running belt at 140 km/h*

The boundary layer at the measured heights is virtually non-existent. The velocities remain above 99% and are within 99.4 % and 100.1 % of the free stream velocity. This is within the requirements of WLTP, which states that the velocities above 30 mm have to be greater than 99 % of the free stream velocity.

## 5 Summary

The DNW introduced a new automotive test section. Due to the large cross-sectional area of 8 m by 6 m, vehicles ranging from small to long, high roofed vans with wheel bases of up to 4.7 m can be measured with reasonably low blockages. Because of the size, special care was taken in the boundary layer treatment. Its development was supported by detailed CFD simulations from DLR and scaled measurements at NLR.

Furthermore, the test section was setup for WLTP measurements. The aerodynamic requirements are kept and in parts well below the given limits. First commercial tests were conducted successfully in 2023. The full commissioning and certification are projected to be completed by the end of 2023.

## 6 Bibliography


[1] European Parliament and Council, *REGULATION (EU) 2019/631 OF THE EUROPEAN PARLIAMENT AND OF THE COUNCIL of 17 April 2019 setting CO2 emission performance standards for new passenger cars and for new light commercial vehicles, and repealing Regulations (EC) No 443/2009 and (EU) No 510/201,* Strasbourg: Publication Office of the European Union, 2023.

[2] Aral Aktiengesellschaft - Marktforschung, "Aral Studie - Trends beim Autokauf 2019," Aral Aktiengesellschaft, Bochum, 2019.

[3] Thomas Schütz, Hucho - Aerodynamik des Automobils, 6th ed., Wiesbaden: Springer Vieweg, 2013.

[4] United Nations - Economic and Social Council, World Forum for Harmonization of Vehicle Regulation - ECE/TRANS/WP.29/2020/77, Geneva, Switzerland: United Nations, 2020.

[5] S. Melber-Wilkending and A. Bergmann, "Aeroacoustic opitimization of the NWB airline and turning vanes based on high fidelity CFD and acoustic simulation," in *18th AIAA/CEAS Aeroacoustics Conference*, Colorado Springs, Colorado, USA, 2012.

[6] D. Martineau, S. Stokes, S. Munday, A. Jackson, B. Gribben and N. Verhoeven, "Anisotropic Hybrid Mesh Generation for Industrial RANS Application," in *AIAA 2006-534, 44th AIAA Aerospace Sciences Meeting and Exhibit, 9-12 January*, Reno, Nevada, 2006.

[7] N. Kroll, C.-C. Rossow, D. Schwamborn, K. Becker and G. Heller, "MEGAFLOW - A Numerical Flow Simulation Tool for Transport Aircraft Design," in *23rd ICAS Congress, ICAS 2002, 1.5-10.5.*, Toronto, 2002.

[8] S. Braun, "Implementation of a ln(ω)-based SSG/LRR Reynolds Stress Model into the DLR-TAU Code," Deutsches Zentrum für Luft-und Raumfahrt e.V., 2019.

[9] J. Wild, "Multi objective constraint optimization in aerodynamic design of high lift systems," *International Journal of Computational Fluid Aerodynamics*, vol. 22, no. 3, March 2008.

[10] T. Rowan, "Functional Stability Analysis of Numerical Algorithms.," University of Texas, Austin, Texas, U.S.A., 1990.

# Thermo-Engineering- Simulation-based Modular Development Process for Thermal Management of Electric Vehicles

Fabian Armbruster, Dr. Peter Ambros

TheSys GmbH
Einhornstraße 10
72138 Kirchentellinsfurt
f.armbruster@thesys-engineering.de
p.ambros@thesys-engineering.de

**Abstract:** In the various phases of the vehicle development, different numerical simulation tools are used in various departments. Focusing on the development of the vehicle thermal management system, there are also multiple numerical simulation tools been used for performance and function prognosis at part, component, module and system level. To enable the optimization of all heat and energy flows, a coupling of the thermal simulation tools with the other vehicular subsystems and the environment is indispensable.

TheSys built up a co-simulation environment integrating thermal 0D-/1D- and 3D-simulation tools for powertrain cooling and HVAC, been coupled to other vehicle subsystems. Main scope is to improve energy efficiency by thermal system and intelligent control measures. Cooling performance requirements have to be met while minimizing the energy requirement for vehicle cooling and air conditioning. The superordinate, modular structure of the simulation model enables modifications of the circuit architecture and component dimensions.

The co-simulation was developed within a French-German research project "InnoTherMS". Scope was the design of an innovative cooling system for an electrically driven, urban delivery truck. The truck was equipped with two temperature-controlled transport compartments for hot (warm meals) and cold (cold drinks) goods. These thermal compartments were coupled to the vehicle cooling system as well as to the cabin-HVAC within one integrated vehicular thermal management architecture. It utilizes a heat pump and thermal storages. As a result of the project, the electric driving range was increased by around 10% compared to a reference vehicle.

# 1 State of research

## 1.1 Thermal Management

Thermal management is the control of heat flows in the vehicle. The task of thermal management is to operate components in the respective optimum temperature range and to generate comfortable temperatures for the occupants in the cabin.

A thermal management system in an electric vehicle is generally more complex than in conventional vehicles with combustion engines. For example, the electric axle must always be cooled, while the battery must either be cooled or heated depending on the situation. Also, the various electric components often require different coolant temperatures levels, which can lead to separated low and high temperature circuits. In addition, waste heat from an internal combustion engine is no longer available for heating the cabin, so energy-efficient systems such as a heat pump are used for this purpose.

To transport the heat in the vehicle and provide the required temperatures, the refrigeration circuit and the different cooling circuits must interact optimally. The interconnection of the circuits changes depending on the heating or cooling requirements, which results in different operating modes and complex control strategies.

In the cooling circuits, cooling water transports heat from where it is generated to where it is needed in the vehicle. Due to its high specific heat capacity, the cooling water can absorb a lot of heat in a very small space, which is necessary, for example, for effective cooling of the electric axis or the battery.

A refrigerant circulates in the heat-pump or air-conditioning circuit, which can be either liquid or gaseous. The evaporation (transition from liquid to gaseous) of the refrigerant generates a cooling capacity that enables cooling even below ambient temperature. This well-known principle for air conditioning the cabin in summer is also used to cool the battery at very high outside temperatures.

In addition, the heat released during condensation (transition from gaseous to liquid) can be used to heat the cabin or battery in the winter. The refrigeration circuit is driven by an electric refrigerant compressor, which compresses the refrigerant to the desired pressure so that evaporation and condensation take place at the respective desired temperature.

Further challenges are system reliability under extreme operating conditions and in widely varying application profiles worldwide, as well as cost requirements and package constraints.

## 1.2 Methods

The rising complexity of the thermal management system and its various control units also requires new methods and approaches for the system development process, making virtual methods indispensable. CAE (Computer Aided Engineering) has become an integral part of today's development process. In addition to an increasing number of target parameters, there is a high time and cost pressure, which makes it necessary to increase efficiency. But how do I find the right simulation approach for my application among the multitude of available tools and methods? When can I investigate a system as a stand-alone system and when is the consideration of system interactions required?

The above questions can be answered with the modular development process “Thermo-Engineering” by our experts at TheSys with decades of professional experience, who understand the development, application and production requirements of manufacturers and supplier companies.

In simulation projects often the most difficult part is to know the limits of the simulation. Thermodynamic simulation ranges from the microscopic level of the radiator fin and tube, over the heat transfer network of the radiator, to the macroscopic level of the underhood cooling module, the cooling system and air conditioning system in the vehicle. The different simulation approaches are clustered as follows:

**0D**:

The 0D simulation does not include a spatial but only a temporal dependency. Our in-house developed software "TheSim" enables the development of new fins, turbulence inserts and tubes for cooling networks with prediction of performance and pressure drop. It also enables the adaptation of heat exchangers to modified installation space and operating requirements. The method is also applicable for 2-phase components such as condensers and evaporators.

**1D**:

For the design and control of the overall system under real load collectives, 1D simulation is used. The objective is to develop the system architecture and to design the cooling components. Also, to define the control strategy, to examine the limits of use or to develop an efficient operating strategy. Thus, at an early stage in the development process, long before prototypes are necessary, this can be steered in a meaningful direction. In the course of this, the required heat exchanger for the heat exchange with the environment is also defined. Common tools also used by TheSys for 1D simulation of thermal management systems are GT-Suite and KULI, Matlab/Simulink is added for the control unit development.

**3D**:

If the project faces installation space restrictions for example, the only option is to improve the heat transfer to the environment. The geometry optimization of fins, radiator network, radiator and cooling air or coolant routing is done with 3D simulation (CFD = Computational Fluid Dynamics). It can be used to examine in detail whether the selected component will also provide the required cooling performance in the installation situation of your specific application. By visualizing the flow in the room, dead spaces and other disturbing factors caused by installation resistances can be identified and eliminated. Due to increased requirements in the project or to increase the efficiency of the system, the optimization of the heat exchanger in the next development step. Another common application for 3D Simulation is the use of internal cabin flow investigations, to improve the passenger thermal comfort.

**Co-Simulation**:

Using co-simulation, the thermal management system and passenger compartment can be coupled with other subsystems and control units in the vehicle. Through the interactions of thermal management, powertrain and vehicle, all energy and heat flows are balanced, and the total energy demand can be optimized. This will decrease the overall energy consumption and increase the driving range of the vehicle.

The switch-on times of pumps and fans have a considerable influence on the overall system efficiency. Since complex interactions, e.g. with the self-heating of the battery, play a major role here, the use of a co-simulation is now necessary. The battery supplier has already developed such a model for his battery; now it is necessary to link this with the cooling model. In this way, it can be ensured that the current values such as temperatures, heat inputs, etc. are exchanged in each time step of a transient simulation.

**Digital twin:**

The concept of the "digital twin" describes the online coupling of the vehicle simulation with the vehicle test. During cooling performance measurements on the vehicle on the chassis dynamometer, driving speed, tractive force and ambient temperature are imposed on a simultaneously running thermal vehicle simulation. Through an automated comparison of the measured values (actual condition) with simulation results (expected condition), it can be detected at an early stage whether there are deviations. Discussion, testing and, if necessary, modification of the measurement program is possible in a timely manner. The medium-term goal is to build a simulation model in real-time with availability of the results at the end of the test.

## 2 French-German Research Project InnoTherMS

With an innovative thermal management system, the Franco-German research project InnoTherMS aims to reduce the energy consumption of electric vehicles to the bare minimum. As part of the project, a virtual, centralized, intelligent and predictive thermal management tool was developed for this purpose. It is based on simulation and modeling software for the cooling circuit and takes the thermal storage system into account. The InnoTherMS solution, which is particularly innovative, allows predicting and controlling the heating or cooling of an electric vehicle while consuming as little energy as possible, maximizing autonomy and ensuring the thermal comfort of passengers. The technologies developed for the InnoTherMS project are expected to improve the ranges of electric cars by at least 10 percent.

The German partners in the project include Fraunhofer, GreenIng, Esslingen University of Applied Sciences and TheSys. On the French side, the following partners are participating in the project: CETHIL (INSA Lyon), IFP Energies Nouvelles, LAGEPP (Université Claude Bernard Lyon 1), Saint Jean Industries and SEGULA Technologies. InnoTherMs benefits from public funding from the Auvergne-Rhône-Alpes region (France) and the Federal Ministry of Education and Research (Germany). TheSys was responsible for the development of the thermodynamic concept with evaluation of the range increase based on the whole vehicle simulation.

### 2.1 Customer Usage Profile

The transport and delivery of hot food and cold beverages to defined stations was specified as the usage profile (usage profile "remote kitchen"). Superimposed are road, traffic and weather profiles with influences of road gradient, driving speed, ambient temperature and solar radiation. In addition to the temperature control of the food, the temperature of the passenger cabin, battery and drive train must also be controlled.

### 2.2 Vehicle Thermal Management and Predictive Operation Control

From the definition of the customer usage profile, the required functionalities of the vehicle thermal management system emerged. The system architecture includes a high temperature (HT) coolant loop and low temperature (LT) chiller coolant loop coupled by a heat pump. The battery is tempered in a separate coolant circuit, which can be coupled to the HT or LT circuit via a shell-and-tube cooler. In addition, heat and cold accumulators as well as various auxiliary heaters are used.

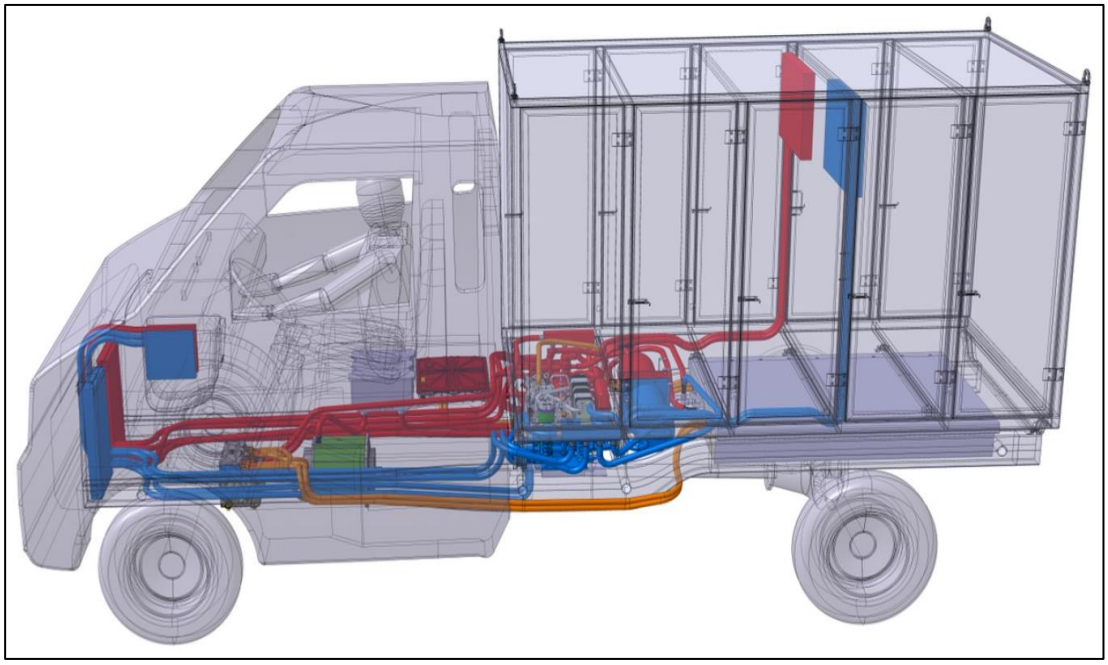

Figure 1: CAD-Model of the electric CEP (courier, express, parcel) vehicle (Source: GreenIng)

The operating control system ensures that the target temperatures of the battery, powertrain and passenger compartment are reached as quickly as possible after the start of the journey and maintained in the respective comfort temperature range for the duration of the journey. At the same time, the hot food must be prevented from cooling to below 65°C, while the cold drinks are cooled to below 8°C. The overriding objective of the operating control is to minimize the electrical energy required for the journey. The potential of a predictive operating strategy is also taken into account.

## 2.3 Sub-models and functional coupling

The project partners provided simulation sub-models for the hot/cold cabin and cargo compartment (Segula) and battery cells (CETHIL) from different simulation tool platforms, which were integrated into the GT-Suite vehicle model as part of a co-simulation with Matlab/Simulink. SJI provided the basic designs of the battery housing and the two thermal accumulators. The transfer to the corresponding GT submodels and integration into the overall vehicle model was also carried out by TheSys. The control system was provided by LAGEPP and IFPEN and adapted to the thermodynamic overall vehicle model in many iteration stages. This also included iterative changes to the model, component parameterization and control strategy.

The "Battery" submodel (CETHIL) provides the waste heat flow of the battery as a function of the electrical power (discharging, charging), the cell temperature and the SOC. The battery model is included as an FMU model in GT-Suite.

In the "cabin" submodel (SEGULA), the respective local environmental conditions such as air temperatures, flow velocities and also the CO2 content of the air are calculated for the driver and front passenger and a comfort value PPD is determined from this. For the overall model, however, only the average cabin air temperature was taken into account. The thermodynamic interface between the cabin model and the overall vehicle is the radiator or cold air heat exchanger, through which a mixture of cabin exhaust air (recirculation mode) and/or ambient air (fresh air mode) flows. The resulting air temperature depends on the coolant flow and is returned to the cabin. The cabin model is generated as a DLL file from Matlab-Simulink and integrated into GT-Suite.

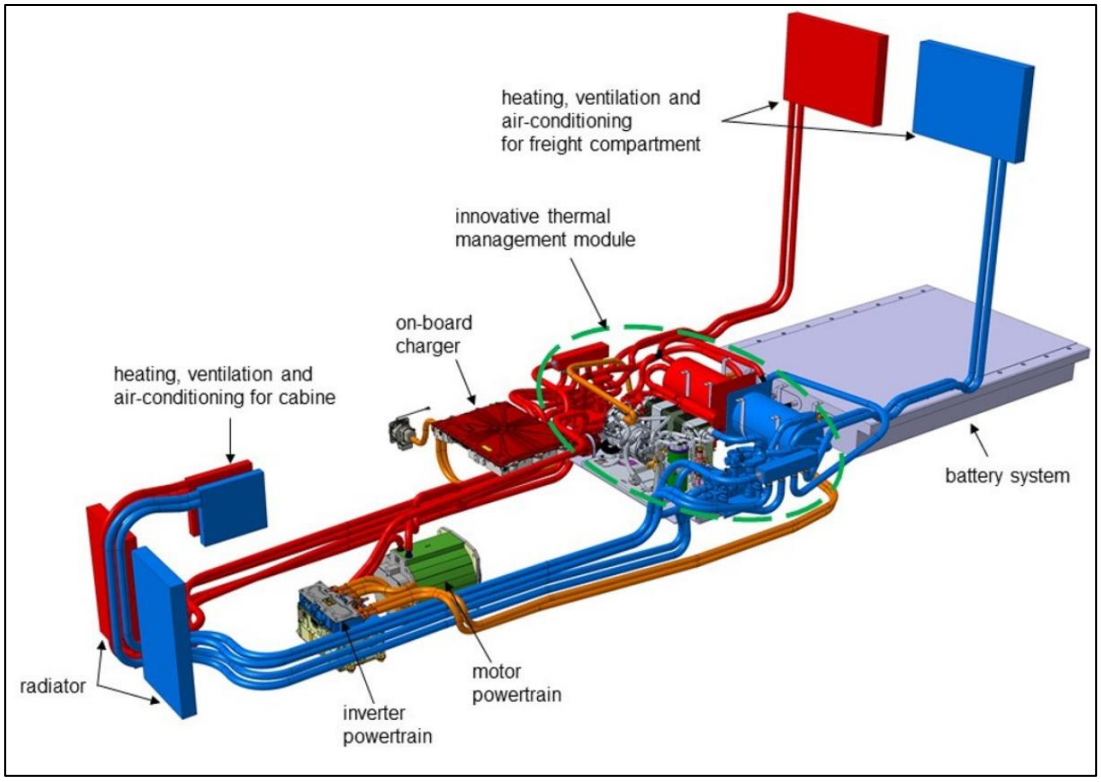


Figure 2: Coolant and Refrigerant Circuits of the vehicle (Source: GreenIng)

The submodel "cargo hold" (SEGULA) was constructed analogously and also integrated as a DLL file. It consists of two temperature-controlled cargo holds "cargo hold/hot" and "cargo hold/cold". Here, the thermodynamic interface is also represented by a cooler module in the hot and in the cold area, which are supplied with air by an electric fan.

The control (IFEN/LAGEP) was developed in parallel in a fast-running Matlab Simulink model, which first had to be aligned with the GT model. After alignment, the structure and parameters of the control of IFPEN could be developed with this model. The resulting CoSim Controls file was then integrated into the GT model by TheSys and tested. Functional safety requirements, for which EMI was responsible, were implemented as operating limits in the control system and prioritized depending on probability of occurrence and risk of damage in the control intervention.

The thermodynamic simulation model was built in a co-simulation environment to integrate software submodels of the project partners. Matlab/Simulink acts here as the master.

## 2.4 Results of the InnoTherMS project

Based on various previously defined usage profiles for hot food and cold beverage transportation, thermodynamic condition of components and passengers as well as the energy demand of a target vehicle were simulated. The calculated energy demand was used to predict the electric range of the target vehicle compared to a thermodynamic reference vehicle. For two usage profiles "Stuttgart" and "Lyon", it was possible to determine an average annual range increase of approx. 13% weighted over the ambient temperature.

Result: A range increase of 10% for a series vehicle is plausible. A conversion of the energy demand in the Stuttgart driving profile to the electric range of the vehicles yields plausible consumption values and allows a quantification of the range differences.

| | **Target vehicle** | **Reference vehicle** | **Range difference** |
|---|---|---|---|
| Summer | 30,4 kWh/100km | 30,2 kWh/100km | - 1% |
| Spring | 22,1 kWh/100km | 27,5 kWh/100km | +25% |
| Winter | 28,9 kWh/100km | 34,3 kWh/100km | +19% |

## 3 Thermo-Engineering

As an expert in vehicle thermal management, TheSys develops new cooling systems, heat exchangers and cooling components for the vehicle drive and passenger compartment air conditioning. In doing so, our solutions meet the specific requirements of electrified powertrains in passenger cars, commercial vehicles and off-road vehicles with traction battery and fuel cell. The increasing use of heat pumps leads to a close coupling of powertrain cooling and vehicle air conditioning. For our customers, global vehicle manufacturers and suppliers, this results in new cooling system architectures and heat exchangers with targeted dimensioning and specification of cooling components.

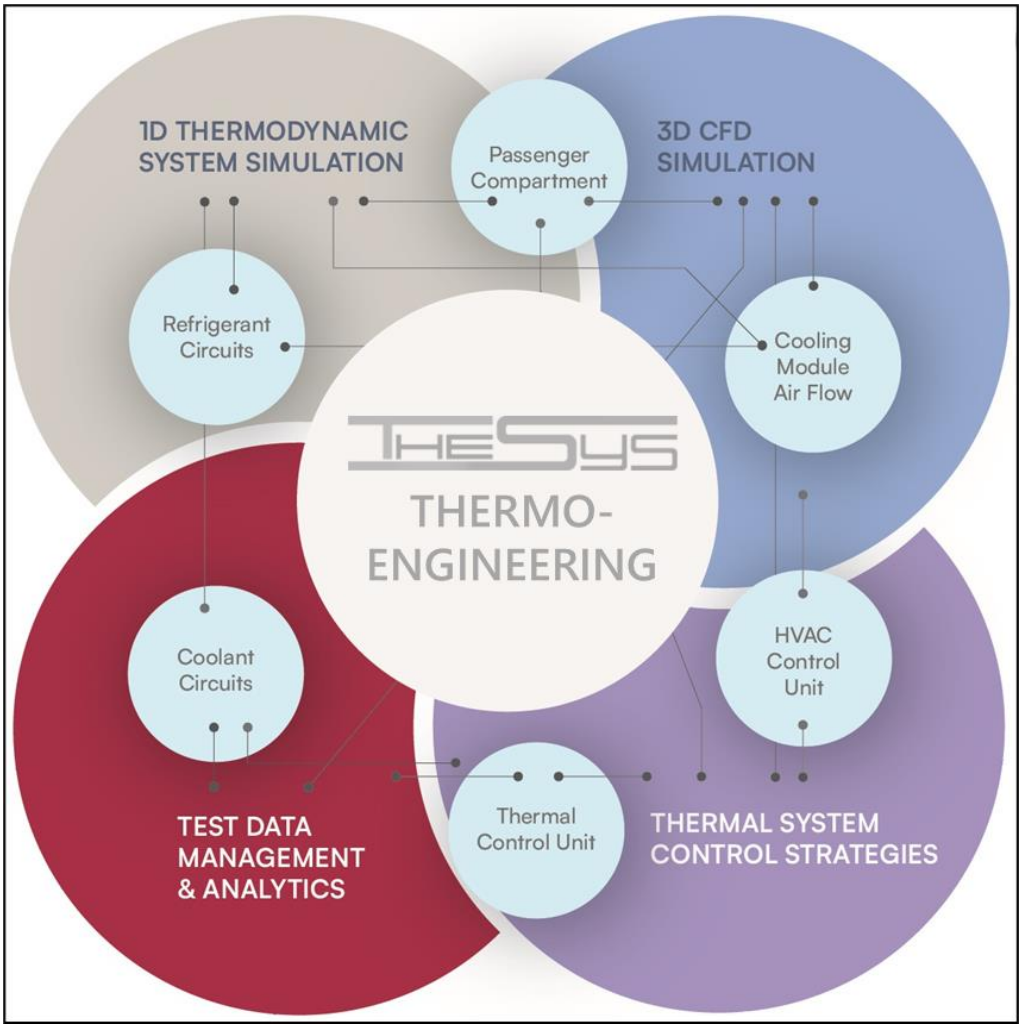


Figure 3: TheSys Thermo-Engineering Development Process

TheSys provides its customers with efficient development methods, which is summarize under the therm “Thermo-Engineering”, which reduces development times and costs in testing. An integral part of this process is the “Thermo Configurator”, which enables the application, series and sales departments to design the cooling system without the need for specific simulation skills.

Special emphasis is placed on the efficient control of all energy and heat flows in the vehicle. Operational control is developed in a co-simulation environment in which the thermal system is coupled with other subsystems of the vehicle. The system simulation is also the basis for in-vehicle operational control incorporating Car2x information and predictive strategies.

Vehicle simulation models are usually so complex that they can only be operated by a few engineers with many years of experience. For our customers, this often leads to significant personnel bottlenecks, and projects get behind schedule. What would it be like if there were a user interface that allowed application engineers, for example, to configure the right cooling system for their application independently without software training? How about if salespeople from supplier companies could quantify the function and customer benefit of their product in the target vehicle?

Our vehicle configurator allows the selection of vehicle, drive, cooling circuit and cooling component from an approved library, similar to the configuration of a new car on the Internet. It prevents unacceptable combinations and creates the associated vehicle simulation model fully automatically in the background. Selection of the driving route and the result is output in a standardized form. Our customers have been using the configurator for years and it is constantly being further developed. Currently it allows the selection from more than 250 circuits, components or even control units for more than 30 different vehicle types. Depending on the focus of your investigation, you can choose between detailed and simplified models. If a subsystem is not relevant it can be replaced by dummy models, to ensure that the overall simulation run time is as fast as possible.

A good simulation model is only as good as the data on which it is based on. The ability to validate the models is essential for the validity of these elements. This modular simulation environment also provides an interface to read and process measurement data and to calibrate the models based on them. The possibility of coupling the same control units as used in the vehicle, enables transient simulations which can be easily compared to measurement driving cycles.

## 4 References


Sachbericht zu Verwendungsnachweis Teil 2 - Projektbericht – Eingehende Darstellung Innovative Predictive High Efficient Thermal Management System (InnoTherMS), Förderkennzeichen 03INT601AD, 10.08.2022, Dr. Peter Ambros

Fa. Mobileye: https://www.next-mobility.de/mobileye-will-fahrerlose-lieferwagenausstatten-a-1014855/

Solarenergieforschung Hameln (ISFH): https://www.next-mobility.de/sonnenanbeter-namens-street-elektro-laster-mit-solaranlage-a-1014329

Fa. Nuro, Fahrzeug R3: (24auto.de) https://www.24auto.de/news/nuro-r3-roboterauto-pizza-stauraum-hoechstgeschwindigkeit-usa-walmart-dominos-fedex-los-angeles-91248025.html

Böhme, M., Gerdts, M., and Trapp, C., "Backend-Based State-of-Charge Control as a Predictive Operating Strategy for a Serial PHEV," SAE Technical Paper 2023-01-1201, 2023, doi:10.4271/2023-01-1201.

Grbavac, A., Angerbauer, M., Grill, M., Itzen, D. et al., "Categorizing Simulation Models Using Convolutional Neural Networks," SAE Technical Paper 2023-01-1217, 2023, doi:10.4271/2023-01-1217.

Dettinger, F., Jazdi, N., Weyrich, M., Brandl, L. et al., "Machine-Learning-Based Fault Detection in Electric Vehicle Powertrains Using a Digital Twin," SAE Technical Paper 2023-01-1214, 2023, doi:10.4271/2023-01-1214.

Hrvanovic, D., Haberl, H., Krammer, M., and Scharrer, M.K., "Distributed Co-Simulation for Effective Development of Battery Management Functions," SAE Technical Paper 2023-01-1200, 2023, doi:10.4271/2023-01-1200.

Salah, A., Abu Mohareb, O., Brosi, F., and Reuss, H.-C., "Coordinated EV Charging Based on Charging Profile Clustering and Rule-Based Energy Management," SAE Technical Paper 2023-01-1226, 2023, doi:10.4271/2023-01-1226.

# Holistic System Simulation to address Thermal Management Challenges in Fuel Cell based Mobility Platforms

Christoph Böttcher, Nils Framke

Thermal Fluid Systems
Gamma Technologies GmbH
Danneckerstr. 37
70182, Stuttgart
c.boettcher@gtisoft.com, n.framke@gtisoft.com

**Abstract:** Thermal security of fuel cell powertrains is very challenging as the optimum operating condition of a fuel cell lies in a very small temperature range and is much lower than for combustion engines. The lower optimum level of the coolant temperature of a fuel cell powertrain makes the heat rejection to the ambient challenging as it leads to smaller temperature differences between the coolant and ambient at the heat exchangers that are used to reject the heat to the ambient. Therefore cooling system concepts need to be re-designed, optimized and verified for dynamic loads to address those thermal management challenges.

In this paper a holistic system simulation methodology is presented to address the thermal management challenges of a fuel cell powertrain of a heavy duty truck at hot ambient conditions and long haul missions. The holistic system simulation methodology includes a design comparison of different heat exchanger layouts, the optimization of the selected heat exchangers, and finally the verification of the optimized heat exchanger stack layout for dynamic loads by performing transient drive cycle simulations.

## 1 Introduction

The transportation sector contributes with around 23% to the global CO2 emission with freight transportation on road as one of the major contributors [1]. As over three quarter of the inland freight transport in the EU is performed by road with heavy duty trucks [2], the reduction of tailpipe emissions of heavy duty trucks is crucial to reach the emission reduction goals defined in the European Green Deal.

Therefore alternative powertrain solutions like fuel cell powertrains are investigated and will play a signification role for the future reduction of greenhouse gas emissions especially in the road freight transportation sector [3].

In comparison to the currently used diesel engine, fuel cell powertrains have no tailpipe emissions and have a higher energy efficiency. In comparison to battery powertrains they are expected to offer a larger range at lower vehicle weight and a faster refueling [3]. Global truck companies like Daimler Truck [4], Volvo Trucks [5], MAN [6], PACCAR [7], and others are focusing on the research and development of a fuel cell powertrains for trucks.

Most truck fuel cell powertrains use a proton exchange membrane fuel cell (PEMFC), which has advantages such as low operating temperature, high energy conversion efficiency, and swift start-ups. However the lower operating temperatures make the thermal management of fuel cell powertrains challenging. Further high temperature gradients in the fuel cell stack during dynamic load variations have a negative impact on the fuel cell stack as they cause thermal stresses and stack material degradation [8].

Therefore it is mandatory to develop a thermal management system that is capable of a fast and efficient heat rejection and obtains the optimum operating temperature even under dynamic load changes to ensure thermal security among all operating conditions. A holistic system simulation of the thermal management system of a fuel cell truck enables fast analysis, comparison and optimization of different cooling concepts and system layouts. Further it enables optimization of selected components of the cooling circuit and verification of the optimized design integrated into the complete fuel cell truck system during dynamic loads by transient drive cycle simulations.

## 2 Fuel Cell Truck System Simulation Model

For the simulation based development methodology a GT-SUITE system model of a fuel cell truck is used. The simulation model in Figure 1 includes a detailed fuel cell powertrain model including two PEM fuel cell stacks, a battery, an electric motor and a power converter. The fuel cell powertrain is connected to a vehicle model of the truck for calculation of the longitudinal vehicle dynamics. Further the simulation model includes a detailed thermal management system that is tightly coupled to the fuel cell powertrain.

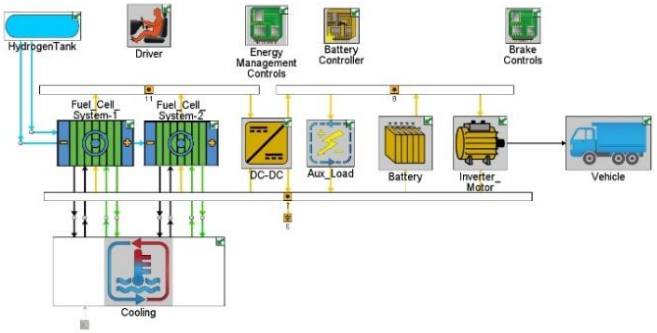


Figure 1: GT-SUITE System Simulation Model

## 2.1 Powertrain System Model

The powertrain system in Figure 2 includes all relevant flow, electrical, electro-chemical and controls components to enable detailed and realistic representation in the simulation model.

The electric model is composed of one electric motor with inverter efficiency integrated, a 80 kWh battery, a DC/DC converter and two fuel cells stacks with 600 cells each, an active surface area of 250 cm² and a maximum rated power of 110 kW. More details on the fuel cell system can be found in section 2.3. The fuel cell stacks are fueled with H2 which comes from the H2 tank of the model.

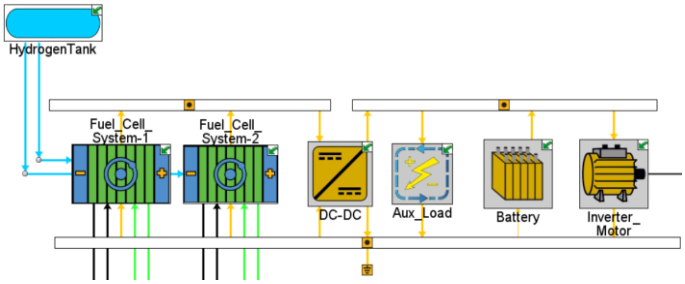


Figure 2: Fuel Cell Truck Model (Electrical Part)

The torque demand and the speed of the electric motor is calculated using the mechanical vehicle model and depends on the drive cycle profile imposed in the simulation model. A driver model is included in the system model to model a realistic driver behavior.

The power split between the battery and the fuel cell stack is defined based on the SOC of the battery and minimum and maximum limits for the power and the ramp rate that can be supplied by the fuel cell stack. Mostly the battery supports the fuel cell at high dynamic loads.

In addition, the electrical powertrain model takes into account the power demand of all the accessories of the different parts of the fuel cell truck, including the fuel cell stack compressors, H2 recirculation pump and cooling pump. This enables to calculate a full system power balance.

## 2.2 Vehicle System Model

The mechanical vehicle model shown in Figure 3 directly interacts with the electrical powertrain model. It includes a truck body, axles, tires and a differential. The truck body consists of a main body and a trailer. Each part is defined by its weight and its aerodynamic properties. With this information the longitudinal motion of the truck is calculated for the different driving profiles.

The axle and tire model include the traction and rolling resistance characteristics. Finally, the differential is an open differential where the axles and the electric motor can operate at different speeds.

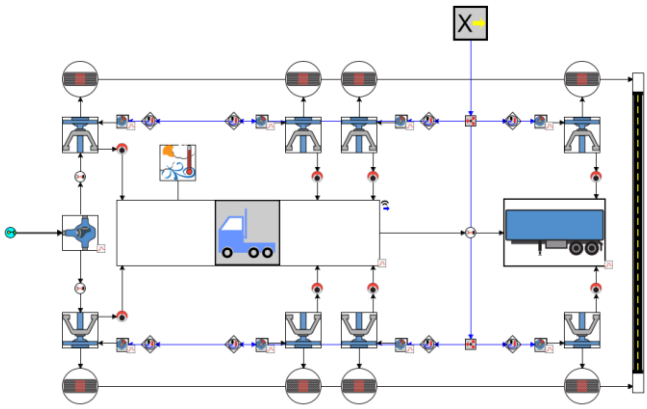

Figure 3: Fuel Cell Truck Model (Mechanical Part)

## 2.3 Fuel Cell System Model

The fuel cell system model in Figure 4 is composed of a fuel cell stack, coupled with the anode loop, the cathode loop, and the cooling circuit. Further the fuel cell stack is directly connected to the electrical circuit.

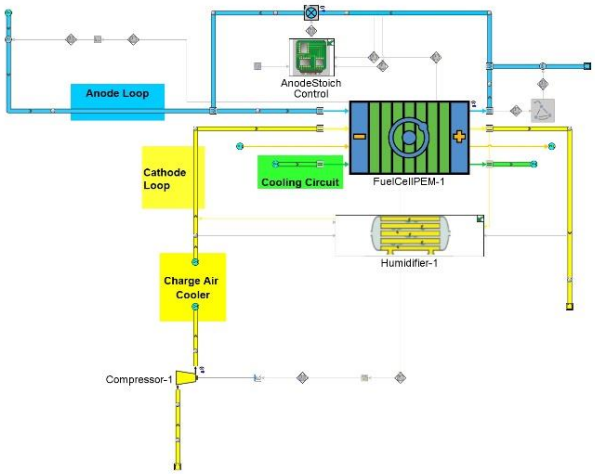


Figure 4: Fuel Cell Balance of Plant Model

The anode loop starts at the H2 tank. A pressure regulating system including valves and controls lowers the 700 bar tank pressure to the anode loop operating pressure. The anode loop simulation model also includes the recirculation blower, stoichiometry control and the purge valve system and controls. This allows to accurately account for the energy losses that are driven by the purging strategy selected for this powertrain model.

The cathode loop includes a compressor, a humidifier and an indirect charge air cooler linked to the cooling circuit. The compressor is controlled based on the fuel cell current power demand and the cathode stoichiometry.

The fuel cell stack is modelled using GT-SUITEs predictive electrochemical model, accounting for the physical characteristics of all layers which compose the fuel cell stack (gas diffusion layers, catalyst layer, membrane, bipolar plates). The fuel cell stack also includes a thermal model which is connected to the cooling circuit and a flow model to model consumption of H2 at the anode and O2 at the cathode, gaseous species crossover, and water crossover [9].

## 2.4 Cooling System Model

The cooling system of the fuel cell truck in Figure 5 consists of two cooling circuits. A high temperature (HT) cooling circuit to ensure the thermal security and best operating condition of the two fuel cell stacks. In addition two indirect water charge air coolers are connected to the high temperature coolant circuit to cool cathode side airflow following its compression.

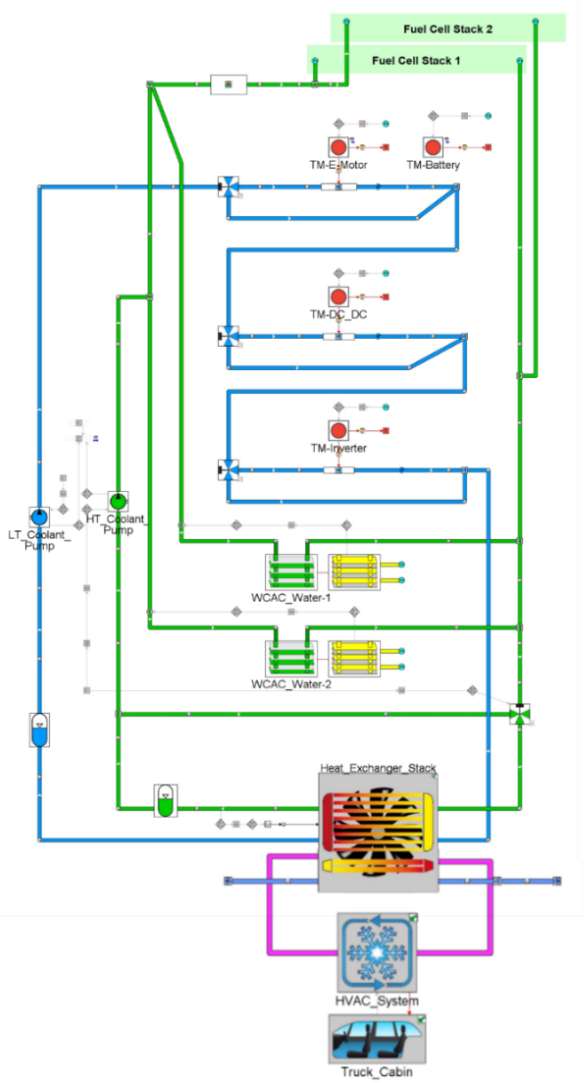


Figure 5: Fuel Cell Truck Cooling System Model

The second cooling circuit is a low temperature (LT) cooling circuit to ensure the thermal security of the electric motor and other power electronic components.

As the battery of the fuel cell truck is used only to support the fuel cell powertrain in phases of highly dynamic load changes its heat can be rejected to the environment using an air cooling concept to ensure the thermal security of the battery. The cooling system model includes an air-conditioning system for thermal conditioning and dehumidification of the truck cabin as well.

The heat exchanger stack in Figure 6 is modelled in GT-SUITEs integrated 3D modelling environment COOL3D. It includes the condenser of the air-conditioning system, the HT and LT radiator of the cooling system and a cooling fan. Further it includes a blockage at the inlet to model the underhood inlet grille. The two radiators are mounted vertically with the coolant inlet at the top of the heat exchanger. The condenser is mounted horizontally.

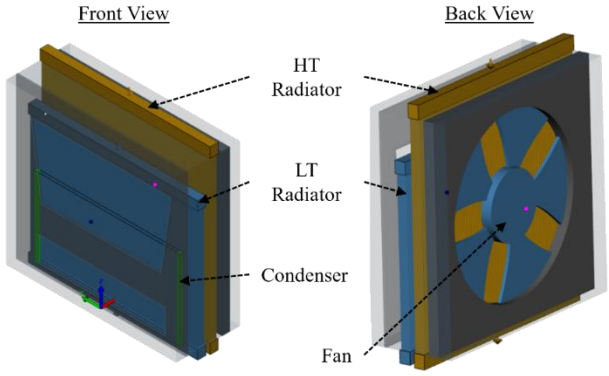


Figure 6: Heat Exchanger Stack Model

The cooling systems includes control functions to control the temperature of the fuel cell stacks and the other fuel cell powertrain components. The input signal of the electric HT coolant pump is controlled by a PID controller which targets the fuel cell stack outlet temperature of 75 °C for best operating conditions of the fuel cell. In addition to that a bypass valve is used to bypass the HT radiator for fast heat-up of the fuel cell stacks at low initial temperature conditions and to prevent low fuel cell temperatures and dynamic loads. The goal of the controls is to keep the fuel cell stack temperature in a range of 65 to 85 °C.

The input signal of the electric LT coolant pump is controlled by a PID controller which targets the temperatures of the electric motor and the power electronics components. All components can be bypassed to ensure a fast heat-up of the components at low initial temperature conditions.

The fan controller controls the fan speed and therefore the air flow through the heat exchanger stack in combination with the vehicle speed. It targets different coolant outlet temperatures of the HT and LT cooling circuit to ensure a suifficient temperature gradient between the cooling temperature and ambient temperature at all operating conditions for efficient heat rejection to the ambient air.

## 3 Simulation based Optimization of the Cooling System

The fuel cell truck system simulation model described in the previous chapter is used to optimize the cooling system of the fuel cell truck. The goal of the simulation based optimization of the cooling system is to ensure the thermal security of the fuel cell powertrain, especially of the fuel cell stacks.

As this study focuses on trucks that are used for long haul routes, constant speed driving at 80 km/h is used as steady-state design condition in the first stage of the simulation based development. As hot ambient conditions cause the smallest temperature gradients at the heat exchangers of the heat exchanger stack, an ambient temperature of 45 °C is used to ensure suifficient heat rejection at hot ambient conditions.

### 3.1 Heat Exchanger Stack Component Selection

The first step of the simulation based development is to find the heat exchanger layout that is best suited to reject the heat of the fuel cell stacks and the other powertrain components by comparing different heat exchanger layouts. Figure 7 shows the two different designs of the heat exchangers stack with different heat exchanger layouts. The single pass design uses single pass heat exchangers as LT and HT radiator. The dual pass design uses heat exchangers with 2 passes as LT and HT radiator.

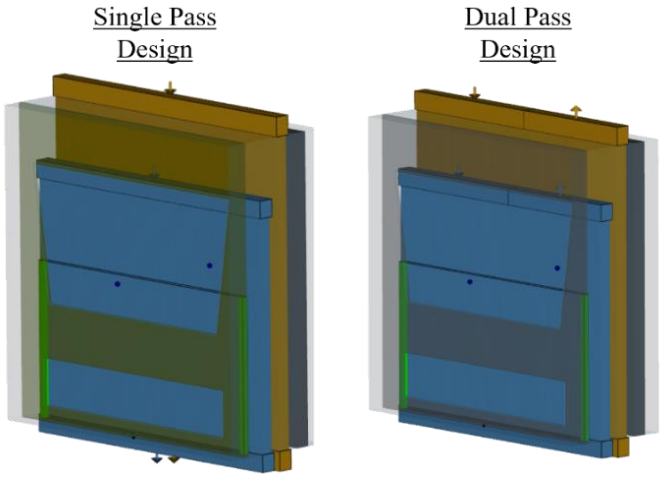


Figure 7: Single and Dual Pass Heat Exchanger Stack Design

Steady-state simulations at a constant vehicle speed of 80 km/h and an ambient temperature of 45 °C are performed to compare both designs under high load conditions. The coolant pumps and the coolant fan are operating at maximum speed to analyze the cooling systems performance at maximum power conditions.

As can be seen in Figure 8, the dual pass design is better suited to ensure suifficient heat rejection at the fuel cell stacks, whereas the single pass design shows advantages for the cooling of the other powertrain components. Therefore a dual pass heat exchanger is used for the HT radiator and a single pass heat exchanger is used as LT radiator.

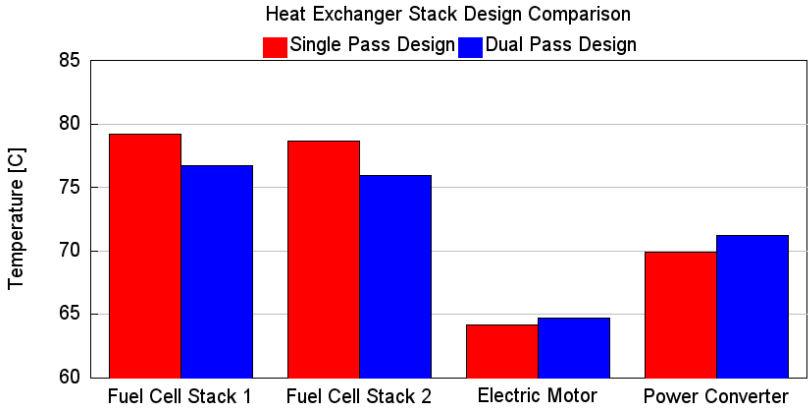


Figure 8: Heat Exchanger Stack Design Comparison

However with neither of the designs, the target fuel cell stack temperature of 75 °C is reached. Therefore the size of the heat exchangers is optimized in a next step.

## 3.2 Heat Exchanger Component Optimization

To optimize the size of the LT and HT radiator, the Integrated Design Optimizer of GT-SUITE is used. The maximum size of the heat exchangers is limited by the available design space of 950 x 950 mm. The size of the two radiators is optimized with respect to the fuel cell stack temperature and the DC/DC converter temperature.

The HT radiator is located downstream of the LT radiator in the heat exchanger stack. Therefore the size of the LT radiator directly influences the free-streaming area of the HT radiator. Therefore the size of both radiators needs to be optimized together. Because the second radiator has two passes and the distribution of the pipes between the two passes needs to be defined for the optimization, the number of tubes of the first pass is optimized and the number of tubes of the second pass is the number of tubes of the first pass minus five.

Figure 9 shows the optimization results of the LT radiator. The best optimization design is marked with a large cross.

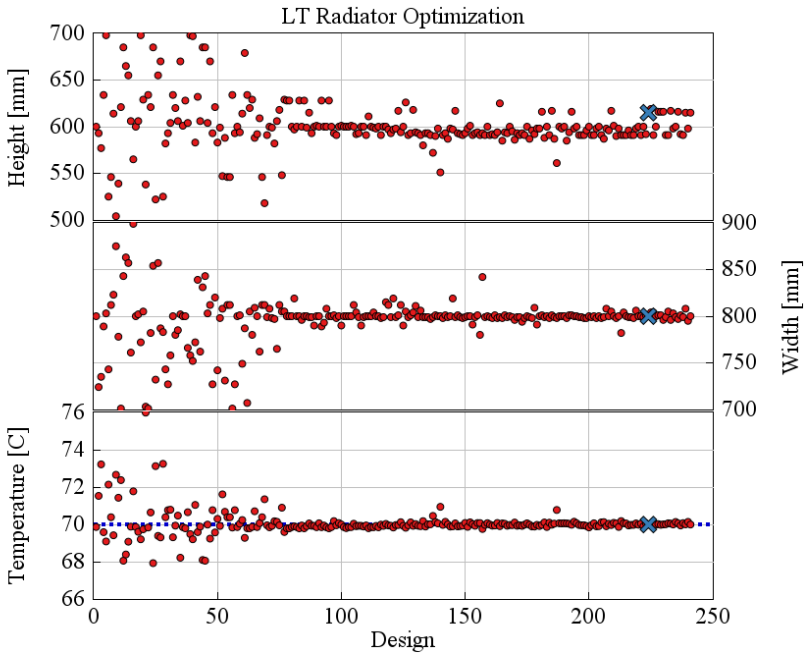


Figure 9: LT Radiator Optimization Results

Figure 10 shows the optimization results of the HT radiator. The best optimization design is marked with a large cross again.

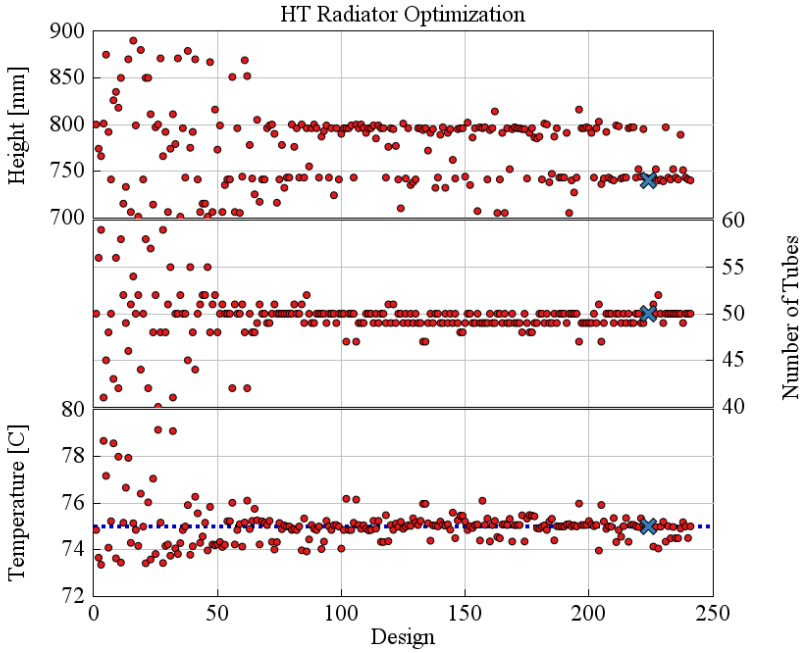


Figure 10: HT Radiator Optimization Results

The optimization results in a LT radiator size of 615 x 800 mm and a HT radiator site of 740 x 756.5 mm. As can be seen in Figure 9 and Figure 10, the target of 75 °C of the fuel cell stack outlet temperature and the target of 70 °C of the DC/DC converter outlet temperature are both reached with the optimization result.

### 3.3 Cooling System Verification through Drive Cycle Simulations

After the optimization of the LT and HT radiator of the heat exchanger stack, the thermal security of the fuel cell powertrain for dynamic load changes is verified by running transient drive cycle simulations. Like the steady-state analysis and optimization, the transient drive cycle simulations are performed at hot ambient conditions and therefore at an ambient temperature of 45 °C. The goal is to keep the fuel cell stack temperature within a range of 65 to 85 °C throughout the whole drive cycle whereas some short peaks to 90 °C or short drops to 60 °C are considered acceptable.

As drive cycles, two VECTO mission profiles long haul and regional delivery are used whereas the long haul is considered the most relevant one for the fuel cell truck in this study. The VECTO mission profiles have a total distance traveled of 100 km and are available on the website of the European Commission [10]. Further a real driving route of the Brenner Pass created with GT-RealDrive is used to test the cooling system at real driving conditions.

The simulation results of the VECTO mission profile long haul in Figure 11 show that the designed cooling system with the optimized heat exchanger stack is capable of keeping the fuel cell stack temperature and the DC/DC converter and electric motor temperature in the desired temperature range.

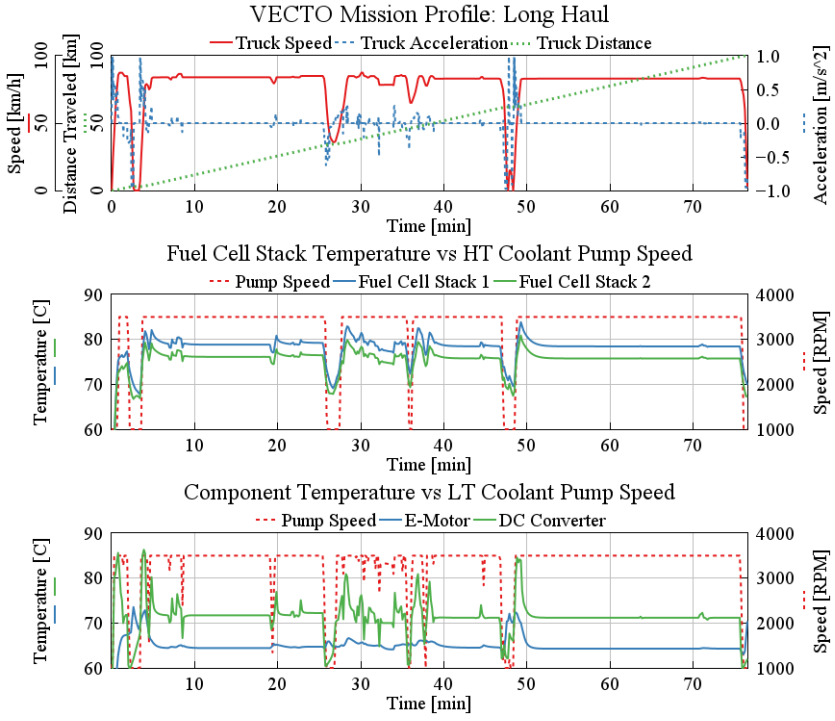


Figure 11: VECTO Mission Profile Long Haul Simulation Results

The simulation results of the VECTO mission profile regional delivery in Figure 12 show that even under more dynamic driving conditions, the designed cooling system with the optimized heat exchanger stack is capable of keeping the temperatures of the fuel cell powertrain in the desired temperature range.

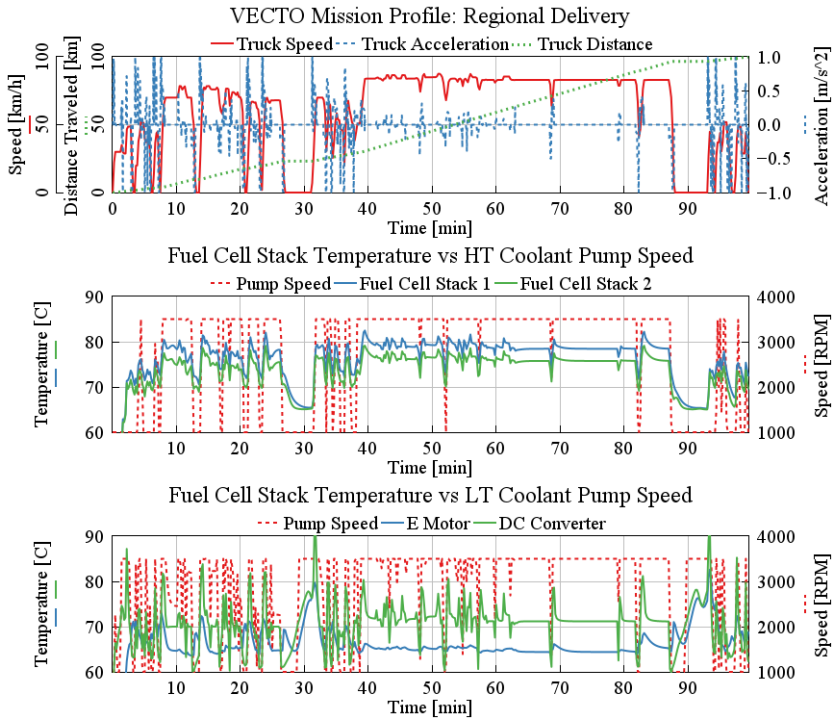


Figure 12: VECTO Mission Profile Regional Delivery Simulation Results

The simulation results of the real driving route over the Brenner Pass from Italy to Austria in Figure 13 show that the designed cooling system is capable of ensuring the thermal security of all fuel cell powertrain components at real driving scenarios.

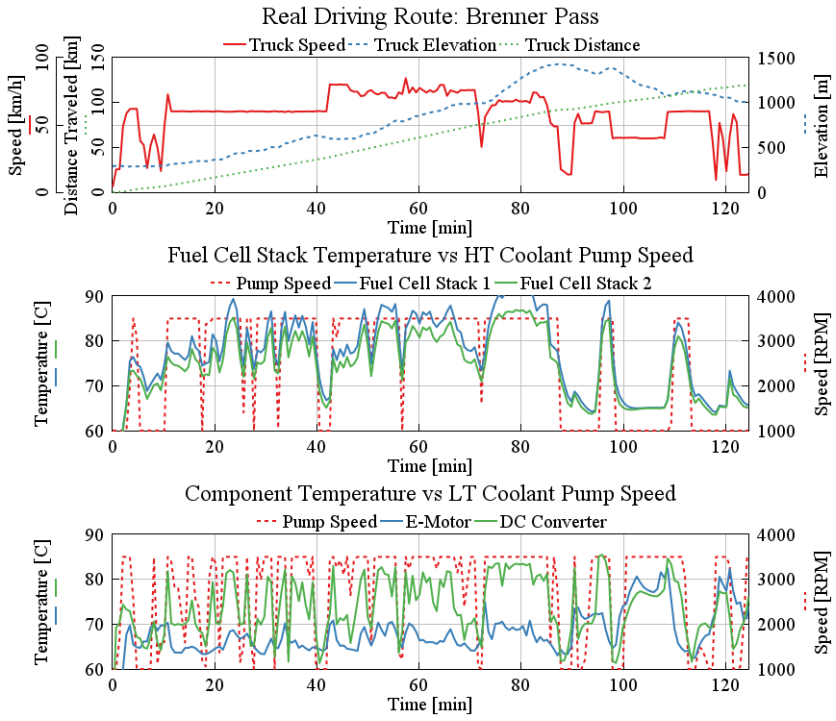


Figure 13: Real Driving Route Brenner Pass Simulation Results

At about 75 minutes of driving in the Brenner Pass scenario it can be observed that the fuel cell stack, that was observed to show overall higher outlet temperatures in the VECTO cycles, reaches an outlet temperature of 90 °C. While under the boundary conditions of this study it also shows that the cooling system is designed with narrow margins at high load high temperature conditions. Also we here we are demonstrating the advantages of the proposed holistic methodology. Following the finding from the Brenner Pass results the holistic system model can easily be used to test additional load cycles or to develop appropriate derating strategies of the powertrain.

## 4 Conclusion

We present a methodology to address the thermal management challenges of fuel cell based mobility platforms with holistic system simulation to design and optimize the cooling system and heat exchanger stack of a fuel cell truck using the simulation software GT-SUITE.

To overcome the challenge of the low temperature difference in the cooling system at hot ambient conditions the design and size of the LT and HT radiators are optimized with respect to the fuel cell stack and powertrain component temperatures to ensure thermal security of the fuel cell powertrain.

The VECTO mission profiles long haul and regional delivery and a real driving route over the Brenner Pass created with GT-RealDrive are used to verify the thermal security of the fuel cell powertrain over the complete operating range at dynamic loads.

For future studies, the holistic system simulation approach can be extended to additional areas like selection and optimization of other components of the fuel cell truck cooling system and its control logics.

## 5 Bibliography


[1] ICCT, “Global Transportation Roadmap Model”, ICCT, https://theicct.org/a-world-of-thoughts-on-phase-2/, 2016.

[2] Publication Office of the European Union: “Key figures on European transport”, Publication Office of the European Union, https://ec.europa.eu/eurostat/, 2022.

[3] Cunanan C, Tran M-K, Lee Y, Kwok S, Leung V, Fowler M.: “A Review of Heavy-Duty Vehicle Powertrain Technologies: Diesel Engine Vehicles, Battery Electric Vehicles, and Hydrogen Fuel Cell Electric Vehicles.” Clean Technologies, 2021.

[4] Daimler Truck: "Touring the Alps with battery and hydrogen – CO2-neutral trucks from Daimler Truck demonstrate their capabilities", Daimler Truck Website, https://media.daimlertruck.com/marsMediaSite/ko/en/52212995, 2023.

[5] Volvo Trucks: "Volvo Trucks to begin customer testing of fuel cell trucks in 2025", Volvo Trucks Website, https://www.volvotrucks.com/en-en/news-stories/press-releases/2022/sep/volvo-trucks-to-begin-customer-testing-of-fuel-cell-trucks-in-2025.html, 2022.

[6] MAN Truck and Bus: "MAN accelerates change to zero-emission drive systems", MAN Truck and Bus Website, https://press.mantruckandbus.com/corporate/man-accelerates-change-to-zero-emission-drive-systems/, 2022.

[7] PACCAR: "PACCAR and Toyota expand hydrogen fuel cell truck collaboration to include commercialization", PACCAR Website, https://www.paccar.com/news/current-news/2023/paccar-and-toyota-expand-hydrogen-fuel-cell-truck-collaboration-to-include-commercialization/, 2023.

[8] Woo, J.; Kim, Y.; Yu, S.: “Cooling-System Configurations of a Dual-Stack Fuel-Cell System for Medium-Duty Trucks.”, Energies, 2023.

[9] C. Altenhofen, A. Mouffouk: "Fuel Cell Prototype Digitization from Component Design to System Analysis", Gamma Technologies LLC, https://www.gtisoft.com/wp-content/uploads/2021/11/GT-Fuel-Cell-Solution_HydrogenExpo.pdf, 2021.

[10] The European Commission’s science and knowledge service – Joint Research Center: “VECTO – Overview” , European Commission, https://climate.ec.europa.eu/system/files/2018-12/201811_overview_en.pdf, 2018.

# Shape Optimization Investigation of Next Generation Truck Design for Aerodynamic Efficiency

Faegheh Ghorbanishohrat, Brian R. McAuliffe

National Research Council Canada
Ottawa, Canada

Faegheh.ghorbanishohrat@nrc-cnrc.gc.ca
Brian.McAuliffe@nrc-cnrc.gc.ca

**Abstract:** Emerging zero-emission heavy-duty vehicle (ZEHDV) concepts provide a unique opportunity in the industry to optimize heavy-duty vehicle (HDVs) shapes with a view to increasing the aerodynamic efficiency of these vehicles. Accordingly, a research project was initiated to examine the potential energy savings and range extension of ZEHDVs associated with reduced aerodynamic drag. Preliminary experiments on a conceptual cab design with a modified front, including shallower surface angle and large corner radii, were performed in the NRC 9m Wind Tunnel using a 30% scale truck model. Results revealed a 7-9% reduction in the aerodynamic drag-area of the vehicle. For further study, Computational Fluid Dynamics (CFD), and parametric design were utilized to examine various cab geometries through airflow, surface pressure, and drag coefficient analyses. Various geometry cases were considered based on aerodynamic characteristics such as corner radii, cab frontal area, windshield angle, bumper shape, and underbody airflow. CFD results have shown up to 8% variability in drag coefficient resulting from changes to the shape of the cab model with these aerodynamic considerations. This investigation has guided the design of a new ZEHDV model for wind-tunnel testing in a subsequent phase of the study.

## 1 Introduction

Aerodynamic drag significantly affects the energy consumption of on-road vehicles, with heavy-duty tractor-trailer combinations using approximately half of their engine power to overcome this resistance at highway speeds [1,2]. As heavy-duty manufacturers transition to new power sources and drivetrain technologies, there are opportunities to enhance the aerodynamic performance of these vehicles. Some manufacturers are introducing radically redesigned zero-emission trucks, while others maintain traditional shapes. These changes can impact overall aerodynamics and alter the benefits of trailer aerodynamic technologies. It's essential to understand the differences in aerodynamic performance between conventional and emerging ZEHDV concepts to evaluate energy efficiency for various duty cycles, informing energy efficiency and regulatory initiatives for a decarbonized future in freight transportation [3,4].

This study addresses this subject by investigating aerodynamic shape optimization of emerging ZEHDVs through wind tunnel testing and computational fluid dynamics analysis.

## 2 Experimental Setup

***Wind tunnel***: The experiments were conducted in the NRC 9m wind tunnel, a closed-loop facility featuring a test section measuring 9.1m wide × 9.1m high × 22.9m long, with a 6.1m diameter turntable. The wind tunnel is equipped with a 6.7 MW DC motor that drives a fan capable of generating wind speeds of up to 55 m/s, and a ground effect simulation system. To measure aerodynamic forces and moments, a 30% scale model is affixed above a rolling road, supported by streamlined struts connected to a six-axis balance.

***Test models****:* Experiments employed a 30% scale tractor-trailer model from NRC, mimicking diverse heavy-duty vehicle (HDV) setups. It offers flexibility for various cabin types and trailer variations, with the default configuration being a dry-van semi-trailer with and without aerodynamic devices. The three tractor variations are characterized as follows and displayed in Figure 1:

- The day-cab tractor: initially resembling an international ProStar short sleeper cab, the tractor underwent adjustments to the bumper, hood, A-pillars, and roof fairing. This adaptation enables it to transform into a more compact high-roof day-cab model, utilizing the same front components while incorporating unique cab-back and high-roof fairing designs by NRC, aimed at enhancing airflow efficiency over the trailer.
- The long-sleeper-cab tractor: is derived from a 3D scan of a 2016 Kenworth T680 high-roof long-sleeper cab. This model closely replicates the external shape of the full-scale vehicle, although some differences exist in engine bay, suspension, and drive-line components due to its underlying structure based on the short-sleeper model.

- The zero-emission-cab tractor: is derived from a ProStar day-cab tractor, but it has been altered with changes above the hood and in front of the windscreen to emulate the features seen in emerging ZEHDVs. These adjustments involve the use of a hand-carved modeling-foam insert to achieve a more gradual surface angle and incorporate larger corner radii. Additionally, the upper front grille was masked to replicate the reduced cooling air-flow [5].

Figure 1: Three wind tunnel tractor-trailer scale models: day-cab tractor(left), sleeper-cab tractor (middle), and zero-emission-cab tractor (right)

## 3 Computational Setup

CFD simulations were conducted using the Ansys-Fluent solver. A simplified 5% scale HDV model was initially used to conduct cross-validation with experimental data and identify the appropriate simulation process. The next step involved the optimization of the ZEHDV cab design through the parametric geometry and selected CFD simulation method [4].

### 3.1 Models

***Preliminary HDV model**:* A 5% scale model of a simplified HDV contained shape characteristics of emerging ZEHDV concepts based on a research model developed at NRC. The cab length represents a model approximately halfway between a day-cab and a sleeper cab with an equivalent 40 ft trailer length [6,7], Figure 2.

***Parametric Cab Design Model:*** For aerodynamic optimization of cab geometry while retaining the legal restrictions of heavy vehicles in North America, a parametric CAD model was created using SolidWorks software. Cab width, height, length, corner and roof radii, area of stagnation region, windshield and roof angles, wheel house shape, and height of under-body from the ground are geometry parameters that affect aerodynamic performance [8] and were considered in preparing the parametric geometry of the ZEHDV model.

The model was initially prepared at 30% scale to be comparable with the existing NRC long-sleeper-cab tractor model. For subsequent analyses, a full- scale version was utilized in CFD simulations. The clearance height from bumper to the ground was set to 0.024 m and the cooling flow was not represented in the tractor model. The trailer model was modified by adding a side-skirt with a chamfered front edge, representing flush-mounted skirts with full-scale dimensions of 7.9 m in length (26 ft) and 0.91 m in height (3 ft), and by simplifying the geometry of the trailer parts and removing design features that were considered to be insignificant. Figure 3 shows the initial design with large-radius corners and an overall shape similar to emerging ZEHDVs with no mirrors added to the geometry. This model was considered the ZEHDV baseline and was used for the first case study in the CFD aerodynamic optimization process.

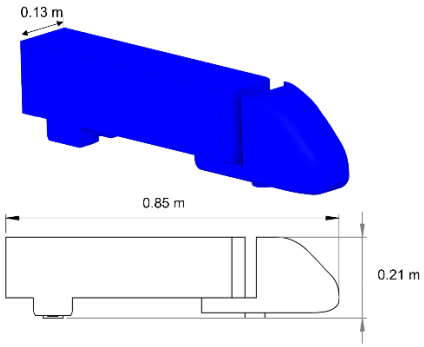


Figure 2: 5% scale preliminary HDV model

### 3.2 Simulation setup

Various turbulence models, such as Reynolds Averaged Navier-Stokes (RANS), Unsteady Reynolds Averaged Navier-Stokes (URANS), Detached Eddy Simulation (DES), and Delayed Detached Eddy Simulation (DDES), were assessed at different yaw angles (0° and 15°) using the 5% scale model and its available experimental data. Although not an exact match, the results showed similarities in flow behavior and the impact of yaw angle on forces. The study employed different turbulence models, poly-hexcore meshes, and boundary conditions based on NRC wind tunnel experiments. The RANS approach with the k-ω SST model was selected for the CFD optimization process, requiring more than 25 updates to achieve the optimized aerodynamic geometry of the ZEHDV model.

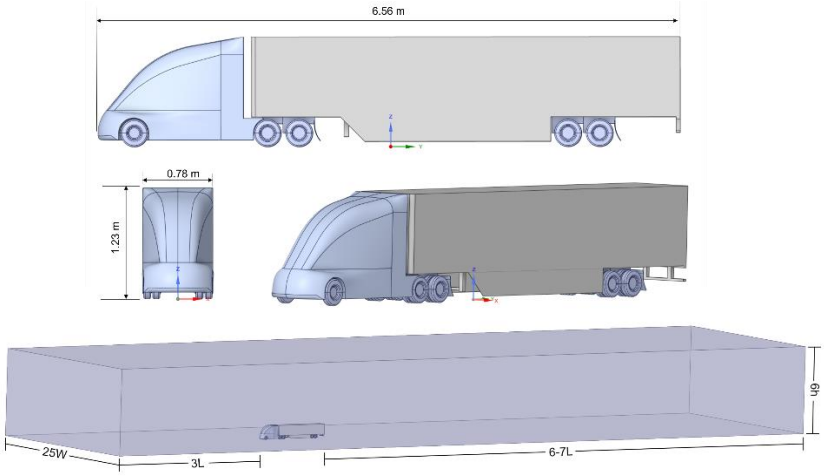


Figure 3: Schematic of the 30% scale model of the baseline aerodynamic model the computational domain

The computational domain was defined based on a literature review and industry best practices for simulating commercial ground vehicles [9,10,11], featuring a length of 242 m, extending 70 m ahead of and 150 m behind the vehicle, with the width of 64 m, and a height of 26 m for ZEHDV model. This represents a domain that extends approximately 3L upstream, 7L downstream, 25W wide, and 6H high according to the vehicle dimensions (L×W×H). The width of the domain was increased for cases where the yaw angle was above 7° to maintain the required clearance distance from the side walls. The domain was divided into multiple bodies of influence to refine the mesh size in regions of interest, such as the curvature around the tractor model and behind the trailer, where the variation of flow properties is significant and all gradients need to be captured. The EPA methodology of using a single yaw angle as a surrogate wind-averaged-drag metric was applied and all ZEHDV cases were simulated at yaw angle of 4.5°, with a speed set to 29 m/s.

Poly-hexcore meshes, which contain polyhedral and hexcore cells, were used for the meshing. In the full-scale ZEHDV simulations, this meshing provides about 16 million cells and 30 million nodes, with a minimum face area of 0.04 $mm^2$ and a minimum volume of 0.95 $mm^3$ specified in regions of high curvature around the tractor model. For regions requiring a lower mesh density, generally at greater distances from the model surfaces, the mesh density is coarsened. To simulate open road conditions for ZEHDV model, moving ground and rotating wheels boundary conditions were applied. Expanding the computational domain size, following SAE standards recommendations [12], reduced blockage, improved surface pressure accuracy in the third decimal point, with only a 1% difference in drag coefficient, affirming the adequacy of the smaller domain for simulations. In addition, the RANS simulations were repeated for a few ZEHDV cases, and each time, the drag coefficient was found to be within a 1% uncertainty range.

# 4 Results and Discussion

## 4.1 Experimental Results

The zero-emission-cab tractor was evaluated alongside three different dry-van semi-trailer configurations including standard trailer, trailer with skirts, and trailer with skirts and tail. Results were compared to the performance of both day-cab and sleeper-cab tractor models using the same three trailer setups. Figure 4 illustrates that the zero-emission-cab and sleeper-cab tractors share lower drag coefficients compared to the day-cab tractor, with sleeper-cabs benefiting from their elongated shape for improved aerodynamics.

The findings from the prior investigation involving the NRC ProStar-based sleeper-cab tractor indicate that cooling drag plays an insignificant role in the total drag. Consequently, the observed drag reduction is attributed to the streamlined design approach employed during its development, which involves strategies such as minimizing perpendicular or nearly perpendicular surfaces to the wind, particularly in the windshield area, and enhancing the curvature of front edges to extend surfaces with low-pressure forward.

A noteworthy finding is the contrast between the zero-emission-cab and sleeper-cab designs when paired with various trailer setups. They display similar drag coefficients, albeit with minor yaw asymmetry, in the case of the standard trailer. However, when equipped with side-skirts and a tail, the zero-emission cab demonstrates lower aerodynamic drag compared to the sleeper-cab, especially at lower yaw angles (approximately ±5◦), suggesting that alterations in the tractor's shape influence the effectiveness of drag reduction measures from trailer add-on devices such as side-skirts and a boat-tail [3].

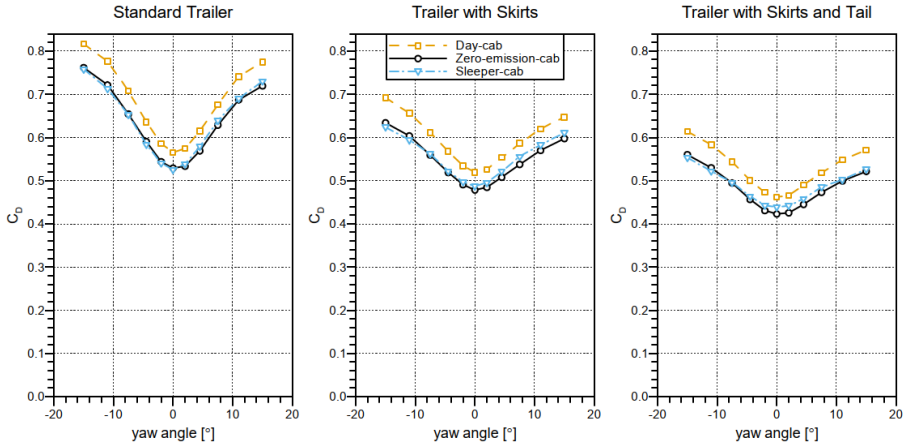


Figure 4: Measured variation of drag coefficient with yaw angle for the three tractor-model configurations paired with the three dry-van-semi-trailer-model configurations [3].

## 4.2 CFD Results

The preliminary experimental study demonstrated that an aerodynamic design could improve drag performance by up to 7-9% compared with a conventional day-cab. To further investigate the potential benefits of innovative cab designs, a CFD study was undertaken to create an optimized aerodynamic ZEHDV cab for further experimental investigation. CFD was used as a cost-efficient method to conduct parametric optimization that would not be feasible with experimental methods.

The study of RANS, URANS, and DES methods for the simplified CFD model showed that RANS simulations tend to underestimate the drag coefficient, but the trend of drag contribution for the tractor portion remained unchanged in RANS and transient solutions. Therefore, the differences in drag associated with shape changes are expected to track appropriately.

Accordingly, aerodynamic shape optimization simulations were performed using the RANS method with the $k-\omega$ SST turbulence model. A total of six design parameters were studied through 26 simulation cases, including: primary edge radii, bumper curve, curvature and angles of wind shield/cab roof, front surface area of the cab, length and width of the cab, air dams and under-body flow control. The objective was to focus on a specific design parameter in each iteration of geometry modification while preserving the overall shape. Although changing one design parameter can affect the overall parametric cab design, it was important to maintain the general shape. Additionally, in subsonic flows, any changes can affect the entire flow field, so modifications to some design parameters were repeated a few times in the optimization process.

*Influence of Corner Radii and Cab's Front Area:* Sharp corner edges can cause flow separation and increase a vehicle's drag. Using a proper curvature profile instead of sharp corners can create a smooth flow transition at the corners of the cab and prevent separation of the flow from the side panels of the cab. Multiple configurations were defined to optimize the corner radii via the parametrically designed geometry. Results showed that increasing the corner radius at the top corner created a high-pressure region, which led to the increased drag, while a slight decrease in the corner radius at the top of the tractor (a gradual decrease in corner radii from top to bottom) reduced the pressure and improved the overall drag coefficient. Additionally, the narrower front area showed the possibility of drag improvement by decreasing the surfaces experiencing the highest pressure. However, decreasing the front area exposes the side panels to the wind and results in an increased surface area perpendicular to the vehicle motion direction. Therefore, the surface experiencing the highest pressure decreased but created more high-pressure regions on the aft side surfaces of the cab, resulting in an increase in drag. Figure 5 shows three case studies investigating the effect of the front area and corner edge radius on surface pressure coefficient distribution and on drag coefficient accumulation. In comparison to the first geometry at left, second geometry (centre) resulted in less than 1% improvement, and the third geometry showed about 3% deterioration in aerodynamic drag coefficient.

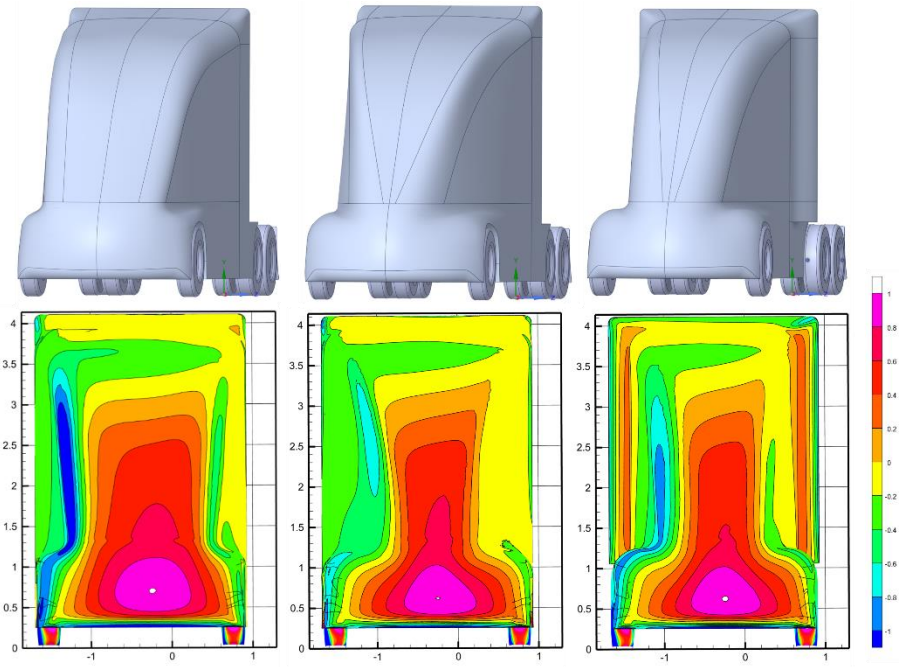

Figure 5: Surface pressure coefficient distribution; initial geometry (left), smaller corner radius (centre), narrower front area (right).

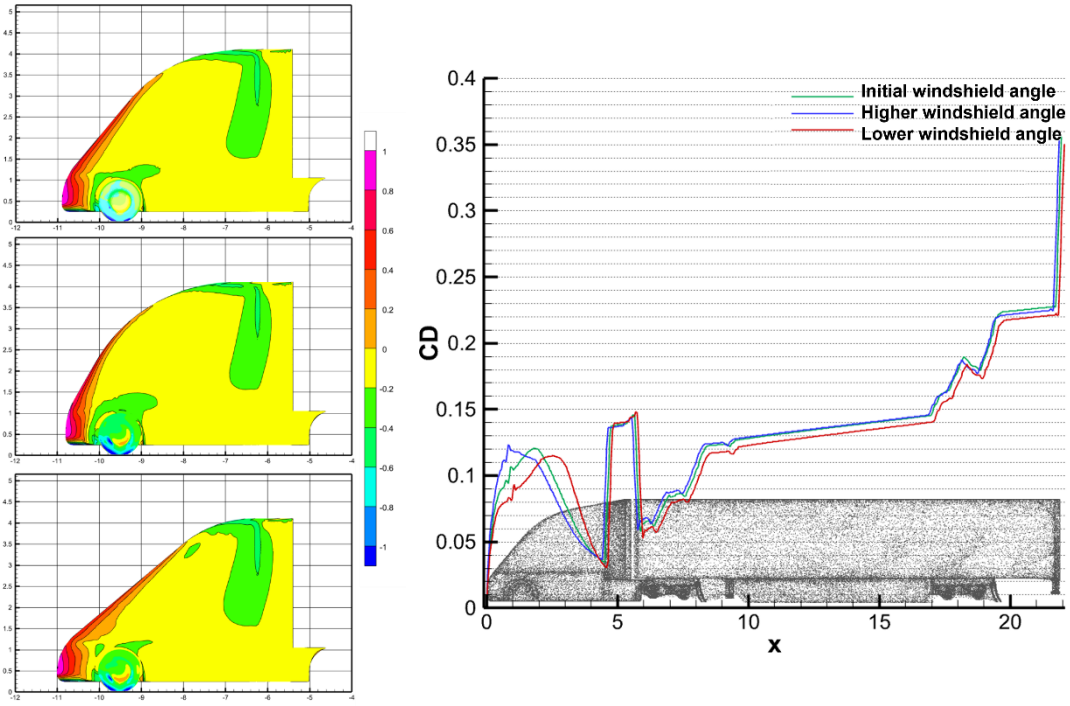


Figure 6: Influence of windshield and cab roof radius angle

*Cab Roof Angle and wheelhouse,* Increasing the cab height to reach the zero-cab roof angle added a 10.6% increase in the drag contribution of the front part of the cab. However, this modification decreased the drag contribution over the tractor-trailer gap region by more than 38%. Additionally, to guide the flow and prevent air from entering the wheelhouse, the front of the cab was slightly widened. Combining these modifications resulted in a 2.6% decrease in drag compared to the middle geometry in Figure 5.

*Influence of Windshield and Cab Roof Radius Angle*: the roof shape, height, and angle can guide the flow over the tractor-trailer gap and affect top edge vortex creation. Although the windshield angle and roof radius are dependent on each other, the effect of the windshield angle was studied by changing it by ±10°. Either increasing or decreasing the windshield angle by 10° decreased improved the aerodynamic drag up to 1.6%. This effect is precisely illustrated in the drag accumulation graph (Figure 6) which demonstrates that increasing the windshield angle moved the greater drag contribution toward the front of the cab by increasing the area of the perpendicular surface to the vehicle motion direction. On the other hand, a lower windshield angle lowered the front pressure drag, increased the suction region over the cab's roof, and also guided the flow along the cab surface, which reduced the contribution of the tractor-trailer's under-body drag.

Air dams can influence the underbody flow rate and considerably affect the aerodynamic performance of HDVs. The drag contribution of the underbody depends on many factors, such as the roughness, rate, and turbulence features of the underbody flow. The best way to mitigate underbody drag contribution, despite the turbulence intensity and underbody roughness, is to decrease the underbody flow rate as much as possible. This approach can be seen in most modern trucks, with flexible air dams extending almost to the ground. Shape and location of air dams were studied in multiple configurations. Adding air dams resulted in an increase of up to 2.3% or a decrease of as much as 1.6% in aerodynamic drag, depending on the configurations.

Individual design parameters were studied through 22 cases. Subsequently, a combination of the beneficial changes in design parameters was applied since, in subsonic flows, any changes affect the entire flow field, which can change the relative effectiveness of individually optimized parameters. Figure 7 shows the final geometry concept with increased windshield angle, improved curvature in the bumper's corner and three air dams including wheel and center ones selected from the CFD optimization process.

The current NRC 30%-scale model has an engine bay with a representative static engine and an electric-wheel-drive system. The new aerodynamically-optimized model would require some changes to the chassis, particularly a reduction in the size of the structure surrounding the engine bay, to provide room for the narrower cab shape at the front. However, the simulated cooling package, which defines the frontal area of this structure, will be needed for the increased cooling-flow necessary for a future fuel-cell variant of the new cab model. Therefore, to prevent any chassis changes, the geometry was slightly adjusted to envelop the chassis without interference. The final geometry concept and the current state of the physical 30% scale model, that is being designed from this concept, are shown in Figure 7.

Figure 7: Optimized Aerodynamic model (left), New designed physical 30% scale model (right)

## 5 Conclusions

The initial experiment demonstrated a 7-9% drag performance improvement with an aerodynamic design over a standard day-cab, prompting a CFD study to optimize an aerodynamic ZEHDV cab. Therefore, RANS simulations and parametric design were utilized to examine various cab geometries. Results showed larger cab corner radii and a gradual decrease in top corner radii improved aerodynamic performance by guiding the flow and mitigating edge vortices. A lower windshield angle reduced front pressure drag, while a flat zero cab roof with a larger roof radius created a larger suction region and improved performance. As expected, decreasing the surface area perpendicular to the vehicle direction of motion helped reduce drag, but decreasing the frontal area of the cab, while flaring its aft surfaces to match the trailer, should be approached with caution. To improve aerodynamics, it was important to have smooth curvature connections and prevent air from entering regions such as the wheelhouse. A smaller bumper radius with a smooth under body, minimum-length wheel air dams, and moving the central air dam further downstream all helped reduce the drag coefficient.

An optimized cab was achieved by studying 26 cases representing various geometries. The CFD results have shown up to 8% variability in drag coefficient resulting from changes to the shape of the cab model with aerodynamic considerations.

## 6 Acknowledgements

This research co-funded by both Transport Canada's ecoTECHNOLOGY for Vehicles program and the National Research Council Canada's Clean and Energy Efficient Transportation program. The views and opinions expressed by the authors do not necessarily state or represent those of Transport Canada.

## 7 Bibliography

[1] National Academy of Sciences, "Technologies and Approaches to Reducing the Fuel Consumption of Medium- and Heavy-Duty Vehicles" Committee to Assess Fuel Economy Technologies for Medium- and Heavy-Duty Vehicles, DOI: 10.17226/12845, National Academy of Sciences, 2010.

[2] Patten, J., McAuliffe, B. R., Mayda, W. and Tanguay, B. "Review of Aerodynamic Drag Reduction Devices for Heavy Trucks and Buses" Report No. CSTT-HVC-TR-205, 2012.

[3] McAuliffe, B. R., Ghorbanishohrat, F. and Barber, H. "Preliminary Investigation Towards Next Generation Truck Design for Aerodynamic Efficiency" NRC Report No. LTR-AL-2022-0069, National Research Council Canada, 2022.

[4] Ghorbanishohrat, F., McAuliffe, B. R.,"Shape Optimization Investigation of Next Generation Truck Design for Aerodynamic Efficiency" NRC Report No. AST-2023-0018, National Research Council Canada, 2023.

[5] McAuliffe, B.R., Hali, B., Ghorbanishohrat, F. "The Influence of Traffic Wakes on the Aerodynamic Performance of Heavy Duty Vehicles" SAE Paper 2023-01-0919, 2023.

[6] McAuliffe, B. R., Desouza, F. and Leuschen, J. "Aerodynamic Testing of Drag Reduction Technologies for HDVs: Progress Towards the Development of a Flow Treatment System" NRC Report No. LTR-AL-2012-0020, National Research Council Canada, 2013.

[7] McAuliffe, B. R., D'Auteuil, A. and de Souza, F. "Aerodynamic testing of drag reduction technologies for HDVs: progress toward the development of a flow treatment system (year 2)" NRC Report No. LTR-AL-2014-0014P, National Research Council Canada, 2016.

[8] Dillmann, A. & Orellano, A. "The Aerodynamics of Heavy Vehicles III: Trucks, Buses and Trains" Springer, 2015.

[9] "Guidelines for Aerodynamic Assessment of Medium and Heavy Commercial Ground Vehicles Using Computational Fluid Dynamics" SAE, 2013.

[10] Hoque, A. Z. U., Islam, M. A. and Shuvo, M. A. H. K. "Aerodynamic Shape Optimization of Vehicles Using CFD Simulation" International Conference on Mechanical, Industrial and Energy Engineering, 2018.

[11] Peng, J., Wang, T., Yang, T., Sun, X. and Li, G. "Research on the Aerodynamic Characteristics of Tractor-Trailers with a Parametric Cab Design" Applied Sciences, 8, 2018.

[12] "Guidelines for Aerodynamic Assessment of Medium and Heavy Commercial Ground Vehicles Using Computational Fluid Dynamics" SAE, 2021.

# Upgrade of the Ontario Tech ACE Climatic Wind Tunnel to a Climatic and Aerodynamic Wind Tunnel

John Komar and Patrick Smith, Ontario Tech University
Trevor J. Bender, Aiolos Engineering Corporation

Ontario Tech University
Automotive Centre of Excellence (ACE)
2000 Simcoe St. N.
L1G 0C5, Oshawa
ON, Canada

John.Komar@ontariotechu.ca
Patrick.Smith@ontariotechu.ca
Trevor.Bender@aiolos.com

**Abstract:** The ACE climatic wind tunnel at the Ontario Technical University was recently upgraded. The test capabilities were expanded with the addition of a full belt rolling road module, which is interchangeable with the dynamometer within the test section turntable. This transforms the ACE climatic wind tunnel into the ACE Climatic and Aerodynamic wind tunnel with the unique ability to perform climatic and aerodynamic testing within the same airstream. In addition to new rolling road, further upgrades were completed to enhance the simulation quality for both climatic and aerodynamic testing.

## 1 Introduction

Ontario Tech University ACE is a core research facility and a solutions provider in Canada designed to serve both industry and academia. ACE nurtures Canada's entrepreneurial spirit by introducing students to the commercial applications of research, supports research and development collaborations between the academic and industry community and serves industry to advance and bring new products to market.

Ontario Tech University took the opportunity to further diversify the multi-sector client base and grow industry/academic partnerships in Canada and internationally through the expansion of aerodynamic capabilities within the ACE climatic wind tunnel. The result is a flexible and market responsive innovation centre that provides thermal, aerodynamic, and aero-acoustic capabilities and address new and emerging global aerodynamic standards in the mobility sector.

“The automotive industry is moving towards lower $CO_2$ emissions and higher efficiency. Especially for higher driving speeds this can be achieved by minimizing aerodynamic drag.”[1] “To improve the aerodynamic efficiency of a vehicle it is essential to have reliable ground simulation in the wind tunnel.”[1] The result of the ACE Enhancement Project is a climatic and aerodynamic test facility that provides excellent underbody simulation to provide test capabilities to achieve high fidelity tests that replicate real-world driving conditions, as either an aerodynamic or climatic platform.

Prior to any improvements, the ACE Climatic Wind Tunnel (CWT), was a multifunctional wind tunnel with unique features. Upon completion of the ACE Enhancement Project, the facility was upgraded to not only improve aerodynamic and acoustic performance but to add improved underbody simulation capabilities with a new rolling road system in a readily reconfigurable “plug and play” exchange of a full-scale dynamometer with a full-scale single belt rolling road. The new ACE Climatic and Aerodynamic Wind Tunnel (CAWT) is now capable of providing climatic, aerodynamic, and acoustic simulation and testing, all within the same wind tunnel, all within the same wind stream.

The paper will detail the transformation and improvements to the ACE CWT, which include:

- Improved air flow quality, realised through the introduction of a new honeycomb flow straightener, a new Helmholtz resonator and a stand-alone collector.
- Improved acoustics, realised with new acoustic panels added to the test section walls.
- Improved under-body flow simulation, realised with a new rolling road system (RRS) and enhanced boundary layer treatment.
- Aerodynamic force measurement via a new custom force balance system for aerodynamic testing of full-scale vehicles in conjunction with the rolling road system.

## 2 Background

The ACE CWT is a large climatic wind tunnel, designed by Aiolos Engineering Corp., that began operation in early 2012 [2]. It is a steel construction with a closed-circuit overhead return, incorporating an open-jet style test section. The nozzle has a variable nozzle area, with flexible sidewalls and a roof that can be lifted, in tall mode, to accommodate class 8 trucks and buses. In normal mode, the nozzle range is from 7 $m^2$ to 13 $m^2$; in tall mode it is 20 $m^2$. The airline drawing of the ACE CWT is given in Figure 1.

The key features of the ACE CWT, prior to the present improvements, were:

- An adjustable nozzle, with flexible sidewalls to achieve 3 standard nozzle sizes: 7 $m^2$, 9.3 $m^2$ and 13 $m^2$.
- Wind speeds in excess of 250 km/h (7 $m^2$ nozzle).
- Good flow quality for thermodynamic and aerodynamic testing.
- Temperature range from -40 °C to +60 °C and a general humidity range from 5% to 95% RH.
- Low background noise level, 64 dB(A) at 50 km/h.
- A primary boundary layer scoop, for reasonable underbody simulation.
- A 750 kW (combined) chassis dynamometer mounted in a turntable to allow for climatic testing at yaw (cross-wind). See Figure 2.
- Solar simulation system (up to 1100 $W/m^2$ intensity) with sunrise/sunset simulation.
- Blowing rain and blowing and falling snow simulations.
- Hydrogen and electric vehicle compatibility.

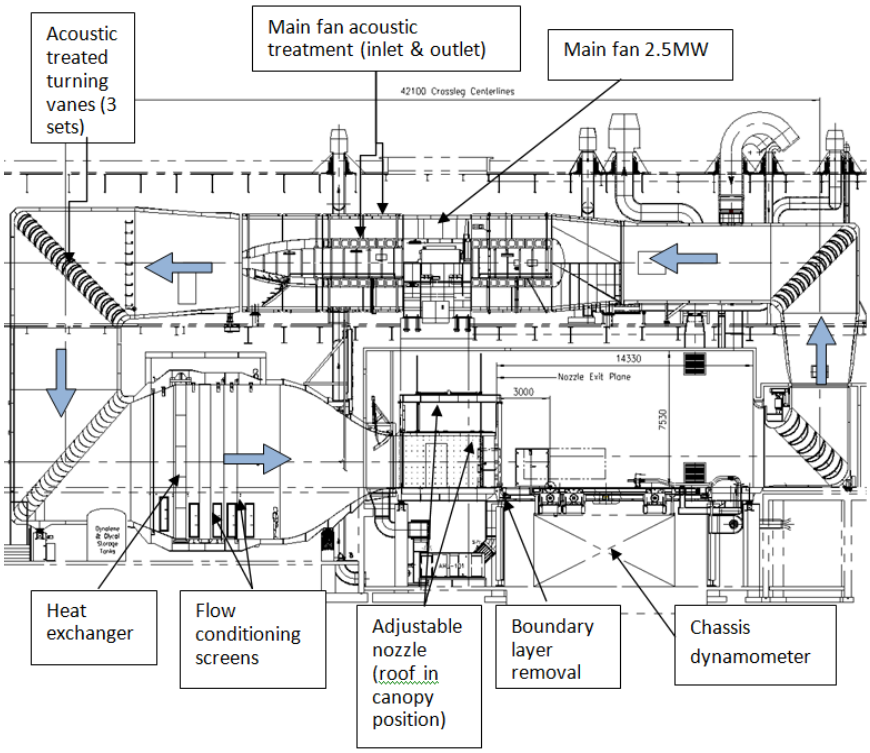


Figure 1: ACE CWT Airline drawing

The ACE CWT was designed and constructed with the present upgrade in mind. The original design included the following provisions:

- A cavity and support for the installation of a honeycomb flow straightener.
- A dedicated area at the front of the turntable for a distributed suction type secondary boundary layer system.
- Provisions for acoustic panels to be installed over the insulated panels.
- A turntable with a removable dynamometer, to allow for the replacement with other devices, such as a rolling road system.

Figure 2: Climatic (snow) Testing at Yaw

## 3 Upgrades

The ACE CWT was purpose built with the intention of having an interchangeable dynamometer and rolling road system. The impetus for the ACE Enhancement project was the availability of a “used” MTS rolling road system. ACE was able to purchase an MTS full belt rolling road that was originally built for an Old Dominion University wind tunnel but was never installed. Upon purchase of the rolling road, the hardware was transported to Oshawa and MTS was employed to reconfigure the system for installation within the ACE wind tunnel.

There have been several wind tunnels that have both a force balance/turntable for aerodynamic testing and a dynamometer for thermal testing [3,4]. In those facilities, the dynamometer is located downstream of the turntable, within a more unstable region of the jet flow. In the newly upgraded ACE CAWT, the dynamometer and rolling road/force balance are interchangeable within the turntable and thus the flow field is the same regardless of a thermal or aerodynamic configuration.

Along with the implementation of the new rolling road module, ACE took the opportunity to further upgrade the CWT. Enhancements were made to compliment the RRS with new boundary layer treatment, improve the flow quality and the acoustic performance of the wind tunnel. ACE took full advantage of the provisions built into the facility for future upgrades and included elements that were not originally envisioned. Aiolos Engineering was employed as a collaborative partner in the overall Enhancement Project.

Rather than shutting down the CWT for an extended period, the various upgrades were staged over a 2-year period, corresponding to regularly scheduled maintenance stoppages. This allowed for less disruption for the various clients and users of the facility.

Descriptions of the primary upgrades are given in the following sub-sections.

### 3.1 Honeycomb

The honeycomb was the first upgrade element to be installed. The honeycomb was fabricated in 35 boxes that were installed 5 wide x 7 high. The cell size of the honeycomb is 38 mm and the length is 600 mm, for an L/D of 15.8. The new flow conditioning arrangement of the CAWT is a honeycomb and 2 fine mesh flow conditioning screens.

### 3.2 Collector

The size and shape (angle of the sidewalls and ceiling to the test section centreline) were configured as part of the model wind tunnel study – see Section 4. However, the collector was constructed with the ability to adjust the wall and ceiling angles, during commissioning to account for any differences to the model scale testing. In addition, the collector has trailing edge flaps that were used to fine tune the axial gradient, something that has proven beneficial in the past [5].

The stand-alone collector is removeable to allow for the continued testing of large trucks and busses. It can be removed or installed within the test section in less than 4 hours. Photographs of the new collector and a model scale collector are given in Figure 3.

Figure 3: The new stand-alone collector (left) and a model scale version, rotated 90 degrees (right)

### 3.3 Boundary layer treatment

The original CWT was equipped with a boundary layer scoop located just downstream of the nozzle exit plane. While this provided adequate boundary layer control for most climatic testing, it, alone, is not sufficient for aerodynamic testing with a rolling road. To compliment the scoop, distributed suction was added along the leading edge of the turntable and on the leading edge of the rolling road insert. To reduce the distributed suctions influence on the static pressure field, every effort was made to minimise the amount of solid floor between the primary scoop and the leading edge of the rolling road.

The distributed suction on the turntable uses a high-loss perforated plate, which provides uniform suction without influence of the static pressure field of the vehicle. Since the leading edge of the rolling road module is closer to the vehicle, the pressure loss needs to be even greater and as such a sintered metal filter plate is employed. The final boundary layer control device is a tangential blowing slot, just upstream of the leading edge of the belt.

### 3.4 Rolling Road System

The Rolling Road System is an MTS single belt rolling road solution. Its effective measurements are 7 m long and 2.4 m wide using a 0.8 mm thick stainless-steel belt. The system has a yaw capability of ±30° and a top speed of 80 m/s. An integrated lift system allows the road to be raised into position level with the turntable while imbedded sole plates in the basement floor ensure the device remains level while in operation. The frame assembly rests on an independent rotation base aligned with the centre of rotation of the main turntable. This allows for the systems angular control to be passive relying on the turntable to set angular position without the need to synchronize two control methods. A photograph of the new rolling road configuration is given in Figure 4.

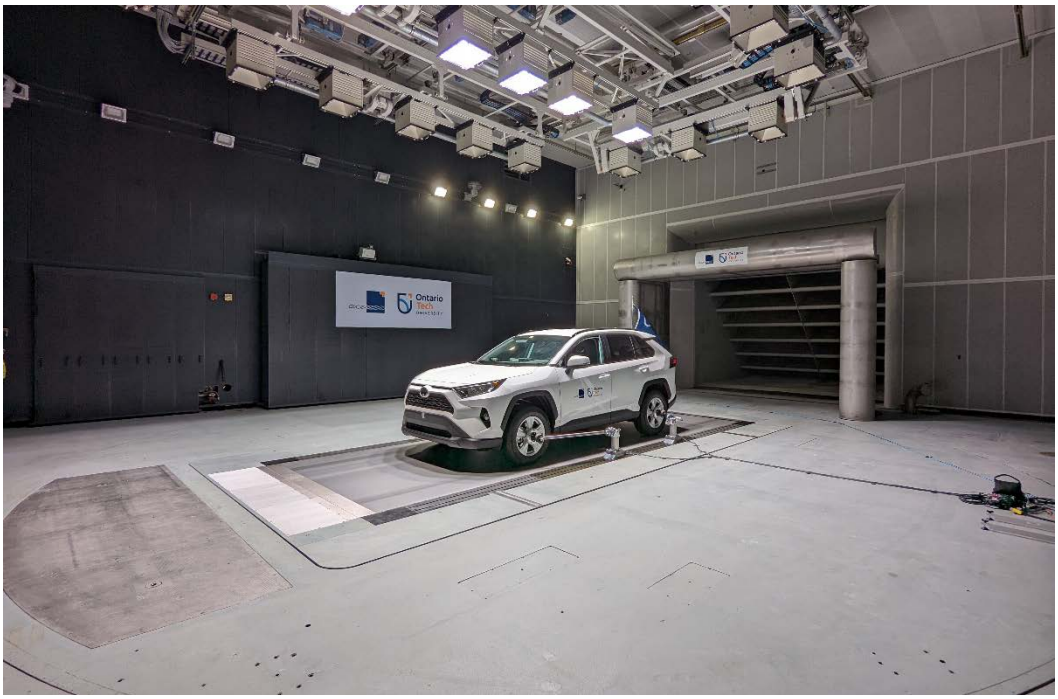

Figure 4: The new rolling road configuration inside the ACE CAWT test section

### 3.5 Force Balance System

Under each high pressure contact patch air bearing consists three uniaxial load cells to measure vertical forces on the vehicle. The system works on the principle that as pressure is applied to float the belt, and vehicle, the resulting force can be measured. Taring the static wind off force required to “hold” the belt/vehicle up results in the measurement of only the lift forces when wind is applied. Combined the three load cells give a maximum calibrated load range up to 8 kN per corner. The vehicle is restrained using a three-post hub mounted restraint system. The restraints, including an integrated ride height system, were designed and provided as part of a collaborative partnership with Multimatic Inc. This serves two purposes as it restrains the vehicle while also incorporating force measurement for lateral and longitudinal forces. Force measurement is attained through the use of inline 5 kN uniaxial load cells mounted on each tie rod between each tower and wheel hub. Coupled with two absolute rotary encoders (Yaw & Pitch) the force vector can be decoupled into cartesian force components resolving for X|Y|Z forces placed on each restraint. By combing this with the through-the-belt measurement, a full six degrees of freedom can be resolved.

### 3.6 Acoustic Wall Treatment

The original design of the wind tunnel allowed for 200 mm thick flat panel absorbers. Compact absorber panels were supplied by TAB Ingenieure GmbH of Germany. The treated walls include the ceiling, the back wall and the side walls from just upstream of the nozzle exit plane to the back wall.

The addition of the acoustic panels compliments the originally installed acoustic treatment. The CWT was designed and constructed with acoustic treatment on either side of the fan and with three acoustically treated turning vane sets: corner 1, corner 2 and corner 3.

## 4 Model Wind Tunnel Testing

Open jet wind tunnels are prone to low frequency pressure fluctuations that can inhibit high fidelity testing at specific velocities or even limit the top speed of a facility. These fluctuations are a result of the excitation of wind tunnel resonant modes through the vortex shedding at the nozzle exit plane. A significant source is an edge-tone feedback mechanism between the nozzle and collector [6].

Over the last 20 plus years, there have been many solutions to control or limit static pressure fluctuations. These include:

- Disruption of the coherent generation of vortex shedding at the nozzle [7]
- Collector design strategies [8,9]

- Active noise control [10]
- Selective attenuation using passive devices [11,12,13]

To control any pressure fluctuations in the ACE CAWT, the authors chose to utilise a stand-alone collector and add in a new Helmholtz resonator, in much the same manner as in [5]. The originally constructed CWT has been equipped with a small resonator with limited effectiveness. This resonator was included in the model wind tunnel.

The first task in the model wind tunnel programme was to configure a collector to provide a good axial static pressure gradient. The size of the collector was limited by the existing design – it had to fit between the turntable and the bell-mouth entrance to corner 1. A variety of collectors were examined with various side wall and ceiling angles. In addition, the sensitivity of the trailing edge flaps was examined.

The second task was to configure the new Helmholtz resonator. This began with an examination of the pressure pulsation within the full-scale wind tunnel. Figure 5 shows the frequency/wind speed dependence of the pulsations. In this diagram, the significant peaks are plotted, along with the excitation modes (natural vortex shedding and edge-tone feedback) and wind tunnel natural frequencies. It clearly shows resonate modes locking in near the excitation modes, with the most intense peaks closest to the crossing locations. The goal of the model wind tunnel testing was to configure a new Helmholtz resonator to attenuate the intensity of the large peaks, while taking into account the attenuation influence of the collector.

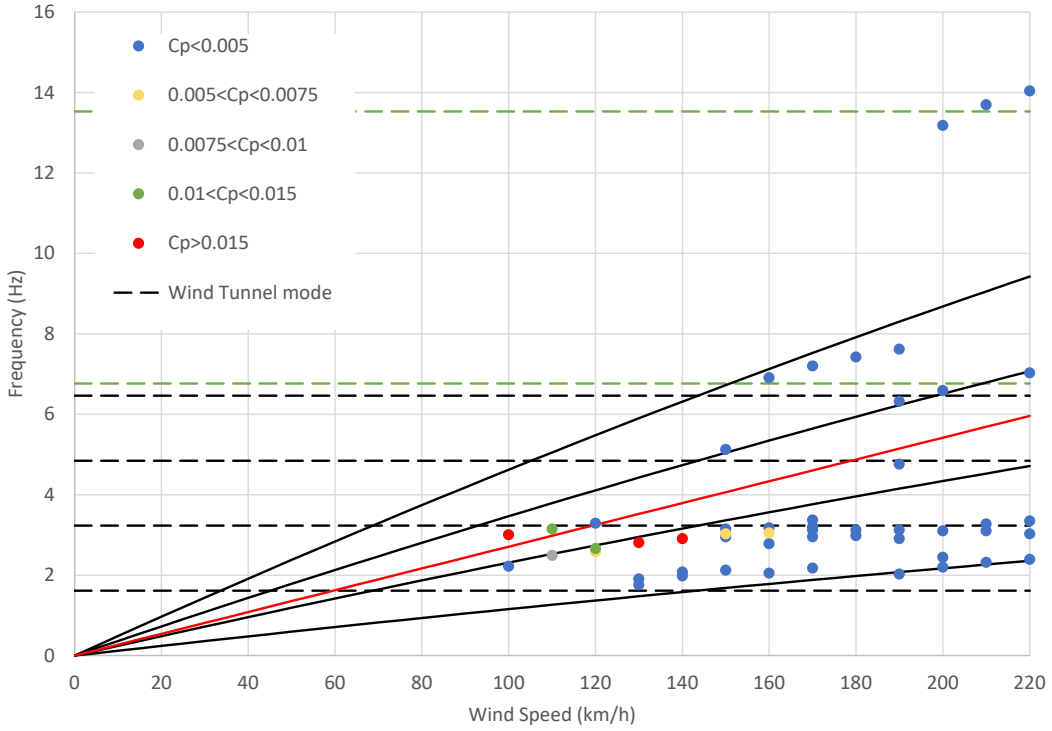


Figure 5: Pressure Pulsation Frequencies in the CWT prior to modifications

Again, the size and location of the resonator were limited by the existing design, predominately the infrastructure around the wind tunnel. In total, 2 suitable locations were tested, with various configurations at each location (volume, neck size and opening). In the end, a large Helmholtz resonator was positioned at cross-leg 1, close to the 2nd corner.

## 5 Summary of Commissioning Measurements

The results of the Enhancement Project can be summarised as: an improvement to the axial static pressure gradient and low frequency fluctuations, an improvement to the overall flow quality, new aerodynamic test capabilities with the new rolling road and force balance arrangement and an improved acoustic performance.

The axial static pressure gradient was measured at various wind speeds and conditions – in general, the centreline gradient is less than $dCp/dx = 0.0025\ m^{-1}$ within the vicinity of the test vehicle. The static pressure fluctuations are summarised in Figure 6 for various configurations, including before and after modifications. Of note, there is good agreement between model and full-scale, and the post modification maximum $Cp_{rms}$ (0 to 20 Hz) is less than 1% over the entire wind speed range.


Figure 6: Measured overall static pressure fluctuations (0 to 20 Hz)

The flow quality (uniformity) was measured pre and post modification. The results are summarised in Table 1. The reported data was from measurements made 1.5 m downstream of the nozzle exit plane and over a width of +/- 1.35 m from the centreline to a height of 2.12 m. The result of adding in the honeycomb was a significant improvement in each of the flow uniformity parameters.

Table 1: Flow Uniformity results (post and pre modification)

| Parameter | After Upgrade | Before Upgrade |
|---|---|---|
| Average Pitch Angle | 0.34° | 0.71° |
| Standard deviation of Pitch Angle | 0.22° | 0.72° |
| Average Yaw Angle | 0.00° | 0.13° |
| Standard deviation of Pitch Angle | 0.23° | 0.59° |
| Standard deviation of Velocity | 0.35% | 0.50% |
| Mean Turbulence level | 0.15% | 0.25% |

The boundary layer systems were calibrated with the new rolling road module and the resulting profiles are within 1% of free-stream down to approximately 1 mm above the moving belt. The resulting profiles for various speeds are shown in Figure 7.

Figure 8 shows the acoustic performance of the CAWT for various conditions, include the pre-modification measurement. The measurements were made out-of-flow, beside the turntable on the control room side. The results show that in general the noise level within the test section was reduced by approximately 5 dB throughout the wind speed range. The results also show that the boundary layer systems have an impact on the noise level at lower speeds, but the collector does not. It also showed a very slight reduction when acoustic shutters are installed over the test section windows.

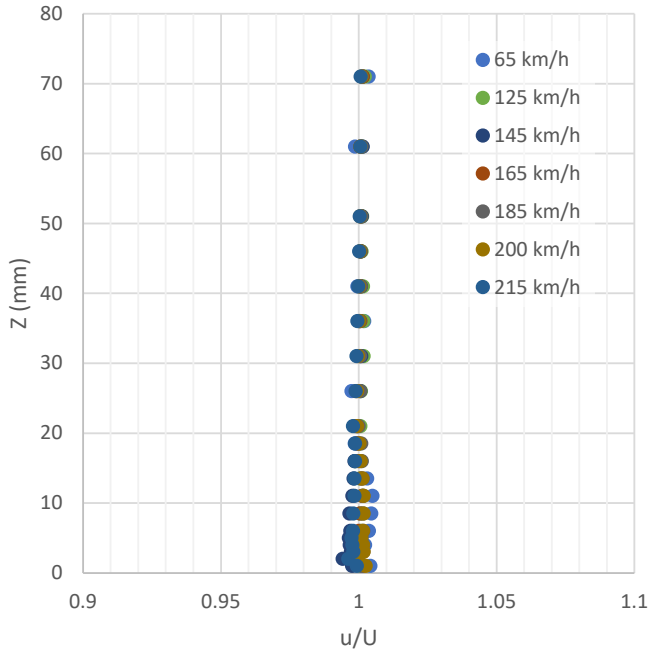


Figure 7: Boundary layer profiles above the rolling road

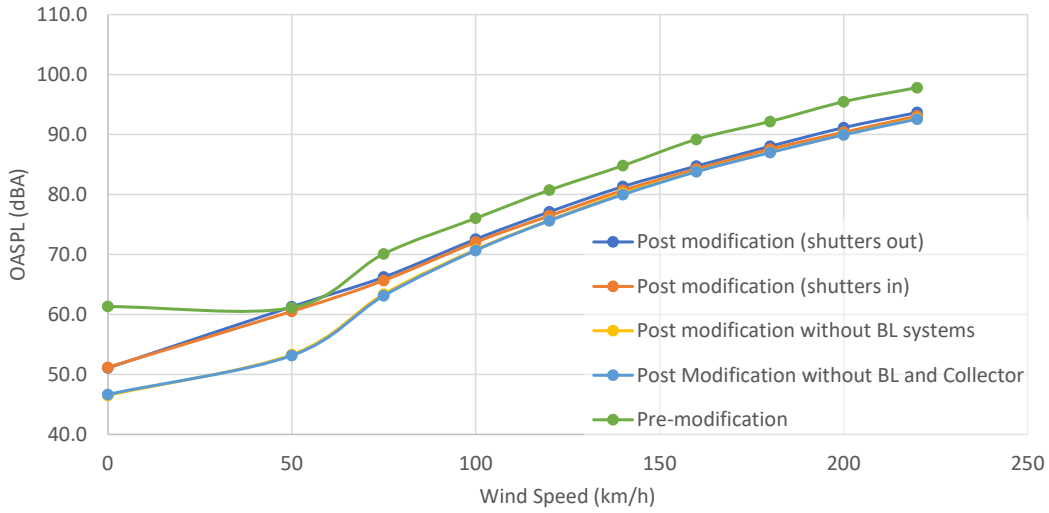


Figure 8: Acoustic performance measured out-of-flow

## 6 Conclusions

The ACE Enhancement project was a success: the addition of the new full belt rolling road expands the unique test capabilities of the ACE CAWT and the overall flow simulation was improved, for both aerodynamic and climatic testing.

## 7 Bibliography

[1] Hennig, A., Widdecke, N., Kuthada, T., and Wiedemann, J., "Numerical Comparison of Rolling Road Systems", SAE Int. J. Engines 4(2):2659-2670, 2011, doi:10.4271/2011-37-0017.

[2] Best, S., Komar, J. and Elfstrom, G., "The UOIT Automotive Centre of Excellence – Climatic Test Facility", SAE Int. J. Passeng. Cars – Mech. Syst. 6(1):2013, doi:10.4271/2013-01-0597.

[3] Nilsson, L.U. and Berndtsson, A., "The New Volvo Multipurpose Automotive Wind Tunnel", SAE paper 870249, 1987.

[4] Kim, M.S., Lee, J.H., Kee, J.D and Chang, J.H., "Hyundai Full Scale Aero-acoustic Wind Tunnel", SAE paper 2001-01-0629, 2001.

[5] Bender, T., Hoff, P. and Kleemann, R., "The New BMW Climatic Testing Complex – The Energy and Environment Test Centre", SAE paper 2011-01-0167, 2011.

[6] Rennie, M., “Effect of jet length on pressure fluctuations in ¾ open-jet wind tunnels”, Motor Research Industry Association, Vehicle Aerodynamics Symposium, October 2000.

[7] Reinhard, B., Widdecke, N., Wiedemann, J., Michelbach, A., Wittmeier, F. and Beland, O., “New FKFS Technology at the Full-Scale Aeroacoustic Wind Tunnel of University of Stuttgart”, SAE Int. J. Passeng. Cars – Mech. Syst. 8(1):2015, doi:10.4271/2015-01-1557.

[8] Rennie, M., Kim, M.S., Lee J.H. and Kee J.D., “Suppression of Open-Jet Pressure Fluctuations in the Hyundai Aeroacoustic Wind Tunnel”, SAE paper 2004-01-0803, 2004.

[9] Lacy, J., “A Study of the Pulsations in a ¾ Open Jet Wind Tunnel”, SAE paper 2002-01-0251, 2002.

[10] Wickern, G., von Heesen, W. and Wallmann, S., “Wind Tunnel pulsations and their active suppression”, SAE paper 2000-01-0869, 2000.

[11] Waudby-Smith, P. and Ramakrishnan, R., “Wind Tunnel Resonance and Helmholtz Resonators”, J. of Canadian Acoustical Assoc., 35(1), March 2007.

[12] Yen, J., Duell, E., Walter, J. and Kharazi, A., “Case study of Helmholtz Resonator Application on Edge-tone Noise Suppression” 18th AIAA/CEAS Aeroacoustic Conference (33rd AIAA Aeroacoustic Conference), page 2103, 2012.

[13] Waudby-Smith, P., Joshi, A., Sooriyakumaran, C., Gabriel, C. and Grabenstein, M., “Using a Passive Feedback Connection to Control Low-Frequency Pressure Fluctuations in a Wind Tunnel”, J. of Canadian Acoustical Assoc., 50(1), March 2022.

# ADVANCED CHT SIMULATIONS FOR BRAKE DISC COOLING APPLICATIONS USING ICONCFD

Rene Devaradja, Christian Taucher, Jacques Papper,
ICON Technology & Process Consulting GmbH
Neuer Wall 50
20354, Hamburg
r.devaradja@iconcfd.com, c.taucher@iconcfd.com, j.papper@iconcfd.com

Christopher Hantschke
Wheel Brake Development
AUDI AG
85045, Ingolstadt
christopher.hantschke@audi.de

**Abstract:** Thermal analysis of complete brake systems poses a significant computational challenge due to the complex physical phenomena involved, including transient Conjugate Heat Transfer (CHT), radiation, rotating meshes, and the necessity for fine grids to resolve the internal ventilation within the brake disc. The escalating turnaround times per simulation have led ICON to devise a streamlined simulation process, tailored for industrial applications, that combines simplicity, speed, accuracy, and robustness. The primary objective of this process is to deliver precise temperature predictions for the brake system and its immediate environment during the cool-down phase.

A new thermal model has been developed to facilitate the description of inter-region heat exchange occurring over a rotating surface whilst using a static mesh. This model, based on the Band-Averaged Flux (BAF) method first introduced by the authors in [1] and [2], is applicable under high rotor speed conditions. It is grounded upon the fundamental assumption that the thermal diffusion time scale of the brake disc is significantly larger than the rotation time scale, a premise that holds true for vehicles moving at a speed of 50 km/h or more.

AUDI AG has emerged as an early adopter of this innovative process, collaborating closely to refine and implement the methods effectively. This industrial partnership has yielded a wealth of experimental data, enabling rigorous validation of the computational model. In this paper, we will present the application of the BAF model in industrial cases. We will discuss both the merits and limitations inherent to this methodology and show that it allows efficient and precise predictions of transient cool-down rates of complex brake disc designs throughout the vehicle development process.

## 1 Introduction

In recent decades, CFD simulations have been extensively utilized in the realm of design assessment and optimization. The accessibility of External Aerodynamics (EA) simulations has notably increased, necessitating only a few hours of training for novices to embark on these tasks. Nonetheless, delving into more intricate challenges, such as the complex thermal phenomena entwined with rotating components like brake disc rotors, underlines the need for the proficiency of seasoned simulation experts when configuring and executing these simulations.

ICON provides an effective solution through its iconPlatform simulation cloud [3] which empowers experts to methodically configure the simulation environment. Subsequently, product designers working on specific projects can readily harness these pre-configured setups. Within the framework of iconPlatform, these tailored configurations are denoted as "Apps". Each App serves a precise purpose, encapsulating industrial best practices and domain expertise, thus ensuring a consistent setup, and streamlining post-processing activities.

## 2 Brake Cooling Application

A dedicated App has been developed to enable the simulation of brake cooling under constant drive speed conditions. This specialized App incorporates a distinct methodology geared towards achieving a precise geometric representation of the brake system containing a multitude of components with heterogeneous sizes. Furthermore, it enables accurate modelling of heat transfer within such systems, encompassing thermal convection in the surrounding air, conduction within the solid components, and radiation. To enhance usability, all results generated are automatically post-processed, allowing the end user to analyse the thermal solution effortlessly.

## 2.1 Computational Domain

Within the framework of iconCFD®, the automatic hex-dominant grid generator seamlessly meshes both the solid and fluid regions, accommodating their distinctive settings, such as the volume refinement levels or the number of wall layers, in a single and streamlined step. Additionally, it accurately represents interfaces between adjacent regions with conformal surface discretization on both sides of the interfaces, ensuring heat conservation is upheld throughout the solver stage. Figure 1 serves as an illustrative example of this meshing approach, demonstrated in its application to a brake assembly.

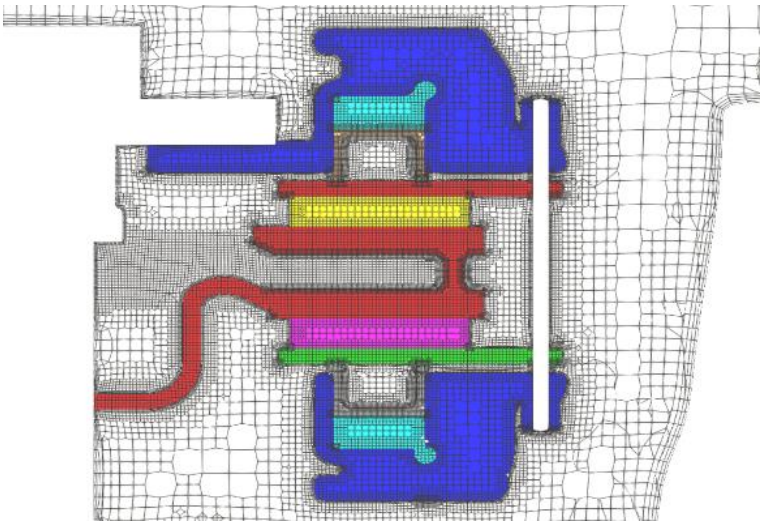

Figure 1: Cross-sectional view of the multi-region fluid-solids mesh.

## 2.2 Thermal model for rotating solids with geometric angular periodicity

A thermal CHT solver is required to compute heat transfer between the different regions. An additional level of complexity arises in the context of brake systems when it comes to simulate the rotating disc region and its interaction with the surrounding static components. Dynamic mesh solutions may offer the highest level of modelling accuracy, however they come at a substantial computational cost making these simulations impractical.

Instead, an alternative model is described in this section to effectively simulate the thermal interaction between a rotating disc and the external medium, without having to resort to any type of mesh motion technique. This model, previously referred to as BAF, operates under the assumption that a circular distribution of points on a rapidly rotating brake disc encounter the same external environment. This hypothesis allows to establish a fundamental equivalence between the time-averaging of a property that would be calculated using a dynamic mesh approach and the space-averaging of the same property calculated with a static mesh.

For this equivalence to be valid, the disc must be divided into distinct parts that are physically exposed to the same external heat load, like for instance the inboard and outboard friction surfaces, the internal vanes, etc. Each of these parts is then automatically subdivided into concentric bands of a given thickness. Specific boundary conditions are then invoked to compute heat transfer for each of these bands by evenly balancing the heat fluxes across them. Figure 2 illustrates this concept for one of the internal surfaces of the disc, discretized into several coloured band macros. The same figure also illustrates the resulting heat fluxes, constant per band, on the entire disc solid. The solver finally uses these band-averaged heat fluxes to solve the multi-region heat equation accordingly.

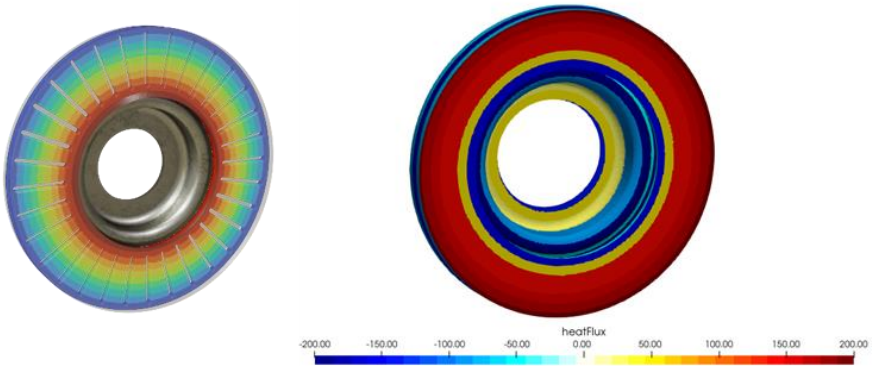


Figure 2: Representation of the internal cooling patch segmented into bands (left) and visualization of calculated heat fluxes per band (right)

The BAF model produces temperature distributions that account for the effects of disc geometric details like vent holes, as depicted in Figure 3. This capability enables engineers to pinpoint hot spots in specific brake disc designs. Additionally, it can be observed that variations in airflow around each side of the disc are reflected in the ranges and contour shapes of temperature.

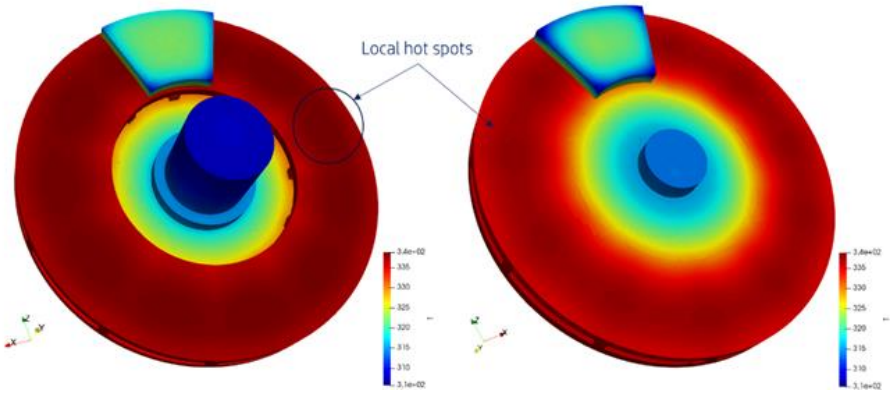


Figure 3: Periodic patterns of temperature distributions obtained with the BAF model

## 3 Impact of other physical models

In this section, the importance of physical models involved in thermal analysis for brake cooling is discussed. As the primary goal is to streamline simulations for time efficiency, this often entails simplifying certain aspects of physical models. However, this simplification inevitably leads to approximations in the solutions, subsequently influencing data analysis. It is imperative to maintain a clear understanding of the engineering objectives when selecting the appropriate level of modelling, ensuring that the right balance between efficiency and retention of essential information is satisfied. In this current context, the chosen methodology should provide accurate predictions for the transient evolution of disc temperature during the cooling phase. In addition to the BAF model previously introduced, several other critical choices in physics modelling need to be made when simulating brake cooling. Specifically, models for flow compressibility, air thermal properties, and radiative heat transfer need to be considered. In the following sections, these specific areas are explored and their impact on the results is analysed.

### 3.1 Flow compressibility

In typical industrial brake cooling simulations, the temperature range spans from approximately 600°C down to 100°C. Given this wide range of temperatures, one might question the necessity of considering compressibility when modelling the airflow. Indeed, if air behaves as a perfect gas, it is important to note that a highly heated brake disc can significantly reduce air density in its immediate vicinity. The reduction in air density leads to a decrease in mass fluxes in that specific region and this, in turn, affects heat convection near the disc's surface.

Figure 4 illustrates the time-dependent evolution of disc temperature for two distinct airflow solutions (note that air flow fields are not updated during the cool-down). Notably, the data reveals that when the air’s density is a function of temperature, the cooling rate of the disc is slower as expected.

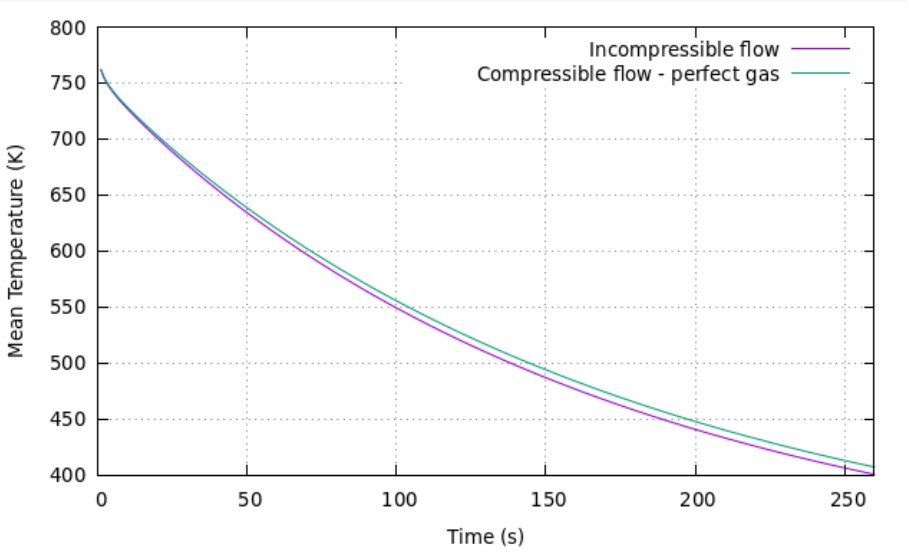


Figure 4: Impact of flow compressibility on brake disc cool-down rate

Even though the two airflows represent the two extreme temperature conditions, their impact on the cool-down curve is relatively small, which in itself justifies the use of a frozen airflow approach in the transient cool-down phase. The choice of flow compressibility is left to the user, however in the cases presented hereafter, the incompressible frozen flow option is selected.

### 3.2 Air properties

Air properties undergo temperature-dependent variations, with certain properties being more responsive to temperature changes than others. Notably, thermal conductivity can go through a considerable increase as temperature rises. Taking this property into account in the CFD simulations with the Sutherland model can lead to significant modifications in the solution, particularly in areas where heat conduction is the predominant mode of heat transfer. These effects illustrated in Figure 5 can be prominently observed in proximity of any solid wall surface. When activating the Sutherland model, at high temperatures the air thermal conductivity increases changing the graph slope and accelerating the cool-down rate in that region. Naturally, at lower temperatures, the cool-down curves for both models once again run parallel to each other.

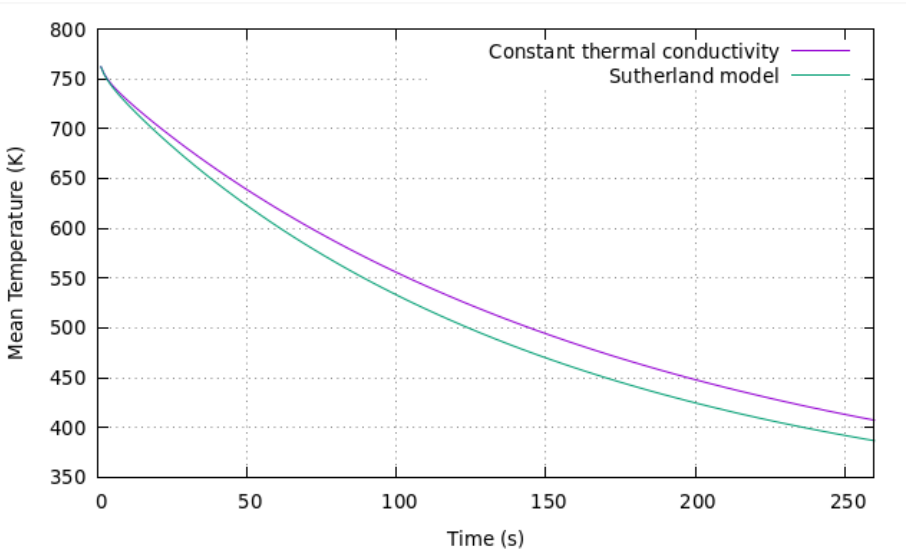


Figure 5: Contrasting brake disc cool-down rates using two distinct thermal conductivity models

### 3.3 Heat radiation

In the scenario of constant cooling drive, while convection remains the dominant mode of heat transfer, it is essential to recognize that radiation also exerts a noteworthy influence on the disc's cooling rate. To emphasize the impact of radiative heat transfer, a transient cool-down simulation is conducted, comparing cases with and without radiation effects. Initially, a simplified radiation model is employed, which approximates incident radiation on the surface by using a constant infinite reference temperature. Furthermore, a more sophisticated surface-to-surface (S2S) radiation model based on view factors is utilized in order to assess the improvement in accuracy compared to the simplified radiation model. The results of this investigation, as presented in Figure 6, clearly indicate an important heat loss due to radiation when it is integrated into the thermal simulation. Also, as anticipated, the S2S model introduces lower radiation losses owing to its more precise calculation of radiative heat fluxes.

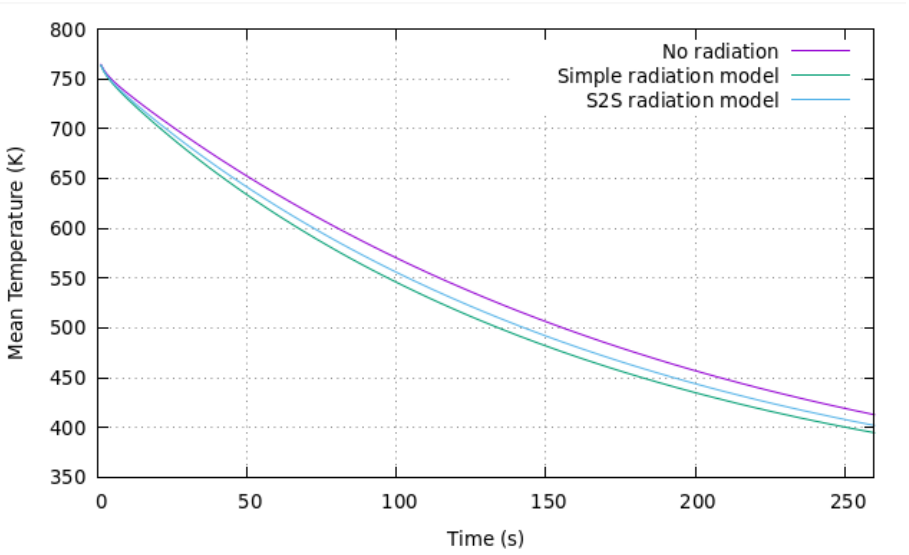


Figure 6: Influence of radiation on brake disc cool-down rate

## 4 Full vehicle simulation

In this section, the BAF model is integrated into a comprehensive thermal model encompassing a fully detailed car geometry. The simulation approach adopted in this context seeks to evaluate the impact of the vehicle's EA on the cooling efficiency of the brake disc. Consequently, high fidelity geometric representation of relevant parts, including but not limited to wheel arch, rim designs, under-hood details, ride height, must be meticulously considered to ensure an accurate and thorough data comparison.

### 4.1 Simulation workflow

As demonstrated in Section 3, in the specific scenario of brake cooling under constant drive speed conditions, the compressibility effects within the air region can be considered negligible. Additionally, buoyancy effects resulting from significant temperature variations are assumed to be substantially smaller compared to the effects of forced convection. Consequently, it is justifiable to decouple the EA simulation from the thermal analysis. In this approach, the EA simulation is initially conducted independently, yielding a converged solution without any thermal modelling. This solution is then preserved and held constant during the subsequent thermal simulations (frozen flow approach).

The thermal simulation of brake cooling is divided into two distinct phases. In the first phase, the brake system is subject to a prescribed heat load at the interface between the brake pad and disc solids resulting from friction. This heat load serves the purpose of elevating the temperatures of the materials and initializing the thermal solution for the subsequent cooling phase. During the cool-down phase, the heat release is discontinued, and an air gap is introduced to model the separation between the brake pad and the disc. This arrangement effectively prevents direct heat conduction between these two regions.

This decoupled approach significantly reduces the overall solver runtime when compared to a fully coupled approach. To provide an indication of the time efficiency of the proposed workflow, the runtime for thermal simulations is less than half that of the steady-state primary flow solver employed in the EA simulation.

### 4.2 AeroSUV Proof-of-concept case

The brake cooling methodology is applied to the AeroSUV geometry [3], which has been modified by ICON to include a brake system on the left wheel. This study investigates three distinct cooling configurations, as depicted in Figure 7 in order to demonstrate the capability of the BAF model to predict the differences in the thermal solution of the brake disc. The first configuration, situated on the left side of Figure 7, represents the baseline setup, wherein no modifications are made to the underbody of the AeroSUV model. In the second configuration, a cooling channel is integrated into the front underbody, designed to direct cold air into the wheel well. Finally, in the third configuration, an additional guide vane is introduced near the steering link. The purpose of this vane is to collect airflow from the cooling ramp and redirect it towards the brake disc rotor's bell, thereby enhancing the cooling process of the disc.


Figure 7: Illustration of brake cooling design on AeroSUV

Examination of the airflow solution for the three different designs is shown in Figure 8 and Figure 9. The baseline case reveals that the upstream flow bypasses the wheelhouse. Consequently, the brake disc is mainly cooled down by the secondary airflow generated through the disc internal blades. With the inclusion of the cooling channel, there is a noticeable redirection of the ambient airflow towards the brake system, leading to an increased mass flow throughput. Finally, with the guide vane in place, the airflow can be directed axially towards the brake disc, further boosting the mass flow rate, and enhancing the cooling process.

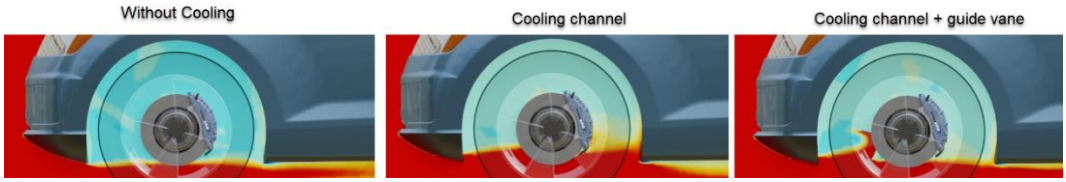


Figure 8: Cross-section of fluid volume with total pressure visualization

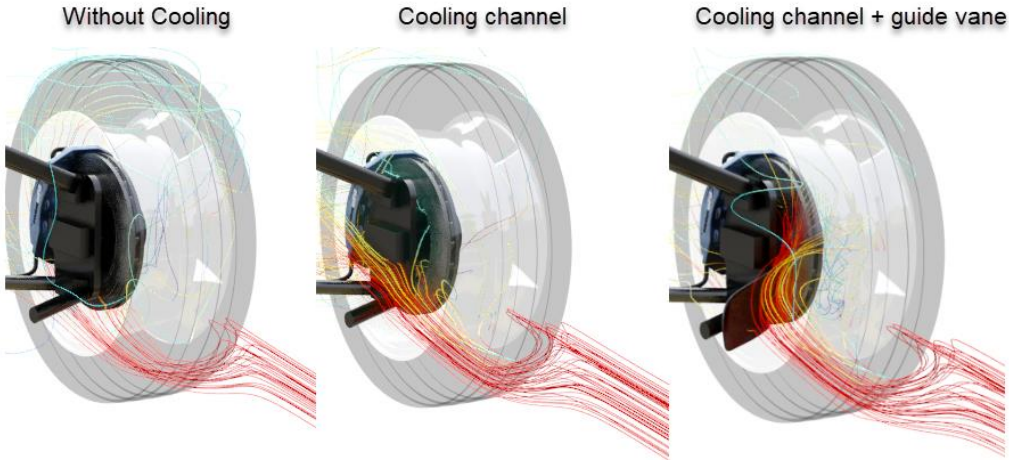


Figure 9: Flow streamlines with total pressure visualization

Figure 10 presents the average material temperature within the brake disc rotor region for the three vehicle variants during the cool-down phase. In the absence of any cooling interventions, the disc requires over 4 minutes and 50 seconds to decrease its temperature from 600°C to 100°C while maintaining a constant vehicle speed of 140 kph. The introduction of wheel house ventilation with cold air reduces this cooling time by 1 minute and 20 seconds. Furthermore, the incorporation of the guide vane results in a further reduction in the cool-down time, bringing it down to 3 minutes. Cumulatively, these measures lead to a reduction in the necessary cool-down time by 1 minute and 50 seconds.

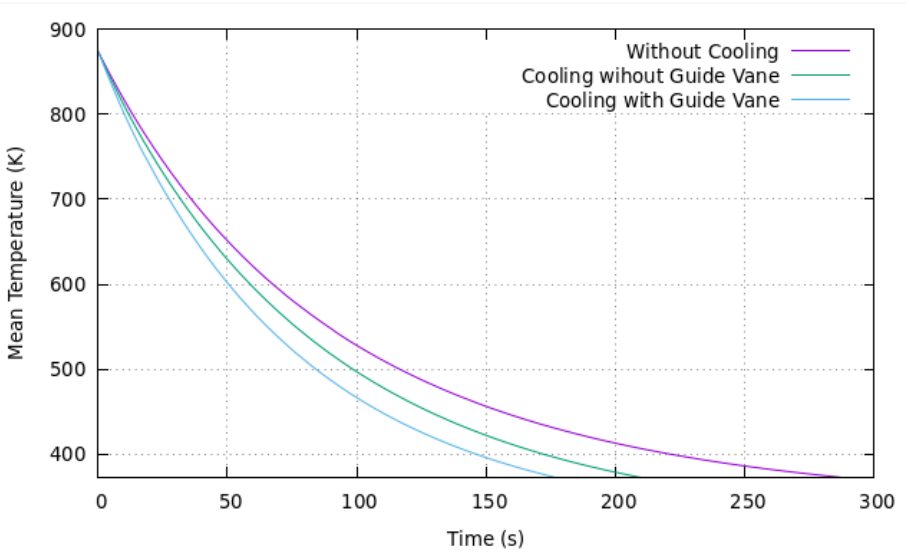


Figure 10: Mean brake disc rotor temperature during cooling phase

Results from this case study show that the BAF model properly accounts for variations in the airflow in the thermal solution of brake cooling simulations.

### 4.3 Audi Validation Case

In this section, the validation of the BAF model in a real-world case is presented. The vehicle model chosen for validation is a SUV from the Audi model palette, which incorporates detailed geometric features in the under-hood, underbody, and wheel regions.

For this case, the CHT mesh has around 93 million cells. It contains 14 solid regions for the brake assembly and 1 fluid region for air. Face clustering is applied to all wall boundaries for the S2S radiation model, resulting in about 920000 coarse boundary faces. The EA solution is calculated using the steady-state SIMPLEC solver. The utilized turbulence model is two-layer realizable k-epsilon and rotating walls are modelled by the MRF approach.

The primary engineering goal revolves around achieving precise prediction of the cool-down rate for initially hot brake discs while the vehicle maintains a constant speed of 160 km/h. To validate the model, the criterion involves successfully matching the transient temperature evolution measured on both the front left and right brake discs. The experimental data have been acquired using embedded thermocouples placed in the brake discs during on-track testing, with measurements conducted under real road conditions for a duration of five minutes.

It's important to note that the nature of on-track testing, as opposed to more controlled wind tunnel experiments, introduces inherently higher variability of experimental data. On-track testing conditions are less controlled and repeatable due to external factors such as variations in road surfaces, fluctuations in ambient weather conditions, and the influence of various vehicle operational characteristics.

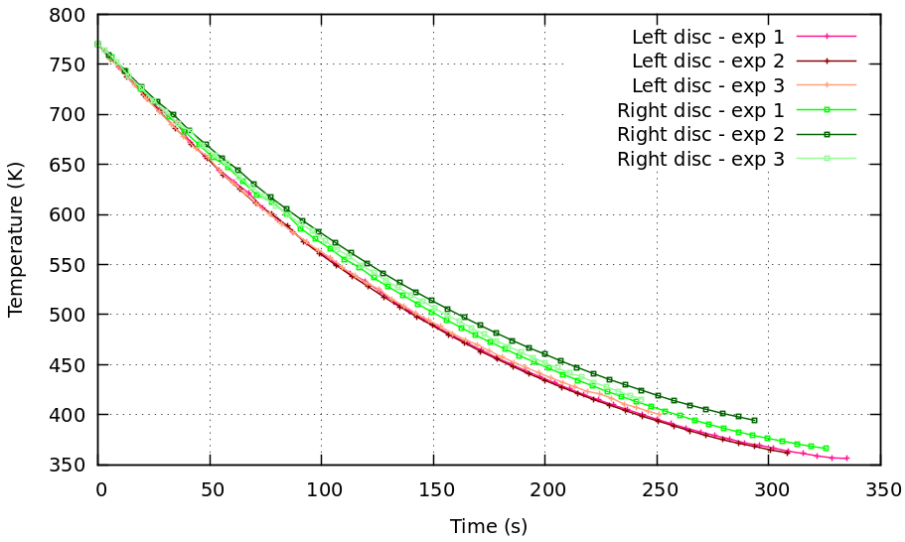


Figure 11 Experimental measurements of cool-down rates for front left and right brake discs

Using the BAF method in conjunction with the S2S radiation model and the Sutherland conductivity model for numerical simulations, the computational results accurately predict the cool-down behaviour for the left disc, as shown in Figure 12.

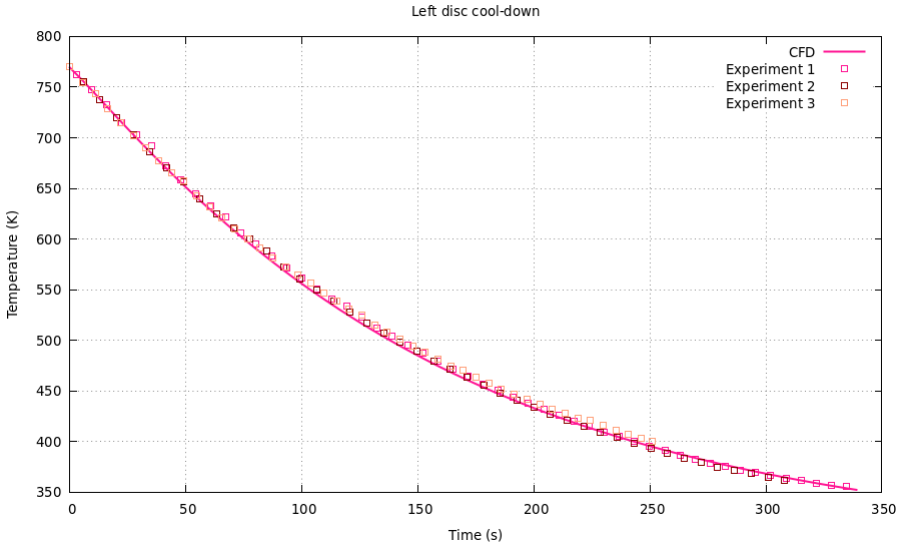


Figure 12 Comparison of cool-down rates for the front left disc

However, for the right disc, our numerical prediction underestimates the cool-down time (see Figure 13).

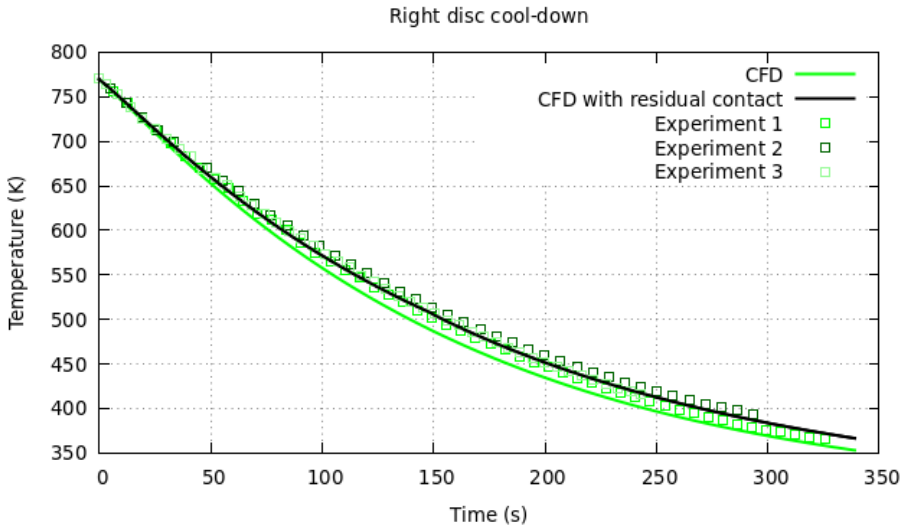


Figure 13 Comparison of cool-down rates for the front right disc

Interestingly, it is worth noting that the cooling curve of that same right disc shows greater spread in measurements in comparison with the left one, as shown in Figure 11. This could indicate the presence of a sensitive transient physical phenomenon in the right wheel arch, which could be difficult to capture with a steady-state airflow solver.

Whereas the collected data reveals a notable difference in the experimental cool-down rates between the left and right brake discs, this is not replicated in the CFD results. Different modelling approaches (e.g. transient DES) for the airflow prediction could be further investigated to help resolve this difference.

Another possible reason for the difference in cool-down observed on the right side may be a residual contact between the pad and the disc which can happen after long braking periods. It was observed that on the prototype vehicle used in the experiment, the pull-back mechanism of the calliper on the front right was not always functioning properly, and thus potentially resulting in this residual contact generating additional heat. Modelling this effect in the CFD simulation results in a better correlation with experiment, as shown in Figure 13.

## 5 Conclusion

An innovative simulation process has been introduced, providing an efficient tool to explore the performance of brake disc cooling designs. In the realm of thermal modelling for rotating brakes, a novel model based on band-averaged heat flux calculation has been developed and presented. This approach ensures precise predictions of thermal distribution while retaining the use of a static mesh, consequently leading to significant reductions in simulation turnaround times.

Furthermore, we have illustrated the practical utility of this model by employing a generic full vehicle model that incorporates a simplified brake assembly. The outcomes strongly demonstrate the impacts of various cooling devices on brake performance.

A practical case study involving an Audi vehicle demonstrates that precise modelling can effectively align with real-world track data. Joint efforts with AUDI AG have confirmed the reliability of this approach, enabling engineers to enhance the cooling efficiency of brake systems. This method demands only a 50% increase in CPU time compared to a stand-alone EA simulation.

## 6 Bibliography


[1] Rene Devaradja, Jacques Papper, “A novel Brake Cooling Simulation Capability”, NAFEMS France Conference Presentation, 2018

[2] Christian Taucher, Jacques Papper, Rene Devaradja, Sebastian Geller, “Cloud-based thermal simulation of brake disc cooling performance”, EuroBrake 2022, EB2022-MDS-013

[3] iconPlatform simulation cloud, https://www.iconcfd.com/product/cfd-simulation-cloud, https://platform.iconcfd.com/

[4] Zhang, C., Tanneberger, M., Kuthada, T., Wittmeier, F. et al., "Introduction of the AeroSUV-A New Generic SUV Model for Aerodynamic Research", SAE Technical Paper 2019-01-0646, 2019, https://doi.org/10.4271/2019-01-0646.

# Sustainable Thermal Management of Passenger Cars using multi-fidelity AI-models

Patrick K.S. Vaudrevange [0000-0002-1528-6430],
Matthias Moullion [0009-0000-1417-0447],
Hendrik von Schöning [0009-0007-8807-0001],
Tobias Rößler [0009-0008-3820-999],
Frank Beutenmüller [0009-0000-3648-4519],
Victor Fäßler [0009-0000-6519-9098]

TWT GmbH Science & Innovation
Ernsthaldenstraße 15, 70565 Stuttgart

patrick.vaudrevange@twt-gmbh.de
matthias.moullion@twt-gmbh.de
hendrik.vonschoening@twt-gmbh.de
frank.beutenmueller@twt-gmbh.de
victor.faessler@twt-gmbh.de

**Abstract:** In the context of the introduction of electromobility, the importance of thermal management will continue to increase, especially in terms of sustainability. In vehicle development, thermal management is validated with both tests and simulations. Due to time constraints, simulations are often performed with simplified models (1D models). In special cases, however, complex and more accurate 3D CFD simulations are also used. Artificial intelligence is just establishing itself here, alongside testing and simulations, as the 3rd pillar in vehicle development. The use of neural networks is particularly well suited for complex problems where many simulations would be necessary to arrive at the optimum. By using AI surrogate models, simulation times are drastically reduced, and the accuracy of the results is increased. This not only makes the development process more economical, but also more sustainable.

## 1 Motivation

As the number of BEVs sold increases, it is becoming clear that availability of materials required for battery cells, such as lithium, will be critical [1] or at least a bottleneck [2], even with new battery technology like lithium iron phosphate and solid state. OEMs are therefore striving to maximize the efficiency of their vehicles so that the same range can be achieved with fewer battery cells. In addition to optimizing the powertrain efficiency the reduction of the $c_W$ value and an optimization of the thermal management are promising measures [3].

Reducing the size of the cooling air inlet area in the front of the vehicle reduces the $c_W$ value [4], but also influences the cooling performance of the vehicle radiators due to the lower cooling air mass flow. This is achieved with electrically controllable shutters, which are located in the front of the vehicle between the air intake and the radiator package. Optimum control can be implemented if the $c_W$ value or drag performance and the cooling capacity of the vehicle radiators as a function of the vehicle speed, the shutter angle and the fan control are known. [5]

Experience from our projects has shown that for an acceptable number of grid points per degree of freedom, a map of several 100 to more than 2000 points may be required (Table 1). A CFD simulation of the complete vehicle can provide $c_W$ values as well as air mass flows of the vehicle radiators, which can be converted into cooling power. However, the simulations are too complex to calculate the complete characteristic map.

Physically based 1D models allow calculations in acceptable time but cannot represent all flow phenomena and therefore show deviations of more than 25% (Figure 6) compared to CFD in some map ranges. The method presented in the following solves this problem by combining results from the 1D models with a limited number of results from CFD simulations and thus reduces the deviation in the entire map range to less than 10%.

The result is sustainable in a double sense, as it reduces both the energy consumption of a BEV and the need for time-consuming CFD simulations.

This work is structured as follows: In Section 2, we elaborate on the need of accurate thermal simulations in more detail and describe our approach of multi-fidelity AI surrogate models. Then, we briefly describe the setup of our thermal simulations in Section 3. Afterwards, the neural network's architecture and training are presented in Section 4. In Section 5, we present our results and, finally, Section 6 gives our conclusions.

## 2 Multi-fidelity surrogate models for thermal simulations

Precise thermal simulations are often very time-consuming. For example, a single, physical accurate CFD simulation for the described case can easily take one day. In addition, during the engineering process or for testing various configurations (like for different speeds of the vehicle) not a single thermal simulation is needed but many – for example, hundreds or even thousands. This renders traditional thermal simulations highly inefficient. Nevertheless, an optimal thermal management is of upmost importance. Examples include: the cooling of the electric motor to maximize the powertrain efficiency and continuous power [6] [7], the cooling of the battery cells to increase their lifetime, and the reduction of the vehicle's $c_W$ value. Hence, thermal management has a large impact on the vehicle's sustainability [4]. Consequently, there is a strong need for faster thermal simulations without downgrading the precision of the results.

Surrogate models based on neural networks can help us out [8]. Once a neural network has been trained to predict the outcome of a thermal simulation, its evaluation only takes a little time. For example, in our case evaluating a trained neural network takes around 20-50 ms on a standard computer. Hence, comparing a CFD simulation with a trained neural network the speed-up is easily of the order $10^6$. However, to train a neural network successfully, one needs enough training data. This training data can originate from simulations or from wind tunnel tests. Both cases are again time consuming and expensive. Hence, the question arises how to successfully train a surrogate neural network without investing too much time and resources into creating training data.

In this paper, we use the approach of multi-fidelity to train a precise thermal surrogate model. The multi-fidelity modelling method exploring abundant low-fidelity (LF) data and limited high-fidelity (HF) data is considered the potential method to effectively reduce the acquisition cost of labelled data [9] [10] [11]. As the name "multi-fidelity" suggests, this training is done stepwise. First, we pre-train a neural network using a lot of training data of low precision. This data has been created using fast physical based 1D simulations. Then, in a second training step, we continue the training of the pre-trained neural network using a few cases from precise CFD simulations, especially in those regions of the parameter space, where the results of the 1D simulations differ most from the results of the precise CFD simulations. In this way, we obtain a precise thermal surrogate AI-model without spending too much time and resources into creating training data. This method is also applicable to new battery technology like lithium iron phosphate and solid state.

In the following, we will describe the setup of our thermal simulation and the corresponding multi-fidelity surrogate model in more detail.

## 3 Setup of the thermal simulation

For the thermal management one needs to simulate the air mass flows at the coolant radiators. Therefore, we built our thermal models with COOL3D from Gamma Technologies. In this 3D tool, the air inlets above and below, the shutters top and bottom, radiators, fan and air outlets are modelled based on CAD data, as shown in the example in Figure 1. The model is then discretized to 1D. Pressure losses of the components are stored in maps. The model allows the air mass flow of the cooler to be calculated as a function of the vehicle speed, fan control and shutter control. In total we sample 2.688 points in this space, see Figure 2.

| Parameter | Number of settings |
|---|---|
| Vehicle speed | 7 |
| Fan control | 6 |
| Shutter top | 8 |
| Shutter bottom | 8 |
| Total number of settings | 2.688 |

Table 1: Parameter space for the 1D simulations

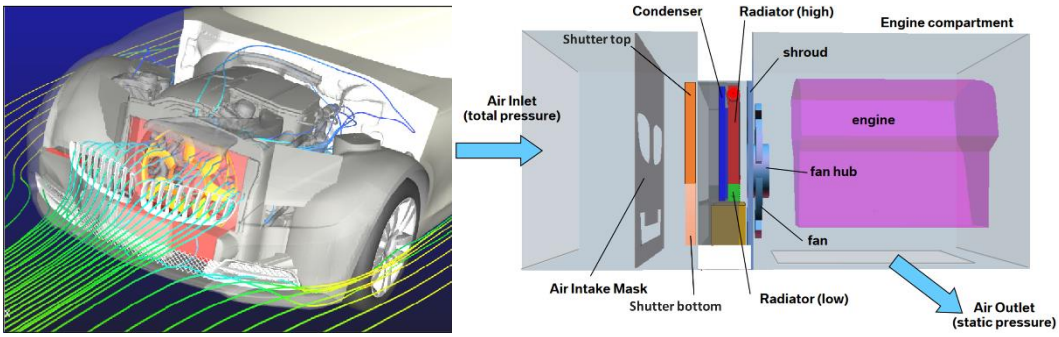


Figure 1: CFD and COOL-3D model of the vehicle front with shutter top and bottom. Right image: Green: radiator for the battery. Red: radiator for the electric motor [12].

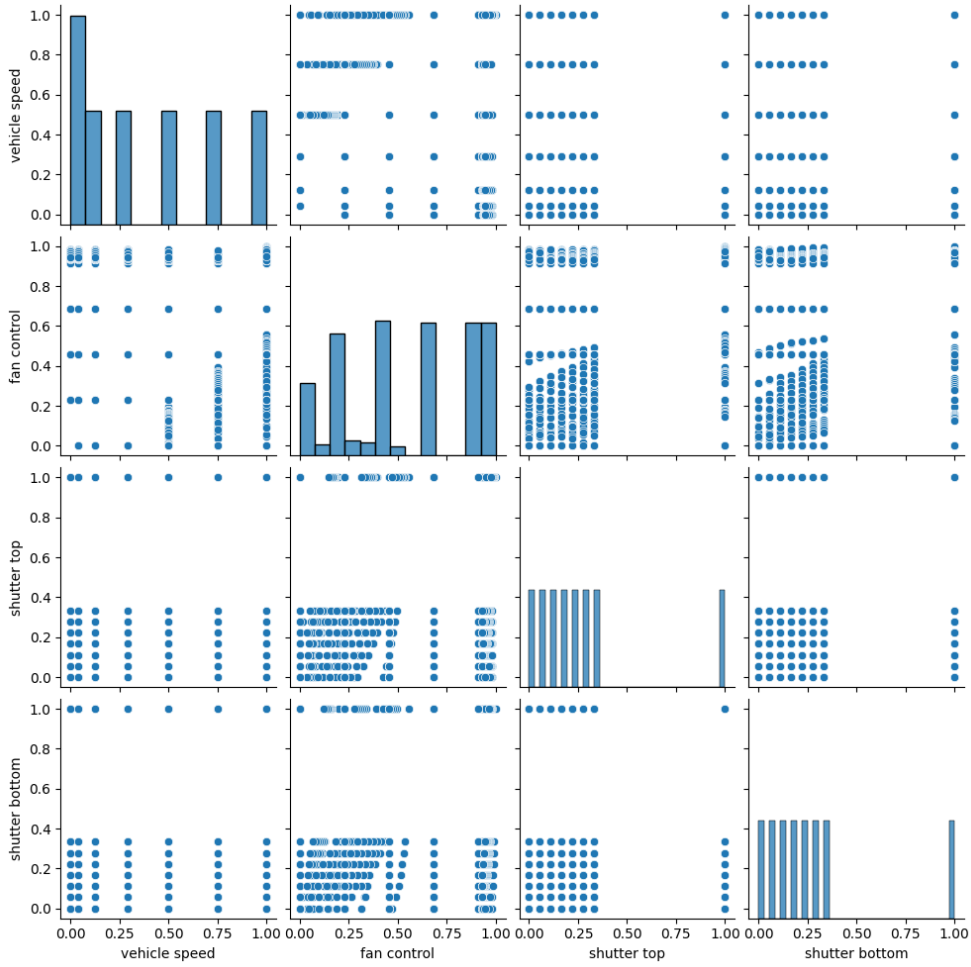


Figure 2: Pair-plot of (normalized) parameter space for the 1D simulations: the plots on the diagonal give histograms of the respective quantities, and the off-diagonal plots visualize the corresponding two dimensions as scatter-plots.

## 4 Multi-fidelity surrogate model

We use two surrogate models, one for the radiators of the electric motor and one for the battery, respectively. On a technical side, our surrogate models are based on neural networks of the following network architecture:

- input layer with 4 neurons corresponding to the four parameters: vehicle speed, fan control, shutter top, shutter bottom,
- 4 hidden (dense) layers with $x$ neurons each and tanh activation function, where $x = 20$ for the radiator of the electric motor and $x = 9$ for the radiator of the battery, respectively,
- 2500 training epochs with callbacks: early stopping and reduce learning rate on plateau,
- 80% training data, 10% validation data, and 10% test data,

- optimizer: Adam,
- activation function of output layer: sigmoid,
- loss function: mean squared error.

For both cases, i.e., radiator of the electric motor and radiator of the battery, the architecture has been identified to be especially suitable by scanning over various configurations. In the following, we briefly describe the two-step procedure to obtain the multi-fidelity surrogate AI models for our use case.

### 4.1 Pre-training with low-precision data

In the first step, we pre-train the neural networks for the air mass flows at the radiator of the electric motor and at the radiator of the battery using the results of the 1D simulations only. Here, we take 80% to train the neural network, 10 % for validation (i.e., to adopt the learning rate and to identify over-fitting), and the final 10 % are used as test data in order to see how our models generalize to previously unseen data.

The resulting losses read:

- for the surrogate model for the radiator of the electric motor:
  - using all data: $1.616 \cdot 10^{-5}$
  - using the test data: $2.885 \cdot 10^{-5}$
- for the surrogate model for the radiator of the battery
  - using all data: $3.881 \cdot 10^{-5}$
  - using the test data: $4.482 \cdot 10^{-5}$

Hence, the surrogate models generalize very well on the test data. Further details will be discussed in Section 7.

### 4.2 Final training with high-precision data

In the second step, the CFD data (consisting of only 57 CFD simulations) is used to specialize the pre-trained neural networks to reproduce the more precise CFD simulations. Before doing so, we compute the losses of both pre-trained models on the respective CFD data, resulting in the following losses:

- for the surrogate model for the radiator of the electric motor:
  - using all CFD data: $90.201 \cdot 10^{-5}$
- for the surrogate model for the radiator of the battery
  - using all CFD data: $985.776 \cdot 10^{-5}$

Consequently, we see that the pre-trained models as such do not generalize well to the CFD data, as expected. For the electric motor the loss increased by a factor 50, while for the battery the loss increased even more: by a factor 250.

Hence, we specialize the pre-trained models using either various fractions of the CFD data or all CFD data (i.e., 1/3, 2/3, or all data) and train for at most 5000 additional training epochs (using an "early stopping callback" that ends training if the accuracy of the validation set is not improving for a certain number of epochs). The results are given in Table 1 and discussed in the next section in more detail.

| **Model** | **Loss of model "Radiator for electric motor"** | **Loss of model "Radiator for battery"** |
|---|---|---|
| Base surrogate model | $90 \cdot 10^{-5}$ | $99 \cdot 10^{-4}$ |
| specialized using 1/3 CFD data | $37 \cdot 10^{-5}$ | $69 \cdot 10^{-4}$ |
| specialized using 2/3 CFD data | $33 \cdot 10^{-5}$ | $8 \cdot 10^{-4}$ |
| specialized using all CFD data | $7 \cdot 10^{-5}$ | $4 \cdot 10^{-4}$ |

Table 1: Losses of the various models evaluated on the CFD data for both radiators (electric motor and battery): the base surrogate models have been trained using only data from 1D simulations, while the specialized surrogate models originate from the respective base models with continued training using 33%, 66% or 100% of the CFD data.

## 5 Results

Our base surrogate models for the air mass flows at the radiators for the electric motor and the battery, respectively, reproduce the results from the 1D simulation to very high accuracies, see Figure 3. If one applies these base surrogate models to the results from the CFD simulations, one sees larger deviations, see

Figure 4. This outcome is expected, since the CFD simulations are physically more accurate than the 1D simulations. The discrepancy is especially large for the radiator of the battery, where many results from CFD simulations differ by more than 20 % from the 1D results.

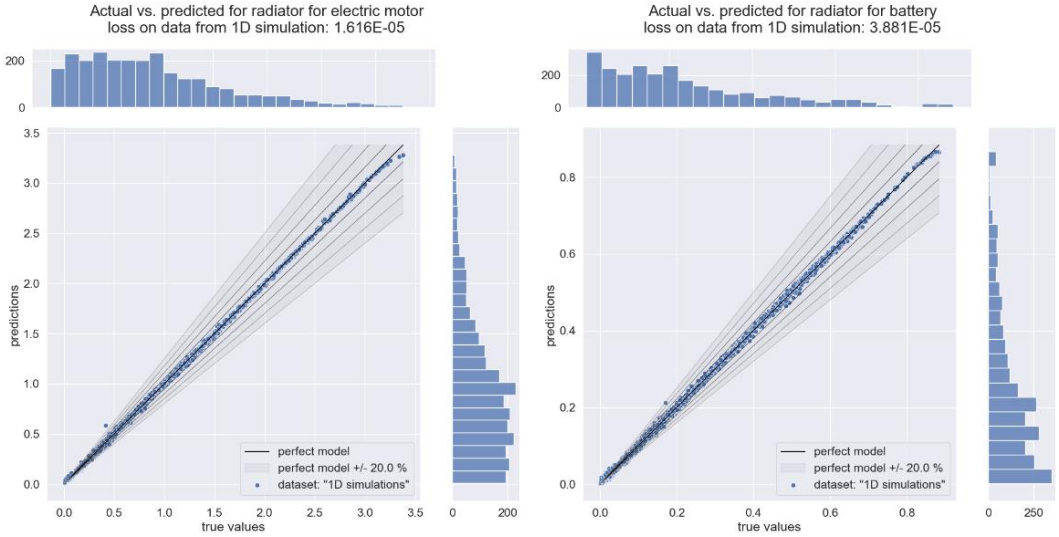


Figure 3: The base surrogate models (trained using data from 1D simulations) reproduce the results from the 1D simulations to a very high accuracy.

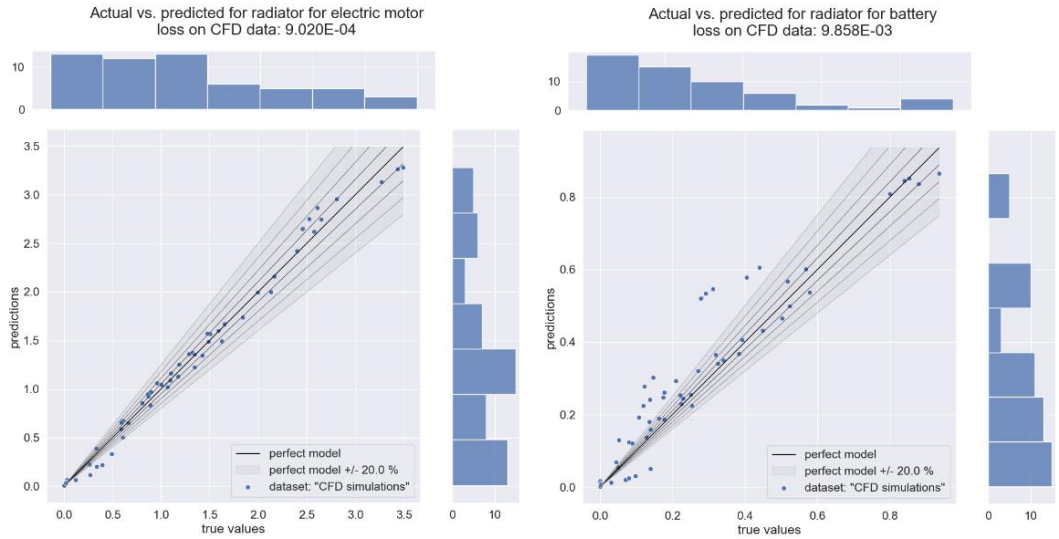


Figure 4: The base surrogate models (trained using data from 1D simulations) cannot reproduce the CFD results. This result is expected, as it is known that CFD simulations are more accurate than 1D simulations.

In addition, we plot histograms of the differences between the predictions of the base surrogate models and the values computed using the CFD simulations. In Figure 5, we show the differences for the air mass flow at the radiator for the electric motor (normalized to the range from 0 to 1). Here, the differences range up to 0.07. On the other hand, the histogram Figure 6 shows that for the battery radiator the corresponding base surrogate model yields differences that range up to 0.25 from the CFD results. This confirms our interpretation of Figure 4 that the CFD simulation is rather similar to the 1D simulation for the radiator of the electric motor but very different for the radiator of the battery.

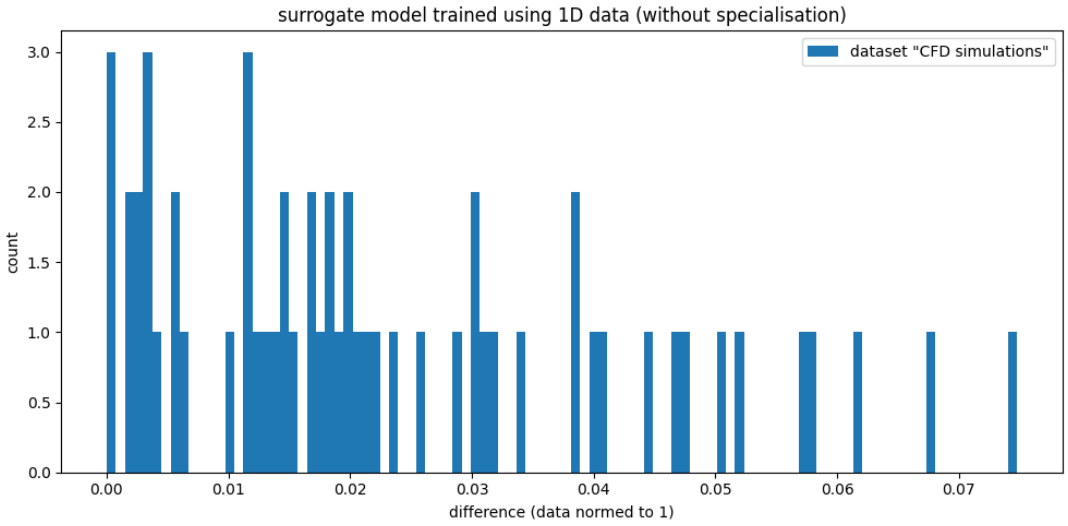


Figure 5: Histogram of absolute errors in the (normalized) air mass flow at the electric motor radiator. Here, the base surrogate model has been evaluated on the full set of CFD data, showing that the CFD results can differ (up to 7% for the normalized data) from the results of 1D simulations.

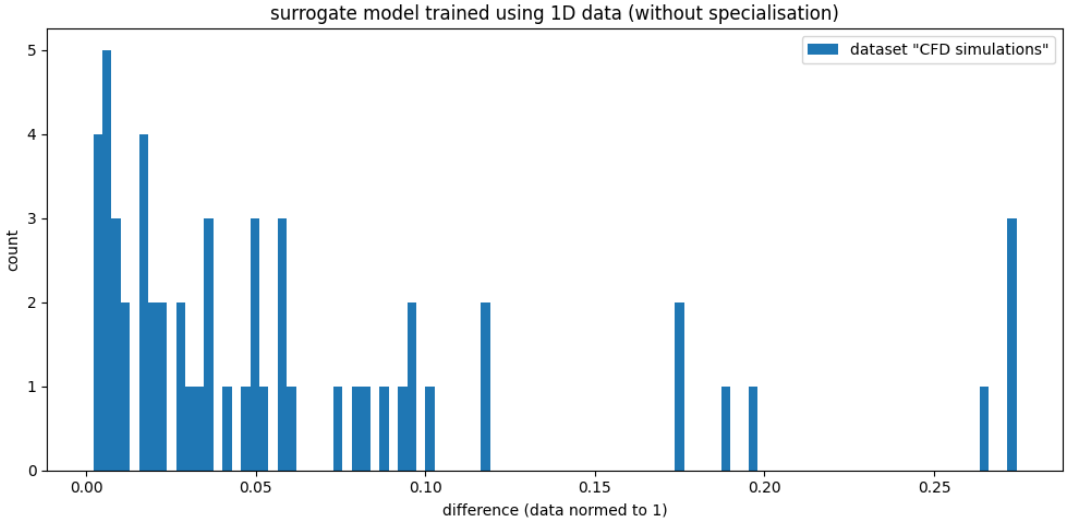


Figure 6: Histogram of absolute errors in the (normalized) air mass flow at the battery radiator. Here, the base surrogate model has been evaluated on the full set of CFD data, showing that the CFD results can differ quite drastically (up to 25% for the normalized data) from the results of 1D simulations.

## 5.1 Air mass flow at the radiator for the electric motor

After continuing training of the base surrogate model for the air mass flow at the radiator for the electric motor using CFD data, the absolute errors from Figure 6 decrease step-by-step when using more and more CFD data. Using all CFD data, the final multi-fidelity surrogate model is in excellent agreement with the results from simulations, see Figure 7.

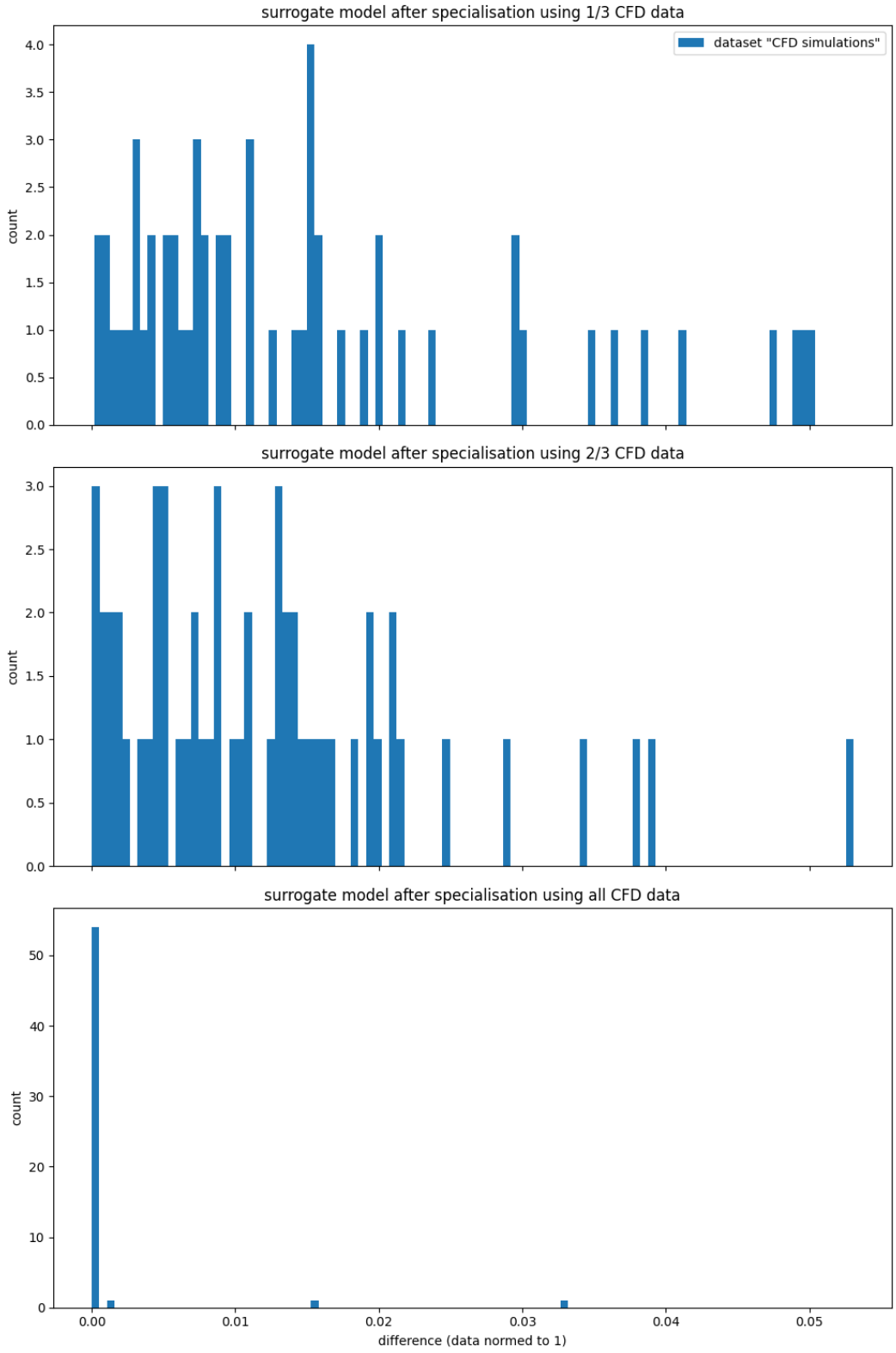


Figure 7: Histograms of absolute errors in the (normalized) air mass flow at the electric motor radiator. From top to bottom: the base surrogate model has been specialized using 33%, 66%, and 100% of the CFD data. In each case, the model has been evaluated on the full set of CFD data.

## 5.2 Air mass flow at the radiator for the battery

Repeating these steps for the surrogate model of the air mass flow at the radiator for the battery, we obtain Figure 8. This is a dramatic improvement compared to Figure 7, illustrating the strength of the multi-fidelity approach for thermal management.

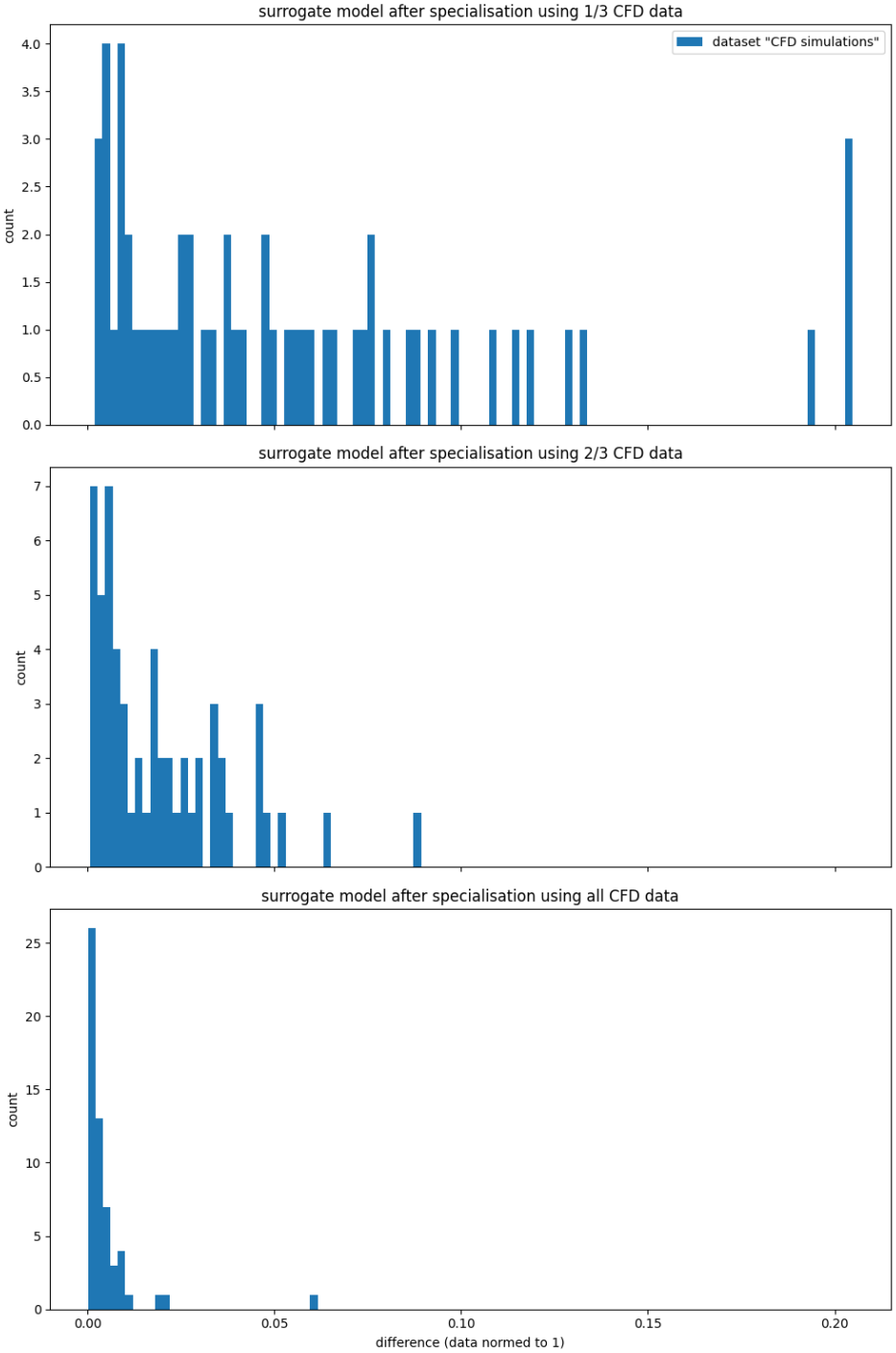


Figure 8: Histograms of absolute errors in the (normalized) air mass flow at the battery radiator. From top to bottom: the base surrogate model has been specialized using 33%, 66%, and 100% of the CFD data. In each case, the model has been evaluated on the full set of CFD data.

## 6 Conclusions

The results from chapter 5 show that with the presented method the accuracy of the cooling air characteristic maps can be significantly increased compared to the physical 1D results. With a deviation of less than 5%, the cooling performance can be predicted very well, which at the same time allows an optimal control of the active shutters and fan in terms of minimizing the energy demand. The methodology can be applied to any problem. It is particularly promising in areas where complex physical processes are to be predicted in real time.

The following areas of application are conceivable:

- The most accurate control of a complex system
- Monitoring of a component with warning of a failure
- Prediction of state variables and reduction of sensors

If CFD simulations are not available or too complex, the method can also use results from measurements [13]. This can be useful if phenomena occur which are very difficult to represent in a CFD simulation. In the example presented, this would be the case when the blades of the shutters bend at high speed.

The method can thus be a supplement to the CFD and 1D models used so far, combining the advantages of both models.

## 7 Reference list


[1] D. Gielen und M. Lyons, Critical materials for the energy transition: Lithium, Abu Dhabi: International Renewable Energy Agency, 2022.

[2] H. Ritchie, „Does the world have enough lithium to move to electric vehicles?,“ *https://www.sustainabilitybynumbers.com/p/lithium-electric-vehicles,* 2023.

[3] A. Enthaler, T. Weustenfeld, F. Gauterin and J. Koehler, "Thermal management consumption and its effect on remaining range estimation of electric vehicles," in *2014 International Conference on Connected Vehicles and Expo (ICCVE), doi: 10.1109/iccve.2014.7297537*, 2014.

[4] T. Rößler, „Systematische Analysen zur Verbesserung der Vorhersage von Kühlluftanteilen am cW-Wert in der frühen Entwicklungsphase von Serienfahrzeugen,“ 2009. doi: 10.1137/16m1082469.

[5] E. Y. Ng, P. W. Johnson and S. Watkins, "An analytical study on heat transfer performance of radiators with non-uniform airflow distribution," *Proceedings of the Institution of Mechanical Engineers, Part D: Journal of Automobile Engineering,* vol. 219, p. 1451–1467. doi: 10.1243/095440705x35116, December 2005.

[6] R. Lehmann, M. Künzler, M. Moullion und F. Gauterin, „Comparison of Commonly Used Cooling Concepts for Electrical Machines in Automotive Applications," *Machines,* Bd. 10, p. 442, June 2022.

[7] R. Lehmann, A. Petuchow, M. Moullion, M. Künzler, C. Windel und F. Gauterin, „Fluid Choice Based on Thermal Model and Performance Testing for Direct Cooled Electric Drive," *Energies,* Bd. 13, p. 5867, November 2020.

[8] J. Maerker, T. Fleischer, T. Rößler und M. Keckeisen, „Welcome to the Data Jungle – Our Way to Tackle AI-Supported Vehicle Development Projects," in *Proceedings,* Springer Fachmedien Wiesbaden, 2021, p. 263–277.

[9] M. G. Fernández-Godino, "Review of multi-fidelity models," . doi: 10.48550/ARXIV.1609.07196. September 2016.

[10] B. Peherstorfer, K. Willcox and M. Gunzburger, "Survey of Multifidelity Methods in Uncertainty Propagation, Inference, and Optimization," *SIAM Review,* vol. 60, p. 550–591. doi: 10.1137/16m1082469, January 2018.

[11] Y. Zhang, Z. Gong, W. Zhou, X. Zhao, X. Zheng and W. Yao, "Multi-fidelity surrogate modeling for temperature field prediction using deep convolution neural network," doi: 10.48550/ARXIV.2301.06674. January 2023.

[12] G. Seider, "Design of Automotive Cooling Systems with GT-COOL and COOL3D," 8 Oktober 2007. [Online]. Available: https://www.gtisoft.com/wp-content/uploads/publication/BMW_Cooling-Systems.pdf.

[13] W. Choi, K. Radhakrishnan, N.-H. Kim und J. S. Park, „Multi-Fidelity Surrogate Models for Predicting Averaged Heat Transfer Coefficients on Endwall of Turbine Blades," *Energies,* Bd. 14, p. 482, January 2021.